Studies in Mechanobiology,
Tissue Engineering and Biomaterials 15

Thomas Franz *Editor*

Cardiovascular and Cardiac Therapeutic Devices

Springer

Studies in Mechanobiology, Tissue Engineering and Biomaterials

Volume 15

Series editor

Amit Gefen, Ramat Aviv, Israel

For further volumes:
http://www.springer.com/series/8415

Thomas Franz
Editor

Cardiovascular and Cardiac Therapeutic Devices

Springer

Editor
Thomas Franz
Faculty of Health Sciences
and Research Office
University of Cape Town
Cape Town
South Africa

ISSN 1868-2006 ISSN 1868-2014 (electronic)
ISBN 978-3-642-53835-3 ISBN 978-3-642-53836-0 (eBook)
DOI 10.1007/978-3-642-53836-0
Springer Heidelberg New York Dordrecht London

Library of Congress Control Number: 2014937264

Printed on acid-free paper

Springer is part of Springer Science+Business Media (www.springer.com)

Preface

According to the World Health Organisation, cardiovascular diseases (CVD) are the leading cause of death worldwide—with a substantial increase of mortalities expected over the next decades in conjunction with epidemics of diabetes and obesity. CVD pathologies range from arteriosclerosis affecting arteries in coronary and peripheral circulation, aortic aneurysms, ischemic heart disease including myocardial infarction, heart valve diseases and heart diseases such as arrhythmia and heart failure.

Tissue engineering, biomaterials and mechanobiology are playing an increasingly important role in the treatment and management of CVD. Therapeutic devices aim more and more at facilitating regenerative and integrative approaches—with biomechanical and mechanobiological concepts being keys to improvement and optimisation of therapies.

This volume aims at providing an insight in the state of the art, current research developments and challenges in the area of implantable devices for treatment and management of cardiovascular and cardiac diseases. The selected contributions report on computational as well as experimental research to advance therapeutic devices and overcome existing shortcomings.

The first three chapters are concerned with treatment of vascular diseases, i.e. the design optimization of endovascular stents for percutaneous interventions in diseased coronary arteries, small-diameter tissue-engineered vascular prostheses for coronary artery bypass procedures required when percutaneous treatment such as balloon angioplasty and stenting renders insufficient, and large-diameter vascular grafts and stent grafts used in open surgical and endovascular treatment of aortic aneurysms.

The following two chapters focus on prosthetic heart valves—providing a review of the state-of-the-art in polymeric heart valves with flexible leaflets and patient-specific computational modelling of biological heart valve prostheses towards treatment decision support for surgical and percutaneous implantation. Although the emphasis of the computational modelling is on biological heart valves, the same or similar approaches are very likely to provide benefits for development and treatment optimisation of non-biological prosthetic valves.

The treatment of cardiac pathologies is the topic of the last two chapters. Myocardial infarction (commonly known as heart attack) leads to an adverse remodelling of the heart—primarily the left ventricle. This remodelling often leads

to heart failure for which organ transplant is the only possible treatment at present. "Cardiac Restraint and Support Following Myocardial Infarction" presents concepts of mechanical support and restraint of the infarcted heart to inhibit the pathological remodelling and prevent the development of heart failure. The final "In Vivo Mechanical Loading Conditions of Pectorally Implanted Cardiac Pacemakers" deals with research into the in vivo biomechanics of cardiac pacemakers. The main focus of previous research and development has been directed towards structural reliability of the pacemaker leads. In contrast, the present contribution describes the assessment of mechanical loadings on the implanted pacemaker body—information that is important in the context of smaller sizes of implantable devices that have become possible with advancing technologies.

Thomas Franz

Contents

Multi-Objective Design of a Biodegradable Coronary Artery Stent

Neil W. Bressloff

Abstract Ever since the mid 1980s when the first-in-man coronary stent procedure was conducted, commercially available coronary stents have evolved from the original stainless steel Palmaz-Schatz style of design to a range of highly flexible, slick structures capable of providing arterial support with very thin struts. The availability of modern alloys such as platinum-chromium has facilitated the evolution to thin strutted, highly flexible devices. However, an important juncture has been reached wherein the combination of thin struts and low numbers of stent links/bridges has introduced a new challenge associated with loss of longitudinal strength. Interestingly, this has coincided with an increasing focus on the use of biodegradable materials (e.g., polymers or magnesium). So, whilst polymer scaffolds currently require relatively thick struts, it might be anticipated that efforts will be made to develop stronger polymers also leading to thinner struts, but with the awareness of the pitfalls associated with emphasis on particular measures of performance (objectives) at the expense of others. In parallel with the evolution of coronary stents, computational methods (and hardware) have developed to a point whereby optimization and simulation tools can now be used to systematically design devices in a realistic time-scale. This chapter demonstrates how these tools can be harnessed to guide the multi-objective design process, with the ultimate aim that superior prototypes, particularly those that are biodegradable, can be designed and refined computationally.

N. W. Bressloff (✉)
Institute for Life Sciences, University of Southampton,
Highfield, Southampton SO17 1BJ, UK
e-mail: nwb@soton.ac.uk

Stud Mechanobiol Tissue Eng Biomater (2014) 15: 1–28
DOI: 10.1007/8415_2013_164

Published Online: 31 May 2013

1 Introduction

Now that metallic stents are approaching a mature stage of evolution and advances in the development of biodegradable scaffolds are supporting the realization of a fourth revolution in interventional cardiology [1], it is timely to consider what lessons have been learnt from the design of permanent metallic devices, and how best practice might be applied to the development of a growing number of polymeric scaffolds, in particular.

Interventional cardiology was first revolutionized in the 1970s when Andreas Gruntzig and colleagues performed the first human coronary balloon angioplasty in 1977. The second revolution occurred in the mid 1980s with the introduction of bare metal stents; even though the Palmaz-Schatz stent was not approved by the Food and Drug Administration (FDA) in the United States until 1994. Nearly a decade later, FDA approval was granted for Johnson & Johnson's Cypher drug eluting stent (DES), signifying a key milestone in the third revolution in interventional cardiology. DESs represent the current state of the art and a useful review of DESs is available in [2]. Whilst most widely available stents are deployed using balloon inflation [3], there is also a range of self-expanding devices which also emerged in the 1990s [4]. Three of the most popular DESs are listed in Table 1 along with the *Cypher* platform and Abbott Vascular's second generation bioresorbable vascular scaffold, *BVS-B*. The *BVS-B* device is one of the major forerunners in the fourth revolution which started in the early to mid-1990s with tests of non-biodegradable and degradable polymers in porcine animal models [5, 6] and with the first-in-man procedure of the fully biodegradable Igaki-Tamai coronary stent in 1998. Early results were presented by Tamai, Igaki and others in 2000 [7].

Some key questions are inevitably posed when considering the evolution of stent design and the implications for fully biodegradable devices. For example: (i) is there sufficient justification for stents that perform the necessary function and then disappear (within approximately 2 years)?; and (ii) will it be possible to develop strong enough polymeric stents, capable of treating the wide range of challenging disease states routinely encountered in the cath-lab? With respect to the first question, there is an increasing body of evidence to support the positive claims of Serruys [1] and others [8], including the long-term evidence (based on a follow-up study lasting more than 10 years) of the first-in-man Igaki-Tamai stents for safe and effective treatment using bioresorbable scaffolds [9], and the recent identification of late positive remodeling and late lumen gain [10], and the implications for the recovery of normal vasomotion. Indeed, there are a number of compelling reasons for favoring the biodegradable scaffold concept over that of the metallic cage.

Despite these encouraging findings, the second question above brings a major issue into focus concerning the material properties of currently available polymers and the geometric constraints associated with them. Whilst platinum-chromium has an elastic modulus, $K = 203$ GPa, the value reported for the polymer used in

Table 1 Comparison of stent platforms

Platform	Company	Material	Elastic modulus (GPa)	Strut thickness (μm)
BVS-B	Abbott Vascular	PLLA	3.3	150
Cypher	Johnson & Johnson	316L SS	193	140
Element	Boston Scientific	PtCr	203	81
Endeavor	Medtronic	CoCr	210–243	90
Xience	Abbott Vascular	CoCr	210–243	81

PLLA poly-l-lactic acid. *SS* stainless steel, *PtCr* platinum-chromium alloy, *CoCr* cobalt-chromium alloy

the Abbott Vascular *BVS-B* device is $K = 3.3$ GPa. 316 L stainless steel has $K = 193$ GPa.

Due to the low stiffness of polymers, all currently known scaffolds have significantly thicker struts than modern metallic stents; for example, the *BVS-B* scaffold has a strut thickness, $t = 150$ μm (0.150 mm) and, in trials, is being restricted to relatively straightforward, non-calcified *de novo* lesions [11]. From the thicknesses listed in Table 1, it is clear that significant research is necessary to bridge the gap between polymeric and metallic materials. For reference, the original Igaki-Tamai stent had a thickness of 170 μm.

However, a further question comes to mind at this point: how will long term performance compare between devices made from the different materials, bearing in mind that the merits of biodegradable scaffolds may more than compensate the geometric disadvantages (e.g. thicker and wider struts) necessitated by inferior material properties? Additionally, the trend towards thinner, narrower struts has recently led to a new problem of stent distortion [12, 13], a phenomenon highlighting the need to carefully consider multiple measures of performance. In this case, the drive towards thinner struts and greater flexibility has dominated all other considerations and has resulted in devices with compromised longitudinal strength. Indeed, the recognition that stent design involves a number of potentially conflicting performance metrics (or objectives) is allied in this chapter to the tools (computational and experimental) that are available to both simulate device performance and to steer the design process itself.

Section 2 focuses on the evolution in design of metallic stents, primarily with respect to geometry. In Sect. 3, currently known biodegradable scaffolds are described and mainly geometric comparisons are made in terms of key defining features. Design methodologies are considered in Sect. 4, including how they might be best exploited in the development of polymeric devices.

2 Evolution in Design

When considering the evolution of coronary stent design, it is immediately apparent that two key geometric differences have emerged relative to the Palmaz-Schatz device: (i) open cells and (ii) thinner struts. The original Palmaz-Schatz

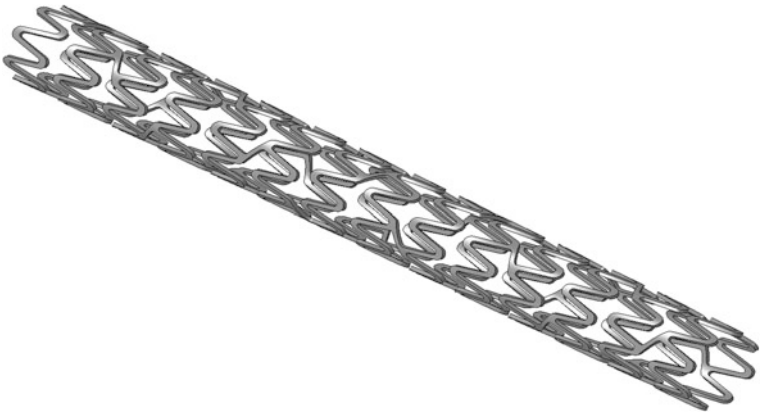

Fig. 1 CAD model of the Boston Scientific *Element* platform

stent had a thick strut, closed cell configuration. Over the years, it has been established that thinner struts reduce the likelihood of in-stent restenosis [14] and greater flexibility and conformability are achievable with open cell designs [15]. Reduced strut dimensions have been made possible by the introduction of modern alloys (including platinum-chromium, cobalt–nickel and cobalt-chromium) [1] allied to advances in manufacturing processes.

Just before the introduction of drug eluting stents, Stoeckel et al. conveniently categorized and differentiated the large number (approximately 100) of stents "being marketed or in evaluation worldwide" [16]. Stoeckel et al. suggested that the stent market would double from $3 billion "with the advent of drug eluting stents" [16]. At approximately the same time, a wide range of stents were appraised in [17]. Although there are still multiple variants of stent design, all probably motivated by intellectual property and commercial considerations, there has been significant convergence in design features towards open cell configurations, comprising rings and links/bridges/connectors (see Figs. 1, 2 in [13]) all cut by laser from thin metallic tubes and deployed by balloon inflation on a catheter. Fig. 1 shows a representative model, constructed in the Rhino Computer Aided Design (CAD) package (Robert McNeel & Associates), of the Boston Scientific *Element* platform. This represents one of the simplest manifestations (in terms of geometry) of the ring-link topology, with just two inclined bridges joining adjacent rings.

Two notable exceptions to this classification should be mentioned here: (i) Medtronic's *Integrity* platform since it is manufactured from a continuous wire and not cut from a tube, and (ii) the group of self-expanding, Nitinol stents including the STENTYS product [18]. Nonetheless, variation in design primarily exists in the relative positions of the peaks in adjacent rings and in the shape and alignment of the links between adjacent rings. Significant non-geometric differences include the platform material and the drug constituents in DESs.

So, even though it is not surprising that many different products are available in a competitive market, it is encouraging to observe, especially from the patient's

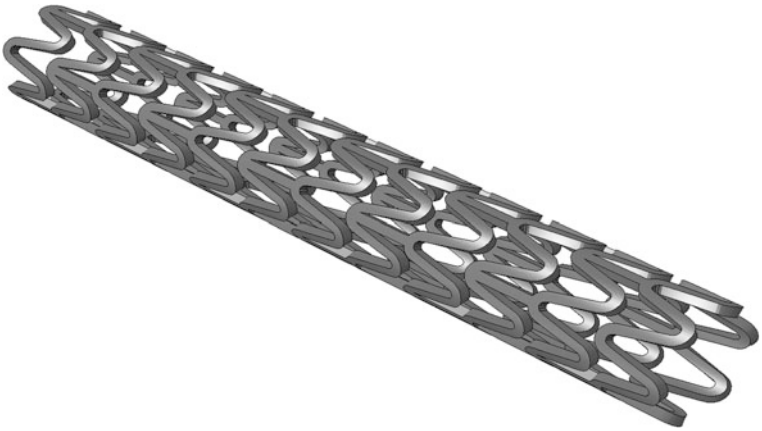

Fig. 2 Generic polymer scaffold with in-phase rings joined by straight bridges (based on the *BVS-B* platform)

perspective, that convergence in (geometric) design has taken place. Divergence (mutation) in design is also to be expected, and so niches in the market exist for self-expanding devices, for example, and other "mutations". Continuing the evolutionary analogy, it might be expected that new "species" could emerge and evolve to become market leaders. Indeed, the fourth revolution in interventional cardiology could result in bioresorbable scaffolds dominating the market. Conveniently, this family of devices is at a relatively early stage of development and so it is instructive to consider their geometric features, in particular, and to explore how design techniques can be exploited to steer their evolution. Since there are only a modest number of devices that have been publicized and shown to have reached a reasonable level of development, and even fewer that have entered clinical trials [19], a survey equivalent to the one by Stoeckel et al. may be a little premature. Nonetheless, inspired by the "stent design pyramid" in [16], the next section focuses on the geometry slice adjacent to the base of the pyramid.

3 A Survey of Bioresorbable Scaffold Geometry

Bourantas et al. [19] have presented a recent survey of bioresorbable scaffolds, principally focusing on ongoing clinical trials. Sufficient information is known concerning 10 scaffolds, each being developed by separate companies, and there are at least another five companies that are involved in the development of biodegradable scaffolds. These are Arterius Ltd (UK), Meril Life Sciences (India), Sahajanand Medical Technologies Pvt Ltd (India), S3 V Vascular Technologies Pvt Ltd (India) and Zorion Medical (US).

Table 2 Geometry configurations of known bioresorbable scaffolds

Scaffold name	Company	Cells	Rings	Links
ABSORB BVS-B	Abbott Vascular	Open	In-phase	Straight bridge
Acute	Orbus-Neich	Hybrid	–	Inclined bridge
ART18AZ	Arterial Remodelling Tech.	Hybrid	Out-of-phase	Straight bridge
Amaranth PLLA	Amaranth	Open	In-phase	Straight bridge
DESolve BCS	Elixir Medical Corp.	Open	In-phase	Straight bridge
DREAMS2	Biotronik	Open	In-phase	Wavy mid-strut
Ideal BioStent	Xenogenics	Open	In-phase	Straight bridge
Igaki-Tamai	Kyoto Medical Planning Co.	Open	Out-of-phase	Inclined bridge
ReZolve2	Reva	Slide & lock	–	–
Xinsorb	Huaan Biotech.	Open	Out-of-phase	Straight bridge

Due to the very different material properties of the polymers and metal alloys used to manufacture stents, it is important to consider whether the respective devices should be designed in the same way. However, much has been learnt over the last 20 years concerning stent geometry, and it is not by chance that many state-of-the-art devices have now converged to similar recognizable configurations; i.e., adjacent circumferential wavy rings joined by an arrangement of links/bridges/connectors. With the appropriate wave amplitude (i.e. longitudinal wave height) and wavelength (i.e. controlled by the number of circumferential peaks/crowns), plastic deformation occurs in the peaks during expansion from diameters of approximately 1 mm to a few mm, such that the device can withhold its expanded shape even when exposed to the elastic loading of a host vessel. So, whilst it might be argued that polymeric stents should *not* be designed in the same way as the well-established metallic counterparts, this is not largely apparent in practice. The understanding and proven performance of ring and link configurations is now being exploited in the designs of the majority of polymeric scaffolds and at least seven of them can be identified in this way (also see Table 2):

ABSORB BVS-B: in-phase rings joined by three longitudinally in-line, straight bridges. Fig. 2 depicts a model (constructed in the Rhino CAD package) of a generic platform with in-phase rings joined by three straight bridges.
ART18AZ: out-of-phase rings. Alternating pairs of rings are joined at all peaks by a very short bridge or at only two peaks which are positioned in a longitudinal spiral arrangement. Fig. 3 shows a CAD model based on the *ART18AZ platform.*
Amaranth PLLA: in-phase rings joined by three longitudinally in-line, straight bridges.
DESolve BCS: in-phase rings joined by three longitudinally in-line, straight bridges.
Ideal BioStent: in phase rings joined by three longitudinally in-line, straight bridges.
Igaki-Tamai: out-of-phase rings joined by three helically arranged short bridges.
Xinsorb: out-of-phase rings, each pair joined by three short straight bridges, longitudinally in-line.

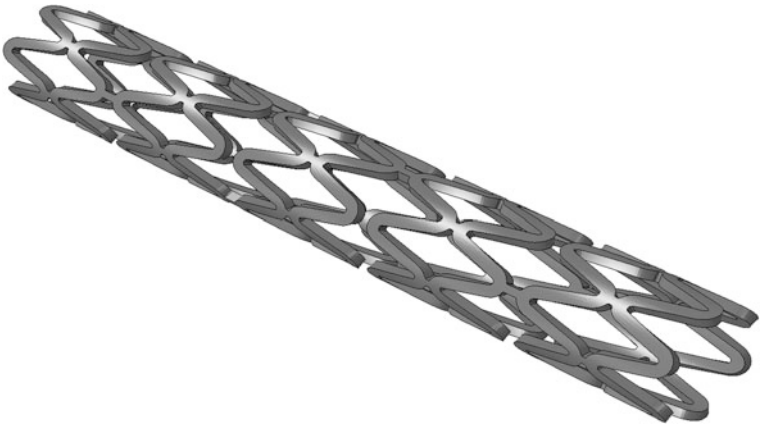

Fig. 3 Generic polymer scaffold with out-of-phase rings (based on the *ART18AZ* platform)

Thus, there are four polymeric devices with in-phase rings and three with out-of-phase rings. The four in-phase devices are topologically very similar, although the *Ideal BioStent* differs due to having very wide struts.

The three out-of-phase devices have more significant differences with respect to the arrangements of bridges between adjacent rings. In particular, the *ART18AZ* design has alternating pairs of rings that form arrays of closed and open cells (c.f. Fig. 3).

The *Acute* device (Orbus-Neich) is less obviously defined in the same way as the seven above. However, in its expanded shape, it can be described as comprising arrays of closed cells (formed by pairs of adjacent rings) with each array joined by three inclined, longitudinal bridges. Since the lengths of the bridges are comparable to the longitudinal length of each closed cell array, it can be classified as a hybrid device.

The two remaining well known biodegradable scaffolds have significant characteristics that distinguish them from the other eight. The *ReZolve2* device (Reva Medical) is polymer based and balloon expandable, but it has a unique slide and lock mechanism. The *DREAMS2* device (Biotronik) is the only non-polymeric bioresorbable scaffold; made from magnesium alloy, it looks like a conventional metallic stent. Geometrically, it can be classified as an open cell device with wavy, in-phase rings joined by wavy mid-strut links.

Most of the information described above has been obtained directly from company internet pages and complemented by images and details in the literature [13, 19]. Accurate dimensions have not been obtained for all platforms and, in general, only strut thicknesses are publicly available. Based on the available data, all known thicknesses range between 150 and 200 μm for polymeric devices, but the magnesium alloy *DREAMS* device is 125 μm thick. As discussed above, these thicknesses are significantly larger than those for state-of-the-art permanent metallic stents. This suggests that current and future research is likely to focus on reducing the thickness (and the width) of bioresorbable scaffolds. Essentially,

material strength needs to be increased through tube/material treatment, additives and/or other methods. Durand et al. have recently demonstrated the effect of co-polymer composition on radial strength and biocompatibility, albeit still at relatively low levels of material stiffness [20]. As advances are made, opportunities will emerge to further enhance the geometries of the underlying platforms, and therein lays the possibility to efficiently develop optimal designs using design optimization tools and high performance computing [21].

4 The Design Process

When undertaking a design study (experimental and/or computational) it is likely that a finite number of different designs can be assessed and compared in the search for an optimal design. This is particularly the case in industry where commercial demands normally restrict the time available to develop a product. Often, satisfactory design improvement is accepted whilst recognizing that too much time would be needed to find the best of all designs. Hence, the designer has to formulate how many different design realizations can be tested in the available time and this depends on

(i) the design methodology (and problem fidelity);
(ii) parameterization (the inputs); and
(iii) measures of performance (the outputs).

Since the focus here is on the computational design of coronary artery stents, these dependences are now considered in this respect, thus introducing a further, specific (modeling) dependency: the availability and power of computers and software. In contrast, a laboratory experimental approach is dependent on the effectiveness of available testing equipment.

4.1 Design Methodology (and Problem Fidelity)

Most coronary stents are supplied pre-crimped on a catheter, so the deployment of balloon inflated coronary stents involves positioning with the aid of angiography, followed by expansion through high pressure filling and inflation of the balloon using a contrast agent. It is possible to simulate the complete interventional procedure using finite element analysis (FEA), although the positioning step is only occasionally included [22], balloons are sometimes replaced by a displacement boundary condition [23] and balloon inflation is controlled by surface pressure applied to the inner surface of the balloon. Although real devices are pre-crimped before delivery to the cath-lab, the crimping procedure can also be simulated in order to capture the pre-strain it generates [24, 25]. At the very least, the structural deformation of the stent is simulated. However, simulations of free expansion ignore

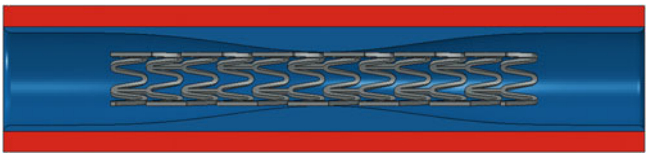

Fig. 4 Representative diseased artery segment before stent deployment

the important interaction that occurs in contact with a diseased host vessel. Relative to this low level of fidelity, high fidelity simulations include crimping, positioning and balloon expansion (see Figs. 5, 6, 7, 8 below) inside a vessel comprising plaque and the artery wall, both modeled by appropriate constitutive formulations [26]. The vessel may be representative [21] or based on a real patient [27].

Figure 4 depicts a representative diseased segment. Such models are relatively simple and fast to setup and manipulate, all within CAD software. Here, the constriction shape is based on a Hicks-Henne definition [28].

In contrast, Fig. 5 shows a reconstructed, patient specific right coronary artery segment. Using a time consuming manual process, a set of intravascular ultrasound (IVUS) slices have been combined with two approximately orthogonal angiogram projections, all obtained in Southampton General Hospital cath-lab. This model has been setup in preparation for ongoing patient specific design studies at the University of Southampton, UK.

Also shown in Fig. 5 are models of the Boston Scientific *Element* stent platform, catheter and guide wire. As mentioned above, a high fidelity simulation involves crimping, positioning and expansion. For this model, preliminary tests have been successfully completed for these steps in Abaqus Explicit 6.11.1. Figures 6, 7, 8 show snap-shots in the three steps.

First, the stent is crimped onto a catheter (c.f. Fig. 6) using an external surface (not shown) with an applied displacement boundary condition on its outer surface. The stent is assumed to be made from the platinum-chromium alloy with an elastic modules of 203 GPa, Poisson ratio of 0.35 and yield stress of 455 MPa.

Once crimped, the stent is moved into position (c.f. Fig. 7) by applying a displacement boundary condition on the proximal end of the catheter. A contact definition between the catheter and the guide-wire forces the catheter to follow the line of the guide-wire, fixed according to the position extracted from the original IVUS images.

Figure 8 depicts the final deployed position of the stent following expansion using a surface, again controlled by a displacement boundary condition. This surface approach offers a faster simulation alternative to modeling the inflation of a balloon [24]. The tissue is modeled as a hyperelastic material using the Holzapfel strain energy potential constitutive model in Abaqus 6.11.1.

In addition to the simulations described above, it may also be necessary to perform other simulations for flow disturbance (using computational fluid dynamics (CFD)) [29] and other structural considerations (e.g. flexibility, fatigue, longitudinal strength) [11].

Fig. 5 Patient specific right coronary artery segment. A Boston Scientific *Element* stent model is also shown before crimping on a catheter, guide-wire system

Fig. 6 Crimping of the Boston Scientific *Element* stent model

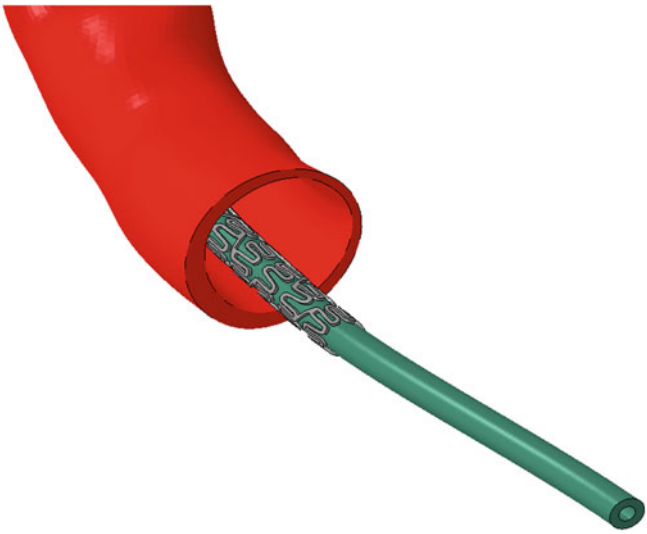

Fig. 7 Positioning of the Boston Scientific *Element* stent model

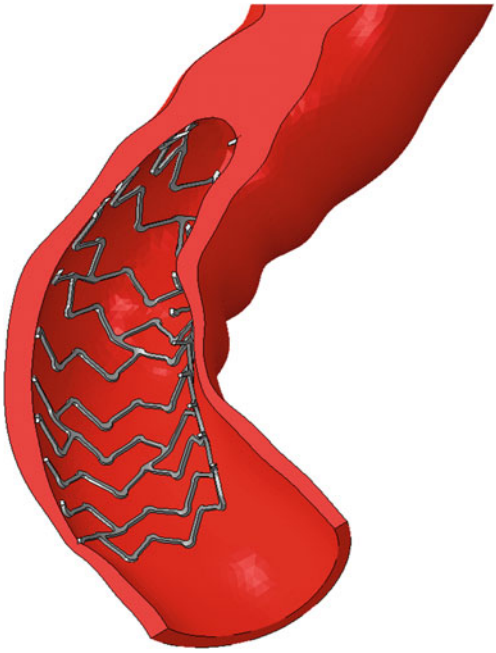

Fig. 8 Expansion of the Boston Scientific *Element* stent model

The time to run simulations of a single design can differ by two orders of magnitude or more. Thus, depending on the amount of time available, a decision has to be made concerning the level of fidelity to use. If a relatively high level of fidelity is required, a number of days are likely to be needed to simulate a single design realization [21] (even when using parallel computing on high performance computers). In contrast, sixty single ring configurations were simulated overnight using low fidelity simulations in [30]. Software licensing may also constrain the speed of computation by restricting the number of parallel licenses that can be used.

4.1.1 Surrogate Modeling

When individual simulations are expensive, the most appropriate way to perform design search and optimization (DSO) involves the response surface methodology wherein a surrogate model (or response surface) is constructed to represent the relationship between design outputs (measures of performance) and design inputs (parameters, often geometry based). Fig. 9 depicts the key steps in response surface modeling. These are shown on the left hand side of the chart (numbered 1–7), whereas the box on the right hand side describes the process of modeling individual designs.

(1) Starting from a new concept, it is necessary to construct a CAD model of the baseline stent. Typically, this is likely to involve hands-on manipulation of shapes using a graphical user interface (GUI), combined with the development of a computer script (or code). Ideally, the script can completely construct the model as a batch process without opening the GUI. This automated approach is favored since significant time can be saved by not having to manually craft individual designs.
(2) During model construction, a number of variables are likely to be setup, but only a relatively small number of them are defined as input parameters (c.f. Sect. 4.2). For each parameter, an appropriate range of acceptable values has to be defined by upper and lower bounds. Similarly, decisions are made at this stage for the measures of performance (or outputs) to be used (c.f. Sect. 4.3) and whether any constraints are to be defined. Also, problem definition and setup requires the appropriate simulation approaches to be setup, tested, verified and validated if possible.
(3) Having constructed a baseline configuration and defined the parameterization, it is now necessary to identify a family of designs (based on the baseline) that is to be analyzed. This initial sample needs to be appropriately distributed throughout the design space and a number of space-filling algorithms (or design of experiments) are available to do this. Decisions concerning the selection of a particular design of experiment and the size of the sample are discussed in [31].
(4) Analysis of each design involves three key stages: (a) model construction including setup of the mesh, boundary conditions and initial conditions;

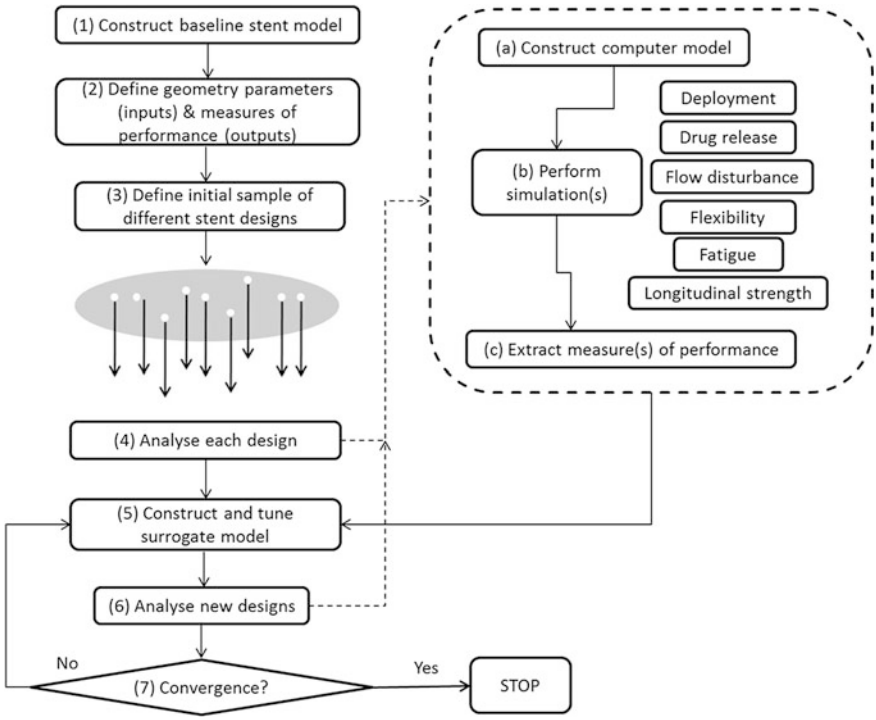

Fig. 9 Flow chart showing the process of surrogate modelling

(b) simulation(s) and (c) post-processing of the simulation(s) to extract appropriate measure(s) of performance. In most cases, some form of deployment simulation is included and then one or more of the other simulations (e.g. CFD, flexibility) are conducted, dependent on the measure of performance needed.

(5) Construction (and tuning) of the surrogate model involves the evaluation of hyper-parameters used in the mathematical formulation of the surrogate model, by substituting the inputs and associated outputs into this formulation. In other words, the surrogate model is a generic mathematical function with unknown terms (or hyper-parameters) that have to be evaluated for the known inputs and outputs, respectively defined and obtained, for the family of designs simulated in step (4). Tuning of the surrogate model is normally required so as to improve its accuracy. Based on the inputs and outputs, tuning maximizes the likelihood that the model reproduces the known outputs for the given inputs. The preferred choice of surrogate model, and the one used to generate the response surfaces shown in this chapter, is Kriging [32, 33], popularized in [34].

(6) Once the model has been constructed it can be searched and tests performed to identify where new designs should be analyzed. So-called update points are then added to the family of designs used to construct the original model.

Normally, the same simulations as were used for the initial sample are performed for each new analysis.

(7) Termination of the process occurs when a suitable level of convergence is reached in the surrogate model and/or the available time for the design process is exhausted. If additional designs need to be analyzed, and time is available, further simulations are performed and the surrogate model is re-constructed. This loop is repeated until convergence. In Sect. 5, a time-limited design study is described for one of the new generation of biodegradable devices.

4.2 Parameterization

Parameterization often involves geometry variables appropriately setup so that a family of different designs can be generated and compared. For a given coronary stent design concept, these variables are likely to define the shapes of the crowns, links and strut cross-section. In [30], five shape parameters were varied: strut width, strut thickness, crown radius, strut length and weld radius. Pant et al. kept strut thickness constant in their study of a generic closed ring metallic stent and assessed the effect of strut width, ring length (equivalent to strut length) and two parameters that define the wavy links [25]. Experience in this work led to a three parameter assessment of the *Cypher* platform in which the wavy links were controlled by a single parameter [21].

In contrast to the direct manipulation of geometry parameters, Wu et al. controlled the shape of a single stent ring unit by moving mesh nodes in a pre-meshed baseline model and used a mesh morphing procedure to maintain a good quality mesh in the morphed shapes [35]. There are also a number of other shape control methods that can be used including free form deformation and spline and surface control point manipulation. Further consideration of optimisation studies is included in [21].

4.3 Measures of Performance

Radial strength often represents the key design objective since, unless a device can resist the elastic recoil of the vessel it is meant to support, other measures of performance are not worth consideration. Fig. 10 shows three stages in the simulation of expansion of the model of the *BVS-B* platform originally shown in Fig. 2. An elastic membrane (representative of a semi non-compliant balloon) is inflated into contact with the inner surface of the stent as shown in Fig. 10a. Note the dog-boning effect at the end of the stents. In Figs. 10b, c, respectively, the stent is shown in its fully expanded and final (post recoil) states. The balloon material has been removed from these views so that the expanded stent can be clearly seen.

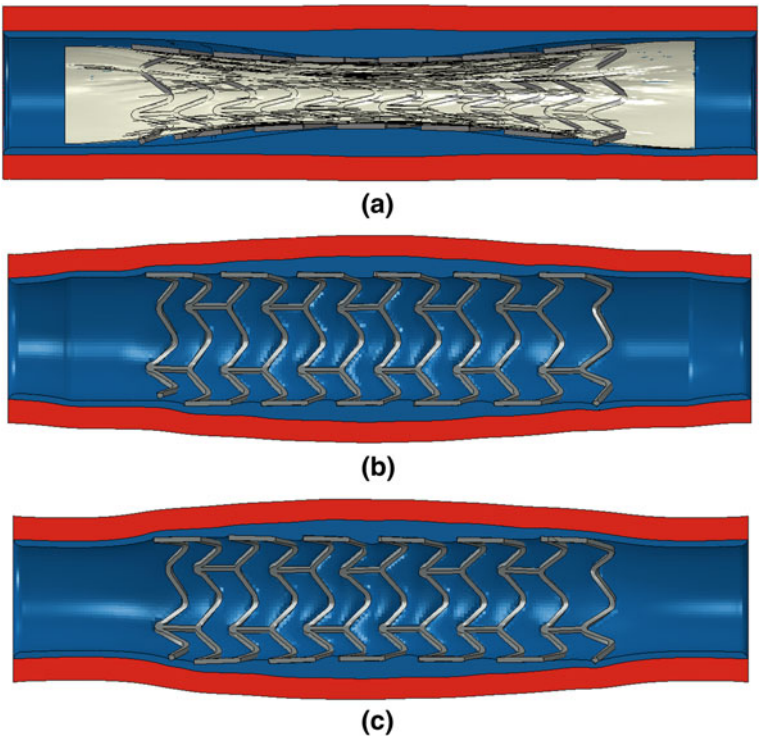

Fig. 10 Expansion and recoil of the *BVS-B* model: **a** balloon inflation; **b** fully expanded; **c** recoil

In this simulation, the polymeric stent had an elastic modulus of 3.363 GPa, a Poisson ratio of 0.45 and a yield stress of 40 MPa. A Neo-Hookean hyperelastic model was assumed for the plaque with shear modulus 0.12 MPa and bulk modulus 1.7 MPa, whilst the single layer artery was assumed to be a hyperelastic material with a six order reduced polynomial strain energy density function. The stent, plaque and artery all had 8-noded linear hex elements. Finally, the balloon was modelled as an elastic membrane with an elastic modulus of 1400 MPa, a Poisson's ratio of 0.3, a thickness of 0.05 mm and was meshed with 4-noded membrane elements. Further details and justification for these models is available in [25].

Figure 11 shows maximum expansion and final recoiled deformation of the *ART18AZ* model, using the same settings as for the *BVS-B* model. The deformations of the *ART18AZ* device appear to be less satisfactory than those of the *BVS-B* device with inferior scaffolding, noticeable prolapse and approximately double the amount of recoil (relative to the respective fully expanded shapes).

Although the *BVS-B* model appears to out-perform the *ART18AZ* model with respect to recoil, this may be due to inaccuracies of the underlying CAD models. For example, there is noticeable distortion in the cells of the *ART18AZ* model which could be the result of poor geometry representation (recall that these models were constructed just using inspection of publically available images). However,

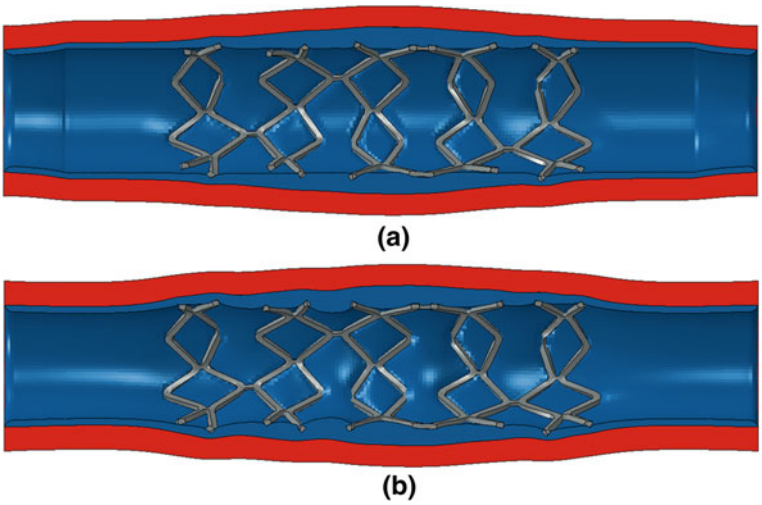

Fig. 11 Expansion and recoil of the *ART18AZ* model: **a** fully expanded; **b** recoil

there is potential concern with respect to having only two bridges joining adjacent rings, in light of the known longitudinal compression problems particularly associated with the Boston Scientific *Element* platform.

In addition to radial strength, devices need to be as flexible as possible for deliverability and conformability. For drug eluting stents, it is favourable to optimize the drug distribution within arterial tissue. Indeed, the clinical control of inflammation and smooth muscle cell proliferation demand consideration of (i) the potential injury to the arterial tissue resulting from the stresses imposed by stent struts embedded into the vessel wall and (ii) the disturbance to the flow and the associated wall shear stress to which the endothelium is exposed. So, metrics are needed for the stresses within the tissue and the (shear) stresses on the surface of the vessel.

In [25], four measures of performance were considered in the DSO of a generic closed cell stainless steel stent: (i) recoil; (ii) tissue stress; (iii) drug distribution and (iv) flexibility. A further two objectives were included in an optimization analysis of the *Cypher* platform [21] to represent flow disturbance and the uniformity in drug distribution. Thus, relative to the study in [25] the additional objectives required a CFD simulation and further post-processing for the variance in drug concentration.

For the study of biodegradable magnesium alloy stents, Wu et al. adopted a twin objective approach (side-stepping the multi-objective problem) whereby the effects of maximum principal strain and mass on biodegradability were recognized. The maximum principal strain was minimized first and then mass (strut width) was maximized by selecting the design with highest mass from all the designs for which the maximum principal strain was less than a prescribed limit [35].

4.4 Multi-Objective Design

If more than one measure of performance is used, the multi-objective design problem often requires trade-off considerations to be made; typically, an improvement in one objective correlates with a deterioration in another. With more than two objectives, both positive and negative correlations can exist simultaneously between different pairs of objectives.

As described above, the multi-objective problem can be avoided when, for example, it is possible to rank objectives a priori [35]. Alternatively, the optimization can be recast as a constrained problem, wherein design improvement is sought in one objective whilst ensuring that other objectives don't deteriorate [25]. Although Pant et al. did not present response surfaces in [25], it is useful to present and discuss them here. The stent parameterisation and the full set of results are available in [25]. The intention here is to demonstrate the way that multi-dimensional design spaces can be presented and interpreted.

So, Fig. 12 depicts the variation in non-dimensional stent recoil against non-dimensional strut width (plotted on the abscissa of each inner tile), non-dimensional strut length (inner tile ordinates), non-dimensional link amplitude (outer abscissa) and non-dimensional link wavelength (outer ordinate). This plot has been created using the Kriging response surface formulation. Since there is only a very slight variation between each tile, this shows that the link parameters have little effect on recoil. The strongest effect is produced by the strut width, whereby wider struts provide greater vessel support.

In contrast to recoil, tissue stress is minimized by narrow struts as shown in Fig. 13. Again, the link parameters have little effect, but strut length has a noticeable impact at large values of strut width, i.e. tissue stress is maximized when both width and length are high. This is to be expected since tissue stress is based on a volume averaged integral which increases with the higher radial force associated with lower recoil.

Since the delivery of drug depends on surface contact, it is to be expected that drug concentration in the tissue is positively correlated with tissue stress. Cast as a minimization problem, the variation in the inverse of drug concentration is depicted in Fig. 14. In general, wider struts predict better drug delivery, but strut length has an unexpected impact. At low values of strut width, it is clear that increasing strut length leads to higher concentrations of drug. However, at high values of strut width, variation in strut length has a negligible effect. This is due to the dependence of the total contact area (including the contribution from the links) on strut length. Since the overall length of the stent is constant, variation in strut length leads to variation in the total arc length of the links and, hence, the contact area.

The fourth objective is flexibility and its non-dimensional variation is shown in Fig. 15. This is an apparently confusing response, largely resulting from noise in the data and the way that the Kriging response surface model has interpolated the data. A smoother response surface model can be generated using regression [36]

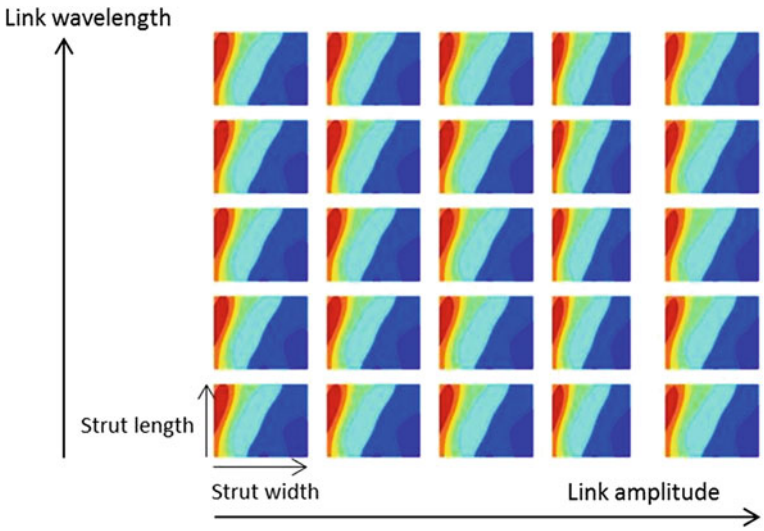

Fig. 12 Response surface model for non-dimensional recoil. Each inner tile has strut width on the abscissa and strut length on the ordinate. The separate tiles are plotted for fixed values [0.00, 0.25, 0.50, 0.75, 1.00] of the non-dimensional wavy link parameters: effective amplitude on the (outer) abscissa and effective wavelength on the (outer) ordinate. Further details can be found in [25]

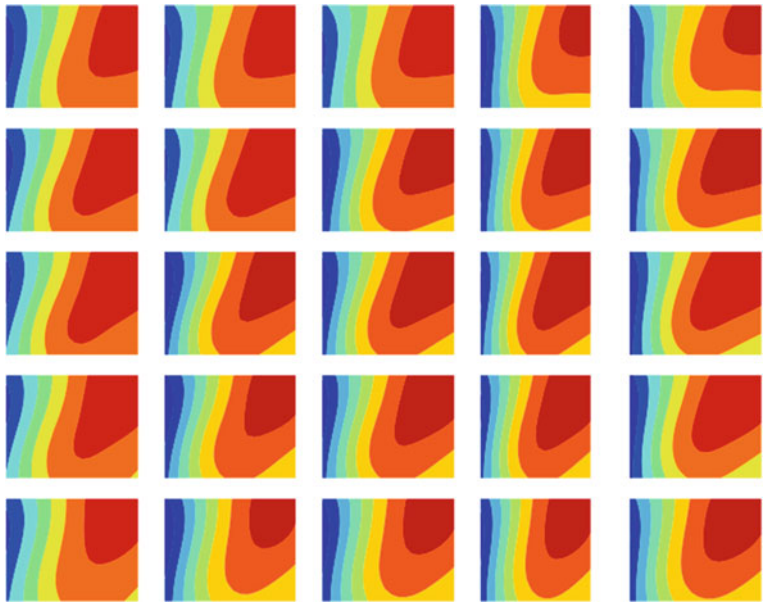

Fig. 13 Response surface model for non-dimensional tissue stress. See caption for Fig. 12

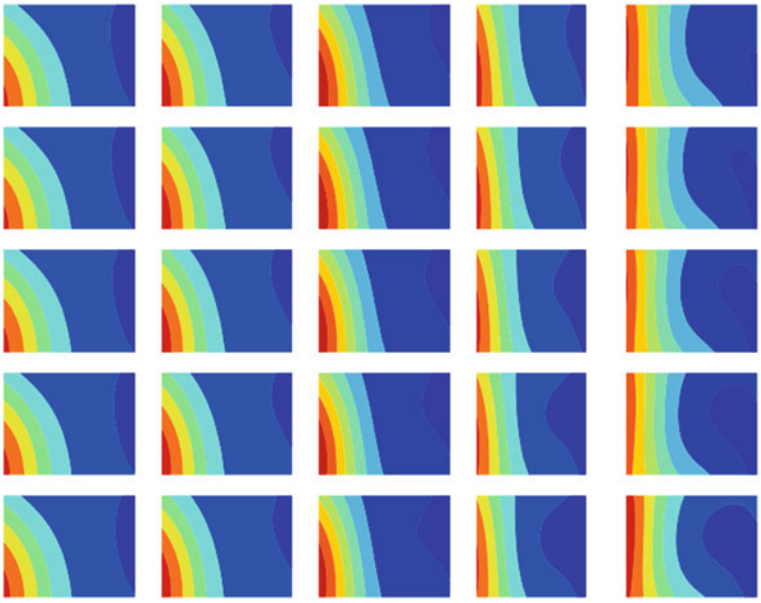

Fig. 14 Response surface model for non-dimensional tissue drug concentration. See caption for Fig. 12

and an example is available in [37] along with a discussion that helps to explain the noise in the data. In essence, when the links deform under load, they can come into self-contact, and this distorts the moment–curvature profile used to extract the flexibility metric. Despite this problem, flexibility is shown to be primarily dependent on the outer abscissa parameter that defines the link amplitude, as evidenced by the fact that individual tiles change far more significantly in Fig. 15 from left to right than they do from bottom to top. Furthermore, a flexibility improvement of 14 %, relative to the baseline design, was demonstrated in [25] without a decrease in the other objectives.

5 A Real Design Case

Based on the knowledge gained in earlier studies [21, 25], a DSO project was undertaken to design a biodegradable polymer stent which was to become the first prototype of the *Arterius Biodegradable Scaffold* (*ABS*), Arterius Ltd. This design cycle needed to be completed within 6 months. Starting from an initial concept, a parametric CAD model was constructed and developed during preliminary design. The process of setting up and developing the CAD model occupied most of the time of problem setup. In contrast, since a range of simulation models were available from other studies of metallic stents [21, 25], relatively modest effort was

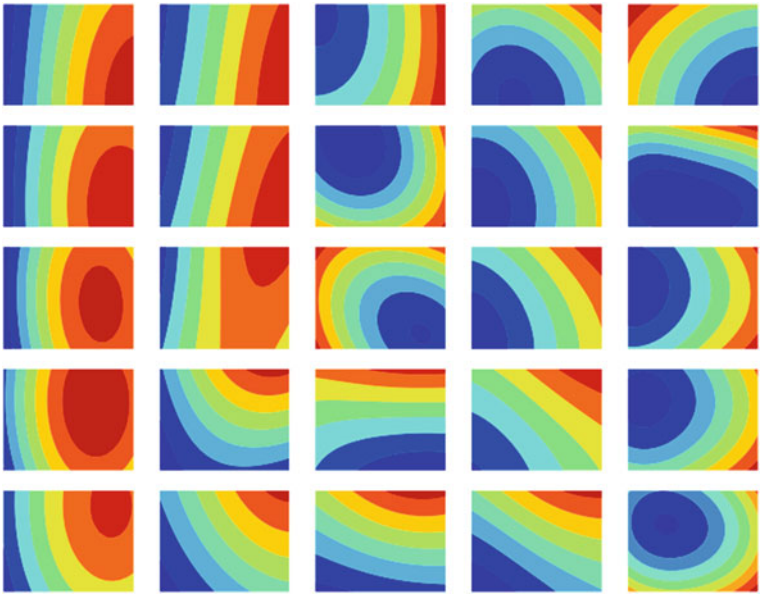

Fig. 15 Response surface model for non-dimensional flexibility. See caption for Fig. 12

needed to modify the associated simulation models for the study of the biodegradable scaffold. The design concept is the subject of an ongoing patent application, so specific details cannot be provided here. Nonetheless, it can be revealed that four design parameters were used including strut width and one related to the shape of the crowns. The strut thickness was fixed at 150 μm. Despite the lack of detail, this test case provides valuable insight to a real coronary artery design problem.

A 78 % symmetric constriction was used, comprising a Neo-Hookean representation of the single constituent plaque, inside a single layer of arterial tissue, similar to the setup described in Sect. 4.3. Although symmetry is exploited here for the demonstration purposes, in reality most coronary plaques are eccentric. Each CAD scaffold model was imported into an Abaqus assembly and placed inside the constriction (i.e. no stent positioning step was needed). Then, using Abaqus Explicit 6.9-1, separate steps were performed to simulate crimping onto a balloon-catheter followed by balloon expansion. In both steps, loading and relaxation were included using a smooth step profile. At the end of each simulation, metrics were extracted for the minimum lumen area (*MLA*) and the average recoil. A third measure of performance was obtained for the predicted drug distribution by running the steady state heat diffusion analogue in Abaqus Standard 6.9.1. Finally, a separate simulation was performed on the crimped stent (again in Abaqus Standard 6.9.1) to extract a fourth metric for the flexibility. Further details concerning the setup of these simulations are available in [25].

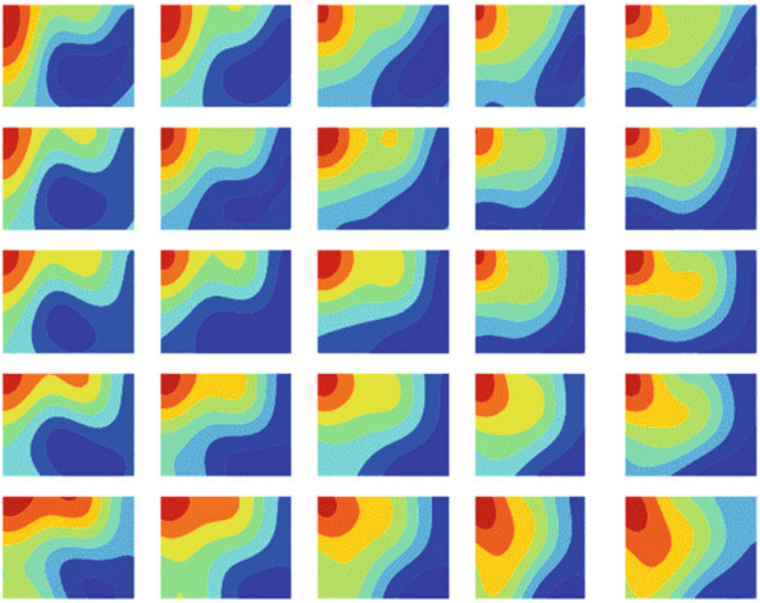

Fig. 16 Response surface model for non-dimensional inverse of minimum lumen area. The abscissa on each small tile represents non-dimensional strut width. The ordinate on each small tile denotes a non-dimensional parameter related to the shape of the crowns and each tile signifies fixed values [0.00, 0.25, 0.50, 0.75, 1.00] of the third and fourth parameters (which cannot be disclosed due to intellectual property protection)

So, the multi-objective problem comprised four input geometry parameters and four output objectives. In the time available for simulation, it was decided to run a 40 point design sample to gain an understanding of the multi-objective design space. Some of this data resulted in the response surface models shown in Figs. 16, 17.

The response surface model for the inverse of *MLA* is shown in Fig. 16. The inverse is used so as to treat each objective as a minimization problem. Each tile represents a slice through the non-dimensional *1/MLA* design space for fixed values [0.00, 0.25, 0.50, 0.75, 1.00] of the other two non-dimensional geometry parameters. Since all tiles are very similar, these two parameters have little effect on *MLA*. However, within each tile, favourable values of *MLA* are observed for high values of strut width (shown on the abscissa) and for low values of the ordinate. This follows a similar pattern to that shown in Fig. 12 and, again, wider struts predict greater radial support.

Also echoing the findings in [25], volume averaged tissue stress (*VAS*) exhibits a response that is in competition with *MLA* as depicted in Fig. 17. It is desirable to minimize tissue stress and, based on the definition of *VAS* [21], low stress occurs for low strut width, due to the lower stent-to-artery ratio of narrow struts and the associated reduced load needed to support the higher recoil in the vessel.

Combined in a multi-objective plot, the relationship between *MLA* and tissue stress can be more readily interpreted as in Fig. 18, wherein each point signifies an

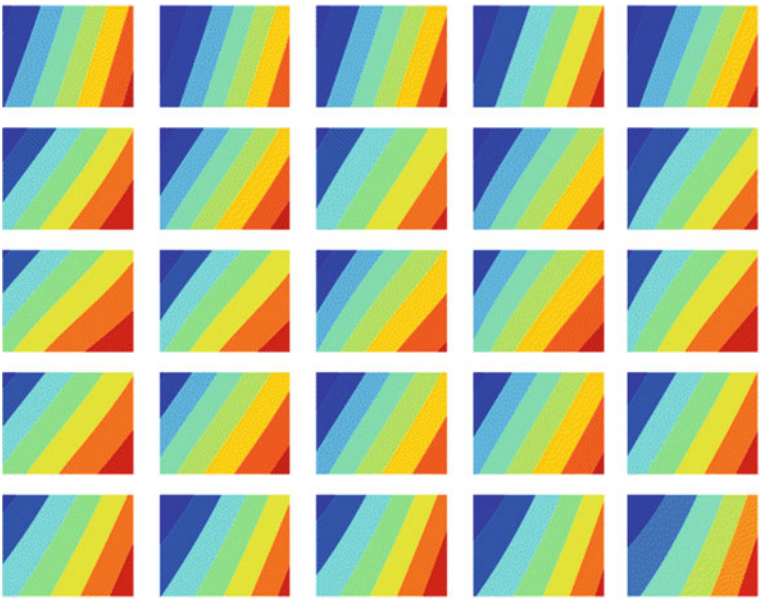

Fig. 17 Response surface model for non-dimensional volume averaged tissue stress (see caption for Fig. 16)

individual design. For example, designs 11 and 29 have wide struts that provide good radial support but at the expense of high tissue stress, whereas designs 8 and 32 generate lower tissue stress but have lower *MLA* (i.e. at higher *1/MLA*).

Of the designs that lie on the Pareto front, designs 24 and 17 bound an envelope of geometries that offer a balanced trade-off between *1/MLA* and tissue stress. When the full data-set was assessed (i.e. including the values of average recoil and flexibility) and combined with visual assessment of performance, it was decided to select design 17 as the prototype to be manufactured and tested. The width of design 17 was very close to 150 μm.

The prototype was manufactured by laser cutting the design from a PLLA tube. Preliminary bench tests demonstrated that the device could be successfully crimped and free-expanded on a balloon-catheter. However, tests of the radial strength of the expanded device revealed a problem in the design, wherein less than satisfactory support was provided at the ends of the device. Indeed, this helped to explain why levels of tissue stress were significantly lower than those obtained from the model of the *BVS-B* device. In effect, the optimizer had guided the process towards designs that imparted low tissue stress at the ends due to the way that these devices were able to adjust to the shape of the deformed vessel. This is a common feature in DSO methods wherein the optimizer can exploit weaknesses/deficiencies in the analysis setup.

A re-design of the *ABS* was needed and a further computational test was constructed to simulate collapse resistance when the expanded device was exposed to

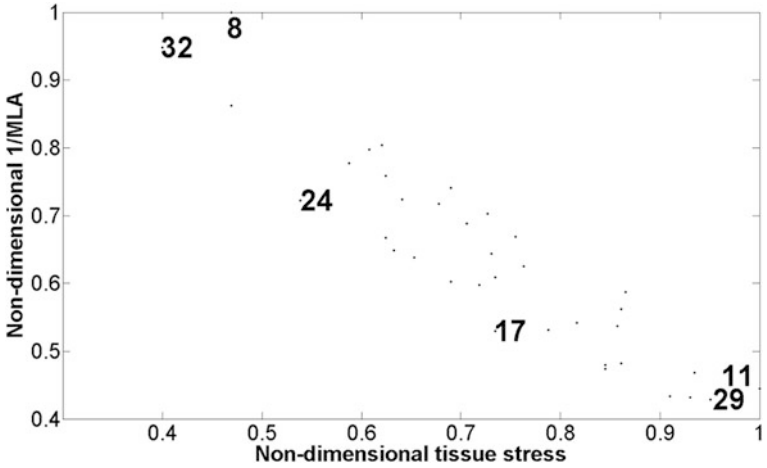

Fig. 18 Non-dimensionalized multi-objective plot of *1/MLA* versus tissue stress

an outer collapse load. This involved increasing (from zero) the pressure applied to the outer surfaces of the stent and monitoring the minimum stent diameter (*MSD*).

The poor overall radial strength of design 17 was confirmed with *MSD* beginning to decrease noticeably *at* 0.65 bar with complete collapse occurring just below 1 bar. In contrast, the *BVS-B* model was able to sustain its shape reasonably well up to approximately 0.95 bar with collapse at 1 bar.

At this stage, it was agreed to spend additional time (beyond the original 6 months) redesigning the *Arterius Biodegradable Scaffold*. Both the width and the thickness were fixed at 150 μm, and modified bounds were applied to the other three parameters. Another design cycle was conducted in which a further eight configurations were tested for *MLA*, tissue stress, flexibility and collapse resistance. The collapse test was added as a quasi-static step in the Abaqus Explicit simulation such that it was applied to the deformed shape produced during the expansion step. The optimal design, selected for manufacture and testing as the second prototype, had similar performance to design 17 in terms of *MLA*, tissue stress and flexibility but was significantly superior in terms of overall radial strength as predicted by the collapse test. A 20 % improvement in radial strength was produced with collapse occurring at approximately 1.2 bar. At the time of writing, the second prototype is about to be laser-cut from tubes manufactured by Arterius Ltd; the tubes used for the first prototype were sourced from elsewhere.

6 Summary and Conclusions

At a time when the design of coronary artery stents would appear to have reached a relatively mature evolutionary stage, geometrically at least, this chapter has sought to highlight how the knowledge gained to date can be exploited in the design of the

new generation of bioresorbable scaffolds. Currently, the main challenge is to reduce strut dimensions. Most bioresorbable devices have strut thicknesses and widths that are close to twice the corresponding dimensions of permanent metallic stents.

Whilst there is compelling clinical evidence from the ISAR-STEREO trials [14] and elsewhere [26] for reduced restenosis with thinner struts, less has been reported concerning the effect of strut width. Nakatani et al. have reported greater neo-intimal hyperplasia and poorer stent coverage associated with relatively wider struts [38]. However, these findings suffer from uncertainty concerning the main cause(s) of the effects since the narrow and wide struts are defined on one and the same *Cypher* stent platform by the wavy links and rings, respectively. Each strut type generates very different flow patterns and shear stresses on the vessel wall and this is known to influence tissue response.

An earlier study by Sullivan et al. [39] demonstrated that damage to the internal elastic lamina (IEL) is critically linked to higher incidence of myointimal hyperplasia and restenosis. Effectively, low profile struts that reduce local stress concentrations are needed so as to minimize abnormal stresses and mechanical damage to the tissue.

So, although wider struts offer greater radial support and larger contact area for drug delivery, most available evidence suggests that tissue damage caused by larger struts is the dominant effect leading to restenosis. However, it is to be noted that thinner struts may cause poor outcomes if they penetrate the tissue and rupture the IEL, possibly due to complications in the stenting procedure, combined with the fact that lower surface area contact may produce higher pressure loading.

Although many computational studies of stent geometry tend to fix strut thickness and assess the effect of strut width, Harewood et al. [30] used an FEA analysis of a simplified single half ring with five parameters, including both width and thickness, and showed that optimal values of width and thickness were reduced by 22 % and increased by 4 %, respectively, when optimizing radial stiffness.

Based on the observations above, future design studies should, if possible, consider the variation of both width and thickness, or other forms of strut cross-section parameterization, combined with other parameters defining the stent topology.

When designing the *Arterius Biodegradable Scaffold*, a time limited, computationally intensive study was conducted that led to the manufacture and testing of a first prototype within 6 months. Following laboratory tests, a shorter study of approximately 3 months culminated in modest re-design and a second prototype. The computational experiments involved four geometry parameters (including strut width and one for the shape of the crowns) and four objectives for design of the first prototype with a further objective—the direct test of radial strength—being added in the subsequent re-design phase. Throughout, strut thickness was kept constant at 150 μm and the multi-objective optimization procedure resulted in a potentially optimal design with an approximately square profile for the strut cross-section.

In contrast to the computationally expensive simulations employed in the Arterius study, Wu et al. applied two-dimensional FEA based optimization to models of the Biotronik biodegradable magnesium alloy stent (*MAS*), complemented by manufacture and testing, and identified four configurations for full three-dimensional simulations. Relative to a baseline design, improved performance (including reduced maximum principal strains and greater radial strength) was demonstrated in the three-dimensional models [35].

These two studies illustrate how computational design methods can be used to develop improved coronary stent designs. The *ABS* study used conceptual and preliminary design to prepare a platform that is nearly ready for pre-clinical trials. The work by Wu et al. was motivated by clinical evidence that had shown severe lumen loss after 4 months. Improved strut dimensions, including wider strut width, were identified that should extend degradation time and enhance radial scaffolding. In both studies, laboratory experiments were used to validate and complement the computational simulations and animal testing was completely avoided. Further mechanical testing will be required and, even though animal models will have to be employed in pre-clinical trials, the *MAS* re-design process illustrates that further re-design can be undertaken computationally (with complementary mechanical testing), again reducing the amount of animal testing that will be necessary.

With respect to biodegradable stents, the key challenge is to develop new materials or to enhance existing ones such that strut dimensions can be reduced. There is, approximately, two orders of magnitude stiffness mismatch between polymers and metal alloys. Sufficient polymer strengthening may ultimately be achieved by temperature controlled extrusion methods or by the use of additives or by using combinations of different materials.

More generally, stent evolution faces a number of other challenges. Even the most advanced metallic devices available today cannot avoid restenosis and thrombosis in all cases. Significant challenges still exist to overcome problems associated with malapposition, under-deployment, vessel tapering and bifurcation stenting. Lee et al. [40] have described the development of an early biodegradable bifurcation stent with comparable mechanical properties to metallic devices, but with very large struts. Ultimately, the only way to overcome these challenges may be through patient-specific stent design, a process likely to be made possible when supported by computational engineering methods and very powerful computers.

The main purpose of this chapter was to highlight a number of the design issues that are typically confronted when performing multi-objective design optimisation. By way of example, non-dimensional data was presented from a previous design study in a way to highlight how response surface models can be assessed for a range of objectives. Then, to illustrate how the same technology could be used in a time limited, industrially relevant design study, key elements of the design of a biodegradable device were presented. Unfortunately, details of the geometry could not be shown due to commercial sensitivity. However, the realities associated with the need to manufacture a prototype were outlined, starting from the findings from a preliminary study depicted in Figs. 16, 17, 18 and culminating in a more ad hoc re-design with consideration of radial collapse resistance. Finally, although the

value of multi-dimensional response surfaces has been demonstrated, more detailed assessment of the sensitivity of different objectives is sometimes necessary as well.

Acknowledgments Thanks to the support of Arterius Ltd and to the invaluable contributions by Dr Sanjay Pant and Mr Giorgos Ragkousis. The author would also like to thank Prof. Nick Curzen at Southampton General Hospital for his learned insight and for the data to reconstruct the patient specific segment used here.

References

1. Onuma, Y., Serruys, P.W.: Bioresorbable scaffold: the advent of a new era in percutaneous coronary and peripheral revascularization? Circulation **123**, 779–797 (2011)
2. Stefanini, G.G., Holmes, D.R.: Drug eluting coronary artery stents. N. Engl. J. Med. **368**, 254–265 (2013)
3. Serruys, P.W., et al.: A comparison of balloon-expandable-stent implantation with balloon angioplasty in patients with coronary artery disease. N. Engl. J. Med. **331**, 489–495 (1994)
4. Serruys, P.W., et al.: Angiographic follow-up after placement of a self-expanding coronary-artery stent. N. Engl. J. Med. **324**, 13–17 (1991)
5. van der Giessen, W.J., Slager, C.J., van Beusekom, H.M., van Ingen Schenau, D.S., Huijts, R.A., Schuurbiers, J.C., de Klein, W.J., Serruys, P.W., Verdouw, P.D. Development of a polymer endovascular prosthesis and its implantation in porcine arteries. J. Interv. Cardiol. **5**, 175–185 (1992)
6. van der Giessen, W.J., Lincoff, A.M., Schwartz, R.S., van Beusekom, H.M., Serruys, P.W., Holmes Jr, D.R., Ellis, S.G., Topol, E.J.: Marked inflammatory sequelae to implantation of biodegradable and non-biodegradable polymers in porcine coronary arteries. Circulation **94**, 1690–1697 (1996)
7. Tamai, H., Igaki, K., Kyo, E., et al.: Initial and 6-month results of biodegradable poly-l-lactic acid coronary stents in humans. Circulation **102**, 399–404 (2000)
8. Ormiston, J.A., Serruys, P.W.S.: Bioabsorbable coronary stents. Circ. Cardiovasc Intervent. **2**, 255–260 (2009)
9. Nishio, S. et al.: Long-term (>10 years) clinical outcomes of first-in-man biodegradable poly-*l*-lactic acid coronary stents: Igaki-Tamai stents. Circulation **125**(19), 2343–2353 (2012)
10. Strandberg, E., Zeltinger, J., Schultz, D.G., Kaluza, G.L.: Late positive remodeling and late lumen gain contribute to vascular restoration by a non-drug eluting bioresorbable scaffold: a four-year intravascular ultrasound study in normal porcine coronary arteries. Circ. Cardiovasc. Interv. **5**(1), 39–46 (2012)
11. Gomez-Lara, J., Diletti, R., Brugaletta, S. et al.: Angiographic maximal luminal diameter and appropriate deployment of the everolimus-eluting bioresorbable vascular scaffold as assessed by optical coherence tomography: an ABSORB cohort B trial sub-study. Eurointervention **8**(2), 214–224 (2012)
12. Hanratty, C.G., Walsh, S.J.: Longitudinal compression: a "new" complication with modern coronary stent platforms—time to think beyond deliverability. Eurointervention **7**(7), 872–877 (2011)
13. Prabhu, S., Schikorr, T., Mahmoud, T., Jacobs, J., Potgieter, A., Simonton, C.: Engineering assessment of the longitudinal compression behaviour of contemporary coronary stents. Eurointervention **8**(2), 275–281 (2012)
14. Kastrati, A., Mehilli, J., Dirschinger, J., et al.: Intracoronary stenting and angiographic results: strut thickness effect on restenosis outcome (ISAR-STEREO) trial. Circulation **103**, 2816–2821 (2001)

15. Kreutzer, J., Rome, J.J.: Open-cell design stents in congenital heart disease: a comparison of Intrastent vs Palmaz stents. Cath. Cardio. Int. **56**, 400–409 (2002)
16. Stoeckel, D., Bonsignore, C., Duda, S.: A survey of stent designs. Min. Invas. Ther & Allied Technol. **11**(4), 137–147 (2002)
17. Serruys, P.W., Rensing, B.J.: Handbook of coronary stents. Dunitz (2002)
18. Amoroso, G., van Geuns, R-J., Spaulding, C. et al.: Assessment of the safety and performance of the STENTYS self-expanding coronary stent in acute myocardial infarction: results from the APPOSITION I study. Eurointervention **7**, 428–436 (2011)
19. Bourantas, C.V., Zhang, Y., Farooq, V., Garcia–Garcia, H.M., Onuma, Y., Serruys, P.W.: Bioresorbable scaffolds: current evidence and ongoing clinical trials. Curr. Cardiol. Rep. **14**, 626–634 (2012)
20. Durand, E., Lemitre, M., Couty, L., Sharkawi, T., Brasselet, C., Vert, M., Lafont, A.: Adjusting a polymer formulation for an optimal bioresorbable stent: a 6-month follow-up study. Eurointervention **8**(2), 242–249 (2012)
21. Pant, S., Limbert, G., Curzen, N., Bressloff, N.W.: Multi-objective design optimisation of coronary stents. Biomaterials **32**, 7755–7773 (2011)
22. Mortier, P., Holzapfel, G. A., De Beule, M. et al.: A novel simulation strategy for stent insertion and deployment in curved coronary bifurcations: comparison of three drug-eluting stents. Ann. Biomed. Eng. **38**(1), 88–99 (2010)
23. Migliavacca, F., Gervaso, F., Prosi, M., Zunino, P., Minisini, S., Formaggia, L., Dubini, G.: Expansion and drug elution model of coronary stent. Comp. Meth. Biomech. Biomed. Eng. **10**, 63–73 (2007)
24. Grogan, J.A., Leen, S.B., McHugh, P.E.: Comparing coronary stent material performance on a common geometric platform through simulated bench testing. J. Mech. Behav. Biomed. Mat. **12**, 129–138 (2012)
25. Pant, S., Bressloff, N.W., Limbert, G.: Geometry parameterization and multidisciplinary constrained optimisation of coronary stents. Biomech Mod. Mechanobiology **11**(1), 61–82 (2011)
26. Holzapfel, G.A., Stadler, M., Gasser, T.C.: Changes in the mechanical environment of stenotic arteries during interaction with stents: computational assessment of parametric stent designs. J. Biomech. Eng. **127**, 166–180 (2005)
27. Gijsen, F.J.H., Migliavacca, F., Schievano, S., et al.: Simulation of stent deployment in a realistic human coronary artery. BioMed. Eng. Online **7**, 23 (2008)
28. Hicks, R., Henne, P.: Wing design by numerical optimization. J. Aircraft **15**(7), 407–412 (1978)
29. Pant, S., Bressloff, N.W., Forrester, A.I.J., Curzen, N.: The influence of strut-connectors in stented vessels: a comparison of pulsatile flow through five different coronary stents. Ann. Biomed. Eng. **38**(5), 1893–1907 (2010)
30. Harewood, F., Thornton, R., Sharp, P.: Step change in design: exploring sixty stent design variations overnight. www.altairproductdesign.com 2011
31. Sobester, A., Leary, S.J., Keane, A.J.: On the design optimization strategies based on global response surface approximation models. J. Glob. Opt. **33**, 31–59 (2005)
32. Jones, D.R.: A taxonomy of global optimization methods based on response surfaces. J. Glob. Opt. **21**(4), 345–383 (2001)
33. Krige, D.G.: A statistical approach to some basic mine valuation problems on the Witwatersrand. J. Chem. Mett. Min. Soc. SA. **52**(6), 119–139 (1951)
34. Forrester, A. I. J., Sóbester, A., Keane, A. J.: Engineering design via surrogate modelling: a practical guide. Wiley, Chichester (2008)
35. Wu, W., Petrini, L., Gastaldi, D., Villa, T., Vedani, M., Lesma, E., Previtali, B, Migliavacca, F.: Finite element shape optimization for biodegradable magnesium alloy stents. Ann. Biomed. Eng. **38**(9), 2829–40(2010)
36. Forrester, A.I.J., Keane, A.J., Bressloff, N.W.: Design and analysis of noisy computer experiments. AIAA J. **44**(10), 2331–2339 (2006)

37. Pant, S.: Multidisciplinary and multiobjective design of coronary stents. PhD Thesis, University of Southampton, UK (2012)
38. Nakatani, S., Nishino, M., Taniike, M. et al.: Initial findings of impact of strut width on stent coverage and apposition of sirolimus-eluting stents assessed by optical coherence tomography. Cath. Cardo. Int. (2012)
39. Sullivan, T.M., Ainsworth, S.D., Langan, E.M., et al.: Effect of endovascular stent strut geometry on vascular injury, myointimal hyperplasia and restenosis. J. Vasc. Surg. **36**(1), 143–149 (2002)
40. Lee, C.-H., Chen, C.-J., Liu, S.-J., Hsiao, C.-Y., Chen, J.-K.: The development of novel biodegradable bifurcation stents for the sustainable release of anit-proliferative sirolimus. Ann. Biomed. Eng. **40**(9), 1961–1970 (2012)

Development of a Fabric-Reinforced Porous Graft for Vascular Tissue Engineering Using Finite Element Methods and Genetic Algorithms

Mark S. Yeoman, B. Daya Reddy, Deon Bezuidenhout, Hellmut C. Bowles, Peter Zilla and Thomas Franz

Abstract Small to medium diameter vascular grafts have met with little success over the past 50 years. Surface thrombogenicity and anastomotic intimal hyperplasia, the main reasons for graft failure, are believed to be governed by a lack of endothelialisation and compliance mismatch between graft and host artery. High-porosity polyurethane grafts allow for cellular ingrowth and vascularization, they however encounter detrimental ballooning and low burst strength. To improve the structural properties, a support is required that will not adversely affect ingrowth permissibility of the graft. In this study, an approach combining finite element methods and genetic algorithms was developed to adopt the concept of arterial mechanics, which are predominantly governed by medial and adventitial layer, to tissue-regenerative vascular grafts. The numerical method was able to identify the mechanical properties of adventitial knit fabrics that optimally complement three different intimal/medial porous polyurethane structures to provide grafts with a

M. S. Yeoman (✉)
Continuum Blue Ltd., Tredomen Innovation and Technology Park, Hengoed, UK
e-mail: mark@continuum-blue.com

B. D. Reddy
Centre for Research in Computational and Applied Mechanics, University of Cape Town, Cape Town, South Africa

D. Bezuidenhout · P. Zilla · T. Franz (✉)
Cardiovascular Research Unit, Chris Barnard Division of Cardiothoracic Surgery, Faculty of Health Sciences, University of Cape Town, Private Bag X3, Observatory, Cape Town 7935, South Africa
e-mail: thomas.franz@uct.ac.za

H. C. Bowles
Finite Element Analysis Services (Pty.) Ltd., Parklands, South Africa

T. Franz
Research Office, University of Cape Town, Cape Town, South Africa

T. Franz
Centre for Research in Computational and Applied Mechanics, University of Cape Town, Cape Town, South Africa

Stud Mechanobiol Tissue Eng Biomater (2014) 15: 29–61
DOI: 10.1007/8415_2013_162

Published Online: 20 June 2013

compliance of 5.3, 5.5 and 6.0 %/100 mmHg. Grafts featuring fabrics manufactured according to the numerically specifications exhibited an in vitro compliance of 2.1 ± 0.8, 3.0 ± 2.4 and 4.0 ± 0.7 %/100 mmHg. Beyond the demonstration of the feasibility of numerical method, it was shown that the graft system of adventitially reinforced polymer with well-defined interconnected porosity can be expected to facilitate the ingrowth and regeneration of vascular tissue for all pore sizes studied.

1 Introduction

Although the mechanisms behind sub-optimal patency and failure of small- to medium-diameter grafts are not fully understood, it is clear that compliance mismatch and the thrombogenetic nature of non-endothelialised surfaces are major contributors [9, 10, 12, 19, 21, 26, 30]. Previous studies have shown that it is a combination of the thrombogenetic nature of the graft material, surface roughness, and the mechanical and hemodynamic properties of the replacement graft in relation to the host artery which add up to the relatively poor performance of prosthetic grafts as compared with vein grafts or arterial grafts [3, 12].

Tissue engineering and regeneration efforts of the past two decades have aimed at the creation of biological interfaces between the blood and the prosthesis. As an alternative to the in vitro endothelialization of conventional vascular prostheses with cultured autologous endothelial cells [6], the concept of transmural endothelialization requires ingrowth-permissive graft structures [11, 12, 15, 30]. Given the defined dimensions of capillaries and arterioles, many of the ill-defined porous structures investigated for this purpose exhibit pore interconnections which are too narrow to allow for complete penetration of the graft wall. Therefore, structures with well-defined interconnected micro-pores and channels have been developed with optimal porosities for both vascular ingrowth and mitigation of inflammation [2]. As much as the biological response patterns seem to require large, open porosity in thin-walled grafts, the resulting structural weakness and the excessive viscoelastic properties may pose a prohibitive obstacle.

Past research has utilized winding methods to reinforce these graft structures [23]. However, these methods cause radial compression, high stress concentrations, excessively reduced compliance and nonlinear effects in the region of the reinforcement. Thus, a better method of reinforcement is required which does not cause localized stress concentrations and hence excessive localized compression of the porous structure while still allowing for tissue regeneration through the support structure.

Fabric or mesh structures may offer advantages in externally reinforcing the porous polymer grafts more uniformly. However, complex mechanics impose a challenge for deriving optimal fabric designs that will, in combination with the porous structures, provide the desired mechanics of the reinforced grafts.

Genetic algorithms (GA) and finite element methods (FEM) have been used to study structural and thermal optimization problems in medicine. Khalil et al. [14] proposed a computational scheme for the elasticity reconstruction of soft tissue.

The scheme comprises finite element (FE) modeling for mechanical analysis with genetic algorithms for parameter estimation, and was successfully applied to the elasticity characterization of atherosclerotic plaques in diseased arteries. A similar approach was followed by Hsu et al. [13] to optimize the design of locking screws used for fracture fixation and bone healing of tibial fractures. The two principal objectives in the design of these orthopedic screws are bending strength and bone holding power. Since these two objectives may conflict with each other, a multi-objective optimization method based on FE modeling and genetic algorithms was used to evaluate and rank various screw designs.

Siauve et al. [20] showed a potential clinical utilization of genetic algorithms coupled with a FE formulation. They developed a treatment tool for local hyperthermia treatment of cancer which optimizes radio-frequency and microwave sources so as to achieve a temperature distribution specific for individual patients. The use of genetic algorithms has also been successfully demonstrated for bio-medical applications. Pandit et al. [18] and Wang et al. [25] utilized GAs for the development of a two-layer three-dimensional constitutive model for porcine coronary arteries. Approximating the arterial wall by an intima-media layer and an adventitial layer, they combined genetic algorithms with experimental testing to determine the material properties of each of the two layers. After testing intact arteries and their corresponding dissected adventitia or intima-media layer, the material properties of the missing layer were computed from the properties of the intact wall and the tested layer.

The aim of this work was to propose the use of an elastic knit fabric structure for the externally, i.e. 'adventitial', reinforcement of a porous polymeric vascular graft [27, 28]. The polymeric structure with well-defined interconnected porosity [1, 2, 5] served as scaffold for tissue integration and regeneration but exhibited low mechanical strength. The adventitial fabric acted as reinforcement for the porous scaffold, providing structural integrity and desired mechanical characteristics of the graft, while permitting cellular activity to take place through its structure. The design of the reinforcing fabric was facilitated with a combination of FE methods and genetic algorithms. The process aimed at the determination of mechanical properties of the fabric structure that, combined with the porous polymeric structure, result in a specific dynamic compliance, nonlinear pressure-diameter response and diastolic diameter of the graft.

2 Development of a Constitutive Model for Warp-Weft Coupled Knitted Fabrics

Knits are fabrics where yarns are inter-looped. Generally, knitted structures are not as stiff as their woven counterparts and are highly porous. Knitted fabrics encompass warp and weft knits. Warp knits, found in many medical implants, are

complex compared to weft knits. Weft knit structures tend to be highly extendible but are structurally unstable, unless interlocking occurs. This interlocking tends to reduce extensibility but does help with elastic recovery. Advantages of knitted fabrics include that being flexible and comfortable in nature, and they tend not to fray or unravel at the edges.

2.1 Formulation of Fabric Constitutive Relationship

Large strain formulations are required when describing coarse knit fabrics under tension. The fabric constitutive model assumed that the material is highly elastic and compressible. Viscoelastic effects were neglected and incompressibility was not enforced. Due to the small thickness compared to the in-plane dimensions of the fabric, plane stress was implemented under consideration of tension and shear deformation. Since the non-linear stress-strain characteristics of fabrics are similar to those of soft tissue, it was proposed to adapt a strain energy function for soft tissue proposed by Chuong et al. [4]:

$$w(E) = \frac{C}{2}\exp\left(a_1 E_{\theta\theta}^2 + a_2 E_{zz}^2 + 2a_4 E_{\theta\theta} E_{zz}\right). \tag{1}$$

By including shear and increasing the number and order of coefficients, the proposed fabric strain energy function in general two-dimensional form was obtained as

$$\begin{aligned} w(E) = \frac{C}{2}\exp\big[&a_1 E_{11}^2 + a_2 E_{22}^2 + a_3\left(E_{12}^2 + E_{21}^2\right) + a_4(E_{11}E_{22}) + a_5 E_{11}^3 \\ &+ a_6 E_{22}^3 + a_7\left(E_{12}^3 + E_{21}^3\right) + a_8\left(E_{11}^3 E_{22}\right) + a_9\left(E_{11}E_{22}^3\right)\big] \end{aligned} \tag{2}$$

where C and a_i ($i = 1$–9) are fabric material coefficients.

An Abaqus® UMAT subroutine was utilized for implementation of the fabric constitutive model. The subroutine provided the material elasticity tensor, stress and solution dependent variable updates at each increment.

The discrete elasticity tensor is defined by

$$K_{ijkl}^{\sigma\varepsilon} = \frac{\partial \sigma_{ij}}{\partial \varepsilon_{kl}}, \tag{3}$$

where σ and ε are the stress and strain, respectively. For large strain computations an appropriate conjugate stress-strain measure is needed. Since the proposed strain energy function is already defined in terms of Green strain E an appropriate conjugate pair is Green strain and the second Piola-Kirchhoff stress S, which are defined as

$$E = \frac{1}{2}\left(\nabla u + (\nabla u)^T + (\nabla u)^T \nabla u\right) \tag{4}$$

and

$$S_{ij} = \frac{\partial w}{\partial E_{ij}}. \tag{5}$$

The stress was explicitly defined as Cauchy 'true' stress using the relationship between Cauchy stress and second Piola-Kirchhoff stress in the form

$$\sigma_{ij} = J^{-1} F_{ik} S_{kl} F_{jl}. \tag{6}$$

Unlike the model by Chuong et al. [4], Eq. (1), incompressibility was not enforced. For the implementation in Abaqus®, the following special conditions were used; *Orientation*: defined the transverse fabric directions to ensure the material properties remained orientated as elements rotated and deformed; *Membrane element thickness*: A thickness of 100 μm was assigned to the membrane elements that were used to model the fabric; *Poisson's ratios* υ_{13} *and* υ_{31}: The use of membrane elements ensured a state of plane stress, thus the thickness was assumed to be constant.

2.2 Assessment of Model Parameters and Verification of Constitutive Relationship

Single and multiple element patch tests were utilized to assess the influence of the material coefficients (C, a_1, a_2, a_3, a_4, a_5, a_6, a_7, a_8 and a_9) and the effects of element orientation and type under uniaxial tensile and simple shear deformation. The single element models used a four-noded bilinear membrane element with boundary and load conditions describing the two modes of deformation, as illustrated in Fig. 1a, b. Arbitrary fabric coefficients were employed and varied slightly to observe their influence on stress and strain behaviour. The effect of element type and orientation was assessed, in tension and shear, with a uniform mesh with consistently ordered four-noded membrane elements and a non-uniform mesh with three and four-noded membrane elements, Fig. 1c, d.

Figure 2 displays the stress-strain curves and the normalized stress, obtained from dividing the stress values obtained at 20 % tensile strain and 10 % shear strain by the stress values achieved with that of the model with $C = 10000$ and $a_i = 10$. The numerically predicted stress-strain curves (Fig. 2a) exhibit a nonlinear stiffening effect characteristic for fabrics. Defining the subscripts i and j to denote the direction of uniaxial tension and the transverse direction, respectively, the following was observed (Note: The results in Fig. 2 are for $i = 2$ being the direction of uniaxial tension). As expected, the magnitude of stress increased proportionately with C. The *nonlinear stiffening effect*: greatly increased with increasing coefficients that affect terms containing E_{ii}^2, i.e. a_1 and a_2; moderately increased with increasing coefficients that affect terms E_{ii}^3, i.e. a_6; slightly increased with

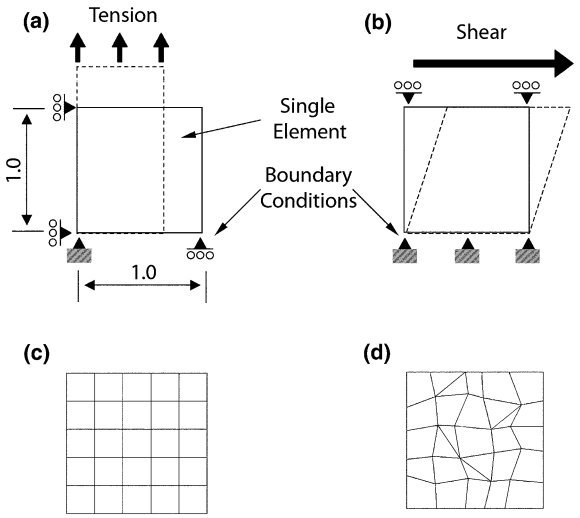

Fig. 1 Patch test models: Single element models for **a** uniaxial tension and **b** simple shear; Multi element models with **c** uniform and **d** non-uniform mesh

increasing coefficients that affect $E_{jj}^3 E_{ii}$, i.e. a_8; greatly decreased with increasing coefficients affecting $E_{ii}E_{jj}$, i.e. a_4; slightly decreased with increasing coefficients that affect E_{jj}^3 and $E_{jj}E_{ii}^3$, i.e. a_5 and a_9; and was not affected by changing coefficients that affect E_{ij}, i.e. a_3 and a_7. The effect of changing a_1 through a_9 depended on the power of the strain terms to which they contribute. Those that affect lower order terms had a larger influence, as expected.

Further information was gained from the normalized stress and the associated transverse strain (Fig. 2b). The magnitude of axial and transverse stress was proportional to C; however, transverse strain was not affected by C. The *transverse strain, or Poisson's effect*: increased with increasing coefficients that affect product terms $E_{jj}E_{ii}$ and $E_{jj}E_{ii}^3$, i.e. a_4 and a_9; decreased with increasing coefficients that affect E_{jj}^2, E_{jj}^3 and $E_{jj}^3 E_{ii}$, i.e. a_1, a_5 and a_8; and was not affected by a_2, a_3, a_6 and a_7. The *axial and transverse stress*: both increased with increasing coefficients that a_2 and a_6 that affect terms E_{ii}^2 and E_{ii}^3, with axial stress being dominant; both decreased with increasing a_4, a_5, a_8 and a_9, with a predominant change in transverse stress for the latter two; and increased and decreased, respectively, with increasing coefficients that affect E_{jj}^2, i.e. a_1. Negative coefficients a_i typically reduced transverse strain. A negative a_4 produced a negative normalized transverse strain, indicating positive strains in this direction. Negative a_2 and a_6 reduced the stress values but did not affect the transverse strain. Negative a_4 and a_9 increased the axial stress while reducing the transverse stress. Negative a_5 did not change the axial stress but reduced the transverse stress. Negative a_2 and a_6 caused compressive axial stress whilst in tension, which is unrealistic. Negative a_8 reduced both the axial and transverse stress values considerably. Negative a_7 did not affect the stress and transverse strain.

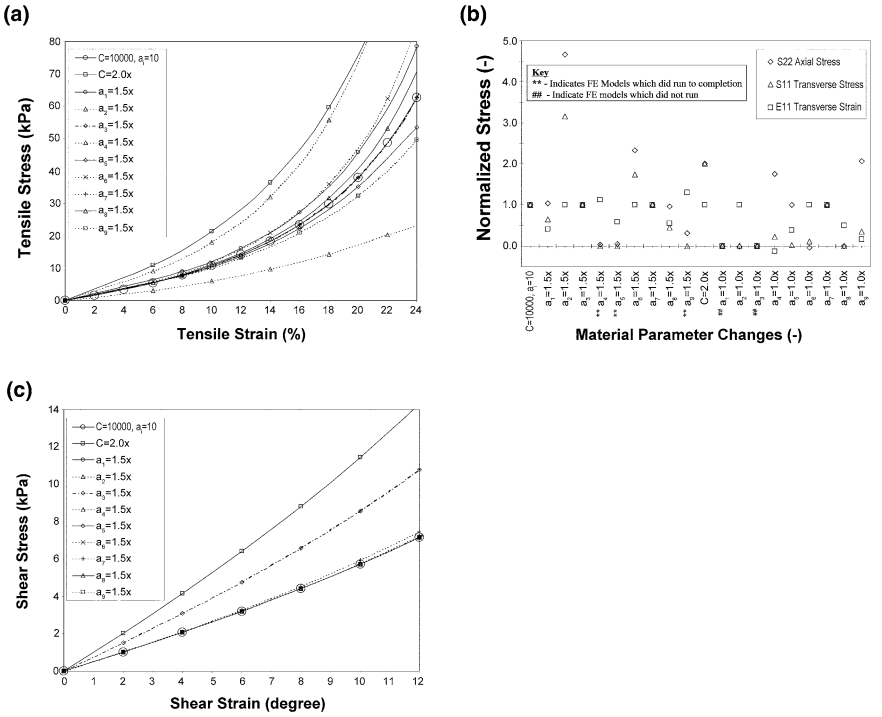

Fig. 2 Effects of fabric material coefficients C and a_i: **a** Stress-strain curves and **b** normalized stress and transverse strain for uniaxial tension; **c** Shear stress–shear angle curves

Figure 2c shows typical curves of shear stress versus shear angle obtained from the simple shear model. Although not clearly observed, the shear stress-strain relation became slightly curved by increasing coefficients a_3 and a_7. Table 1 summarizes the results of the comparative tests with the uniform and non-uniform multi-element models and the single element model for uniaxial tensile and simple shear.

2.3 Implementation and Validation of Fabric Constitutive Model

To assess the ability of the constitutive model to simulate the physical fabric mechanics, four distinctly different fabrics were obtained (Finitex (Pvt.) Ltd., Cape Town, South Africa): (1) basic warp knit, (2) warp knit with Lycra® support, (3) coarse warp knit and (4) monofilament warp knit. The selected fabrics were part of standard production lots that underwent routine quality assessment with regard to consistency. Figure 3 provides scanning electron micrographs of the fabrics.

Table 1 Patch test results for uniform and non-uniform multi-element model and single element model for uniaxial tension and simple shear

	Multi element uniform	Multi element non-uniform	Single element
Tensile			
$S11$ (Pa)	6.776	6.776	6.776
$S22$ (Pa)	0.168×10^7	0.168×10^7	0.168×10^7
$S12$ (Pa)	0	0	0
$U1$ (mm)	−0.581	−0.581	−0.581
Shear			
$S11$ (Pa)	$-0.24 \times 10^5 \rightarrow 1.75 \times 10^5$	$-0.23 \times 10^5 \rightarrow 1.73 \times 10^5$	0.41×10^5
$S22$ (Pa)	$-0.188 \times 10^5 \rightarrow 4.92 \times 10^5$	$-0.193 \times 10^5 \rightarrow 4.82 \times 10^5$	0.59×10^5
$S12$ (Pa)	$0.072 \times 10^5 \rightarrow 2.86 \times 10^5$	$0.097 \times 10^5 \rightarrow 2.81 \times 10^5$	0.86×10^5

Ranges are given for the simple shear test. Notations: $S11$, $S22$ Normal stress in 1 and 2 directions; $S12$ Shear stress; $U1$ Displacement in 1 direction

Uniaxial tensile tests were performed on samples with dimensions 60 × 20 mm at 37 °C (Instron® 5544, Instron Corp., Norwood, MA), see Fig. 4a. The loading protocol comprised: (1) Pre-load to 1 % nominal strain at a strain rate of 50 mm/min to reduce material inconsistencies, and (2) Extension to 50 % nominal strain at a strain rate of 200 mm/min, the strain rate stipulated by medical implant standards [16, 17]. Due to difficulties in monitoring lateral strain effects during the Instron® tests, caused by curling effects at the sample edges, fabric samples were strained on a flat bed at 37 °C in steps of 10, 20 and 30 %. For both the Instron® and the flat bed tests, a 5 × 5 mm grid was marked on each sample to visualize localized strain effects. Strengthening stitches were sewn at both ends of the samples to minimize localized stress concentrations. Using digital images recorded during the tests, the longitudinal and transverse strain was determined from a single grid cell located in the center of the sample.

A quarter-symmetric FE model was used to simulate the physical uniaxial tensile tests. The model, see Fig. 4b, utilized a mesh of four-noded membrane elements. The boundary conditions were selected such that edge AB was free to move horizontally but constrained vertically, while edges AD and DC were free to move vertically but constrained horizontally. A quasi-static displacement at 200 mm/min [16, 17] was applied to edge DC. The loaded boundary DC and the edge BC were expected to have a greater variation in stress and deformation. Hence the element mesh was refined toward these edges. The mesh sensitivity was assessed by increasing and biasing the element density toward edges BC and DC and center point A until the stress, strain and displacement fields became consistent.

2.3.1 Optimisation of Fabric-Specific Constitutive Coefficients

A genetic algorithm GA1, programmed using Perl®, was utilized to iteratively optimize the fabric model coefficients to represent the physically tested fabrics. Using a single set of fabric coefficients, GA1 ran mutually orthogonal uniaxial

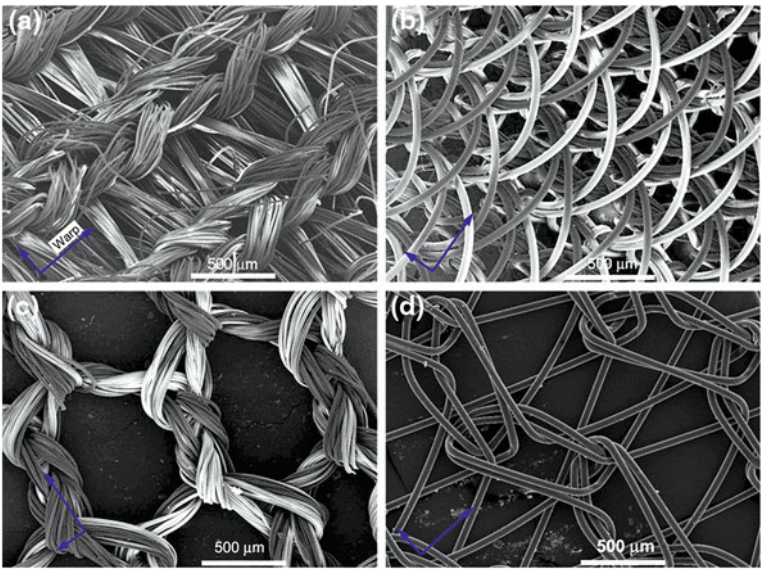

Fig. 3 Scanning electron micrographs (50x) of fabrics tested with arrows indicating warp and weft directions. **a** Basic warp knit (sample 1), **b** Warp knit with Lycra® support (sample 2), **c** Coarse warp knit (sample 3) and **d** Monofilament warp knit (sample 4)

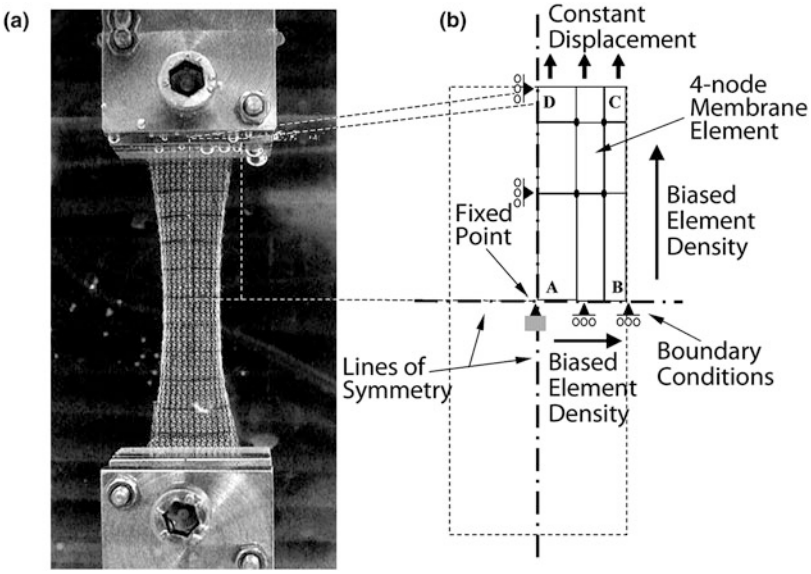

Fig. 4 **a** Photograph of fabric sample and customized clamps during uniaxial tensile test and **b** Schematic of FE model for uniaxial tensile test utilizing symmetry

tensile FE models in order to predict stress-strain curves for the warp and weft directions. Subsequently, GA1 analyzed the predicted results with respect to the fit with physical test data utilizing objective, penalty and fitness functions. This process was repeated until a desired fitness value $f(C, a_i)$ was achieved or when 50 generations were reached.

Dynamic Range and Resolution of the Search Space

The search space of GA1 was dynamically confined and refined over the generations. An initial large range with low resolution allows GA1 to maximize its initial search over a wide search space. With increasing generations, the range of the search space was reduced and the resolution was increased, in order to constrain GA1 for the refinement of the acceptable solutions obtained. Using initial values of $C = 10000$ and $a_i = 10$ (i = 1–9), the initial search ranges, $\{R\}$, of $0 < C \leq 20000$ and $0 < a_i \leq 20$ (i = 1–9) were biased 3:2 between the first and second ranked solutions of the previous generation. In addition, the search space range was reduced linearly by 2.5 % over each generation. An explicit constraint for the search space range of C ensured that its value remained positive over the generations, $C|C > 0$, to prevent unrealistic compressive or zero stress solutions under tensile strain of the fabric.

The resolution of the search space was increased after each generation. A binary number of m bit was used to encode each scaled coefficient into the chromosome. With the initial value of $m = 5$, the resolution of the search space, $\{R\}/2^m$, was $20/2^5 = 0.625$ for a_i and $20000/2^5 = 625$ for C. The bit size was increased by 1 every 10th generation, reaching $m = 10$ at the 50th generation. Consequently, the range $\{R\}$ was reduced by 50 %, the final resolution was $10/2^{10} = 9.7656 \times 10^{-3}$ for a_i and $10000/2^{10} = 9.7656$ for C. Figure 5 illustrates the reduction of the range and increase of the resolution of a two-dimensional parameter search space.

Objective, Penalty and Fitness Functions

The same set of fabric material model coefficients were utilized in two FE models that describe uniaxial tension in the warp and weft direction, respectively. This was implemented in the FE model by swapping the material model coefficients a_1 with a_2, a_5 with a_6, and a_8 with a_9. For the warp and weft directions, the numerical results for axial stress ($\sigma_{A,i}^{Model}$), localized axial strain ($\varepsilon_{A,i}^{Model}$), and localized transverse strain ($\varepsilon_{T,i}^{Model}$) were compared with the equivalent physical data of axial stress ($\sigma_{A,i}^{Data}$), localized axial strain ($\varepsilon_{A,i}^{Data}$) and localized transverse strain ($\varepsilon_{T,i}^{Data}$) at pre-defined axial strains of 10, 20 and 30 %.

Partial Objective and Penalty Functions

The partial objective functions were calculated from the normalized differences between the model and physical data. The partial objective functions for stress were

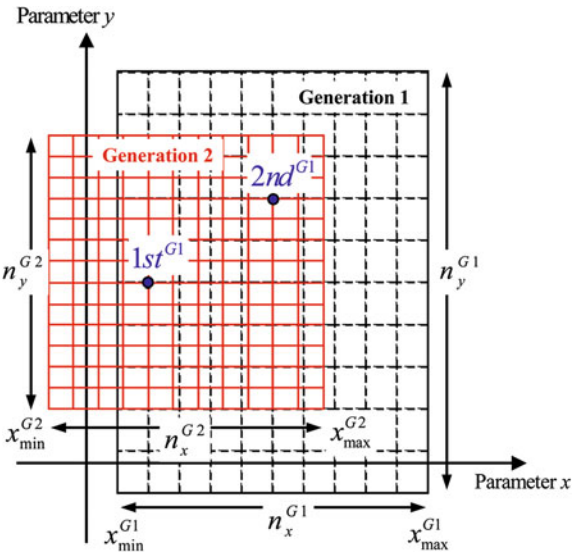

Fig. 5 Schematic illustrating the reduction of a two-dimensional parameter search space from $(x_{\max}^{G1} - x_{\min}^{G1})$ to $(x_{\max}^{G2} - x_{\min}^{G2})$, biased 3:2 between the first and second ranked solutions of generation 1 ($1st^{G1}$, $2nd^{G1}$) and the resolution of the search increased from n_x^{G1} to n_x^{G2} for parameter x and n_y^{G1} to n_y^{G2} for parameter y

$$\phi^{\sigma_A^n} = \frac{\sum_{i=10\,\%,10\,\%}^{30\,\%} w_{\sigma_{A,i}}^n \left[1 - \left\{\left|\triangle\sigma_{A,i}^n\right|\left(\frac{1}{m_{\sigma_{A,i}}^n - 1}\right)\right\}\right]}{\sum_{i=10\,\%,10\,\%}^{30\,\%} w_{\sigma_{A,i}}^n}, \tag{7}$$

with

$$\triangle\sigma_{A,i}^n = \frac{\sigma_{A,i}^{Model,n} - \sigma_{A,i}^{Data,n}}{\sigma_{A,i}^{Data,n}}, \tag{8}$$

and

$$m_{\sigma_{A,i}}^n = \left\{ \begin{array}{ll} 1 + \left|\frac{\sigma_{A,i}^{\max,n} - \sigma_{A,i}^{Data,n}}{\sigma_{A,i}^{Data,n}}\right| & \text{for } \sigma_{A,i}^{Model,n} > \sigma_{A,i}^{Data,n} \\ 1 + \left|\frac{\sigma_{A,i}^{\min,n} - \sigma_{A,i}^{Data,n}}{\sigma_{A,i}^{Data,n}}\right| & \text{for } \sigma_{A,i}^{Model,n} \leq \sigma_{A,i}^{Data,n} \end{array} \right\}. \tag{9}$$

where n is the direction of the uniaxial tensile test (warp or weft), i the pre-defined axial strains of 10, 20 and 30 %, $w_{\sigma_{A,10\,\%}}^n = 6$, $w_{\sigma_{A,20\,\%}}^n = 4$ and $w_{\sigma_{A,30\,\%}}^n = 1$ are the weightings for the pre-defined axial strain field values.

Similarly, the partial objective functions for localized axial strains were

$$\phi^{\varepsilon_A^n} = \frac{\sum_{i=10\,\%,10\,\%}^{30\,\%} w_{\varepsilon_{A,i}}^n \left[1 - \left\{\left|\triangle\varepsilon_{A,i}^n\right|\left(\frac{1}{m_{\varepsilon_{A,i}}^n - 1}\right)\right\}\right]}{\sum_{i=10\,\%,10\,\%}^{30\,\%} w_{\varepsilon_{A,i}}^n} \tag{10}$$

where

$$\triangle\varepsilon_{A,i}^{n} = \frac{\varepsilon_{A,i}^{Model,n} - \varepsilon_{A,i}^{Data,n}}{\varepsilon_{A,i}^{Data,n}}, \tag{11}$$

$$m_{\varepsilon_{A,i}}^{n} = \left\{ \begin{array}{ll} 1 + \left| \frac{\varepsilon_{A,i}^{\max,n} - \varepsilon_{A,i}^{Data,n}}{\varepsilon_{A,i}^{Data,n}} \right| & \text{for } \varepsilon_{A,i}^{Model,n} > \varepsilon_{A,i}^{Data,n} \\ 1 + \left| \frac{\varepsilon_{A,i}^{\min n} - \varepsilon_{A,i}^{Data,n}}{\varepsilon_{A,i}^{Data,n}} \right| & \text{for } \varepsilon_{A,i}^{Model,n} \leq \varepsilon_{A,i}^{Data,n} \end{array} \right\}. \tag{12}$$

The partial objective functions for local transverse strains were

$$\phi^{\varepsilon_T^n} = \frac{\sum_{i=10\,\%,10\,\%}^{30\,\%} w_{\varepsilon_{T,i}}^{n} \left[1 - \left\{ \left| \triangle\varepsilon_{T,i}^{n} \right| \left(\frac{1}{m_{\varepsilon_{T,i}}^{n} - 1} \right) \right\} \right]}{\sum_{i=10\,\%,10\,\%}^{30\,\%} w_{\varepsilon_{T,i}}^{n}}, \tag{13}$$

where

$$\triangle\varepsilon_{T,i}^{n} = \frac{\varepsilon_{T,i}^{Model,n} - \varepsilon_{T,i}^{Data,n}}{\varepsilon_{T,i}^{Data,n}}, \tag{14}$$

$$m_{\varepsilon_{T,i}}^{n} = \left\{ \begin{array}{ll} 1 + \left| \frac{\varepsilon_{T,i}^{\max,n} - \varepsilon_{T,i}^{Data,n}}{\varepsilon_{T,i}^{Data,n}} \right| & \text{for } \varepsilon_{T,i}^{Model,n} > \varepsilon_{T,i}^{Data,n} \\ 1 + \left| \frac{\varepsilon_{T,i}^{\min,n} - \varepsilon_{T,i}^{Data,n}}{\varepsilon_{T,i}^{Data,n}} \right| & \text{for } \varepsilon_{T,i}^{Model,n} \leq \varepsilon_{T,i}^{Data,n} \end{array} \right\}. \tag{15}$$

The differences $\triangle\sigma_{A,i}^{n}$, $\triangle\varepsilon_{A,i}^{n}$ and $\triangle\varepsilon_{T,i}^{n}$ were normalized and weighted to ensure that those solutions which model the test results accurately at lower strains were retained for further generations. The partial objective values tended to unity as model stresses, localized axial and transverse strains tended toward physical data. Similarly, parameters $m_{\sigma_{Ai}}^{n}$, $m_{\varepsilon_{Ai}}^{n}$ and $m_{\varepsilon_{Ti}}^{n}$ were multiples used to bias future generations from a certain side and partially penalize their respective partial objective functions.

The partial penalties and weightings for GA1 were as follows:

$$\text{if } \left\{ \sigma_{A,i}^{n} | \sigma_{A,i} \leq \sigma_{A,i}^{\min,n} \text{ and } \sigma_{A,i} \geq \sigma_{A,i}^{\max,n} \right\} \text{ then } \phi^{\sigma_A^n} \text{ negatively weighted;} \tag{16}$$

$$\text{if } \left\{ \varepsilon_{A,i}^{n} | \varepsilon_{A,i}^{n} \leq \varepsilon_{A,i}^{\min,n} \text{ and } \varepsilon_{A,i}^{n} \geq \varepsilon_{A,i}^{\max,n} \right\} \text{ then } \phi^{\varepsilon_A^n} \text{ negatively weighted;} \tag{17}$$

$$\text{if } \left\{ \varepsilon_{T,i}^{n} | \varepsilon_{T,i}^{n} \leq \varepsilon_{T,i}^{\min,n} \text{ and } \varepsilon_{T,i}^{n} \geq \varepsilon_{T,i}^{\max,n} \right\} \text{ then } \phi^{\varepsilon_T^n} \text{ negatively weighted;} \tag{18}$$

$$w_{x,10\,\%}^{n} > w_{x,20\,\%}^{n} > w_{x,30\,\%}^{n}. \tag{19}$$

In Eq. (19), x represents either axial stress σ_A, localized axial strain ε_A, or localized transverse strain ε_T. This ensured that numerical models which did not run to completion were weighted accordingly. Tests that failed to reach 10 % axial strain were given a lower ranking to those which reached an axial strain of 20 %, similarly for 20 and 30 %, thus favoring those models which ran to completion.

Global Objective, Penalty and Fitness Function

The objective function was represented in terms of the partial objective functions by

$$\phi = \frac{w_{obj}^{\sigma_A^{Warp}} \phi^{\sigma_A^{Warp}} + w_{obj}^{\sigma_A^{Weft}} \phi^{\sigma_A^{Weft}} + w_{obj}^{\varepsilon_A^{Warp}} \phi^{\varepsilon_A^{Warp}} + w_{obj}^{\varepsilon_A^{Weft}} \phi^{\varepsilon_A^{Weft}} + w_{obj}^{\varepsilon_T^{Warp}} \phi^{\varepsilon_T^{Warp}} + w_{obj}^{\varepsilon_T^{Weft}} \phi^{\varepsilon_T^{Weft}}}{w_{obj}^{\sigma_A^{Warp}} + w_{obj}^{\sigma_A^{Weft}} + w_{obj}^{\varepsilon_A^{Warp}} + w_{obj}^{\varepsilon_A^{Weft}} + w_{obj}^{\varepsilon_T^{Warp}} + w_{obj}^{\varepsilon_T^{Weft}}}, \tag{20}$$

where w_{obj}^{i} are pre-defined weightings and i represents the partial objective function to which the weightings apply. These weightings were used to bias the objective value to either the warp or weft direction, to stresses, to localized axial and or transverse strains. From Eq. (20), ϕ tends to unity as $\phi^{\sigma_A^{Warp}}$, $\phi^{\sigma_A^{Weft}}$, $\phi^{\varepsilon_A^{Warp}}$, $\phi^{\varepsilon_A^{Weft}}$, $\phi^{\varepsilon_T^{Warp}}$ and $\phi^{\varepsilon_T^{Weft}}$ tend to unity. The pre-defined values of the weightings are $w_{obj}^{\sigma_A^{Warp}} = w_{obj}^{\sigma_A^{Weft}} = 200$, $w_{obj}^{\varepsilon_A^{Warp}} = w_{obj}^{\varepsilon_A^{Weft}} = 10$ and $w_{obj}^{\varepsilon_T^{Warp}} = w_{obj}^{\varepsilon_T^{Weft}} = 100$.

The global penalty functions, p, were defined as

$$\text{if } \sigma_{A,10\,\%}^{n} \leq 0 \text{ then } p = -\infty \text{ else } p = 1, \tag{21}$$

$$\text{if } \sigma_{T,10\,\%}^{n} \leq 0 \text{ then } p = -\infty \text{ else } p = 1, \tag{22}$$

$$\text{if } \varepsilon_{T,10\,\%}^{n} \geq 0 \text{ then } p = -\infty \text{ else } p = 1, \tag{23}$$

and ensure that the models run and the results obtained are reasonable and acceptable.

The fitness function, f, for the comparison of model solutions and physical data for warp and weft uniaxial tension was:

$$f = p \times \phi. \tag{24}$$

2.3.2 Optimised Model Solutions

For the four fabric samples, convergence of GA1 on a set of single solutions was found after 47, 42, 39 and 45 generations, respectively. Table 1 provides the model coefficients and the fitness, objective and partial objective values obtained from GA1 for each fabric. The fitness values coincided with the objective values, all of which closely approached unity. The average partial objective values obtained for

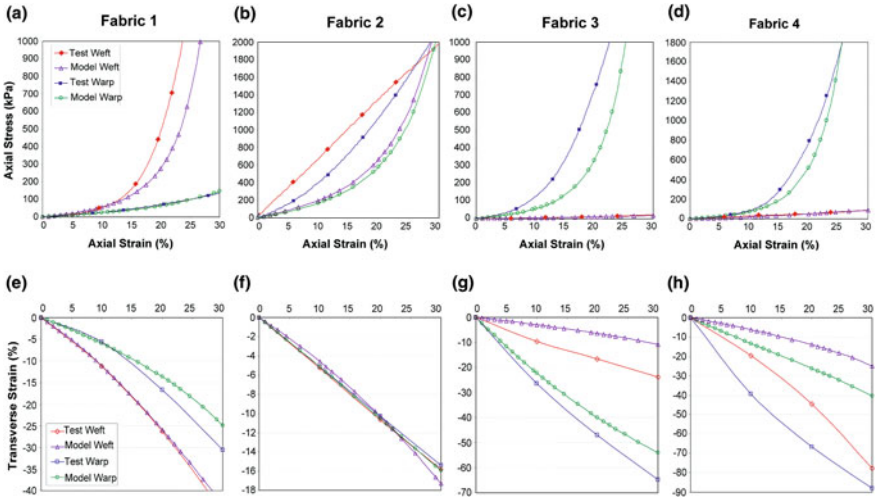

Fig. 6 Nominal stress and engineering strain data of physical tensile tests and model predictions for the warp and weft direction of fabrics 1 to 4: **a–d** Uniaxial tensile stress versus axial strain, **e–h** Transverse strain versus axial strain

fabrics 1 to 4 were 0.99976 ± 0.00020, 0.99971 ± 0.00021, 0.99973 ± 0.00026 and 0.99968 ± 0.00027, respectively.

Figure 6 compares model predictions, obtained using the coefficients identified with GA1, see Table 2, for the axial nominal stress versus axial engineering strain (Fig. 6a–d) and transverse engineering strain versus axial engineering strain (Fig. 6e–h) with data obtained from physical tests. For experimental axial stress and axial strain, fabric samples 1, 3 and 4 exhibited a high degree of anisotropy and nonlinear stress-strain relationships in both the warp and weft directions, see Fig. 6 a, c, d. For these three fabrics, the model solutions fit very well to test data in either warp direction (fabric 1) or weft direction (fabrics 3 and 4), while a reasonable fit between model and test data was obtained in the respective transverse direction. For fabric 2, the physical test data indicated a nearly linear stress-strain relationship in the weft direction and a lower degree of anisotropy (Fig. 6b). Considerable deviation was observed between the model and physical data for this fabric. For transverse strain versus axial strain, fabric 1 exhibited a difference between model and test data of $<1.2\,\%$ in weft direction and $<20\,\%$ in warp direction (Fig. 6e). Close correlation between model and test was obtained for fabric 2 (Fig. 6f), with differences of <1 and $1.5\,\%$ in the warp and weft direction, respectively. However, the solution for fabric 2 was largely linear, while fabric 1 showed an increase in Poisson's effect with an increase in axial strain. Large differences were observed for fabric 3 (Fig. 6g) and fabric 4 (Fig. 6h), except for the weft direction for fabric 3 with a small difference between model and test data of $<2\,\%$ in transverse strain.

Table 2 Model coefficients for fabric samples and associated values for the partial objective functions, objective function and fitness function obtained with the genetic algorithm and the number of generations required to obtain the presented solution

Fabric sample	1	2	3	4
Constitutive coefficients				
C	26444.0	9766.2	12401.0	10299.0
a_1	9.6714	12.77	38.689	81.086
a_2	15.815	15.414	5.2838	35.152
a_3	86.94	12.895	25.122	39.747
a_4	15.742	12.322	19.878	84.289
a_5	−3.8816	2.3294	−9.9038	−22.657
a_6	21.377	−5.3519	0.92224	20.526
a_7	−39.528	−13.246	28.778	43.484
a_8	−5.0215	5.1202	10.485	94.932
a_9	8.5257	−1.9179	12.086	124.26
Fitness value $f(C, a_i)$	0.99985	0.99962	0.99968	0.99970
Objective value $\phi(C, a_i)$	0.99985	0.99962	0.99968	0.99970
Partial objective values				
$\phi^{\sigma_A^{warp}}$	0.99980	0.99957	0.99998	0.99998
$\phi^{\sigma_A^{weft}}$	0.99993	0.99938	0.99947	0.99974
$\phi^{\varepsilon_A^{warp}}$	0.99972	0.99981	0.99989	0.99987
$\phi^{\varepsilon_A^{weft}}$	0.99938	0.99967	0.99991	0.99980
$\phi^{\varepsilon_T^{warp}}$	0.99991	0.99987	0.99935	0.99934
$\phi^{\varepsilon_T^{weft}}$	0.99981	0.99993	0.99979	0.99935
Generation	47	42	39	45

3 Constitutive Modelling of Porous Polymeric Scaffolds

The porous scaffolds featuring well-defined, interconnected pores, see Fig. 7, were manufactured using a biostable ether-free aliphatic segmented polyurethane (PUR) [24] and extractable highly regular spherical porogen (gelatin micro-spheres, Thies Technologies, St. Louis, MO, USA) of three different nominal size ranges of 90–106, 106–125, and 125–150 µm. On average, the pores created in the polyurethane structure were 1.21 ± 0.07 times the diameter of the porogen from which they were formed, while the interconnecting windows were 0.52 ± 0.04 times the diameter [1].

A hyperfoam strain energy function ψ [22] was used to describe the porous polymer:

$$\psi\left(\bar{\lambda}_1, \bar{\lambda}_2, \bar{\lambda}_3\right) = \sum_{i=1}^{N} \frac{2\mu_i}{\alpha_i^2}\left[\left(\bar{\lambda}_1^{\alpha_i} + \bar{\lambda}_2^{\alpha_i} + \bar{\lambda}_3^{\alpha_i} - 3\right) + 3\left(J^{-\frac{1}{3}\alpha_i} - 1\right) + \frac{1}{\beta_i}\left(J^{-\alpha_i\beta_i} - 1\right)\right]. \tag{25}$$

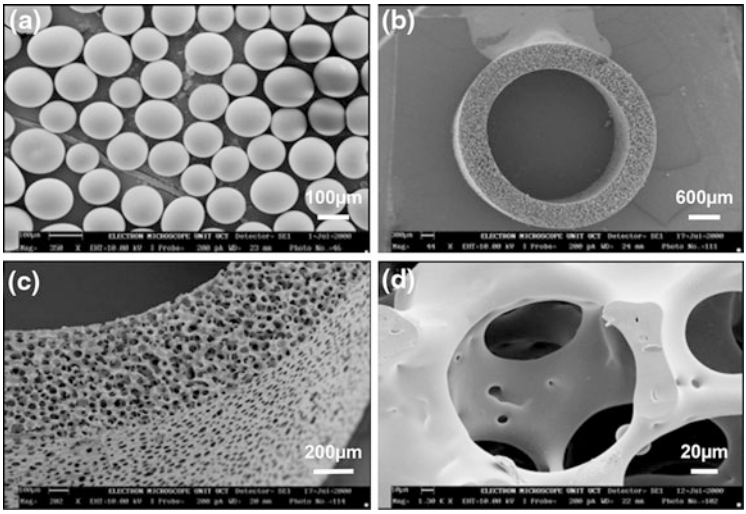

Fig. 7 SEM images of **a** porogens gelatin microspheres, **b** porous graft cross-section, **c** porous graft wall and **d** porous structure [29]

Here $\lambda_k (k = 1, 2, 3)$ are the principal stretches, J is the Jacobian of the deformation gradient and represents the ratio of current to initial volume change, $\overline{\lambda}_i = J^{1/3}\lambda_i$ are deviatoric stretches, and α_i, β_i, and μ_i are material constants.

The material model was validated through experimental tensile, compressive and shear tests. The tests were performed under physiological conditions on unit disk samples of the porous PUR of the various porogen size groups. The experimental and numerical data agreed well for tensile strain below 55 % and compressive strain below 30 %. Since the porous structures experience a maximum tensile strain of about 30 % under physiological conditions, these limits were not deemed problematic.

4 Development and Optimisation of Reinforced Graft System

4.1 Finite Element Models and Optimisation Algorithm

4.1.1 Graft FE Model

The graft model was used to find the static and dynamic compliance values and pressure-diameter curves for different adventitial reinforcing fabric material model coefficients C and $a_i (i = 1, \ldots, 9)$, Eq. (3), with a particular porous graft. Figure 8 illustrates the element, boundary and load conditions used for the graft model. The model simulates the behaviour of the porous graft structure reinforced externally

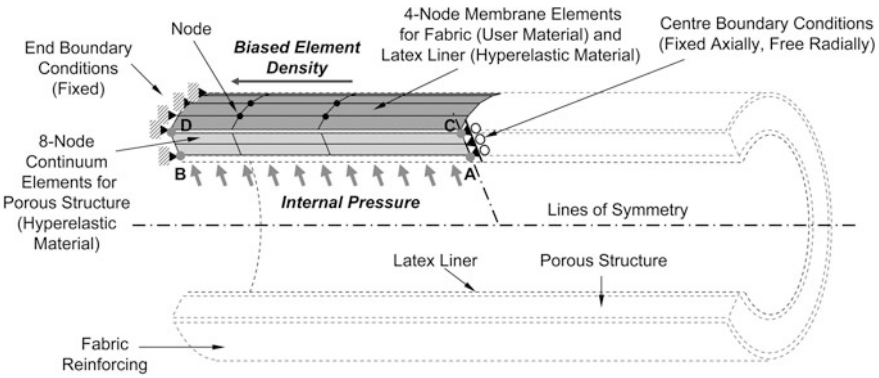

Fig. 8 Graft FE model

with the fabric reinforcing. Due to the symmetry of the problem, only one half of the longitudinal section of the graft and a quarter of the graft in the circumferential direction was modelled.

Eight-node continuum elements without twist were used to model the porous polymer structure, while four-node linear membrane elements without twist were used for the fabric reinforcing. Two load cases were utilized to simulate static and dynamic compliance loads. In both cases, a pre-defined longitudinal (axial) strain of 10 % was initially applied before an internal pressure was applied on the inner surface of the porous structure. For the static load case the internal pressure applied to the inner graft surface was linearly ramped from 0 to 300 mmHg (39996 Pa) over 30 s. This mimicked the physical static compliance test carried out on a graft. For the dynamic load case, the internal pressure on the graft lumen wall was linearly ramped from 0 to 100 mmHg (13332 Pa) over a period of 4 s, after which a pulsatile pressure wave, described by a seven-term Fourier series

$$\begin{aligned} \alpha &= A_o + \sum_{1}^{6} (B_n \sin n\varpi(t - t_o)) \quad \text{for } t \geq t_o, \\ \alpha &= A_o \quad \text{for } t < t_o, \end{aligned} \tag{26}$$

was applied to mimic the pressure pulse applied in physical studies. Here ϖ is the frequency ($\varpi = 15.14$ rad/s and period $T = 0.83$ s), t_o the time at which cyclic load starts ($t_o = 0$), A_o the initial amplitude ($A_o = 13332$ Pa), and B_n are the Fourier constants ($B_1 = 2418.5$, $B_2 = 691.0$, $B_3 = 230.33$, $B_4 = 115.17$, $B_5 = B_6 = 114.7$).

Symmetric boundary conditions were applied to the graft model, with the end nodes fully fixed, and the central nodes fixed in the axial direction, allowing no angular twist, while being free to move radially. The graft element mesh was refined longitudinally towards the fixed end, but remained uniform in the radial and circumferential directions. The level of mesh refinement was verified through mesh sensitivity studies ensuring acceptable numerical accuracy.

4.1.2 Fabric FE Models

The circumferential and longitudinal tensile models were used to provide mutually orthogonal stress-strain curves of the optimized fabric reinforcing solution obtained from the graft model and the genetic algorithm. The stress-strain curves obtained from the circumferential and longitudinal models were then used to produce reinforcing fabrics for the physical studies. The FE model corresponding to experimental circumferential tensile test performed on fabrics at 37 °C is illustrated in Fig. 9a. Due to the geometry of the problem and loading conditions, a 1/8 symmetric model was analysed. Two steps were used in the circumferential tensile model: an initial contact step, which established contact between the analytically rigid pin and the fabric, and a second step which displaced the top pin at a rate of 200 mm/min [16, 17], until 50 % circumferential strain was obtained. A 'soft' contact model was used which takes the form of an exponential function for the pressure-clearance relation. This allowed for the gradual transfer of load from the pin to fabric. The pin was assumed to be smooth and frictionless. The orientations of the optimized material properties obtained from the graft model solutions were mapped onto the membrane elements, ensuring that the fabric principal directions were in-plane with the membrane surface. Longitudinal fabric sample lengths of 48.0 mm were clamped flat at the ends and subjected to uniaxial tension. Figure 9b shows the full and quarter symmetric FE model used to obtain curves of force per unit length vs. displacement curves for the fabric reinforcing in the longitudinal direction. The longitudinal tensile model used a single step, which displaced the end of the fabric tube at a strain rate of 200 mm/min [16, 17] to 100 % axial strain.

A mesh refinement study was performed for each FE model. Critical nodes were monitored and mesh density was increased until the stress, strain and displacements observed became stable and consistent, thus reducing the error in model solutions.

4.1.3 Genetic Algorithm for Graft Optimization Procedure

A genetic algorithm GA2 was used to optimize the fabric model coefficients $C, a_i (i = 1, \ldots, 9)$ in Eq. (3) to obtain a dynamic compliance C_d of 6 %/100 mmHg, a diastolic diameter d_{dia} of 4.0 mm, and to display non-linear stiffening from a dynamic graft FE model. The FE analysis was executed with a particular fabric model with penalty and fitness functions of GA2. The process was repeated until a desired result was obtained or a pre-defined number of generations were reached. A number of 'good' solutions were then kept over the generations, and were then utilized in the tensile test models to obtain a range of circumferential and longitudinal stress-strain curves for possible physical solutions for the fabric reinforcing.

As for GA1, the search space of GA2 was dynamically adjusted over the generations; an initial range was set for each coefficient and thereafter the range was biased 3:2 between the first and second ranked solutions for the generation. The range of the search space was also reduced linearly, confining and refining the

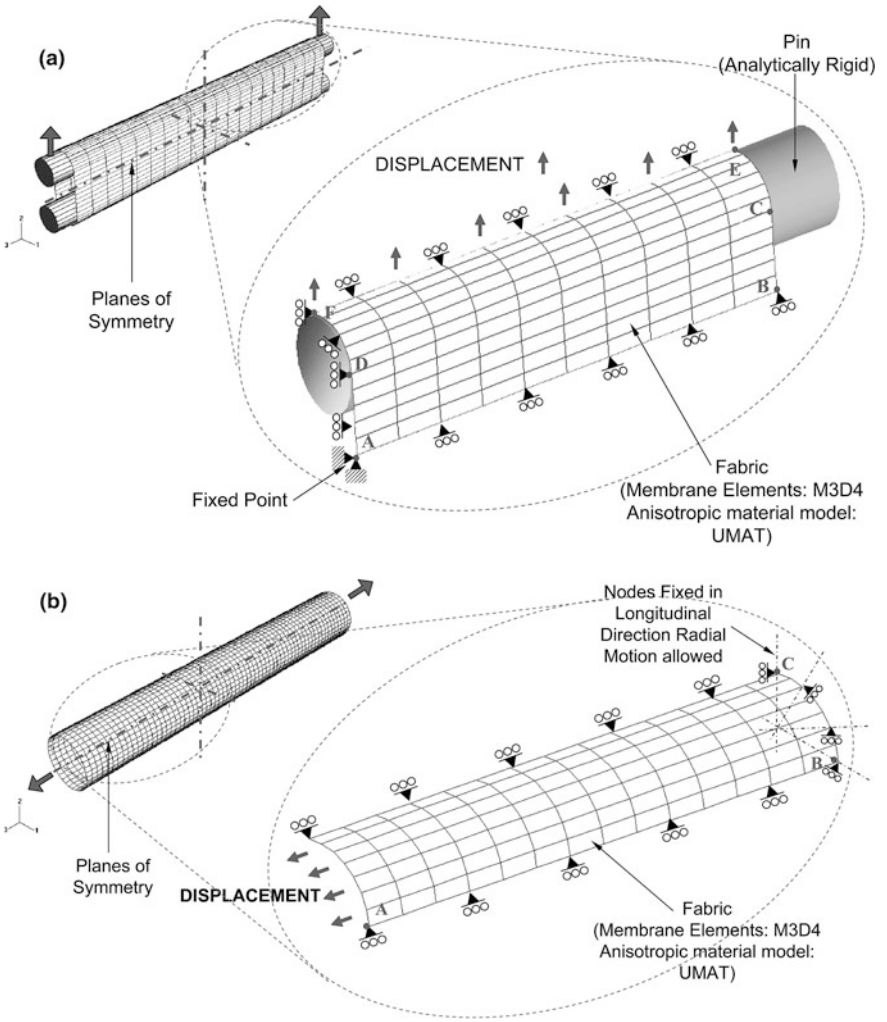

Fig. 9 Quarter-symmetric FE mesh for circumferential (**a**) and longitudinal (**b**) tensile test simulation

search area after each generation. The initial search space coefficient ranges were $0 < C \leq 20000$ and $0 < a_i \leq 20$, with the initial values $C = 10000$ and $a_i = 10$.

The compliance C_d and non-linear stiffening characteristic J were calculated according to

$$C_d = \frac{d_{sys} - d_{dia}}{d_{dia}} \times \frac{100}{P_{sys} - P_{dia}} \times 100, \tag{27}$$

$$J = \frac{(d_{dia} - d_{init})(P_{sys} - P_{dia}) - P_{dia}(d_{sys} - d_{dia})}{P_{dia}}. \tag{28}$$

Here d_{init} is the initial internal diameter, d_{dia} and d_{sys} are the diastolic and systolic internal model diameters, and P_{dia} and P_{sys} are the diastolic and systolic pressures. Values of d_{dia}, d_{sys}, P_{dia} and P_{sys} were obtained from the dynamic graft FE model analysis. The non-linear stiffening characteristic J was the difference in diameter change per unit pressure from zero to P_{dia} and from P_{dia} to P_{sys}. C_d and d_{dia} were used to calculate the partial objective values for the model, while J was used as a penalty function.

From Eq. (27) a partial objective function formulated for compliance was given by

$$\phi^{\triangle C_d} = \left[1 - \left\{\left|\triangle C_d^{norm}\right|\left(\frac{1}{(m^{\triangle C_d} - 1)}\right)\right\}\right], \tag{29}$$

where

$$\triangle C_d^{norm} = \frac{C_d - C_d^{target}}{C_d^{target}} \tag{30}$$

and

$$m^{\triangle C_d} = \begin{cases} 1 + \left|\frac{C_d^{\max} - C_d^{target}}{C_d^{target}}\right| & \text{for } C_d > C_d^{target} \\ 1 + \left|\frac{C_d^{\min} - C_d^{target}}{C_d^{target}}\right| & \text{for } C_d \leq C_d^{target}. \end{cases} \tag{31}$$

From Eq. (29), $\phi^{\triangle C_d}$ tended to unity as C_d approached C_d^{target}.

The partial objective function for the diastolic diameter was given by

$$\phi^{\triangle d_{dia}} = \left[1 - \left\{\left|\triangle d_{dia}^{Normalized}\right|\left(\frac{1}{(m^{\triangle d_{dia}} - 1)}\right)\right\}\right], \tag{32}$$

where

$$\triangle d_{dia}^{normalized} = \frac{d_{dia} - d_{dia}^{target}}{d_{dia}^{target}}, \tag{33}$$

$$m^{\triangle d_{dia}} = \begin{cases} 1 + \left|\frac{d_{dia}^{\max} - d_{dia}^{target}}{d_{dia}^{target}}\right| & \text{for: } d_{dia} > d_{dia}^{target} \\ 1 + \left|\frac{d_{dia}^{\min} - d_{dia}^{target}}{d_{dia}^{target}}\right| & \text{for: } d_{dia} \leq d_{dia}^{target}. \end{cases} \tag{34}$$

Like Eq. (29), Eq. (32) tended to unity as the model diastolic diameter d_{dia} tended to the target diastolic diameter d_{dia}^{target}.

The parameters $m^{\triangle C_d}$ and $m^{\triangle d_{dia}}$ were multiples used to bias future generations from a certain side. For example, due to tissue ingrowth in the porous grafts, compliance will be reduced after implantation; thus higher compliance values at time of implantation are preferred. These parameters were also used to partially

penalize $\phi^{\triangle C_d}$ and $\phi^{\triangle d_{dia}}$ by making them negative if model C_d or d_{dia} go above or below pre-defined boundary values $C_d^{\max}$and $C_d^{\min}$. Thus,

$$\begin{aligned} &\text{if } \left\{C_d | C_d \leq C_d^{\min} \text{ and } C_d \geq C_d^{\max}\right\} \\ &\text{then } \phi^{\triangle C_d} \text{ was negatively weighted,} \\ &\text{if } \left\{d_{dia} | d_{dia} \leq d_{dia}^{\min} \text{ and } d_{dia} \geq d_{dia}^{\max}\right\} \\ &\text{then } \phi^{\triangle d_{dia}} \text{ was negatively weighted.} \end{aligned} \tag{35}$$

From these partial objective functions an objective function

$$\phi^{GA2} = \frac{\left(w^{C_d} \times \phi^{\triangle C_d^{dyn}}\right) + \left(w^{d_{dia}} \times \phi^{\triangle d_{dia}}\right)}{\left(w^{C_d} + w^{d_{dia}}\right)} \tag{36}$$

was used to calculate the objective value, where $w^{C_d} = 1.75$ and $w^{d_{dia}} = 1.0$ were pre-defined weightings used to bias the objective value to either the compliance or diastolic diameter. From Eq. (36), ϕ^{GA2} tended to unity as $\phi^{\triangle C_d^{dyn}}$ and $\phi^{\triangle d_{dia}}$ tended to unity.

The global penalties used were as follows:

$$\text{If } \begin{cases} C_d \leq 0 \\ C_d = C_d^{target} \\ d_{dia} = d_{dia}^{target} \\ J \leq 0 \end{cases} \text{ then } p^{GA2} = -\infty, \text{ else } p^{GA2} = 1 \tag{37}$$

Equation (37_1) ensured that the FE results gave an expected positive compliance. With Eqs. (37_2) and (37_3), although we were optimizing for C_d^{target} and d_{dia}^{target}, due to numerical errors, such as round-off, these exact solutions will never be achieved. Equation (37_4) ensured that those solutions which did not display nonlinear stiffening were dismissed. Thus these penalties ensured that models which did not converge or do not show nonlinear stiffening were eliminated from future generations, while the partial penalties described by Eqs. (35) and (37) only weight a solution negatively, but do not necessarily expel the solution from future generations.

The fitness function f^{GA2} used to compare the FE solutions obtained was defined by

$$f^{GA2} = p^{GA2} \times \phi^{GA2}. \tag{38}$$

Termination of GA2 was set when a fitness value $f(C, a_i)$ of 0.95 or 50 generations were achieved. Typically, good solutions were found within 35 generations.

4.2 Manufacture and Characterization of Fabrics and Grafts

4.2.1 Manufacture of Fabric Socks

Fabric socks were manufactured using braiding and knitting processes, respectively, (Secant Medical LLC, Perkasie, PA, USA) according to the required specification including longitudinal and circumferential force-displacement characteristics, inner diameter, fabric wall thickness, fiber thickness, pore size and surface coverage. The force-displacement characteristics of the manufactured prototypes were determined experimentally. In an iterative process, the comparison of the experimental data with the numerically predicted requirements was utilized to select the most promising prototype candidates and to guide the manufacturing of subsequent fabric generations.

4.2.2 Mechanical Characterization of Fabric Socks

Longitudinal and circumferential tensile test were conducted using an Instron 5544 universal testing machine (Instron Corp., Norwood, MA, USA) in phosphate-buffered saline solution at 37 °C) to determine the force-displacement relationships in the two principal directions of the fabric socks. For circumferential tests, samples (length: 36.0 mm) were placed over two pins whereas for longitudinal tensile tests, samples (length: 48.0 mm) were clamped flat at both ends using custom-made fabric clamps. The cross-head speed was 200 mm/min [16, 17] for all tests. The samples were tested to a maximum strain of 50 % and 100 % for circumferential and longitudinal tests, respectively. All tests were conducted in accordance with relevant standards [16, 17] as indicated in Sect. 4.1.2.

4.2.3 Manufacture of Graft Samples

Non-reinforced graft samples comprised a 50 mm porous graft sections (manufactured as described in Sect. 3) and two 20 mm e-PTFE graft anastomoses (inner diameter: 4 mm, wall thickness: 30 μm; Atrium, Hudson, NH). The e-PTFE sections anastomosed to the porous graft by repeated application and drying of a polyurethane solution (5 % PUR by mass in Chloroform) while the segments were constrained on a central mandrel. The e-PTFE graft ends ensured a) that graft samples were not damaged due to attachment in the test fixture and b) consistent longitudinal strains during testing. For reinforced grafts, fabric socks were applied over the porous scaffolds ensuring uniformity. At one of the anastomotic regions of the porous graft, the fabric was anastomosed to the structure by additional application of a polyurethane solution (10 % PUR by mass in Chloroform). A higher concentrated polyurethane solution was used to reduce the absorption into the porous structure. Once this anastomotic region was cured, the fabric sock was

strained, by uniformly and evenly stretching the fabric over the graft sample to the required amount and fixed to the porous graft by again applying repeated layers of polyurethane solution.

4.2.4 Compliance Testing of Grafts

In vitro static and dynamic compliance tests were conducted using a custom-built test rig featuring a closed flow loop system (phosphate buffered saline, 37 °C) [29]. For static tests, the range of the internal pressure was 0–200 mmHg. For dynamic tests, pressure of 80–120 mmHg or equivalent pressure values accounting for the luminal latex liner (as described further below in this section). The outer diameter of the graft samples was monitored with macroscopic digital imaging (Leica MS5 stereo microscope (Leica, Wetzlar, Germany), Sony CCD-IRIS digital camera (Sony, Tokyo, Japan), Strata Videoshop (Strata, Santa Clara, UT, USA)). The compliance was determined using the inner diameter values. These were calculated from the measured outer graft diameter, the wall thickness and numerically predicted wall compression. In addition, compliance was based on the outer graft diameter for selected experiments for comparison purposes. Custom-made latex liners (outer diameter: 3.62 ± 0.15 mm, wall thickness: 0.19 ± 0.02 mm; Roynhardt Pvt. Ltd., Johannesburg, South Africa) were inserted into the graft samples to prevent pressure loss due to the scaffold porosity during the test procedure. The stiffening effect of the latex liner was compensated using the following procedure during a preliminary static compliance test for each graft sample:

1. Subtraction of pressure-diameter curves of the latex liner from the pressure-diameter curves of the graft sample with latex liner.
2. Calculation of equivalent pressure values for the graft-liner samples corresponding to diastolic and systolic pressure of 80 and 120 mmHg for a graft sample without latex liner.

The equivalent diastolic-systolic pressure values used in dynamic compliance tests were 126–203, 144–218 and 163–243 mmHg for the non-reinforced graft samples and 83–128, 102–150 and 116–168 mmHg for the fabric-reinforced samples (for porogen size groups of 90–106, 106–125 and 125–150 μm, respectively).

4.3 Non-Reinforced Porous Graft Predictions

Table 3 gives the dynamic and static compliance values obtained from the graft numerical models for each of the porous graft structures without fabric reinforcing. Other values displayed include wall compression and diastolic and systolic internal diameters. As expected, compliance increases with increased pore size. Little difference was observed between the dynamic and static compliance values;

Table 3 Numerical predictions for diametric compliance, internal diameter, and wall compression of non-reinforced graft models for static and dynamic loading

Porogen size (μm)	90–106	90–106	106–125	106–125	125–150	125–150
Loading type	Stat	Dyn	Stat	Dyn	Stat	Dyn
C_d (%/100 mmHg)	16.9	16.0	20.3	19.2	33.9	31.5
Internal diameter ϕ_i (mm)						
Diastolic	4.088	4.064	4.160	4.133	4.378	4.342
Systolic	4.377	4.319	4.516	4.445	5.002	4.879
Wall compression (%)						
Diastolic	5.46	1.91	6.25	1.97	8.31	1.28
Systolic	7.72	5.68	8.99	6.51	13.06	8.77

however, as pore size increased, a slight increase was seen in static compliance. Diastolic and systolic internal diameters reflected similar characteristics with respective static and dynamic compliance. However, there was a large difference between the static and dynamic wall compression values obtained; for dynamic values the compression observed was much lower, due to the lagging wall response with pulsatile pressure. Figure 10a–c displays the dynamic circumferential, radial and axial stress fields through the various pore size non-reinforced graft structures at mean internal pressure (100 mmHg). The stress fields and sizes are displayed to the same scale to highlight the difference in field and diameters. The profiles of circumferential, radial and axial stress are illustrated in Fig. 10d–f for the various porogen size non-reinforced graft structures. The contour plots and graphs in Fig. 10 indicate that the circumferential stress increased with increased pore size, with the difference between the 90–106 and 106–125 μm being less than that observed between the 106–125 and 125–150 μm. The magnitude of the radial stress for each pore size group was equal through the wall thickness. It was also observed that the axial stress fields decreased considerably in magnitude with increased pore size. The shape of the circumferential and radial stress profiles through the graft wall were similar for increasing pore size. However, a variation in axial stress profiles was observed between the pore size grafts. The stronger 90–106 μm porogen size graft had a higher axial stress at the luminal surface which decayed towards the adventitial surface, while the axial stress profiles through the wall were almost constant for the weaker 106–125 and 125–150 μm. Thus, the weaker large pore sized grafts appeared to distribute the axial load more evenly through the wall.

4.4 Optimised Reinforced Graft Solutions

A total of 39 and 34 generations were required before model solutions the desired 0.95 fitness value were obtained for the 106–125 and 125–150 μm porogen size, respectively. For the 90–106 μm graft type, the full 50 generations were needed before the model reached a fitness value 0.948. The results obtained from GA2 gave

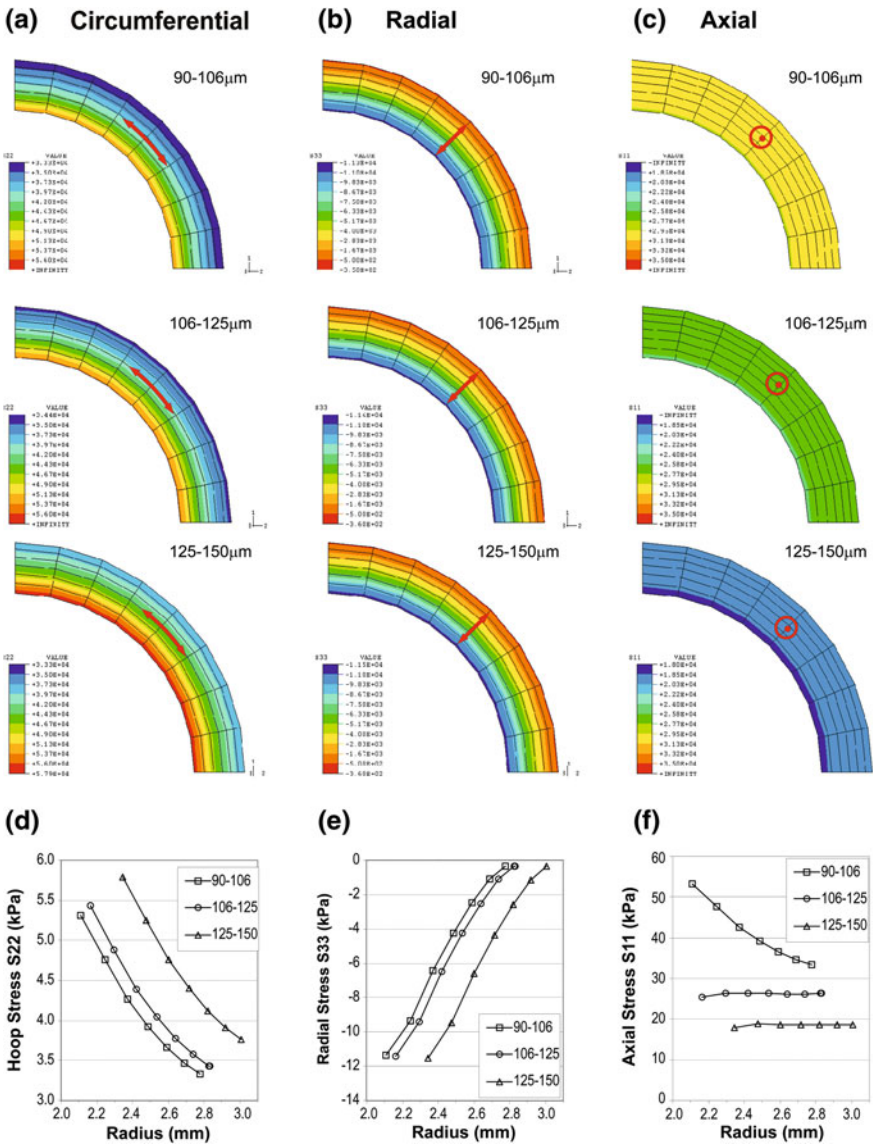

Fig. 10 Contour plots and graphs showing the stress variation through the wall thickness of 90–106, 106–125 and 125–150 μm porous grafts at a luminal pressure of 100 mmHg: Circumferential stress (**a**, **d**), radial stress (**b**, **e**), axial stress (**c**, **f**)

dynamic diameter compliance values of 6.4, 6.9 and 7.1 %/100 mmHg and diastolic diameters of 3.965, 3.998 and 4.000 mm for the fabric reinforced 90–106, 106–125 and 125–150 μm porogen grafts, respectively. A maximum wall compression of 6.20 % was observed for the 125–150 μm porogen graft. The circumferential strain

Table 4 Optimal solutions for fabric reinforced porous grafts of 90–106, 106–125 and 125–150 μm porogen size class

Graft porogen size (μm)	90–106	106–125	125–150
Dynamic C_d (% /100 mmHg)	6.4	6.9	7.1
Internal diameter ϕ_i (mm)			
Diastolic	3.965	3.998	4.000
Systolic	4.067	4.109	4.113
Wall compression (%)			
Diastolic	2.93	3.24	3.82
Systolic	4.82	5.31	6.20
Fabric circumferential strain (%)			
Diastolic	6.61	7.19	7.08
Systolic	8.13	8.85	8.70
Fabric model coefficients			
C	607.969	977.145	3881.518
a_1	0.028	15.885	17.748
a_2	270.643	204.607	133.838
a_3	1.719	21.012	6.662
a_4	24.310	16.631	25.734
a_5	2.745	−28.013	13.785
a_6	64.376	50.642	66.498
a_7	8.014	−24.693	−18.083
a_8	−8.797	−13.284	2.018
a_9	−9.155	14.190	20.619
Fitness value $f(C, a_i)$	0.9484	0.9552	0.9509
Objective value $\phi(C, a_i)$	0.9484	0.9552	0.9509
Partial objective values			
$\phi^{\triangle C_d^{dyn}}$	0.9693	0.9329	0.9230
$\phi^{\triangle d_{dia}}$	0.9119	0.9943	0.9996
Generation number	50	39	34

in the fabric reinforcement was greatest for the reinforced 106–125 μm porogen graft, with a value of 8.85 %, while values of 8.13 % and 8.70 % were observed for the reinforced 90–106 and 125–150 μm porogen grafts, respectively. In contrast, the internal diameter at the systolic pressure was less for the 90–106 and 106–125 μm grafts than for the 125–150 μm porogen graft, implying that the adventitial reinforcing fabric plays a larger role in the weaker structures, or increased pore size. Table 4 displays the optimal fabric model solutions obtained from GA2 for each of the pore size grafts.

Figure 11 displays the dynamic circumferential, radial and axial stress through the wall thickness for the various pore size adventitial fabric reinforced grafts at mean pressure (100 mmHg). The high fabric stress values, indicated by the sharp change in stress profile in Fig. 11d, f, obtained for the 125–150 μm reinforced graft compared to the 106–125 and 90–106 μm structures, illustrated that the fabric reinforcing played a dominant role in the weaker 125–150 μm graft, while this role was reduced in the 106–125 and 90–106 μm structures. Comparing Fig. 10d–f and

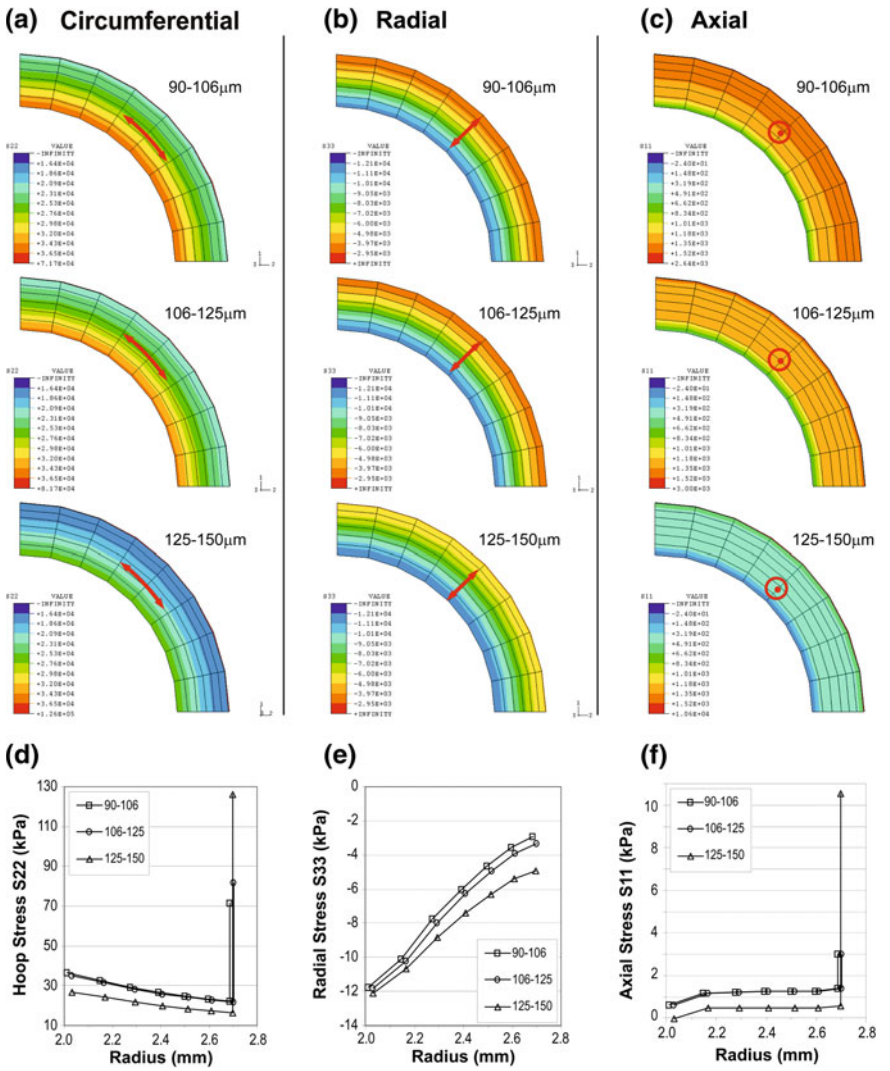

Fig. 11 Contour plots and graphs showing the stress variation through the wall thickness of 90–106, 106–125 and 125–150 μm porous grafts with adventitial fabric reinforcement at a luminal pressure of 100 mmHg: Circumferential stress (**a**, **d**), radial stress (**b**, **e**), axial stress (**c**, **f**)

Fig. 11d–f, the fabric reinforcing reduced and levelled out the circumferential stresses for all porogen sizes. The axial stress was similarly reduced for all porogen sizes whereas levelling out of axial stress was only observed in the 125–150 μm graft but not in the 106–125 and 90–106 μm structures. With the addition of the reinforcing, the compressive radial stress increased toward the outer (adventitial) surface, while relatively small changes were observed at the lumen for all graft types.

The three highest ranked fabric model solutions were implemented in the circumferential and longitudinal tensile numerical models to obtain the fabric requirements in terms of force per unit length vs. displacement for porous grafts of each porogen size group. These curves were used to develop physical fabrics.

In an iterative process, the comparison of the experimental data with the numerically predicted requirements was utilized to select the most promising prototype candidates and to guide the manufacturing of subsequent fabric generations. From an initial generation of 16 different fabric socks, six designs were identified as potential candidates to comply with the required specification with respect to force-displacement characteristics and promotion of tissue ingrowth. A refined evaluation resulted in exclusion of four of the six fabric sock designs from further review. The short-listed two designs underwent two iterations of design adjustment, manufacturing and experimental assessment. The final generation of the two prototype designs (prototypes I and II) featured knits of Dacron fibre threads (fibre diameter: 50 μm) with pore diameter of 0.35 mm and surface coverage of 70–75 %. To enable a feasible assembly procedure of the fabric sock and the porous graft structure (OD: 5.0 mm), it was found that an inner diameter of the fabric socks of 6.0 mm was preferential to the value of 5.0 mm predicted numerically. The difference in inner diameter of the sock and outer diameter of the graft was accommodated by longitudinally stretching the fabric sock by $59 \pm 1.9\,\%$ (prototype I) and $91 \pm 1.7\,\%$ (prototype II) during the assembly procedure. Figure 12a displays the circumferential force-displacement curves of the two prototype socks, without (i.e. as manufactured) and with longitudinal pre-strain, and the optimal fabric model solution for the graft of 90–106 μm porogen size. Figure 12b, c displays experimental data and optimised model solutions with pre-straining. The models represented the physical behaviour of the fabrics very well in circumferential direction (Fig. 12b). For longitudinal tension (Fig. 12c), the agreement between model and experiment was reasonable for longitudinal strains up to approximately 60 %.

Using these fabric model solutions, the FE model for fabric-reinforced grafts predicted compliance values that deviated from those obtained with the optimal fabric model solutions (see Table 4). Table 5 presents the static and dynamic compliance values numerically, predicted and experimentally measured, for non-reinforced grafts and grafts reinforced with prototype I fabric socks. For the compliance based on inner graft diameter, $C_{d,dyn}$(ID) and $C_{d,stat}$(ID), the numerical models markedly overestimated the compliance in all cases. The overestimation was more pronounced in the fabric-reinforced grafts compared to the non-reinforced grafts, except for the largest porogen size class 125–150 μm. The variation between numerical and experimental values increased with increasing porogen size for the non-reinforced grafts whereas the variation decreased with increasing porogen size for the fabric-reinforced grafts. A considerably better agreement between numerical and experimental results was obtained when the compliance, $C_{d,stat}$(OD), was calculated using the outer diameter of the graft. This was demonstrated for the static case. The improvement was more apparent for the non-reinforced grafts compared to the reinforced grafts.

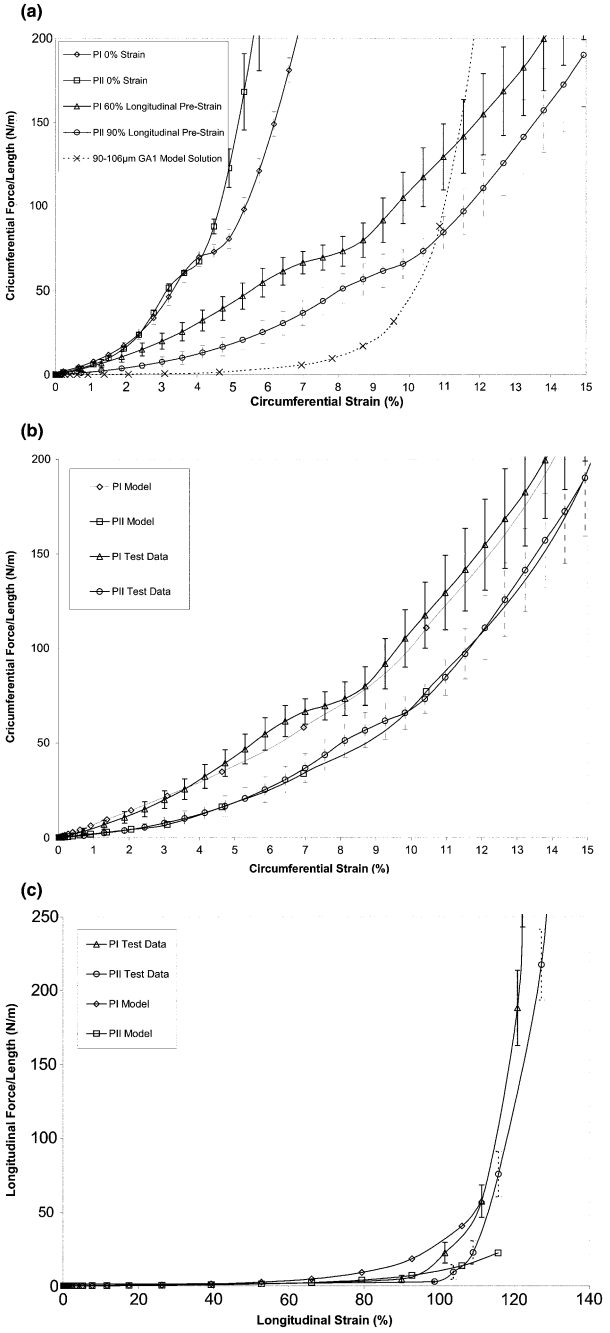

Fig. 12 Experimental and numerical data for the final fabric sock prototypes I (PI) and II (PII): **a** Force-displacement curves from circumferential tensile tests of the samples without and with longitudinal pre-strain and the optimal fabric model solution for 90–106 μm porogen size graft, **b** Fabric model solutions and experimental data for circumferential tensile tests of pre-strained fabric samples, **c** Fabric model solutions and experimental data for longitudinal tensile tests of pre-strained fabric samples

Table 5 Static ($C_{d,stat}$) and dynamic ($C_{d,dyn}$) compliance of non-reinforced and prototype I fabric-reinforced graft samples from in vitro compliance tests (Experiment) and numerical predictions (Model)

	Non-reinforced grafts			Fabric-reinforced grafts		
Porogen size (μm)	90–106	106–125	125–150	90–106	106–125	125–150
$C_{d,dyn}$ (ID)						
Experiment	13.3 ± 1.2	12.7 ± 2.9	15.5 ± 1.3	2.1 ± 0.8	3.0 ± 2.4	4.0 ± 0.7
Model	16.0	19.2	31.5	5.3	5.5	6.0
$C_{d,stat}$ (ID)						
Experiment	13.0 ± 2.4	12.9 ± 7.8	16.4 ± 4.6	1.3 ± 1.2	2.5 ± 3.3	4.1 ± 4.9
Model	16.9	20.3	33.9	5.5	5.8	6.2
$C_{d,stat}$ (OD)						
Experiment	10.1 ± 1.9	9.7 ± 5.9	12.2 ± 3.9	0.5 ± 0.7	1.7 ± 2.1	2.4 ± 4.5
Model	9.7	9.8	14.2	2.0	2.8	2.0

The compliance values were based on inner graft diameter (ID) for the dynamic case and both inner (ID) and outer (OD) graft diameter for the static case. All values given in %/100 mmHg

5 Discussion

The objective of this study was to find an optimal structural design of a tissue-regenerative vascular prosthesis exhibiting arterial-like mechanics. Adopting from native arteries a layered structure of intima/media and adventitia, the challenge was to identify the mechanical characteristics of an adventitial fabric layer that provide together with the given properties of a porous polymeric intima/media layer the desired biomechanical properties of the graft structure. It was shown that by combining finite element methods and genetic algorithms, complemented with experimental methods, the required mechanical characteristics of the adventitial fabric reinforcement can be specified. The finite element methods were used to study the structural mechanics of the two-layer graft system, whereas the genetic algorithms served to optimize the mechanical characteristics of the adventitial fabric. As part of this numerical framework, experimental methods were employed to determine constitutive material parameters. Beyond the demonstration of the feasibility of numerical method, it was shown that the graft system of adventitially reinforced polymer with well-defined interconnected porosity can be expected to facilitate the ingrowth and regeneration of tissue such as arterioles, endothelial cells and smooth muscle cells for all pore sizes studied.

With respect to vascular tissue engineering, wall compression at systolic pressure (during dynamic loading) was predicted to be 5.68, 6.51, and 8.77 % in non-reinforced porous grafts (Table 3) and 4.82, 5.31, and 6.20 % in the fabric reinforced grafts (Table 4) for the 90–106, 106–125, and 125–150 μm porogen size group. These values represented a reduction of wall compression in the reinforced grafts by 15.2, 18.4, and 29.3 % compared to the non-reinforced grafts of the three porogen size groups. Considering that the predicted dilation was larger in the non-reinforced grafts compared to the reinforced grafts, these findings indicated that

the wall compression was predominantly governed by the dilation of the graft inducing transverse wall contraction. The compression of the wall due to internal pressure load played a secondary role even in samples with fabric reinforcement. The reduced wall compression in reinforced samples also suggested that the fabric reinforcement contributed to maintaining the dimensions of the interconnected pores required for tissue ingrowth. The diameter of interconnecting pore windows was on average $0.52 \pm 0.04\,\%$ of the porogen diameter [1]. For the porous grafts of the 90–106, 106–125, and 125–150 μm porogen size, the minimum pore window diameter was approximately 47, 55, and 65 μm. With the predicted wall compression at systolic pressure, the minimum pore window sizes, available for cellular ingrowth, decreased to 44, 52, and 59 μm in the non-reinforced porous grafts feature (while the minimum window size was slightly larger in the reinforced porous structures due to the lower wall compression). The average diameter of a capillary is 8–10 μm, while the diameter of a functional arteriole, endothelium and a single layer of smooth muscles is in the order of 30 μm [7, 8]. Thus, all three pore size graft groups permit ingrowth of arterioles, endothelial cells and smooth muscle cells.

The comparison with experimental results indicated that the numerical solutions predicted higher values for the graft compliance for most of the cases studied. For the non-reinforced grafts it was observed that a considerably improved agreement between model and experiment was achieved when the outer graft diameter, instead of the inner diameter, was used for compliance calculations. The relative differences decreased from 64.7 ± 38.9 to $4.5 \pm 10.6\,\%$ (average for the three porogen size groups). For the fabric-reinforced grafts, the relative differences observed were larger and the change of diameter reference resulted in a less pronounced improvement from 168.8 ± 139.6 to $116.0 \pm 164.4\,\%$. The best agreement for reinforced grafts was however achieved for the dynamic compliance with $95.2 \pm 52.2\,\%$. In view of the markedly different compliance values for the non-reinforced and the fabric-reinforced grafts, the absolute differences between experiments and models were reviewed additionally. For the dynamic compliance based on inner diameter, the model predictions exceeded the experimental results on average by a mere $2.6 \pm 0.6\,\%/100$ mmHg for the grafts with fabric reinforcement and by $8.4 \pm 6.9\,\%/100$ mmHg for the non-reinforced grafts. These values indicated in fact an acceptable agreement, in particular for the fabric-reinforced grafts. For the static compliance associated with the change of inner diameter, the absolute difference decreased to similar values of $0.7 \pm 1.0\,\%/100$ mmHg and $0.6 \pm 1.3\,\%/100$ mmHg for the reinforced and the non-reinforced grafts, respectively. Despite the satisfactory agreements of the absolute differences, various factors were identified as potential contributors to the observed deviations. The fabric models did not optimally represent the physical behaviour of the fabric prototypes I and II in longitudinal tension for strains exceeding 60 %, see Fig. 12c. In addition, the fabric model solutions were not optimized for transverse strain due to lack of experimental data for the fabric samples. The mechanical characterization of the porous polymer was performed on samples prepared from cast rods as compared to the grafts which were cast as tubes. This

may have caused different material/structural properties due to potentially varying packing configurations of the porogen. The latex liners obtained and used for compliance testing of the graft samples displayed a variation in mechanical properties. Furthermore, applying longitudinal strain to the graft samples according to the protocols for compliance testing may have caused the luminal latex liners to collapse inside the graft sample affecting the graft's behaviour. An appreciable variation of the experimental results, indicated by the large standard deviations of the measured compliance values (Table 5), may also be attributed to the intensive manual processes during manufacturing of the graft samples.

While the presented problem focused on the optimization of a fabric-type layer, the numerical solutions may be applied to other materials and structures, functioning as an adventitial reinforcement. Furthermore, the numerical method offers potential for the application to optimization problems with different concepts of modular, or composite, vascular prostheses. This may, in particular with emphasis on tissue regeneration, include the consideration of the biodegradation of the prosthetic materials and the incorporation of tissue in the initial mechanical design of vascular prostheses.

Acknowledgments This work was mainly funded through a research collaboration grant by Medtronic Inc. (Minneapolis, MN, USA) to the University of Cape Town. The authors acknowledge the assistance of Richard Steventon with the GA coding.

References

1. Bezuidenhout, D.: Porous Polymeric Superstructures as In-Growth Scaffolds for Tissue-Engineered Vascular Prosthesis. Ph.D. Thesis, Stellenbosch University, 2001
2. Bezuidenhout, D., Davies, N., Zilla, P.: Effect of well defined dodecahedral porosity on inflammation and angiogenesis. ASAIO J. **48**, 465–471 (2002)
3. Burkel, W.E: The challenge of small diameter vascular grafts. Med. Prog. Technol. **14**, 165–175 (1988)
4. Chuong, C.J, Fung, Y.C: Three-dimensional stress distribution in arteries. J. Biomech. Eng. **105**, 268–274 (1983)
5. Davies, N., Dobner, S., Bezuidenhout, D., Schmidt, C., Beck, M., Zisch, A.H., Zilla, P.: The dosage dependence of VEGF stimulation on scaffold neovascularisation. Biomaterials **29**, 3531–3538 (2008)
6. Deutsch, M., Meinhart, J., Zilla, P., Howanietz, N., Gorlitzer, M., Froeschl, A., Stuempflen, A., Bezuidenhout, D., Grabenwoeger, M.: Long-term experience in autologous in vitro endothelialization of infrainguinal ePTFE grafts. J. Vasc. Surg. **49**, 352–362 (2009)
7. Fung, Y.C: Biomechanics: Mechanical Properties of Living Tissue, 2nd edn. Springer, New York (1984)
8. Gamble, J., Matthias, L., Meyer, G., Kaur, P., Russ, G., Faull, R., Berndt, M., Vadas, M.: Regulation of in vitro capillary tube formation by anti-integrin antibodies. J. Cell Biol. **121**, 931–943 (1993)
9. Hasson, J.E., Megerman, J., Abbott, W.A: Increased compliance near vascular anastomosis. J. Vasc. Surg. **2**, 419–423 (1985)
10. Hayashi, K.: Experimental approaches on measuring the mechanical properties and constitutive laws of arterial walls. J. Biomech. Eng. **115**, 481–487 (1993)

11. Hess, F., Jerusalem, C., Braun, B.: The endothelialisation of a fibrous polyurethane microvascular prosthesis after implantation in the abdominal aorta of the rat. J. Cardiovasc. Surg. **24**, 516–524 (1983)
12. How, T.V., Guidon, R., Young, S.K: Engineering design of vascular prosthesis. Proc. Inst. Mech. Eng. [H] **206**, 61–71 (1992)
13. Hsu, C.-C., Chao, C.-K., Wang, J.-L., Lin, J.: Multiobjective optimization of tibial locking screw design using a genetic algorithm: evaluation of mechanical performance. J. Orthop. Res. **24**, 908–916 (2006)
14. Khalil, A.S., Bouma, B.E., Kaazempur Mofrad, M.R: A combined FEM/genetic algorithm for vascular soft tissue elasticity estimation. Cardiovasc. Eng. **6**, 93–103 (2006)
15. Kim, J.H.: Fabric Mechanics Analysis Using Large Deformation Orthotropic Shell Theory. Ph.D. Thesis, North Carolina State University, 1991
16. NN: Cardiovascular Implants—Vascular Prosthesis. American National Standard Association for the Advancement of Medical Instrumentation, AAMI standard edition, 1994
17. NN: Cardiovascular Implants—Tubular Vascular Prosthesis. ISO International Standard 7198, 1998
18. Pandit, A., Lu, X., Wang, C., Kassab, G.S.: Biaxial elastic material properties of porcine coronary media and adventitia. Am. J. Physiol. Heart Circ. Physiol. **288**, H2581–H2587 (2005)
19. Seifert, K.B., Albo, D., Knowlton, H., Lyman, D.J: Effect of elasticity of prosthetic wall on patency of small-diameter arterial prosthesis. Surg. Forum **30**, 206–208 (1979)
20. Siauve, N., Nicolas, L., Vollaire, C., Marchal, C.: Optimization of the sources in local hyperthermia using a combined finite element-genetic algorithm method. Int. J. Hyper. **20**, 815–833 (2004)
21. Stewart, S.F.C, Lyman, D.J: Effects of vascular graft/natural artery compliance mismatch on pulsatile flow. J. Biomech. **25**, 297–310 (1992)
22. Storåkers, B.: On material representation and constitutive branching in finite compressible elasticity. J. Mech. Phys. Solids **34**, 125–145 (1986)
23. Tai, N.R., Salacinski, H.J., Edwards, A., Hamilton, G., Seifalian, A.M: Compliance properties of conduits used in vascular reconstruction. Br. J. Surg. **87**, 1516–1524 (2000)
24. Takahara, A., Coury, A.J., Hergenrother, R.W., Cooper, S.L: Effect of soft segment chemistry on the biostability of segmented polyurethanes. I. In vitro oxidation. J. Biomed. Mater. Res. **25**, 341–356 (1991)
25. Wang, C., Garcia, M., Lu, X., Lanir, Y., Kassab, G.S.: Three-dimensional mechanical properties of porcine coronary arteries: a validated two-layer model. Am. J. Physiol. Heart Circ. Physiol. **291**, H1200–H1209 (2006)
26. Weston, M.W., Rhee, K., Tarbell, J.M: Compliance and diameter mismatch affect the wall shear rate distribution near end-to-end anastomosis. J. Biomech. **29**, 187–198 (1996)
27. Yeoman, M.S., Reddy, B.D., Bowles, H.C., Bezuidenhout, D., Zilla, P., Franz, T.: A constitutive model for the warp-weft coupled non-linear behavior of knitted biomedical textiles. Biomaterials **31**(32), 8484–8493 (2010)
28. Yeoman, M.S., Reddy, B.D., Bowles, H.C., Zilla, P., Bezuidenhout, D., Franz, T.: The use of finite element methods and genetic algorithms in search of an optimal fabric reinforced porous graft system. Ann. Biomed. Eng. **37**, 2266–2287 (2009)
29. Yeoman, M.S.: The Design and Optimisation of Fabric Reinforced Porous Prosthetic Grafts Using Finite Element Methods and Genetic Algorithms. Ph.D. Thesis, University of Cape Town, June 2004
30. Zilla, P., Bezuidenhout, D., Human, P.: Prosthetic vascular grafts: Wrong models, wrong questions and no healing. Biomaterials **28**, 5009–5027 (2007)

Aortic Aneurysms: OSR, EVAR, Stent-Grafts, Migration and Endoleak—Current State of the Art and Analysis

Shahid Manzoor Toor, Igor Sazonov, Heyman Luckraz and Perumal Nithiarasu

Abstract In this work, a thorough clinical review of aortic aneurysms and repair procedures is provided. The article covers statistics associated with thoracic and abdominal aortic aneurysms, in addition to discussing in detail the pros and cons of Open Surgical Repair (OSR) and Endovascular Aortic Repair (EVAR) of aortic aneurysms. A detailed discussion and statistics on the use of grafts and stent grafts is provided to make an assessment on the current state of art of their design and effectiveness. In addition, suitability of different repair procedures, complications and mortality and morbidity statistics are also provided. Finally, a brief overview on the computational methods applied to patient-specific aorta geometries is presented.

1 Introduction to Aortic Aneurysms

Arterial aneurysm is defined as the portion of an artery where focal dilation involving all layers of the vessel and results in at least 50 % increase in normal diameter [1, 2]. Most widely reported blood vessel, inflicted with aneurysms is the

S. M. Toor · I. Sazonov · P. Nithiarasu (✉)
Swansea Biomedical Computing Lab, College of Engineering, Swansea University, Swansea SA2 8PP, UK
e-mail: P.Nithiarasu@swansea.ac.uk

S. M. Toor
e-mail: shahidtoorm@gmail.com

I. Sazonov
e-mail: I.Sazonov@swansea.ac.uk

H. Luckraz
Consultant Cardiothoracic Surgeon, Heart & Lung Centre, New Cross Hospital, Wolverhampton WV10 0QP, UK
e-mail: heyman.luckraz@nhs.net

Stud Mechanobiol Tissue Eng Biomater (2014) 15: 63–92
DOI: 10.1007/8415_2013_165

Published Online: 19 June 2013

aorta. Aorta is the largest artery, emerges from heart and runs through chest and abdomen. Aortic aneurysms have been found in both the chest and the abdomen areas of the aorta and may be classified (according to the Crawford classification in Types I to IV) into Thoracic Aortic Aneurysms (TAAs) and Abdominal Aortic Aneurysms (AAAs) respectively, as shown in Fig. 1a, b. Among the two types of aortic aneurysms, AAA is highly prevalent, supported by the fact that 80 % of all reported aortic aneurysm are those of AAAs [1]. Aneurysms can also be categorised into true and pseudo types. A true aneurysm is a result of pure arterial wall dilation (involving all the layers of the arterial wall—intima, media and adventitia) of a diseased section commonly has a fusiform morphology (see Fig. 1a, b), but can be of saccular in some cases (Fig. 1c). Whereas, pseudo aneurysms develop as a result of arterial tear or dissection of aorta [3] as shown in Fig. 1d. Arteriosclerosis and weakening of arteries, contributed by factors such as gender, age, smoking, family history (connective tissue disorders such as Marfan's Syndrome) and hypertension, are usually linked to an increased risk of arterial dilatation [2, 4].

Aortic aneurysm rupture is ranked as the *thirteenth* commonest cause of death in the western world. It has been documented that it leads to about 15,000 deaths each year in the US and about 8,000 deaths per year in England [5]. The incidence of abdominal aortic aneurysm is higher in the elderly men than in women and young people. A systematic review of a large number of studies has shown that prevalence of AAA disease is 60−90 % among the elderly male population [6–8]. Unfortunately, majority of the aneurysms grow asymptomatically, and are encountered incidentally during routine clinical test, such as ultrasound or X-ray performed to diagnose other diseases [9]. The chances of abdominal aortic aneurysm to be symptomatic are rare, i.e., 1 in 1250 patients can show symptoms such as back pain, sensation of pulsation, abdominal or chest pain and occasional sudden death [4, 10, 11]. Aneurysm being asymptomatic, tends to grow until rupture or dissection occurs at one or more sites, which is often catastrophic, and carries an overall mortality rate of as high as 90 %. However, for the patients who managed to reach hospital, lower mortality rates i.e. 40−50 % have been reported [11–13]. In contrast to the ruptured cases, for electively repaired aneurysms mortality rates documented are around 3−10 % [11]. One argument to minimise mortality related to rupture is to screen the elderly and at risk population and if an aneurysm is identified, it could be repaired electively. Screening studies carried out in the UK have suggested that prevalence of abdominal aneurysm varies between 1.3−12 %, depending on the age group and definition of aneurysm [4].

In the earlier studies, diameter has been regarded as a deterministic parameter of prime importance, which characterises the risk of aneurysm rupture [14, 15]. It has been postulated that the rate of aneurysm rupture is directly related to the aneurysm size [16]. The threshold size, if crossed, heightens the risk of preoperative rupture. In case of abdominal aneurysm, threshold diameter is 5.0−5.5 cm; whereas for thoracic aortic aneurysm it is 6.0 cm (ascending aorta with Marfan's syndrome 4.5 cm is usually the limit) [17, 18]. However, it has become a controversial issue, due to the fact that 10−20 % of aneurysm cases rupture even

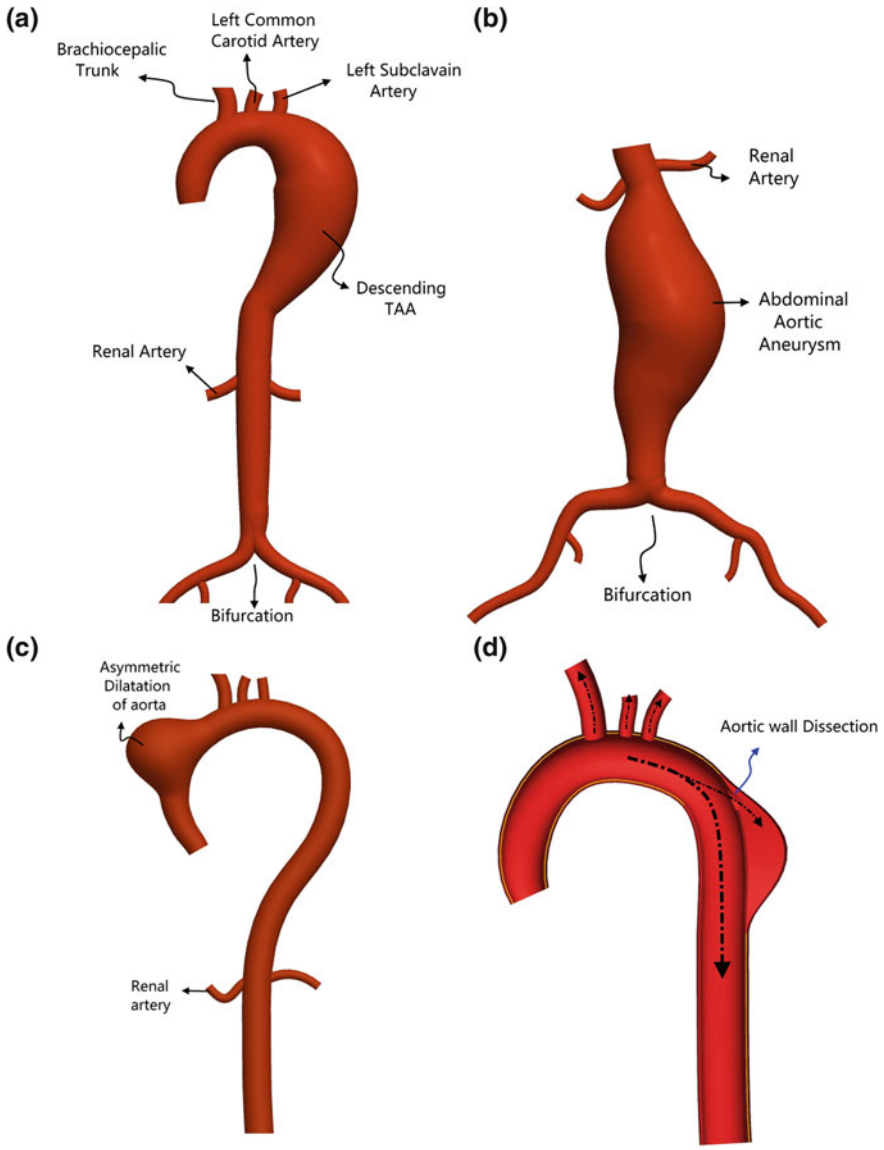

Fig. 1 Different type of aortic aneurysms. **a** TAA, **b** AAA, **c** saccular aneurysm, **d** pseudo aneurysm

before reaching to threshold limit [18]. Different studies have evolved to find a true parameter, which can predict the risk of aneurysm rupture. A finite element (FE) analysis of the wall has shown that the maximum wall stress is a far better indi-

cator, because it combines size of aneurysm with other parameters like blood pressure and geometry [19–21].

Numerous surveillance studies of aneurysm, have indicated that without treatment rupture is imminent [4, 22]. Five year reported survival rates of un-operated aneurysms, are between 20−50 %, depending on the presence and severity of atherosclerosis and other cardiovascular diseases [9, 23]. Zarins et al. [14] have documented that preoperative aneurysm size also controls long term results after treatment. Therefore, it is a common practice to treat an aneurysm once it meets the threshold criterion, since any delay in repairing causes it to enlarge in size, which leaves the patients at increased risk of unfavourable post-operative outcomes [24].

2 Treatment Techniques

The risk of aneurysm rupture can be prevented by repairing it with either open surgical repair (OSR) or endovascular aneurysm repair (EVAR) (see Fig. 2). The basic goal behind both of these techniques is to exclude the arterial portion afflicted with aneurysm from luminal pulsatile blood flow. This may be carried out by providing with an artificial blood flow passage via a synthetic conduit. Both of repairing procedures are described below.

2.1 Open Surgical Repair (OSR)

OSR is a traditional and standard treatment modality based on a well established procedure to repair aneurysms (depending on where the aneurysm is, the repair technique may vary). Its use dates back to early 1950s [16, 25]. OSR involves a large incision at the site of the aneurysm to have access to diseased section of the aorta, where to remove intraluminal thrombus and calcification first it is clamped. A synthetic graft is then sewn to the healthy aortic neck to exclude the aneurysm [26] as shown in Fig. 2a. Open repair is substantially invasive procedure, implicated with a large amount of blood and fluid transfusion, it also requires increased hospital stay and long recovery time. Overall, mortality rates for electively repaired aneurysms with OSR found in literature are 2−10 % [16, 27–29]. The good results obtained by elective-open-repair are in contrast to those of ruptured-aneurysm for which reported mortality rates are 28−60 % [30–35]. Despite of the fact that open repair is regarded as a good treatment option for young patients having long term life expectancy, for the patients with ruptured aneurysm, aortic dissection, severe co-morbidities and complications, it has limited use due to worse outcomes in terms of peri- and post-procedural mortalities and morbidities.

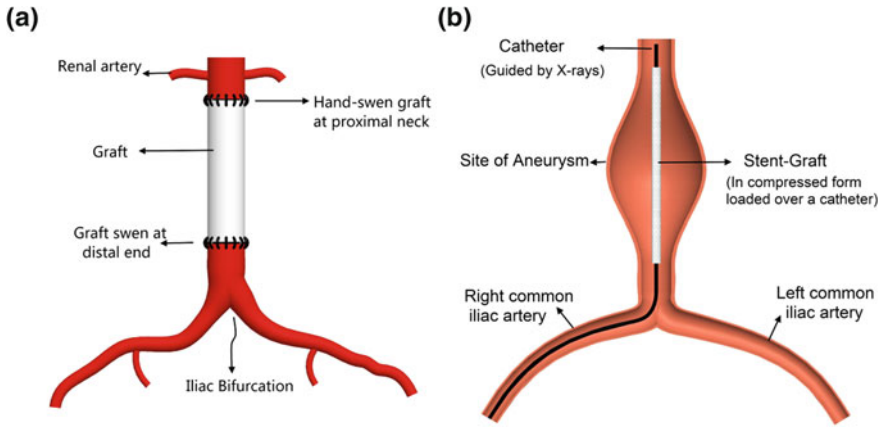

Fig. 2 Aneurysm repair procedures. Open surgical repair (OSR, **a**) and endovascular aneurysm repair (EVAR, **b**)

2.2 Endovascular Aneurysm Repair (EVAR)

Surgical repair for aged and co-morbid patients is not only difficult to tolerate but also carry high mortality rates. Endovascular aneurysm repair (*EVAR*) has emerged as an alternative treatment option which avoids major operation by deploying an endovascular graft through a remote site [36]. The presentation of this method is controversial; however, this idea has been debated since the late 1960s. It has been reported that it was Dotter [37, 38] who first used endoluminal repair in 1969 in an animal trial, whereas the idea of deploying prosthetic graft transfemorally was first presented in 1986 [39]. The first successful report of implanting stent graft endovascularly was credited to Parodi [40], who performed the first endoluminal treatment of an abdominal aortic aneurysm in 1991 with a custom made stent graft. For patients with ruptured aneurysm, EVAR was first used in 1994.

In the endovascular repair, prosthetic graft supported by a metallic wire-frame called stent, is implanted transfemorally to the diseased site with a catheter, guided by fluoroscopy and deployed by either balloon or self-expanding mechanism [37] (see Fig. 2b). *EVAR* treatment provides patient with a minimally invasive procedure, significantly reduced perioperative mortality, decreased hospital stay and prompt recovery. *EVAR* is a useful treatment option, offering good short term results and similar midterm outcomes as those of open repair. However, short term good results do not sustain for longer period of time [41].

2.3 EVAR: A Viable Treatment Option?

EVAR was first developed and used for the patients who were not candidates for *OSR*. Therefore, to make a comparison, special consideration should be given to their respective selection criteria. However, with continuous evolution to date it is the most commonly used technique to repair aortic aneurysm in the US. Currently, 40−60 % [42, 43] of the patients suffering from the AAAs are treated endovascularly. After 30 years from its innovation, EVAR has undergone several modifications and improvements in both technology and devices used. The evolution phase can be described through ongoing changes such as: uni-body to modular devices; tube graft to aorta-uni-iliac and to bifurcated devices; use of barbs and hooks for active fixation; introduction of fenestrated and branched graft, and suprarenal versus infrarenal fixation etc.

To evaluate post-procedural outcomes of EVAR, numerous studies have been carried out, and have shown satisfactorily good short and midterm results. Some of these studies are outlined in the Table 1. The early success of EVAR is measured in terms of peri-procedural survival rates, absence of technical failure and secondary clinical interventions, and most importantly freedom from rupture. According to the reported results, peri-operative and 30 days mortality noticed ranges between 1.0 and 2.3 %. From data listed in the table it is evident that, technical and clinical success along with freedom from aneurysms rupture is achieved in majority of cases.

The reported results by different investigators clearly indicate that EVAR is a feasible alternative treatment option for the patients with suitable anatomy. However, good results of EVAR do not sustain for the patients with unfavourable anatomical features and those already unfit for OSR. The outcomes of EVAR trial-2 [48] conducted in the United Kingdom on patients to whom OSR was not feasible shows a considerable peri and 30-days mortality rates.

2.4 Contraindications to the EVAR

The primary restrictions to the liberal use of EVAR are unfavourable anatomical and morphological characteristics, mainly include aneurysm size and anatomy of proximal aortic neck. In most of guidelines limiting value of aneurysm size considered is 5.5 cm. The proximal neck for AAAs is defined as part of healthy aorta between the most caudally located renal artery and beginning of the aneurysm. Hostile behaviour of aortic neck is defined by its size, length, pulsatility, and thrombus and calcification lining [49]. If special consideration is not paid in selecting suitable candidate for EVAR, then it complicates the EVAR procedure not only peri-operatively, but also post-operatively, with increased demand of secondary intervention, which in worst case can lead to conversion to open repair.

Most of the devices used in endoluminal treatment require healthy infrarenal aortic neck of at least 10−15 mm long [10, 50] in order to obtain a landing zone

Table 1 Short and midterm EVAR outcomes

Reference	Number of reported EVAR cases	Mean patient age (years)	Male patients (%)	Technical success (%)	Clinical success (years)	Freedom from rupture (years)	Perioperative and 30 days mortality (%)
Marin et al. [6]	817	74.30	83	93.8	65 ± 8 % (8)	98 ± 1 % (9)	2.3
Verhoeven et al. [44]	365	74.0	89	91.0	71 % (3.5)	92 % (7)	1.1
Wahlgren et al. [45]	1000	74.0 ± 7	86				1.8
EVAR trial-1 [8]	531	74.20	91	99.2			1.7
Wang et al. [46]	192	73.0	88	97.9	78(4)	100 (6)	1.0
De Bruin et al. [47]	170	70.7	93	98.2	69 (6)		1.8

and secure seal between the endovascular graft and aortic wall. In the early generations of prosthetic grafts, unfavourable aortic neck length has been found to contraindicate EVAR in 40–50 % of the diagnosed cases [51, 52]. However, with the ongoing improvement and advent of new branched, fenestrated and suprarenal fixation devices, now short aortic neck length is no more a predominant factor of contraindication [53]. The outcomes of several studies have shown that unfavourable neck anatomy is linked to the increased incidence of migration, endoleaks and proximal attachment failure [51, 54].

Patient considered as suitable candidate for EVAR, should have aortic neck diameter ≤ 32 mm, that is bounded by maximum size of available stent graft. While measuring the diameter of aortic neck the local variation in aorta size over a cardiac cycle should be accounted as well, usually ranges between 0.9 and 2.4 mm [55]. Arko et al. [54] have reported periodic variations in the aortic diameter of up to 11 % during a cardiac cycle. Moreover, changes in dimensions were observed both along the anterio-posterior (AP) and lateral directions. It is always ideal to use dynamic imaging tool to dimension aorta for sizing prosthetic graft. However, in case of static imaging stent-graft may need oversizing by an appropriate factor.

Post-procedural aortic neck dilatation (AND) is a continuous risk and significantly associated with pre-procedural aortic neck diameter. Cao et al. [56] have reported the outcomes of EVAR trial with 230 patients. They observed aortic neck dilatation in 28 % of the patients, where in 77 % cases dilation was 3−4 mm after median follow up of 2 years. The rate of intervention was higher in patients with AND. Litwinski et al. [57] have found a strong correlation between the aortic neck dilatation, and the migration of devices.

Several investigators have claimed that neck angulations is one of the prominent factors associated with severe post-EVAR complications. With the advent of new flexible devices, maximum treatable aortic neck angle is 60°. The risk of experiencing adverse event after EVAR is directly related to the degree of angulations [50, 58, 59]. However, recently Goncalves et al. [60] have carried out

a study with the endurant stent graft and obtained satisfactory post-procedure results for the patients with angulated aortic neck.

It was reported that aortic neck thrombus and calcification lining covering more than 50 % circumference contraindicate EVAR. Proximal endoleak and migration have been reported to occur after EVAR, as a result of inadequate seal due to the presence of plaque in the neck [50]. Moreover, some investigators are of the opinion that thrombus lining is also responsible for endotension, since it can cause pressure force to transfer from neck to the aneurysm sac [61]. In contrast, Sampaio et al. [62] have reported that presence of the thrombus in the aneurismal sac is advantageous because it can occlude the lumbar and mesenteric arteries thereby reducing type-II endoleak (see Fig. 3b). The presence of the branch vessels in the aneurysm sac have been found to be associated with increased risk of type-II endoleak and ischemia of healthy organs. The retrogradations of blood stream in the side branches, which is responsible for endoleak, is a severe complication, often demands reintervention.

Another problem associated with EVAR is deployment of the stent graft through small arteries and tortuous paths. Transfemoral implantation through tortuous, angulated, diseased and too small arteries, especially in women is often encountered. This may result in technical failure of EVAR. Different guidelines have reported that for deploying stent graft without causing any rupture, diameter of common femoral arteries should be at least 7 mm without being tortuous and atherosclerotic [10].

Limiting values of hostile aneurysm features are summarized in Table 2, and due to patient specificity it is hard to standardize the design of devices based on listed contraindications. However, for patients without such hostile features, good postoperative results are expected. Choke et al. [49] have reported that with the ongoing improvements and increased experience, more and more patients with hostile aortic neck are being offered with EVAR. Moreover, they studied a hostile group of patients treated endovascularly, and found that short term results are encouraging for EVAR.

3 Design and Development of Stent Grafts

A stent graft is an artificial flexible blood conduit, designed to act as a false lumen at the site of an aneurysm. It consists of a biocompatible graft, supported by the foldable metallic frame called stent. In the early generations of endovascular prosthetic graft, the use of stents was limited to proximal and distal parts of the graft only, as was the case in the Parodi's [63] implantation, where stents were used only proximally, to provide with an anchorage. However, soon after the early deployment, it was realized that in order to provide with columnar strength, avoid compression and kinking, stents should be provided along the entire length of the graft [64].

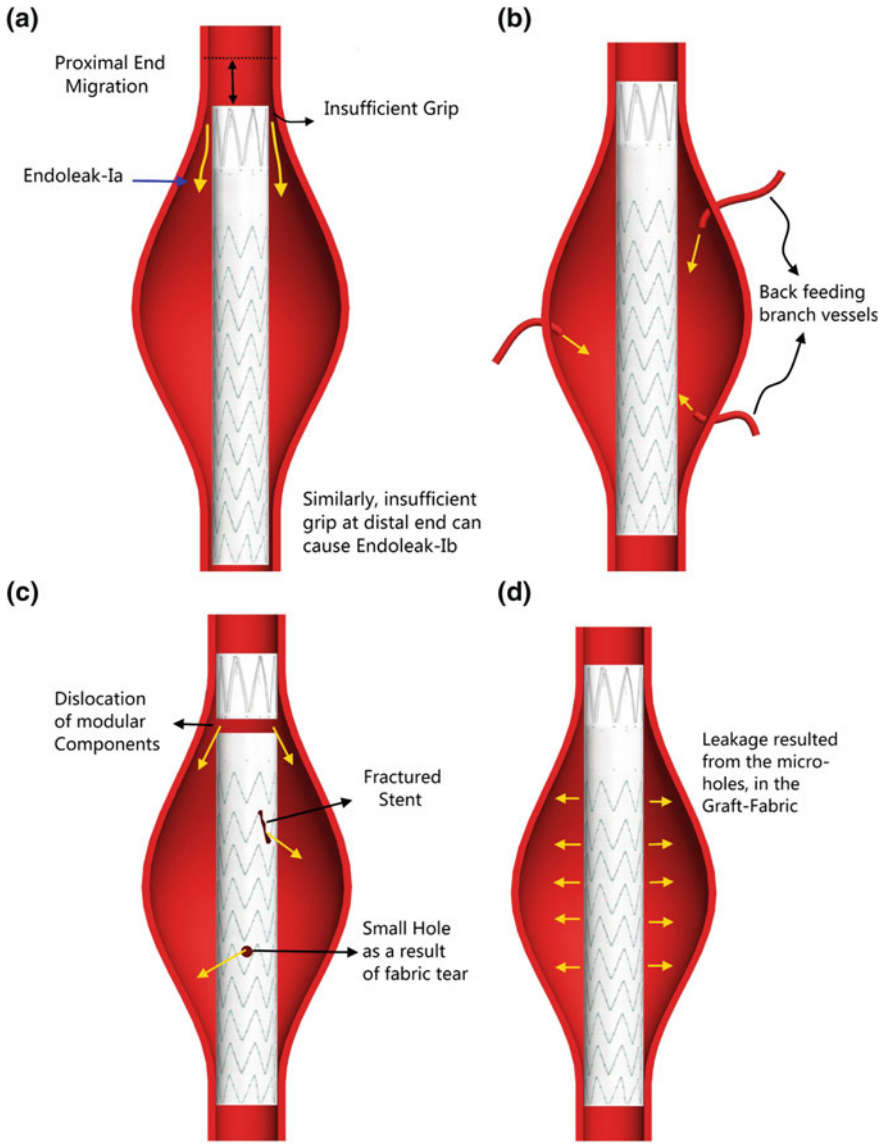

Fig. 3 Different types of endoleaks. **a** Type I—Proximal leak, **b** Type II—Leak through branch vessels, **c** Type III—Mechanical failure, **d** Type IV—Leakage due to graft porosity

In the commercially available endoluminal prostheses, both endoskeleton (inside) and exoskeleton(outside) stent patterns are used (see Fig. 4). For the patients with severe angulations, endoskeleton profile could lead to abrasion of fabric against the ends of the stents, thereby leading to perforation induced by graft porosity [65]. On the other hand, the liberal use of exoskeleton profile leaves the

Table 2 Contraindications to EVAR for AAAs

AAA anatomical parameter	Hostile features
Aneurysm diameter	≤55 mm
Aneurysm neck diameter	≤32 mm
Infra- renal aortic neck length	≤10 mm
Proximal neck angulation	≤60 °C
Circumferential thrombus lining	≤50 %
Calcification lining	≤50 %
Iliac fixation length	≤10 mm
Access vessel diameter	≤7 mm
Number of distal and branch vessels	Minimum

patients at continuously increased risk of vessel injury. This may result in thrombus and embolus formation. In an endoluminal prosthesis, stents are positioned at three different locations: regular stents placed in the middle portion of graft; oversized sealing stents used in the proximal and distal ends to provide with extra radial strength; and oversized bare metal stents used for proximal fixation [66].

Stent grafts used in aortic aneurysm repair vary in diameter (20−40 mm) and length (30−60 mm). They are compressed into a sheath of 18−24 Fr, so that they can be deployed through restricted dimensions of access arteries. Therefore, an ideal stent material should be strong, flexible and thin, so that it can be folded. The stent material should also be high in stiffness, since it has to withstand radial pressure of blood flow. Most commonly used materials for stents are Nitinol and stainless steel. Nitinol is a shape memory alloy consists of an equiatomic amount of Nickel and Titanium, and the shape memory effect of this material is triggered either thermally or mechanically. In most of endovascular prosthesis, supported by Nitinol, shape memory effect is achieved mechanically, i.e., by superelasticity or changing stress state [67]. In some designs, stents used are manufactured using stainless steel (316 L) as it is cheap, easy to fabricate into desired profiles, it has high tensile strength and resistant to corrosion. However, in contrast to stainless steel, Nitinol stents are the preferred choice due to their shape memory effect, good flexibility, and their ability to be positioned and tracked by magnetic resonance imaging (MRI) [68, 69].

On the basis of deployment procedure, the stents may be classified into two categories i.e. self expandable and balloon expandable. It is difficult to establish superiority of one over other. Nonetheless self expandable stents are easier to implant. The balloon expandable devices are the first commercially available designs, manufactured in the crimped state and expanded by inflating a balloon resulting in plastic deformation of stents. Whereas, self expandable stents are manufactured in a predefined vessel size and then compressed into a smaller size so that it can be delivered at the site by a minimally invasive procedure. Self expandable stents are normally made from shape memory alloys, and have super-elasticity properties. Therefore, they have no strength limitations. For an identical

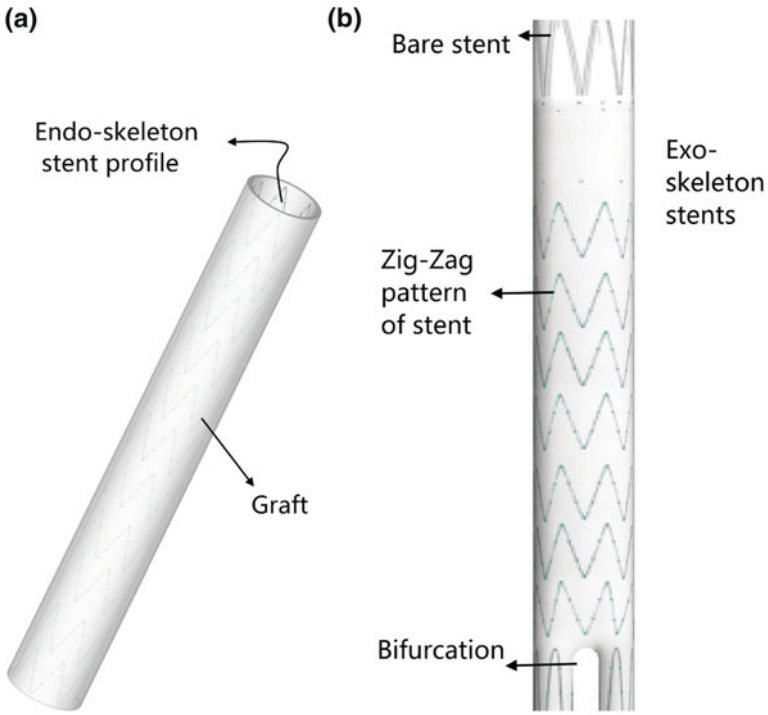

Fig. 4 Endoskeleton (**a**) and exoskeleton (**b**) zigzag stent patterns

design, balloon expandable stents are stiffer compared to self expandable stents as the material (stainless steel) used in the former has a higher modulus of elasticity. The balloon expandable stents also have better properties of apposition to the aortic neck, thereby limiting endoleak and migration [27]. Most commonly used stents in concert with vascular graft are self expandable. It has been reported that self expandable stents are more friendly to adapt the postoperative changes during remodelling of an excluded aneurysm. On going research proposes to combine the best features of both of these designs into one, i.e., to develop a balloon expandable, superelastic stent [70].

Stents used in endvascular graft are mainly the derivative of cardiovascular stents in shape and material. The design considerations for both cardiovascular and endovascular stents are similar, including radial strength, flexibility, and easy deployment. Stent design is believed to be the second strongest factor, contributing towards the postprocedural complications, after morphology of a vessel. Currently, there are numerous geometrical configurations under use. However, multicellular is the one which combines best possible features of both coil and tubular designs [65, 68, 71, 72]. A comparison of structural properties of different stent designs are outlined in Table 3.

Table 3 Comparison of structural properties of stents

Design	Flexibility characteristics	Stiffness	Radial strength
Mesh	Not good	High	Strong
Coil	Good	Low	Weak
Tubular	Not good	High	Strong
Multicellular	Good	High	Strong

Another important aspect of stent-graft design is the selection of suitable material for the graft. Since alongside stents, material of graft is believed to be equally responsible for postoperative outcomes of EVAR. The direct complication related to graft material is endoleak resulting from porosity and fatigue failure (Fig. 3c, d). The material used for manufacturing graft in both custom made and commercially available devices is either polyethylene terephthalate (PET or Dacron), or expanded Polytetrafluoroethylene (ePTFE), which are biocompatible and have long degradation life. The grafts are usually flexible and can be manufactured in any desired shape with a thickness of 0.1−0.3 mm [10, 64, 67]. Generally, stents are sewn to the graft by polypropylene suture, however in some new designs, chemical bondage has been used as well.

The stent grafts are available in both flexible and rigid designs. The rigid structure has columnar strength, e.g. Aneurx graft, whereas flexible design, e.g. Talent device, can adapt anatomical changes during remodelling. After the complete exclusion of aneurysm by EVAR, in the absence of any radial force of bloodstream during remodelling phase, diameter of aneurysm sac decreases. This results in geometrical changes in anatomy and morphology of the diseased area. The best design should adapt these geometrical changes without causing any dislocation between stent and graft, and their modular components. In a design, the selection of suitable strut diameter is a critical feature as it controls both the flexibility and stiffness. In most of the cases, diameter of struts for aortic stents is about 0.10 mm [64].

Stent grafts are available in both modular and unibody configurations. The unibody devices include straight tube and aortouniiliac graft. Often, due to the extension of abdominal aneurysm to the aortic bifurcation, less than 10 % of AAA patients are candidates for tube graft. Secondly, the use of straight tube is responsible for increased incidence of endoleaks. The most widely used stent grafts are bifurcated in modular form [73]; however, in case of uniiliac favourable anatomy, aortouniiliac devices followed by femoro-femoral bypass have proven to be useful [74]. Major advantage of modular devices are: their ability to offer easier deployment due to small sized individual components and to provide with the high degree of dimensional adaptability during the procedure [64]. Currently, there are a large number of devices commercially available, which are approved by American Food and Drug Administration (FDA). Desai et al. [10], Eliason et al. [1] and Kamineni et al. [16] have reported the characteristics of FDA approved devices as listed in Table 4. Moreover, they have found that all of the these

Table 4 Salient features of FDA approved stent grafts used in EVAR

Devices	Manufacturer	Configuration	Stent material	Graft material	Proximal fixation	Available size (AAA neck diameter) (mm)
Aneurx	Medtronic AVE, Santa Rosa, CA	Bifurcated	Nitinol	Woven polyester	Over-sizing	18–26
Talent	Medtronic AVE Sunrise, FL	Bifurcated	Nitinol	Polyester	Over-sizing	16–36
Excluder	WL Gore and Associates, Flagstaff AZ	Bifurcated	Nitinol	PTFE	*Anchors* ≈ 2 mm	19–26
Powerlink	Endologix, irvine, CA	Unibody	Co-Cr alloy	Woven polyester	Over-sizing	26
Zenith	Cook Inc., Bloomington, IN	Bifurcated	Stainless steel	Polyester	Suprarenal barbs	22–32
Endurant II	Medtronic	Bifurcated	Nitinol	Polyester	Suprarenal barbs	19–32

devices are self expandable and require aortic neck length of ≥ 15 mm, except Aneurx for which 10 mm neck length is sufficient for proximal fixation.

Although stent grafts have evolved through several changes and improvement in geometry and material, there is still no device categorized as optimum [69]. One of the problems, common to all devices, lies in their compactness which is restricted due to the presence of metallic stents.

4 Complications Associated with EVAR

The primary aim of endovascular treatment is the exclusion of aneurysm from systemic blood circulation, thereby preventing the risk of aneurysm rupture. Despite of several improvements, EVAR still demands continuous, lifelong surveillance due to associated post-procedural complications. The number of patients experiencing postoperative complications are higher among those undergo endoluminal repair, compared with those treated with open repair [8]. In the learning curve of endovascular repair, high mortality rates were observed due to its application to only high risk patients. However, to date, with its widespread applications and established procedure, initial mortality rate has dropped down to approximately 3 % [75]. Several other complications of minor importance related to endovascular repair of an aneurysm have been found and most often these can be resolved with satisfactory outcomes. Among different researchers [76–78], it is a well established fact that major complications dictating success of EVAR are those including endoleaks and migration. Since these problems have directly challenged the success of EVAR, they demand special considerations through secondary interventions, which otherwise could lead to the enlargement of an aneurysm and hence rupture. According to the outcomes of EVAR trial-1 [8], rate of intervention was 20 % among the patients treated endoluminally.

4.1 Endoleak

Endoleak is the most common complication associated with the endovascular repair, defined as persistent blood flow in the aneurysm sac, i.e. portion between the outside wall of the graft and the interior wall of aneurysm [76]. In some studies, endoleak has been reported as the principal cause of EVAR failure, since accumulation of blood in the sac causes an increase in endolumnial pressure and hence reinstate patient to the increased risk of aneurysm enlargement and rupture. However, this argument has been contradicted, since there had been cases of rupture with small sized aneurysm [79]. The overall incidence of endoleak has a wide range of between 10 and 50 %.

Endoleaks are classified into five different types on the basis of the source of the leakage and usually named numerically. First four types of endoleakage are extensively reported, so there exist a well defined description, as depicted in Fig. 3. Type-I originates from proximal and distal attachment sites; Type-II reported as a result of retrograde flow in the sac related branch vessels; Type-III caused by dislodging of modular component and structural failure, and Type-IV is related to graft porosity. The final category is marked as Type-V (Endotension) and is defined as pressurization of the aneurysm sac without any evident source of leakage [80]. Description of perigraft leakage along with possible causes, treatment options and incidence are listed in Table 5.

Endoleaks have seen to occur at various stages. However, they are more prevalent during the first 30 days after the endvascular procedure [80] and thus classified as the primary endoleaks. Endoleak seen in the early stages may vanish in a follow up due to thrombus formation and similarly, it can appear in the long run due to remodelling and device failure. In a clinical study, Clouse et al. [80] identified that large incidence of endoleak (52.3 %) noticed at the time of discharge, did not sustain in the long run, since it dropped down to 30.9 % after 1 year. However, thereafter in upcoming years, rate of occurrence was almost constant, i.e. by the end of fourth year it was 30.4 %.

4.1.1 Surveillance and Management of Endoleak

Three different imaging modalities, ultrasound (US) or sonography; computed tomography(CT); and magnetic resonance imaging (MRI), have been proposed in contrast enhanced mode for detection of endoleak. For early detection, CT scan is the best option. However, for surveillance, use of the contrast enhanced ultrasound is advantageous as it avoids radiation exposure and it is a fast, inexpensive, noninvasive and high temporal resolution method [76, 80].

Surveillance of endoleak involves measuring pressure in the aneurysm sac as it is directly associated with the risk of endoleakage and hence the rupture. Thrombus formation after EVAR is considered responsible for transmission of intra-aneurysm sac pressure. In an experimental study, Chaudhuri et al. [83] have

Table 5 Types of Endoleaks, their description, possible causes, treatment options and overall incidence

Endoleak	Definition	Causes	Treatment options	Average Incidence
Type-I	It includes blood leakage from either proximal (Ia) or distal (Ib) attachment sites of stent graft	It is usually result of inappropriate case selection i.e. patient with hostile neck or incorrect deployment [59, 79]	Treatment is mandatory usually repaired by intervening with cuffs and extenders [27], and oversizing by 20 % could minimize risk of late endoleak	For AAA $\leq 6.5\,\%$ [59] and for TAA $\leq 20\,\%$ [82]
Type-II	It is defined as retrograde or back bleeding of blood through the branch vessel into aneurismal sac	It is not a graft related complication, rather it is from patent vessels including lumbar and mesenteric arteries in the sac	It is usually treated by Embolization. However process of thrombus formation can minimize it [62]	8.0–45 % [74]
Type-III	This perigraft leakage resulted from the dislocation of modular components and mechanical failure of stent graft material	Because of insufficient frictional grip between modular components of stent-graft, and hostile anatomy	This demands emergency treatment, usually treated by using additional limbs, redo EVAR procedure, and conversion to open repair as a last resort	0.7–3.8 % [74]
Type-IV	This endoleak commonly seen at the initial stages of procedure, as a result of permeation through the graft material	The reason is porosity of thin walled fabric graft	Usually, requires no treatment, seal off itself within first 30 days of EVAR procedure	Initial high incidence
Type-V or Endotension	Endotension is pressurization of aneurysm without any evident sign of leakage	No well defined reason, however researchers believe that thrombus lining and attachment of graft to aortic wall might be responsible for transferring pressure wave to the sac [27, 61]	This demands watchful surveillance, could be treated by redo or open conversion	2–5 % [79]

reported, that intrasac pressure waveforms measured post-operatively are reliable indicators of the Type-I endoleaks, but not of Type-II or combined types. The standard and most reliable method to measure intraluminal pressure is by placing a catheter percutaneously through common femoral or iliac artery on the side of contralateral limb. In the absence of endoleak, intraluminal pressure will significantly be lower than the systemic pressure, whereas it would be of the same order in the presence of endoleak [76]. In a clinical study carried out by Dias et al. [10], have revealed that high sac pressure is related with AAA expansion and low pressure with shrinkage of aneurysm. In contrast to results presented in [83], Dias et al. [10] found that since embolization appears to result in pressure reduction, Type-II endoleak may be responsible for AAA pressurization after EVAR.

Management of endoleak includes balloon dilation of unexpandable stent graft, additional endvascular procedure with extenders and cuffs, embolization, or conversion to open repair. In general, Type-I endoleaks are addressed by additional cuff placement and balloon angioplasty, whereas Type-II endoleaks are treated by embolization [46]. In any case, conversion to open repair is always considered as a last resort. In many cases, intervention results in successful exclusion of aneurysm from perigraft leakage. However, until some results are available, it is difficult to say that outcomes of repaired endoleak are successful [76].

4.2 Migration

Stent-graft migration is defined as the longitudinal displacement of an AAA stent graft by a distance greater than a predefined *threshold* value in the downstream direction with reference to the most caudally located renal artery (in some studies reference point is superior mesenteric artery) [57, 84]. The *threshold* value for defining migration is often taken as 10 mm; however, stringent 5 mm criterion is also used. Migration usually is a result of inadequate proximal fixation, short aortic neck, aneurysm neck dilatation and remodelling of aneurysm sac [11]. Stent graft migration is a problem unique to endoluminal repair. This is due to the fact that in contrast to the open repair, stent grafts are not sewn to the aortic neck in EVAR. Resch et al. [85] have carried out an experimental study, and showed that median force required to dislodge a hand sewn graft is 150 N, whereas it is only 5−25 N for stent graft deployed in EVAR, depending upon the device being used.

Stent grafts are implanted and provided with apposition to the aortic wall by either passive or active fixation. Passive fixation is the most common fixating mechanism among commercially available designs. In this mechanism, the device is usually oversized by 10−20 % in diameter to provide with a frictional grip [10]. On the other hand, active fixation involves the use of suprarenal bare metal stents attached with barbs and hooks. This provides with a seal without penetrating into full length of the aorta. It has been observed that first generation of stent grafts with passive fixation suffered from increased risk of positional stability compared to the present design. Tonnessen et al. [86] have compared 5 mm migration

freedom among the patients treated with AneuRx (passive fixation) and Zenith (active fixation) and found that overall rate of migration occurrence was 67.4 % versus 90.1 % respectively at 4 years of follow up. The prevalence of losing positional stability in devices with passive fixation of up to 15.9 % (stringent criterion) has been documented in [57]. Similarly, Heikkinen et al. [87] have observed 10 % incidence of post-implantation movement of ≥ 10 mm with respect to superior mesenteric artery with a mean follow up of 2 years. Zarins et al. carried out a review of multicentre trial and identified that overall percentage of migration was 19.8 %, after 3 years of surveillance [88].

However, in current designs with a number of novel methods devised to engage proximal and distal aortic neck, high rate of migration is now contained. These novel method include use of barbs and hooks, fenestrated and branched limbs, extended bare metal stents, high columnar strength, bifurcated device, and iliac fixation. As documented by Thompson [11] and Won et al. [82] that migration may occur in up to 3 % of the patients with a follow-up at 18–24 months. Migration is a highly time dependent phenomenon. In a comparative study, it has been reported that at a 1 year follow up of patients who received Zenith device, there was no migration, whereas, by the end of 4 years 2.4 % of the patients have shown migration of at least 10 mm [86].

Migration is also correlated with type-I endoleak, which is a primary cause of device failure and rupture [10]. Proximal stent graft failure should not be judged on the basis of caudal movement of device as it has been observed that pure migration is less likely to occur. It is rather always accompanied by aortic neck dilatation, shortening and elongation. Lintwinski et al. have reported outcomes of a study, where migration occurred, without causing patients to lose proximal fixating zone and hence no EVAR failure was observed [57].

The importance of iliac fixation has not been considered in detail as a contributing factor in developing late migration. Nonetheless, currently, a number studies exist, showing that it is also equally important in inhibiting migration. Heikkinen et al. [57] have noticed that short proximal aortic neck length can be compensated by deploying devices having more columnar support (AneuRx) and by achieving proximity to iliac bifurcation at the distal site. Benharash et al. [89] reported that in patients with good iliac fixation, in addition to suprarenal and infrarenal fixation, no migration was observed. Waasdrop et al. [84] have carried out a study with the Zeinth device to establish a relationship between fixating length and migration, and found that vast majority of migrations were observed in the group having short distal and proximal fixation zones.

4.2.1 Management of Migration

Management of migration involves following considerations.

- Oversizing of stent grafts by 10−20 % to counteract aortic neck dilatation in the follow up [10].

- Use of barbs and hooks with bare metal stent ring at the proximal site of aneurysm, can provide with active fixation.
- With the use of branched and fenestrated graft, the length of proximal fixation zone can be increased by including suprarenal and hostile neck.
- In addition to proximal fixation, device should be fixed at the distal attachment site as well, extending bilaterally, till hypogastric arteries [87, 89].
- A new approach, involving endostapling and laparoscopy may be used to prevent endoleak-1 and hence migration [90].

5 Special Topics

In this section, some of the special topics related to the aortic aneurysms are presented. The topics discussed include ruptured aneurysm repair, conversion to open repair, fenestrated and branched grafts, suprarenal and infrarenal devices, and cost effectiveness of EVAR versus OSR.

5.1 Ruptured Endovascular Aneurysm Repair (REVAR)

Motivated from the consistent use of EVAR in elective treatment of aortic aneurysms, which has proven to be a feasible alternative with satisfactory short and midterm results, has led experienced units to offer endoluminal repairing to the patients with ruptured aneurysms, subjected to suitable anatomy. The first such case was performed in Nottingham in 1994 by deploying a aortouniiliac graft, followed by femorofemoral bypass [91]. This case showed the feasibility of EVAR for ruptured aneurysms. Since then several endoluminal procedures have been performed on patients with ruptured aneurysms. Reported outcomes indicate that short term mortality rate are promising among patients treated by REVAR [92]. Verhoeven et al. [30] have compared mortality rate of REVAR with open repair for ruptured abdominal aortic aneurysm, and reported 13.9 % versus 28.1 % respectively. Harkin et al. [28] have reported that half of the patients suffered from ruptured abdominal aortic aneurysm are offered REVAR, with mortality rates of 18 % compared with 34 % in open repair.

5.2 Conversion to Open Repair

Once treated with EVAR conversion to open repair is always considered as a last option. The only candidates for conversion are those patients to whom endvascular interventions could not resolve failure led by: peri-operative rupture, migration or structural failure of device, endotension, or post-operative rupture. The open conversions are rare and seen both at the early stages and in the long run after an

endovascular repair. Primary conversion (PC) involves conversion within the first 30 days after the EVAR procedure, generally carried out in case of technical or clinical failure, or if ischemia of basic organs happens. Whereas secondary conversion (SC) is the one performed in long run, usually as a result of rupture or mechanical failure of an endograft [93]. In a French multicentre trail with 1588 cases, registered across 8 different centres, it has been documented that conversion was performed in only 34 patients, i.e., 2.1 % of patients, including 14 primary, and 20 secondary conversions [93]. Similarly, Prinssen et al. have reported a rate of conversion of up to 2.5 % [94]. Moulakakis et al. have reviewed literature from 2002−2009 and noticed that there is up to 1.5 % incidence of primary conversions and up to 1.9 % of late conversions [95]. Both primary and secondary conversions have been found to be associated with significant risk of mortality. Reported results of mortality stand at as high as 28.5 % for PC and 0.4−25 % for SC [93, 95].

5.3 Fenestrated and Branched Stent Graft

Majority of aneurysms do not involve critical branch vessels in their development and therefore can be repaired with satisfactory post procedural outcomes. However, in cases critical branch vessels are encountered, they undermines the repair with EVAR. Since repair with EVAR could leads to ischemic complications, which have no solution, other than open conversion [93, 96]. The basic criterion for successful endovascular implantation of stent graft include hemostatic seal along with secure and stable attachment site to check migration and endoleak [96]. In 44.0–49.5 % of the AAA patients, aortic neck length has a dimension less than 15 mm and considered ineligible for EVAR [52, 97]. However, to address these restrictions, new devices with fenestrated and branched stents have been proposed and successfully used, which can keep critical vessel patency and also capable of providing with an option to extend proximal fixation zone to the non-dilated aorta [74]. Fenestrated grafts are now commercially available in Europe and have been approved for CE mark, however they are still undergoing clinical trials in the United states for FDA approval [53].

Fenestrated stent grafts have small holes along their body, and scallops at the edges in order to accommodate positioning of branch vessels. Fenestrated stent grafts were the first devices developed to deal with hostile neck and patency of branch vessels. Fenestrated devices were used to repair both abdominal and thoracic aneurysms; however, due to its inadequacy to obtain a durable seal, branched stent grafts have been proposed as an alternative for suprarenal and thoracoabdominal aortic aneurysms. Branched stent graft can be manufactured in both modular and unibody configurations, however modular is more flexible in dimensional adaptability and easy to deploy [96, 98]. The short and mid term outcomes have been analysed by different researchers. Muhs et al. [53] have reported their experience of treating patients with fenestrated and branched endografts and they found that 30-day mortality rate was 2.4 % and all cause

mortality of up to 13 %, after a median follow-up of about 2 years. They also identified that successful hemostat sealing was achieved in 97.40 % of cases and cumulative vessel patency after about 4 years was 92 %. For finding outcomes of implanting fenestrated and branched endografts, for the patients suffered from thoraco-abdominal aortic aneurysm (TAAA), Bakoyiannis et al. [99] reviewed the English literature available between 2000 and 2009. By statistical analysis of the data, they found that overall mortality was 16.1 % with mean follow up of 11.8 months, and identified that technical success was achieved in 94.2 % of the cases; among other complications the incidence of renal failure was 5.8 %. Their results are encouraging in the use of EVAR with fenestrated and branched stent grafts as an alternative therapeutic treatment option. Greenberg [100] has reported in a clinical case study that introduction of fenestrated and branched stent graft has led one to believe that almost all patients can now be treated by EVAR, regardless of anatomical restrictions.

5.4 Suprarenal and Infrarenal Fixation

Excluding the cases repaired with fenestrated and branched stent grafts, about 55−61 % of the patients suffering from AAAs are currently treated endoluminally with bifurcated and aortouniiliac endografts [52, 101]. Among postprocedural complications, migration and type-I endoleak are largely associated with short proximal aortic neck deployment and aortic neck dilation [57, 88]. It has been reported that suprarenal aortic neck is more stable to postoperative dilatation and resistant to atherosclerosis formation, thus is an ideal site for fixation [102]. Suprarenal fixation can provide patients with an alternative landing zone for anchoring and secure attachment, especially to those having adverse anatomical restrictions in terms of short and angulated neck with severe calcification and thrombus lining [52]. Suprarenal fixation has widened the spectrum of EVAR applications by offering it now to 70 % of patients suffering from AAA [75, 103]. However, implantation of suprarenal stents may result in partial occlusion of renal arteries by stent struts, thereby raising concerns of renal dysfunction. Numerous investigators have carried out comparative studies of EVAR with suprarenal versus infrarenal fixations, and identified that different patients have faced post-procedural renal dysfunction irrespective of the landing zone. However, it is documented that suprarenal fixation does not play any role in the progression of renal artery stenosis and acute renal events [103–107]. Malina et al. [108] have carried out a short term trial with a mean follow up of 6 months, after deploying Gianturco Z-stent across renal arteries. They reported that suprarenal fixation does not lead to any renal complication. It has been observed that suprarenal and infrarenal fixations are not even associated with proximal neck dilatation after EVAR, instead it is governed by morphology and remodelling of the aneurysm [109]. However, larger studies with longer postprocedural outcomes are required to correlate suprarenal fixation with incidence of renal complication if there is any.

5.5 Cost Effectiveness of EVAR Versus Open Repair

The cost of EVAR is defined as cumulative sum of cost associated with first procedure, CT scan surveillance, interventions during follow up and conversion if any. For patients with favourable anatomical and morphological features, EVAR seems to be more cost effective as it offers short term hospital stay, and is associated with less mortality and morbidity rates. However, short term cost benefits do not sustain during the follow up. Prinssen et al. [94] have reported an estimated EVAR cost of $3631 at the time of implantation, which increased to $9729 after the follow up of 5 years, i.e., increase of up to 268 %, indicating that cost is a strong function of time. They have also identified that CT scan surveillance contributed up to 65 % towards the total cost. Similarly, Patel et al. have reported that for about 8 years of quality-adjusted life there was 49.6 % additional cost associated with EVAR compared to open repair [110]. Due to the sophisticated manufacturing facilities and modular component production in small lots also led EVAR to be an expensive procedure. Fotis et al. [111] have compared short term cost effectiveness of EVAR versus OSR and reported that a major contribution towards the overall cost of EVAR is associated with the expensive endograft (median cost $24836.50), which according to their results 11.2 time more expensive than its counter part graft used in open repair. However a large number of investigators are of the opinion that if late complications do not occur then EVAR is cost effective [94, 110]. A true assessment is difficult until long term results are analysed, since cost of EVAR is time dependent.

6 Computational Modelling of Aortic Aneurysm

For investigating aneurysm biomechanics, numerical modelling is regraded as a useful tool. It provides with methods that have been employed in determining flow pattern, drag forces, and wall stresses, both pre and post-operatively. Computational fluid dynamics (CFD) and Finite element analysis (FEA), have been extensively used to simulate blood flow in the aortic aneurysm [112–117]. Using fluid structure interaction (FSI) to understand the interplay between the flow and wall (or stent graft) is one of the hot areas of current research.

6.1 Computational Techniques as Diagnostic Tool

Patient-specific computational fluid dynamic simulation may be regraded as a useful tool in evaluating the risk of rupture and success of EVAR. Following paragraphs provide a brief overview on the modelling research in these areas.

Progression and enlargement of aneurysm: Formation of aneurysms is understood to be a result of degradation of elastin and smooth muscle cells together with stress-mediated collagen turnover [118] within the walls. A computational model of aneurysm progression can be developed and analysed to study the history of development and associated rupture risk. To this end, new computational frame work have been proposed where vascular growth and remodelling (G&R) is coupled with short term hemodynamic simulation over a cardiac cycle [119]. Sheidaei et al. [118], have studied the evolution and growth of AAAs by coupling (G&R), with hemodynamic simulation. They found that there is a direct correlation between regions of low WSS and those of higher expansion. Thus it strengthens the argument that aneurysm growth commonly occurs in the regions, associated with abnormal variation of hemodynamic parameters i.e., wall sheer stress and pressure.

Risk of aneurysm rupture: Vorp and co-authors [120, 121], have advocated that the use of patient specific approach to predict the risk of aneurysm rupture is superior to the widely accepted maximum diameter criterion. They carried out patient specific simulations, where a non-linear constitutive model is used to characterise mechanical properties, and FEM is employed for the solution of the system. They have reported that growth of aortic aneurysm is accompanied by an increase in wall stress, as well as corresponding decrease in wall strength. A non-dimensional parameter called rupture potential index (RPI), defined as ratio of locally acting wall stress to local wall strength, can be used to quantify risk of aneurysm rupture [121]. The RPI varies from 0 to 1 with values close to unity indicate higher rupture risk.

Positional stability: Variety of fixation mechanism are used during implantation of EVAR devices to overcome the post-operative downward movement. Large displacement forces (DF) are believed to be responsible for axial displacement, thereby leading to migration, a primary cause of EVAR failure. Zarins and coauthors [122–124] have studied positional stability to correlate displacement forces with movement of devices by carrying out patient specific CFD. In [122] five patient specific CFD simulations of AAAs were considered, including cases were those of with and without clinical migration. They have reported that endograft movement appears to be related to the magnitude and direction of the DF. In general the orientation of DF was found to be perpendicular to largest curvature than along longitudinal medial axis of aorta.

In [123] results of CFD simulation of two different patient-specific thoracic aortic aneurysm cases, treated endovascularly, are reported. The results presented, contradict the intuitive notion that migration is caused by displacement forces. They found that direction and location of displacement forces is cranial rather than caudal on axial images. Therefore, migration of stent graft in thoracic aorta, is different from that of abdominal aortic aneurysm. In [124], type-III endoleak caused by, disconnection of modular components of stent graft has been modelled by CFD tool, where first displacement forces are computed, followed by contact stress evaluation between modular components. Thus CFD based simulations may be useful in evaluating placement strategies and stent graft design.

7 Chapter Summary

It appears that the Endovascular aneurysm repair (EVAR) has emerged as an alternative viable option over open surgery (OS), which offers good short term results. However, in long run EVAR has seen increased secondary interventions. Since its innovation, EVAR has undergone several modifications and improvements in both technology and devices being used. In the early generations of prosthetic grafts, unfavourable anatomical features have been found to contraindicate EVAR in as high as 50 % of the diagnosed cases. However, with the ongoing improvements and increased experience, more and more patients with hostile aortic neck are now being offered EVAR.

The evidence shows that ideal materials for stent are Nitinol and stainless steel. Polyethylene terephthalate (PET or Dacron), or expanded Polytetrafluoroethylene (ePTFE), are commonly employed as graft material, since they are biocompatible and have long degradation life. The most commonly employed stent grafts are those available in bifurcated configuration, with modular extension. Although stent grafts have evolved through several changes and improvements in geometry and design, yet there is no device categorized as optimum.

The major complications dictating failure of EVAR are those of endoleaks and migration. Endoleak may be repaired with balloon dilation of unexpandable stent graft, additional endvascular procedure with extenders, cuffs, embolization, or conversion to open repair. Management of migration involves the use of barbs and hooks with bare metal stent at proximal site, and over-sizing of stent graft.

EVAR may also be offered to patients with ruptured aneurysm. Suprarenal and infrarenal fixation has widen the spectrum of EVAR by making it possible to offer EVAR to the patients with smaller aortic neck length. Furthermore, with the advent of fenestrated and branched stent grafts, now almost all patients can be treated by EVAR, regardless of anatomical restrictions. Compared with OSR, EVAR is a cost effective procedure if late complications do not occur.

The emerging areas of using computational techniques as diagnostic tool to quantify positional stability, progression of aneurysm, and risk of rupture associated with an aneurysm etc. are encouraging.

References

1. Eliason, J., Upchurch, G.: Endovascular treatment of aortic aneurysms: state of the art. Curr. Treat. Options Cardiovasc. Med. **11**, 136–145 (2009). doi:10.1007/s11936-009-0014-8
2. Crawford, C.M., Hurtgen-Grace, K., Talarico, E., Marley, J.: Abdominal aortic aneurysm: an illustrated narrative review. J. Manip. Physiol. Ther. **26**(3), 184–195 (2003)
3. Coselli, J.S., Bket, S., Djukanovic, B.: Aortic arch operation: current treatment and results. Ann. Thorac. Surg. **59**(1), 19–27 (1995)
4. National Institute for Health and Clinical Excellence. Endovascular stent-grafts for the treatment of abdominal aortic aneurysm. NICE technology appraisal guidance 167, Feb. 2009 (reviewed Jan. 2012)

5. Choke, E., Cockerill, G., Wilson, W.R.W., Sayed, S., Dawson, J., Loftus, I., Thompson, M.M: A review of biological factors implicated in abdominal aortic aneurysm rupture. Eur. J. Vasc. Endovasc. Surg. **30**(3), 227–244 (2005)
6. Marin, M.L., Hollier, L.H., Ellozy, S.H., Spielvogel, D., Mitty, H., Griepp, R., Lookstein, R.A., Carroccio, A., Morrissey, N.J., Teodorescu, V.J., Jacobs, T.S., Minor, M.E., Sheahan, C.M., Chae, K., Oak, J., Cha, A.: Endovascular stent graft repair of abdominal and thoracic aortic aneurysms: a ten-year experience with 817 patients. Ann. Surg. **238**(4), 586–595 (2003)
7. Lederle, F.A, Johnson, G.R, Wilson, S.E: Abdominal aortic aneurysm in women. J. Vasc. Surg. **34**(1), 122–126 (2001)
8. Greenhalgh, R.M.: Comparison of endovascular aneurysm repair with open repair in patients with abdominal aortic aneurysm (evar trial 1), 30-day operative mortality results: randomised controlled trial, Sept. 2004
9. Thompson, B.W., Meek, G., Hara, M.: Resection of abdominal aortic aneurysms. Am. J. Surg. **116**(5), 682–685 (1968) (Papers of the Southwestern Surgical Congress)
10. Desai, M., Eaton-Evans, J., Hillery, C., Bakhshi, R, You, Z., Lu, J., Hamilton, G., Seifalian, A.: Aaa stent grafts: Past problems and future prospects. Ann. Biomed. Eng. **38**, 1259–1275 (2010). doi:10.1007/s10439-010-9953-1
11. Thompson, M.: Infrarenal abdominal aortic aneurysms. Curr. Treat. Options Cardiovasc. Med. **5**, 137–146 (2003). doi: 10.1007/s11936-003-0022-z
12. Laganá, D., Carrafiello, G., Mangini, M., Giorgianni, A., Caronno, R., Castelli, P., Dionigi, G., Cuffari, S., Fugazzola, C.: Management and endovascular treatment of symptomatic abdominal aortic aneurysms. La Radiologia Medica **111**, 959–970 (2006). doi:10.1007/s11547-006-0094-4
13. Sadat, U., Boyle, J.R., Walsh, S.R., Tang, T., Varty, K., Hayes, P.D.: Endovascular vs open repair of acute abdominal aortic aneurysmsa systematic review and meta-analysis (July 2008)
14. Zarins, C.K, Crabtree, T., Bloch, D.A, Arko, F.R, Ouriel, K., White, R.A: Endovascular aneurysm repair at 5 years: does aneurysm diameter predict outcome?. J. Vasc. Surg. **44**(5), 920–930 (2006)
15. Peppelenbosch, N., Buth, J., Harris, P.L., van Marrewijk, C., Fransen, G.: Diameter of abdominal aortic aneurysm and outcome of endovascular aneurysm repair: does size matter? A report from eurostar. J. Vasc. Surg. **39**(2), 288–297 (2004)
16. Kamineni, R., Heuser, R.R: Abdominal aortic aneurysm. J. Interv. Cardiol. **17**(6), 437–445 (2004)
17. Klippel, A.P, Butcher, H.R Jr: The unoperated abdominal aortic aneurysm. Am. J. Surg. **111**(5), 629–631 (1966)
18. Fillinger, M.: Who should we operate on and how do we decide: predicting rupture and survival in patients with aortic aneurysm. Semin. Vasc. Surg. **20**(2), 121–127 (2007) (Changing Techniques in the Evaluation of Aortic Disease)
19. Larsson, E., Labruto, F., Gasser, T.C, Swedenborg, J., Hultgren, R.: Analysis of aortic wall stress and rupture risk in patients with abdominal aortic aneurysm with a gender perspective. J. Vasc. Surg. **54**(2), 295–299 (2011)
20. Fillinger, M.F, Marra, S.P, Raghavan, M.L, Kennedy, F.E: Prediction of rupture risk in abdominal aortic aneurysm during observation: wall stress versus diameter. J. Vasc. Surg. **37**(4), 724–732 (2003)
21. Heng, M.S, Fagan, M.J., Collier, J.W., Desai, G., McCollum, P.T, Chetter, I.C: Peak wall stress measurement in elective and acute abdominal aortic aneurysms. J. Vasc. Surg. **47**(1), 17–22 (2008)
22. Brown, P.M., Zelt, D.T., Sobolev, B.: The risk of rupture in untreated aneurysms: the impact of size, gender, and expansion rate. J. Vasc. Surg. **37**(2), 280–284 (2003)
23. Perko, M.J., Nrgaard, M., Herzog, T.M., Olsen, P.S., Schroeder, T.V, Pettersson, G.: Unoperated aortic aneurysm: a survey of 170 patients. Ann. Thorac. Surg. **59**(5), 1204–1209 (1995)

24. Finlayson, S.R.G, Birkmeyer, J.D., Fillinger, M.F., Cronenwett, J.L: Should endovascular surgery lower the threshold for repair of abdominal aortic aneurysms? J. Vasc. Surg. **29**(6), 973–985 (1999)
25. Kaufman, J.A, Geller, S.C, Brewster, D.C, Fan, C.-.M., Cambria, R.P, LaMuraglia, G.M, Gertler, J.P, Abbott, W.M, Waltman, A.C: Endovascular repair of abdominal aortic aneurysms. Am. J. Roentgenol. **175**(2), 289–302 (2000)
26. Creemers, E., Limet, R., Van Damme, H., Deprez, M: Intrinsic structural failure of polyester (dacron) vascular grafts. A general review. Acta chirurgica belgica **105**(3), 249–255 (2005) (Publisher: Acta chirurgica belgica)
27. Hinchliffe, R., Ivancev, K.: Endovascular aneurysm repair: current and future status. CardioVasc. Interv. Radiol. **31**, 451–459 (2008). doi:10.1007/s00270-008-9295-7
28. Harkin, D.W., Dillon, M., Blair, P.H., Ellis, P.K., Kee, F.: Endovascular ruptured abdominal aortic aneurysm repair (evrar): a systematic review. Eur. J. Vasc. Endovasc. Surg. **34**(6), 673–681 (2007)
29. Schermerhorn, M.L, Giles, K.A, Hamdan, A.D, Dalhberg, S.E, Hagberg, R., Pomposelli, F.: Population-based outcomes of open descending thoracic aortic aneurysm repair. J. Vasc. Surg. **48**(4), 821–827 (2008)
30. Verhoeven, E.L, Kapma, M.R, Groen, H., Tielliu, I.F, Zeebregts, C.J., Bekkema, F., van den Dungen, J.J: Mortality of ruptured abdominal aortic aneurysm treated with open or endovascular repair. J. Vasc. Surg. **48**(6), 1396–1400 (2008)
31. Visser, J.J., Bosch, J.L., Myriam Hunink, M.G., van Dijk, L.C., Hendriks, J.M., Poldermans, D., van Sambeek, M.R.H.M.: Endovascular repair versus open surgery in patients with ruptured abdominal aortic aneurysms: clinical outcomes with 1-year follow-up. J. Vasc. Surg. **44**(6), 1148–1155 (2006)
32. Tambyraja, A.L., Fraser, S.C.A., Murie, J.A., Chalmers, R.T.A: Functional outcome after open repair of ruptured abdominal aortic aneurysm. J. Vasc. Surg. **41**(5), 758–761 (2005)
33. Cho, J.-S., Kim, J.Y., Rhee, R.Y., Gupta, N.Y., Marone, L.K., Dillavou, E.D., Makaroun, M.S: Contemporary results of open repair of ruptured abdominal aortoiliac aneurysms: effect of surgeon volume on mortality. J. Vasc. Surg. **48**(1), 10–18 (2008)
34. McPhee, J., Eslami, M.H., Arous, E.J., Messina, L.M., Schanzer, A.: Endovascular treatment of ruptured abdominal aortic aneurysms in the united states (2001-2006): a significant survival benefit over open repair is independently associated with increased institutional volume. J. Vasc. Surg. **49**(4), 817–826 (2009)
35. Starnes, B.W., Quiroga, E., Hutter, C., Tran, N.T., Hatsukami, T., Meissner, M., Tang, G., Kohler, T.: Management of ruptured abdominal aortic aneurysm in the endovascular era. J. Vasc. Surg. **51**(1), 9–18 (2010)
36. Corbett, T.J., Callanan, A., Morris, L.G., Doyle, B.J., Grace, P.A., Kavanagh, E.G., McGloughlin, T.M.: A review of the in vivo and in vitro biomechanical behavior and performance of postoperative abdominal aortic aneurysms and implanted stent-grafts. J. Endovasc. Ther. **15**, 468–484 (2008)
37. Moore, W.S: The role of endovascular grafting technique in the treatment of infrarenal abdominal aortic aneurysm. Cardiovasc. Surg. **3**(2), 109–114 (1995)
38. Nicholson, T.: Endovascular stent grafting of abdominal aortic aneurysms—a radiologist's view on a new potential issue in renovascular disease. J. Renovasc. Dis. **2**, 34–36 (2003)
39. Towne, J.B.: Endovascular treatment of abdominal aortic aneurysms. Am. J. Surg. **189**(2), 140–149 (2005)
40. Veith, F.J., Marin, M.L., Cynamon, J., Schonholz, C., Parodi, J.: Parodi, montefiore, and the first abdominal aortic aneurysm stent graft in the united states. Ann. Vasc. Surg. **19**, 749–751 (2005)
41. Stone, D.H., Brewster, D.C., Kwolek, C.J., LaMuraglia, G.M., Conrad, M.F., Chung, T.K., Cambria, R.P: Stent-graft versus open-surgical repair of the thoracic aorta: mid-term results. J. Vasc. Surg. **44**(6), 1188–1197 (2006)

42. Choi, E.T., Wyble, C.W., Rubin, B.G., Sanchez, L.A., Thompson, R.W., Flye, M.W., Sicard, G.A.: Evolution of vascular fellowship training in the new era of endovascular techniques. J. Vasc. Surg. **33**(2, Part B), 106–110 (2001)
43. Myhre, H.O., Lundbom, J., Hatlinghus, S.: Endovascular treatment of aortic disease. Int. J. Angiol. **9**, 10–17 (2000). doi:10.1007/BF01616322
44. Verhoeven, B.A.N., Waasdorp, E.J., Gorrepati, M.L., van Herwaarden, J.A., Vos, J.A., Wille, J., Moll, F.L., Zarins, C.K., de Vries, J.P.P.M.: Long-term results of talent endografts for endovascular abdominal aortic aneurysm repair. J. Vasc. Surg. **53**(2), 293–298 (2011)
45. Wahlgren, C.M, Malmstedt, J.: Outcomes of endovascular abdominal aortic aneurysm repair compared with open surgical repair in high-risk patients: results from the swedish vascular registry. J. Vasc. Surg. **48**(6), 1382–1388 (2008)
46. Wang, G.J., Carpenter, J.P.: The powerlink system for endovascular abdominal aortic aneurysm repair: six-year results. J. Vasc. Surg. **48**(3), 535–545.e3 (2008)
47. De Bruin, J.L., Baas, A.F., Buth, J., Prinssen, M., Verhoeven, E.L.G., Cuypers, P.W.M., van Sambeek, M.R.H.M., Balm, R., Grobbee, D.E., Blankensteijn, J.D.: Long-term outcome of open or endovascular repair of abdominal aortic aneurysm. N. Engl. J. Med. **362**(20), 1881–1889 (2010) (PMID: 20484396)
48. Rutherford, R.B: Endovascular aneurysm repair and outcome in patients unfit for open repair of abdominal aortic aneurysm (evar trial 2): randomized controlled trial. Perspect. Vasc. Surg. Endovasc. Ther. **18**(1), 76–77 (2006)
49. Choke, E., Munneke, G., Morgan, R., Belli, A.-M., Loftus, I., McFarland, R., Loosemore, T., Thompson, M.: Outcomes of endovascular abdominal aortic aneurysm repair in patients with hostile neck anatomy. CardioVasc. Interv. Radiol. **29**, 975–980 (2006). doi:10.1007/s00270-006-0011-1
50. Dillavou, E.D, Muluk, S.C, Rhee, R.Y, Tzeng, E., Woody, J.D, Gupta, N., Makaroun, M.S: Does hostile neck anatomy preclude successful endovascular aortic aneurysm repair?. J. Vasc. Surg. **38**(4), 657–663 (2003)
51. Ricotta, J.J, Oderich, G.S: Fenestrated and branched stent grafts. Perspect. Vasc. Surg. Endovasc. Ther. **20**(2), 174–187 (2008)
52. Arko, F.R., Filis, K.A., Seidel, S.A., Gonzalez, J., Lengle, S.J., Webb, R, Rhee, J., Zarins, C.K.: How many patients with infrarenal aneurysms are candidates for endovascular repair? The northern california experience. J. Endovas. Ther. **11**(1), 33–40 (2004)
53. Muhs, B.E., Verhoeven, E.L.G., Zeebregts, C.J., Tielliu, I.F.J., Prins, T.R., Verhagen, H.J.M., van den Dungen, J.J.A.M.: Mid-term results of endovascular aneurysm repair with branched and fenestrated endografts. J. Vasc. Surg. **44**(1), 9–15 (2006)
54. Azizzadeh, A., Sanchez, L.A., Rubin, B.G., Parodi, J.C., Godshall, C.J., Geraghty, P.J., Choi, E.T., Flye, M.W., Curci, J.A., Sicard, G.A.: Aortic neck attachment failure and the aneurx graft: Incidence, treatment options, and early results. Ann. Vasc. Surg. **19**(4), 516–521 (2005)
55. van Keulen, J.W., van Prehn, J., Prokop, M., Moll, F.L., van Herwaarden, J.A.: Dynamics of the aorta before and after endovascular aneurysm repair: a systematic review. Eur. J. Vasc. Endovasc. Surg. **38**(5), 586–596 (2009)
56. Cao, P., Verzini, F., Parlani, G., De Rango, P., Parente, B., Giordano, G., Mosca, S., Maselli, A.: Predictive factors and clinical consequences of proximal aortic neck dilatation in 230 patients undergoing abdominal aorta aneurysm repair with self-expandable stent-grafts. J. Vasc. Surg. **37**(6), 1200–1205 (2003)
57. Litwinski, R.A., Donayre, C.E., Chow, S.L., Song, T.K., Kopchok, G., Walot, I., White, R.A.: The role of aortic neck dilation and elongation in the etiology of stent graft migration after endovascular abdominal aortic aneurysm repair with a passive fixation device. J. Vasc. Surg. **44**(6), 1176–1181 (2006)
58. Sternbergh, W.C., Carter, G., York, J.W., Yoselevitz, M., Money, S.R.: Aortic neck angulation predicts adverse outcome with endovascular abdominal aortic aneurysm repair. J. Vasc. Surg. **35**(3), 482–486 (2002)

59. Hobo, R., Kievit, J., Leurs, L.J., Buth, J.: Influence of severe infrarenal aortic neck angulation on complications at the proximal neck following endovascular aaa repair: a eurostar study. J. Endovasc. Ther. **14**(1), 1–11 (2007)
60. Goncalves, F.B., de Vries, J.-P.P.M., van Keulen, J.W., Dekker, H., Moll, F.L., van Herwaarden, J.A., Verhagen, H.J.M.: Severe proximal aneurysm neck angulation: Early results using the endurant stentgraft system. Eur. J. Vasc. Endovasc. Surg. **41**(2), 193–200 (2011)
61. White, G.H: What are the causes of endotension?. J. Endovasc. Ther. **8**(5), 454–456 (2001)
62. Sampaio, S.M, Panneton, J.M, Mozes, G.I, Andrews, J.C, Bower, T.C, Kalra, M., Cherry, K.J., Sullivan, T., Gloviczki, P.: Aneurysm sac thrombus load predicts type ii endoleaks after endovascular aneurysm repair. Ann. Vasc. Surg. **19**(3), 302–309 (2005)
63. Parodi, J.C: Endovascular repair of abdominal aortic aneurysms and other arterial lesions. J. Vasc. Surg. **21**(4), 549–557 (1995)
64. Allen, R.C., White, R.A., Zarins, C.K., Fogarty, T.J.: What are the characteristics of the ideal endovascular graft for abdominal aortic aneurysm exclusion. J. Endovasc. Surg. **4**(2), 195–202 (1997)
65. Fogarty, T.J., Arko, F.R., Zarins, C.K.: Endograft technology: highlights of the past 10 years. J. Endovasc. Ther. **11**(Suppl. II), II-192–II-199 (2004)
66. Koenen, B., van de Vosse, F.N., Speelman, L., Rutten, M.C.M., van Donkelaar, C.C.: Towards the design of a patient specific stentgraft for endovascular aortic repair. Graduation thesis, Eindhoven University of Technology, Netherlands (2007). http://www.mate.tue.nl/mate/showabstract.php/7883
67. Kaori, K.: A novel foldable stent graft, Chapter 02, pp. 10, 26. PhD thesis, Mathematical, Physical & Life Sciences Division - Engineering Science, University of Oxford (2004)
68. Shedden, L., Oldroyd, K., Connolly, P.: Current issues in coronary stent technology. Proc. Inst. Mech. Eng. Part H: J. Eng. Med. **223**(5), 515–524 (2009)
69. Brunkwall, J.: How to design the optimal stent graft—what have we learnt. Scandinavian J. Surg. **97**(2), 191–194 (2008)
70. Duerig, T.W, Wholey, M.: A comparison of balloon- and self-expanding stents. Minim. Invasive Ther. Allied Technol. **11**(4), 173–178 (2002)
71. Sangiorgi, G., Melzi, G., Agostoni, P., Cola, C., Clementi, F., Romitelli, P., Virmani, R., Colombo, A.: Engineering aspects of stents design and their translation into clinical practice. Annali dellÍstituto superiore di sanitá ISSN 0021-2571 **43**(1), 89–100 (2007)
72. Yoshino, D., Inoue, K.: Design method of self-expanding stents suitable for the patient's condition. Proc. Inst. Mech. Eng. Part H: J. Eng. Med. **224**(9), 1019–1038 (2010)
73. Greenberga, R.K., Lawrence-Brownb, M., Bhandaria, G., Hartleyb, D., Stelterc, W., Umscheidc, T., Chuterd, T., Ivanceve, K., Greenf, R., Hopkinsong, V., Semmensh, J., Ouriela, K.: An update of the zenith endovascular graft for abdominal aortic aneurysms: Initial implantation and mid-term follow-up data. J. Vasc. Surg. **33**(2, Part B), 157–164 (2001)
74. Baril, D.T., Kahn, R.A., Ellozy, S.H., Carroccio, A., Marin, M.L.: Endovascular abdominal aortic aneurysm repair: emerging developments and anesthetic considerations. J. Cardiothor. Vasc. Anesth. **21**(5), 730–742 (2007)
75. Vallabhaneni, S.R., Harris, P.L: Lessons learnt from the eurostar registry on endovascular repair of abdominal aortic aneurysm repair. Eur. J. Radiol. **39**(1), 34–41 (2001)
76. White, G.H., Weiyun, Y., James, M., Xavier, C., Stephen M.S.: Endoleak as a complication of endoluminal grafting of abdominal aortic aneurysms: classification, incidence, diagnosis,and management. J. Endovasc. Surg. **4**(2), 152–168 (1997)
77. Wain, R.A, Marin, M.L, Takao, O., Sanchez L.A, Lyon R.T, Alla, R., Suggs, W.D., Yuan, J.G., Veith, F.J.: Endoleaks after endovascular graft treatment of aortic aneurysms: classification, risk factors, and outcome. J. Vasc. Surg. **27**(1), 69–80 (1998)
78. Grande, W., Stavropoulos, S.W.: Treatment of complications following endovascular repair of abdominal aortic aneurysms. Semin. Intervent. Radiol. **23**(02), 156–164 (2006)

79. Heikkinen, M.A., Arko, F.R., Zarins, C.K.: What is the significance of endoleaks and endotension. Surg. Clin. N. Am. **84**, 1337–1352 (2004)
80. Dill-Macky, M.J., Wilson, S.R., Sternbach, Y., Kachura, J., Lindsay, T.: Detecting endoleaks in aortic endografts using contrast-enhanced sonography. Am. J. Roentgenol. **188**(3), W262–W268 (2007)
81. Clouse, W.D., Brewster, D.C., Marone, L.K., Cambria, R.P., LaMuraglia, G.M., Watkins, M.T., Kwolek, C.J., Fan, C.-M., Geller, S.C., Abbott, W.M.: Durability of aortouniiliac endografting with femorofemoral crossover: 4-year experience in the evt/guidant trials. J. Vasc. Surg. **37**(6), 1142–1149 (2003)
82. Won, J.Y., Suh, S.-H., Ko, H.-k., Lee, K.H., Shim, W.H., Chang, B.-C., Choi, D.H., Park, S.J., Lee, D.Y.: Problems encountered during and after stent-graft treatment of aortic dissection. J. Vasc. Interv. Radiol. **17**, 271–281 (2006)
83. Chaudhuri, A., Ansdell, L.E., Grass, A.J., Adiseshiah, M.: Intrasac pressure waveforms after endovascular aneurysm repair (evar) are a reliable marker of type-{I} endoleaks, but not type-{II} or combined types: an experimental study. Eur. J. Vasc. Endovasc. Surg. **28**(4), 373–378 (2004)
84. Waasdorp, E.J., de Vries, J.-P.P.M., Sterkenburg, A., Vos, J.-A., Kelder, H.J.C., Moll, F.L., Zarins, C.K.: The association between iliac fixation and proximal stent-graft migration during evar follow-up: mid-term results of 154 talent devices. Eur. J. Vasc. Endovasc. Surg. **37**(6), 681–687 (2009)
85. Resch, T., Malina, M., Lindblad, B., Malina, J., Brunkwall, J., Ivancev, K.: The impact of stent design on proximal stent-graft fixation in the abdominal aorta: an experimental study. Eur. J. Vasc. Endovasc. Surg. **20**(2), 190–195 (2000)
86. Tonnessen, B.H., Sternbergh, W.C. III, Money, S.R.: Mid- and long-term device migration after endovascular abdominal aortic aneurysm repair: A comparison of aneurx and zenith endografts. J. Vasc. Surg. **42**(3), 392–401 (2005)
87. Heikkinen, M.A., Alsac, J.M., Arko, F.R., Metsänoja, R., Zvaigzne, A., Zarins, C.K: The importance of iliac fixation in prevention of stent graft migration. J. Vasc. Surg. **43**(6), 1130–1137 (2006)
88. Zarins, C.K, Bloch, D.A, Crabtree, T., Matsumoto, A.H, White, R.A, Fogarty, T.J: Stent graft migration after endovascular aneurysm repair: importance of proximal fixation. J. Vasc. Surg. **38**(6), 1264–1272 (2003)
89. Benharash, P., Lee, J.T., Abilez, O.J., Crabtree, T., Bloch, D.A., Zarins, C.K.: Iliac fixation inhibits migration of both suprarenal and infrarenal aortic endografts. J. Vasc. Surg. **45**, 250–257 (2007)
90. Trout, H.H., Tanner, H.M.: A new vascular endostaple: a technical description. J. Vasc. Surg. **34**(3), 565–568 (2001)
91. Yusuf, S.W., Whitaker, S.C., Chuter, T.A.M., Wenham, P.W., Hopkinson, B.R.: Emergency endovascular repair of leaking aortic aneurysm. The Lancet **344**(8937), 1645– (1994)
92. Mastracci, T.M., Garrido-Olivares, L., Cinà, C.S., Clase, C.M.: Endovascular repair of ruptured abdominal aortic aneurysms: a ystematic review and meta-analysis. J. Vasc. Surg. **47**(1), 214–221.e14 (2008)
93. Millon, A., Deelchand, A., Feugier, P., Chevalier, J.M., Favre, J.P: Conversion to open repair after endovascular aneurysm repair: causes and results. a french multicentric study. Eur. J. Vasc. Endovasc. Surg. **38**(4), 429–434 (2009)
94. Prinssen, M., Wixon, C.L, Buskens, E., Blankensteijn, J.D: Surveillance after endovascular aneurysm repair: diagnostics, complications, and associated costs. Ann. Vasc. Surg. **18**(4), 421–427 (2004)
95. Moulakakis, K.G., Dalainas, I., Mylonas, S., Giannakopoulos, T.G., Avgerinos, E.D., Liapis, C.D.: Conversion to open repair after endografting for abdominal aortic aneurysm: a review of causes, incidence, results, and surgical techniques of reconstruction. J. Endovasc. Ther. **17**(6), 694–702 (2010)
96. Chuter, T.A.M.: Branched and fenestrated stent grafts for endovascular repair of thoracic aortic aneurysms. J. Vasc. Surg. **43**(Suppl 2), A111–A115 (2006)

97. Elkouri, S., Martelli, E., Gloviczki, P., McKusick, M.A., Panneton, J.M., Andrews, J.C., Noel, A.A., Bower, T.C., Sullivan, T.M., Rowland, C., Hoskin, T.L., Cherry, K.J.: Most patients with abdominal aortic aneurysm are not suitable for endovascular repair using currently approved bifurcated stent-grafts. Vasc. Endovasc. Surg. **38**(5), 401–412 (2004)
98. Verhoeven, E.L.G., Tielliu, I.F.J., I., Muhs, B.E, Bos, W.T.G>J, Zeebregts, C.J., Prins, T.R., Oranen, B.I., van den Dungen, J.A.M.: Fenestrated and branched stent-grafting: a 5-years experience. Acta Chirurgica Belgica **106**, 317–322 (2006)
99. Bakoyiannis, C.N, Economopoulos, K.P, Georgopoulos, S., Klonaris, C., Shialarou, M., Marina, K., Papalambros, E.: Fenestrated and branched endografts for the treatment of thoracoabdominal aortic aneurysms: a systematic review. J. Endovasc. Ther. **17**(2), 201–209 (2010)
100. Greenberg, K.R.: Endovascular aneurysm repair using branched or fenestrated devices. Clinical case studies in the third dimension, vol. 1, section 7: Vascular and interventional imaging, pp. 205–214
101. Carpenter, J.P, Baum, R.A, Barker, C.F, Golden, M.A, Velazquez, O.C, Mitchell, M.E, Fairman, R.M: Durability of benefits of endovascular versus conventional abdominal aortic aneurysm repair. J. Vasc. Surg. **35**(2), 222–228 (2002)
102. Greenberg, R.K.: Abdominal aortic endografting: fixation and sealing. J. Am. Coll. Surg. **194**(Suppl. 1), S79–S87 (2002)
103. Waasdorp, E., van't Hullenaar, C., van Herwaarden, J., Kelder, H., van de Pavoordt, E., Overtoom, T., Moll, F., de Vries, J.-P.: Renal function after endovascular aortic aneurysm repair: a single-center experience with transrenal versus infrarenal fixation. J. Endovasc. Ther. **14**(2), 130–137 (2007)
104. Lau, L.L., Hakaim, A.G, Oldenburg, W.A., Neuhauser, B.e.a.t.e., McKinney, J.M., Paz-Fumagalli, R., Stockland, A.n.d.r.e.w.: Effect of suprarenal versus infrarenal aortic endograft fixation on renal function and renal artery patency: a comparative study with intermediate follow-up. J. Vasc. Surg. **37**(6), 1162–1168 (2003)
105. Parmer, S.S., Carpenter, J.P.: Endovascular aneurysm repair with suprarenal vs infrarenal fixation: a study of renal effects. J. Vasc. Surg. **43**(1), 19–19.e9 (2006)
106. Lalka, S., Johnson, M., Namyslowski, J., Dalsing, M., Cikrit, D., Sawchuk, A., Shafique, S., Nachreiner, R., OBrien, E.: Renal interventions after abdominal aortic aneurysm repair using an aortic endograft with suprarenal fixation. Am. J. Surg. **192**(5), 577–582 (2006)
107. Choke, E., Munneke, G., Morgan, R., Belli, A.-M., Dawson, J., Loftus, I., McFarland, R., Loosemore, T., Thompson, M.: Visceral and renal artery complications of suprarenal fixation during endovascular aneurysm repair. CardioVasc. Interv. Radiol. **30**, 619–627 (2007). doi:10.1007/s00270-007-9008-7
108. Malina, M., Brunkwall, J., Ivancev, K., Lindh, M., Lindblad, B., Risberg, B.: Renal arteries covered by aortic stents: clinical experience from endovascular grafting of aortic aneurysms. Eur. J. Vasc. Endovasc. Surg. **14**, 109–113 (1997)
109. Pintoux, D., Chaillou, P., Azema, L., Bizouarn, P., Costargent, A., Patra, P., Gouffic, Y.: Long-term influence of suprarenal or infrarenal fixation on proximal neck dilatation and stentgraft migration after evar. Ann. Vasc. Surg. **25**(8), 1012–1019 (2011)
110. Patel, S.T., Haser, P.B., Bush, H.L. Jr, Kent, K.C: The cost-effectiveness of endovascular repair versus open surgical repair of abdominal aortic aneurysms: a decision analysis model. J. Vasc. Surg. **29**(6), 958–972 (1999)
111. Fotis, T., Tsoumakidou, G., Katostaras, T., Kalokairinou, A., Konstantinou, E., Kiki, V., Perdikides, T.: Cost and effectiveness comparison of endovascular aneurysm repair versus open surgical repair of abdominal aortic aneurysm: a single-center experience. J. Vasc. Nurs. **26**(1), 15–21 (2008)
112. Morris, L., Delassus, P., Walsh, M., McGloughlin, T.: A mathematical model to predict the in vivo pulsatile drag forces acting on bifurcated stent grafts used in endovascular treatment of abdominal aortic aneurysms (AAA). J. Biomech. **37**, 1087–1095 (2004)

113. Doyle, B.J, Callanan, A., McGloughlin, T.M: A comparison of modelling techniques for computing wall stress in abdominal aortic aneurysms. BioMed. Eng. OnLine **6**(1), 1–12 (2007)
114. Scotti, C., Finol, E., Amon, C.: Computational fluid dynamics and wall mechanics of pre- and post-operative abdominal aortic aneurysms. In: Groth, C., Zingg, D.W. (eds.) Computational Fluid Dynamics 2004, pp. 329–334. Springer, Berlin (2006)
115. Sun, Z., Chaichana, T., Allen, Y.B., Sangworasil, M., Tungjitkusolmun, S., Hartley, D.E., Lawrence-Brown, M.M.D.: Investigation of hemodynamic changes in abdominal aortic aneurysms treated with fenestrated endovascular grafts. In: Lim, C.T., Goh, J.C.H. (eds.) 13th International Conference on Biomedical Engineering, vol. 23 of IFMBE Proceedings, pp. 1676–1679. Springer, Berlin (2009)
116. Bevan, R.L.T, Sazonov, I., Saksono, P.H, Nithiarasu, P., van Loon, R., Luckraz, H., Ashraf, S.: Patient-specific blood flow simulation through an aneurysmal thoracic aorta with a folded proximal neck. Int. J. Numer. Methods Biomed. Eng. **27**(8), 1167–1184 (2011)
117. Roy, D., Kauffmann, C., Delorme, S., Lerouge, S., Cloutier, G., Soulez, G.: A literature review of the numerical analysis of abdominal aortic aneurysms treated with endovascular stent grafts, Computational and Mathematical Methods in Medicine. **2012**, 16 p (2012) doi:10.1155/2012/820389
118. Sheidaei, A., Hunley, S.C., Zeinali-Davarani, S., Raguin, L.G., Baek, S.: Simulation of abdominal aortic aneurysm growth with updating hemodynamic loads using a realistic geometry. Med. Eng. Phys. **33**(1), 80–88 (2011)
119. Figueroa, C.A, Baek, S., Taylor, C.A., Humphrey, J.D: A computational framework for fluid-solid-growth modeling in cardiovascular simulations. Comput. Methods Appl. Mech. Eng. **198**(4546), 3583–3602 (2009)
120. Raghavan, M.L, Vorp, D.A, Federle, M.P, Makaroun, M.S, Webster, M.W: Wall stress distribution on three-dimensionally reconstructed models of human abdominal aortic aneurysm. J. Vasc. Surg. **31**(4), 760–769 (2000)
121. Vorp, D.A., Geest, J.P.V: Biomechanical determinants of abdominal aortic aneurysm rupture. Arter. Thromb. Vasc. Biol. **25**(8), 1558–1566 (2005)
122. Figueroa, C.A., Taylor, C.A., Yeh, V., Chiou, A.J., Gorrepati, M.L., Zarins, C.K: Preliminary 3d computational analysis of the relationship between aortic displacement force and direction of endograft movement. J. Vasc. Surg. **51**(6), 1488–1497 (2010)
123. Figueroa, C.A., Taylor, C.A., Chiou, A.J., Yeh, V., Zarins, C.K.: Magnitude and direction of pulsatile displacement forces acting on thoracic aortic endografts. J. Endovasc. Ther. **16**(3), 350–358 (2009)
124. Prasad, A., To, L.K., Gorrepati, M.L., Zarins, C.K., Figueroa, C.A: Computational analysis of stresses acting on intermodular junctions in thoracic aortic endografts. J. Endovasc. Ther. **18**(4), 559–568 (2011)

Flexible Leaflet Polymeric Heart Valves

Deon Bezuidenhout and Peter Zilla

Abstract Lifelong function and durability without the need for anticoagulation remains the holy grail of replacement heart valves. The use of polymers to produce flexible leaflet valves that have the positive attributes of current commercial bioprosthetic and mechanical valve types without any of their drawbacks, has been a focus of research since the mid 1950s. Although many different polymers have been considered, thermoplastic polyurethanes were by far the most prevalent due to their processability, general chemico-physical properties, and advances in their formulation that resulted in improved biocompatibility and stability. While accelerated in vitro durability of 600–1,000 million cycles has been achieved using polycarbonate urethanes, resistance to degradation, calcification and thrombosis in vivo has been shown with a new generation of polysiloxane-based polyurethanes. Despite these advances, however, polymeric valves have remained relegated to use in temporary ventricular assist devices for bridging heart failure to transplantation, where decreased exposure and resultant requirements are less stringent than with permanently implanted devices. As recent studies suggest a greater degree of instability in thermoplastic materials than hitherto believed, the remaining challenge remains the achievement of a combination of durability and biocompatibility in valve design and polymer formulation. This would allow polymeric valves to become a clinical reality for surgical implantation, as well as suitable candidates for use in applications where minimally invasive, transcatheter procedures are used to replace diseased valves. As polymers are amenable to relatively inexpensive mass production techniques, attainment of this goal could potentially benefit millions of patients in developing and emerging countries, who currently have no access to treatment of rheumatic heart disease so prevalent in these areas.

D. Bezuidenhout (✉) · P. Zilla
Cardiovascular Research Unit, Christian Barnard Division of Cardiothoracic Surgery, Faculty of Health Sciences, University of Cape Town, 203 Cape Heart Centre, Anzio Road, Observatory, Cape Town 7925, South Africa
e-mail: Deon.Bezuidenhout@uct.ac.za

Stud Mechanobiol Tissue Eng Biomater (2014) 15: 93–129
DOI: 10.1007/8415_2013_166

Published Online: 18 September 2013

1 Introduction

1.1 Need and Scope

The large and ever increasing need for heart valve replacements is underlined by an estimate that the total number of patients requiring heat valves would triple from 290,000 in 2003 to over 850,000 by 2050 based on population growth and ageing [1]. Due to the high incidence of rheumatic heart disease in developing and emerging nations, this number is likely to be much higher [2]. For current clinical application, there is a choice between five types of prosthetic heart valves—four of which require open-heart surgery, while the fifth can be placed via a catheter without major surgical intervention.

In order to provide context, these valve types, as well as tissue engineered valves will be briefly discussed before the main topic of flexible leaflet polymeric heart valves (PHVs) is addressed in detail. The review will cover materials, processing techniques and geometries used in the production of the prostheses, as well as their performance when used in surgical, transcatheter, and ventricular assist device (VAD) applications. We will assess how far PHVs have progressed to fulfil their promise of combining the positive characteristics of the two main commercially available valve types, i.e. that of high durability and good haemodynamics without the need for lifelong anticoagulation.

1.2 Commercial Heart Valve Prostheses

Auto- and allografts are human valves obtained from the recipient or cadaver donors, respectively, and together make up only a small percentage of implants due to limited availability and demanding surgical techniques (Table 1). The two main types of commercially available prosthetic valves that account for an overwhelming majority of implants are mechanical and bioprosthetic valves, with 55 and 45 % prevalence, respectively [3, 4]. Modern mechanical valves typically comprise annular rings containing one or two pyrolytic carbon occluders, have very high durability but unphysiological haemodynamics in terms of turbulence and shear stress, and require lifelong anticoagulation due to their thrombogenicity [2, 5]. Bioprosthetic valves on the other hand, consist of leaflets made from chemically treated (fixed) animal valves/leaflets or pericardial tissues and can be either stented or stentless. The bioprosthetic valves provide good haemodynamics due to their resemblance to natural flexible leaflet valves and do not require anticoagulation, They have limited durability due to calcification and degeneration [2, 5–7] and typically have smaller effective orifice areas (EOA) than modern mechanical valves [8]. Degeneration of the valves is particularly aggressive and rapid in younger patients, for example those with so-called third world diseases such as rheumatic heart disease.

Table 1 Summary of heart valve types [2–9, 11, 12, 31, 32]

	Valve type Clinical/Experimental Surgical/Catheter	Material and or valve source	Description	Advantages	Disadvantages
1	Autografts Clinical Surgical	(i) Natural, pulmonic valve from the recipient patient's own heart. (ii) Pericardium briefly fixed in glutaraldehyde in a 2-part stent	(i) Pulmonic valve used in aortic position and replaced with allograft (Ross procedure) (ii) Intraoperative fashioning of valve	No calcification. Autologous tissue that does not require anticoagulation and growing valve in case (i)	(i) Limited to exchange procedures, additional replacement valve still needed. Two valve surgeries for problem with one. (ii) In-theatre manufacturing and tears at commissures
2	Allografts Clinical Surgical	Valves (aortic) from human cadaver donors	Usually cryopreserved after treatment with antibiotics etc.	Possibly lower calcification than xenogeneic valves	Low availability due to low donor rate. Possibility of infection
3	Mechanical valves Clinical Surgical	Metal/pyrolytic carbon rings + pyrolytic carbon disk(s) (Older: Polymer balls and metal cages)	Tilting disk or bileaflet occluders in annular ring (Older: ball and cage)	Very durable. Lasts for lifetime of patient. Large EOA	Requires anticoagulation Can be noisy; non-physiological haemodynamics
4	Bioprosthetic valves Clinical Surgical	Animal tissue (pericardium or valve leaflets with or without stent). Porcine, bovine or equine origin	Tissue fixed by chemical treatment then attached onto scalloped stent/frame or used as whole root	No anticoagulation required. Good haemodynamics	Limited durability especially in young patients due to calcification and degeneration. May need replacement. Smaller EOA
5	Transcatheter valves Clinical Catheter	Animal tissue in collapsible/expandable stent/cage made from stainless steel, Co-Cr, Nitinol etc.	Pericardial leaflets fixed and sewn into/attached to stents. Valves crimped and inserted into heart via catheter	Does not require open-heart surgery. Less traumatic	Long-term durability not established; currently limited to patients not suitable for open-heart surgery and high risk patients
6	Tissue Engineered Experimental Surgical/Catheter	Decellularized bioprosthetic tissue or degradable polymers with cells and extracellular matrix materials	Living valves formed from scaffolds and cells in bioreactor or by using the body as bioreactor	Potential of growing with patient. Living, growing valves from patients own cells	Long production time, expensive, restricted to large centres, not yet clinically viable
7	Polymeric Experimental Surgical/Catheter	Polyurethane, silicone, ePTFE, SIBS, PVA, Hexsyn, etc.	Experimental valves mostly trileaflet design, although other designs evaluated	Ease of manufacture, low cost, good haemodynamics, potential for high durability	Some designs/polymers plagued by thrombogenicity, calcification and mechanical failure

While the abovementioned valves all require open-heart surgery, transcatheter valves that can be delivered using minimally invasive techniques (through a vein, an artery, or the apex of the heart) are a more recent development [9]. These valves were initially limited to patients who are not able to withstand the trauma of open-heart surgery or for young patients whose surgery is postponed to limit multiple invasive procedures [10, 11], but indications are expanding [12]. Clinically employed transcatheter valves in this class typically consist of collapsible/expandable metal stents containing soft leaflets similar to those used in surgically implantable bioprosthetic valves.

1.3 Availability and Costs

It is not the intention of this chapter to detail the economic aspects of clinical replacement valves, but as these factors clearly play a role in research and development strategies for taking complex devices like heart valves to market, they require some comment.

Surgically implantable bioprosthetic and mechanical heart valve prostheses are expensive due to high costs associated with research, development, clinical trials, regulatory approval etc. In addition, bioprosthetic valve manufacture is very labour intensive while mechanical valves use very high-tech/cost metallic and pyrolytic materials. Although the prices of these devices are adjusted to suit local economies (e.g. mechanical and bioprosthetic valves that cost approximately $5,000 in the developed world could cost approximately $1,000 to $2,000 in developing and emerging economies), the costs may still be prohibitive.

One way of decreasing the cost of the product itself is exemplified by the Chitra valve, manufactured in India and costing approximately a third to a half of that of an imported mechanical valve (Rs. 18,000 or $350) [13, 14]. The valve occluders are made from high molecular weight polyethylene (UHMWPE; as opposed to the pyrolytic carbon used in most other mechanical valves), which dramatically cuts the cost and increases availability, and added cost saving is realized by the fact that they (as well as the frame or complete valve) may be ordered from the manufacturer (TTK Healthcare Limited) online at Indiamart® [15]. These valves have met with much success in India [16, 17], where the need is great due to RHD (60,000 valves implanted since early 1990s), and the affordability increases the number of patients who are able to benefit.

In the case of transcatheter valve replacements, for which the need is greatest in developing and emerging economies [2], the affordability gap is currently so large as to make widespread implementation inconceivable. The cost of a standard surgical valve implantation (valve plus procedure) in the USA ($150,000 to $180,000) is an order of magnitude more expensive than in India ($9,500 to $12,000). As the cost of a TAVI valve alone is $20,000 to $30,000, it is clear that

transcatheter valves will thus currently remain limited to the patients in industrialised nations [18, 19].

The development of methods suitable for the inexpensive mass production of valves that would provide similar function and durability to current bioprosthetic variants is thus required. There is thus a very strong case to be made for the use of polymeric materials, as they lend themselves to mass-production (per the Chitra example), and they are becoming increasingly sophisticated in their chemical and mechanical properties. The remainder of this chapter is dedicated to the efforts of researchers who have worked for more than half a century on this exciting and important problem.

1.4 Experimental Valves

A broad class of experimental valves employs the use of tissue engineering and regenerative medicine techniques, combining decellularised biological or degradable polymeric scaffolds with cells to grow living heart valves in vitro and/or in vivo [20, 21]. These methods may well eventually provide the ultimate viable, growing, autologous valve, but require sophisticated production and cell culture techniques, and have other technical challenges that could limit implementation [22]. Although valves of this type often initially contain flexible leaflets made from polymeric materials, the materials are usually degradable, as they are only required for initial mechanical strength, cell attachment and remodelling. These valves fall outside the scope of this review.

A second experimental class comprises valves fabricated from durable polymeric materials. As valves with hard polymeric disk occluders [23], ball and cage valves with polymeric balls [5], and other non-standard designs in which essentially non-flexing polymers are used [24] are more readily classified as mechanical valves, the current review will be limited to "soft-leaflet" valves containing flexible polymeric leaflets.

Flexible leaflet polymeric valves date back to the pioneering work in the late 1950s by Akutsu [25], Roe [26] and Braunwald [27], leading to the first human implants in the mitral [27, 28] and aortic [29, 30] positions in 1960. Despite the fact that polymer heart valves were first implanted into humans more than half a century ago, they have not yet gained clinical acceptance as suitable surgical replacements, and clinical use remained limited to total artificial hearts and ventricular assist devices. Although classification may be done according to a variety of criteria, polymeric heart valve development will be discussed according to the polymers used, the geometries used for the leaflet designs and the production techniques used in their fabrication. Catheter based and VAD valves will be discussed separately from the main body of work done on surgically implantable valves (Table 1).

2 Surgically Implantable Valves

2.1 Polysiloxane Valves

Polysiloxanes, more commonly referred to as silicones (Dow Corning: Silastic®) are polymers of alternating Silicon and Oxygen atoms in the backbone, and can contain a variety of pendant reactive groups on the silicon –[Si(R_2)–O]–, with polydimethylsiloxane (PDMS: R = CH_3) comprising the structural chain moiety. Crosslinking through radicals, condensation or addition reactions leads to highly elastic materials which have been used in a wide range of implantable devices due to their biostability and flex and fatigue resistance [33].

Benson Roe and colleagues in San Francisco developed one of the first flexible trileaflet valves from a silicone material (Silastic 50, Ellay Rubber Company) in the late 1950s [26, 34]. The 380 μm thick leaflets were originally housed in a silicone cylinder, and valves evaluated in acute dog ascending aorta [34] showed satisfactory function, but long-term survival could not be achieved in a subsequent subcoronary model [35]. Later versions were made from a different silicone (General Electric SE-555) and with composite of a steel band/silicone sponge/Dacron sewing ring that contained slightly thicker leaflets (430–500 μm) [30]. Although some valves were shown to remain intact for 786 million cycles (mc) in accelerated tests (58 Hz; 18 years equivalent at 80 beats per minute; bpm) the program was discontinued due to high mortality rates in clinical trials with 18 selected patients between 1960 and 1962 [29, 30]. The authors noted that the high mortality in this case did not reflect failure of the leaflet mechanism, as most deaths resulted from surgical complications, although emboli from clot formation on the valve were evident in 3 cases. It should be noted, however, that the high cycle rate of 58 Hz is not conducive to proper valve opening and closing, and that lower rates were subsequently used by later researchers, as seen below.

Mohri et al. revisited trileaflet silicone valves and tested various Dow Corning (DC) silicone formulations and leaflet designs ranging from 225 to 510 μm in thickness with a preferred thickness of 330 μm [36]. Some of the initial combinations exhibited poor durability with tearing at 3.9 years (dome shaped; DC Silastic 372), but the preferred embodiment valves were able to withstand 17.7–23.8 equivalent years in accelerated tests (average 900 mc at 17 or 33 Hz; triangular leaflets; DC MDX4-4059 experimental polymer). This study also showed, however, the significant effect of valve fabrication as well as the consistency of raw materials on durability, as valves made from a different batch of the same material failed after 4–10 year equivalents. Another design reported by Gerring et al. (the Oxford valve) comprised silicone (DC Silastic 5505) coated Terylene (polyester) fabric and had a thickness of 120 μm [37]. In vivo evaluation in the pulmonary position of calves showed good survival of growing animals up to 30 months, with only 2 out of 7 animals in one series dying of thromboembolic events.

Room temperature vulcanizing silicone (RTV-615; General Electric) was used by Chetta and Lloyd to produce two valve designs with 256 μm leaflets using a cavity moulding method and achieved 65 and 280 mc respectively at 21 Hz [38]. Pulse duplication studies highlighted the need for test sections to be standardized and as close to physiological shape as possible, as the geometry of the test section significantly affects the valve performance.

2.2 PTFE and ePTFE Valves

Polytetrafluoroethylene, commonly known by the tradename Teflon®, is a highly crystalline fluorinated polymer that is well known for its inertness, low surface tension (high water contact angle), and low coefficient of friction.

Nina Braunwald and Andrew Morrow reported on clinical trials using flexible tricuspid Teflon fabric prostheses, based on the Muller-Littlefield valve [39] for aortic valve replacement in 23 patients between 1961 and 1963 [40]. The prostheses were either of plain Teflon fabric valves, Teflon fabric valves with a Teflon dispersion, or single Bahnson leaflets of jersey-knit Teflon. In most cases valves removed at reoperation or autopsy were stiffened, with regurgitation through holes in the leaflets and tears of varying sizes from small cracks to complete shredding and disruption of the fabric integrity. Nodular calcific deposits were evident but extensive calcification was not observed.

Gore-Tex® trileaflet valves (23–25 mm; WL Gore & Associates) were reinvestigated in an animal study in 1990 (weanling sheep tricuspid up to 34 weeks) [41]. Leaflets were all unretracted, but half the valves had one or more stiffened leaflet, and macroscopic calcification was evident in the commissural areas. Ando and Takahashi reported the use of hand-made valves comprising Gore-Tex leaflets suspended in Dacron conduits for the treatment of 139 paediatric patients undergoing pulmonary reconstruction due to Ross procedures and complex congenital heart disease [42]. The valves showed functional in vivo durability for up to 10 years and are considered to be a good alternative to homo and xenografts in this position.

The experiences with textile and expanded PTFE thus indicate that PTFE valves calcify and stiffen, and it seems, apart from the hand-made valves mentioned above, that the use of this material for heart valves is limited to employment as chordae tendineae for mitral valve repair [43, 44].

2.3 Polyurethane Valves

Polyurethanes are a broad class of materials with a very wide range of properties depending on the chemistries involved in their manufacture. They can be either thermosets or thermoplastics; in the latter case the polymers may form virtual

crosslinks by microphase separation to produce elastomeric materials that are heat and solvent processable and thus relatively easy to form into complex shapes. The segmented thermoplastic polyurethanes (TPUs) and polyurethane ureas (TPUUs) are composed of hard and soft segments and have been the most popular materials for use in polymeric heart valves over the history of their development. The polymers have undergone many improvements from first generation materials containing polyester soft segments that were hydrolytically degradable, to second generation polyether based materials (Polyether urethanes: PEU and Polyether urethane ureas: PEUU) that were susceptible to oxidation, to third generation materials that have greater chemical stability, such as those containing polycarbonate (PCU) and/or polysiloxane soft segments, and polycarbonate based materials that additionally contain polyhedral oligomeric silsequioxanes (POSS) nanoparticles [45, 46].

Nina Braunwald produced early bileaflet heart valves by impregnating lock-knit Dacron fabric in a mould cast from natural mitral valves from a catalysed liquid prepolymer formulation used to make open-cell foams (American Latex Company) and subsequently attaching woven Teflon® cordae [27, 28]. After gaining surgical experience by implanting the valves in dogs, she performed the first successful mitral valve replacement on a patient that survived to leave the hospital and do well for several months thereafter [47]. Also in the late 1950s the first three-cusp polyurethane (Estane, a PEU by BF Goodrich) valves (130–180 μm thickness) resembling native semilunar valves were made and implanted in the mitral, tricuspid and aortic position in dogs. Simultaneous development of valves and surgical techniques led to high mortality, and many of the valves showed marked fibrin deposition resulting in stenoses and emboli [25]. A second version of the Oxford valve (see Sect. 2.1) was produced with a segmented polyurethane urea (Biomer, a PEUU by Ethicon) with leaflet thicknesses from 70 to 80 μm, but without the reinforcing fabric used in the silicone version. Three calves receiving these valves in the pulmonary position survived for more than 18 months. Growth of the animals and associated increased stroke volumes resulted in increased right ventricular systolic pressures, but descriptions of the explanted valves were not given [37]. Two similar polyurethane ureas, namely Biomer and a DuPont Lycra® Spandex-type material, were used in the 1980s to produce trileaflet valves [48–50]. The Lycra valves had low regurgitation in vitro, and although the valves were durable for at least a year in adult ovine and caprine models, calcification and subsequent thrombosis was seen in growing calf tricuspid and mitral positions [50]. Calcification of the 280 μm leaflets of the Biomer valves implanted in juvenile sheep was also the principal finding, with mean calcium values of 42.7 ± 21 mg/g [49].

Two groups situated in or near Glasgow Scotland and Aachen Germany, respectively, have dominated work on polyurethane valves in the next two decades. The one is a collaboration between the University of Strathclyde and the Glasgow Royal Infirmary, while the other involves research at the Univ. of Aachen, The Helmholtz Institute Aachen, the spin-off company ADIAM, and the company Mecora GmbH which made Medos (Medos® Medizintechnik AG) PU

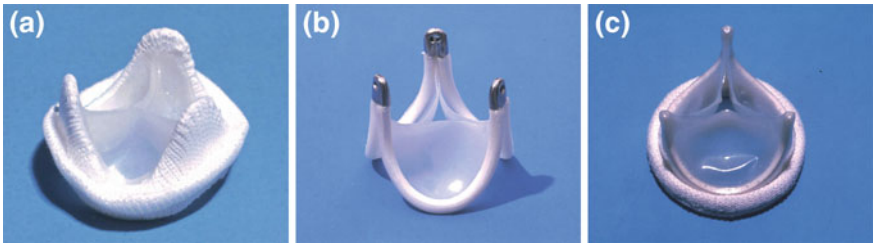

Fig. 1 Polyurethane valves by the Helmholz Institute Aachen, from *left* to *right*: **a** the Reul-Ghista trileaflet valve, **b** the Reul-Häussinger valve and **c** the Helmholz Institute valve (with permission: [51])

VADs and PU transcatheter valves for the group in Kiel (see Sects. 3 and 4). Examples of valves made by the German group can be see in Fig. 1.

Earlier work by the group of Helmut Reul in Aachen involved the optimized design of Avcothane-51 (a polyether/PDMS based polyurethane [45]) valves for smooth washout, minimum leaflet stress and maximum durability [52]. By October 1976, these valves had operated the equivalent of 10 years in accelerated tests at 12 Hz (378 mc).

The J-3 polyurethane (an aliphatic PCU; ENKA 1025/1; Enka/AKZO) valve was subsequently developed by Josef Jansen et al. by forming the leaflets on a stretched stent in the half-open position in order to minimize stresses during opening and closing. The valves showed very low energy losses, and reached 400–648 mc (11–17 years equivalent) in accelerated tests. Mitral implants in growing calves (5 month intended duration) showed thrombotic deposits that appeared to be associated with surface roughness on the cusps, and the most extensive deposits contained extrinsic calcification [53, 54]. In the decade thereafter, the company ADIAM developed both bi- and trileaflet polyurethane valves (Fig. 2a, b) from polycarbonate urethane (PCU, ADIAMat®) for the mitral and aortic positions respectively [55–58]. In vitro durability of the mitral valves ranged from 600 million to 1 billion cycles at 12 Hz (15.8–26 years) [55, 57, 58], while the aortic trileaflet valve showed steady improvement from 300 million [56] to 450 million [55] to 600 million [58] cycles. In vivo comparisons of the bileaflet valves with two different bioprosthetic valves by Sabine Daebritz et al. in the growing calf mitral model for 20 weeks showed trivial regurgitation, mild leaflet thickening and calcification, and no degeneration of the PCU valves, while the calves receiving bioprostheses had to be sacrificed after 1–4 weeks because of congestive heart failure due to severe calcification, degeneration and thrombosis [57]. When the trileaflet valves were compared to the same bioprostheses in the aortic position, the synthetic valves had a variable degree of calcification and degeneration was mild, and there was not an increase in thrombogenicity of the valves when compared to the bioprostheses. In comparison, both animals with bioprostheses had to be sacrificed after a short period due to heart failure [56].

The collaborations of David Wheatley in the United Kingdom concentrated on valve leaflets originally made from Estane (a PEU, BF Goodrich) (Fig. 3a) and

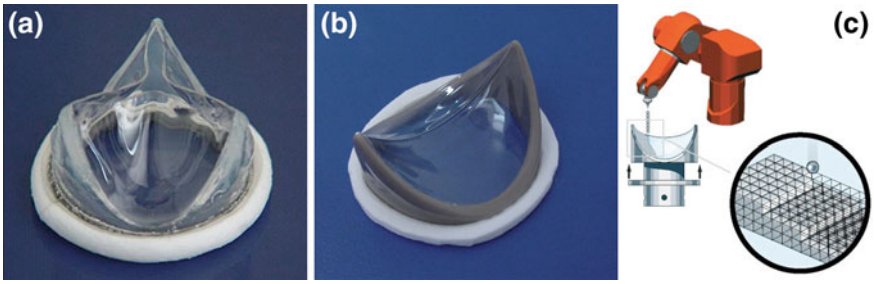

Fig. 2 **a** Tri- and **b** bileaflet polycarbonate urethane valves for the aortic and mitral positions respectively, produced by ADIAM life sciences, Erkelenz, Germany. A schematic of the robotic droplet deposition technique used in the manufacture of these valves is shown in **c** (**a**, **b** with permission: [2]; **c** courtesy of Josef Jansen, personal communication)

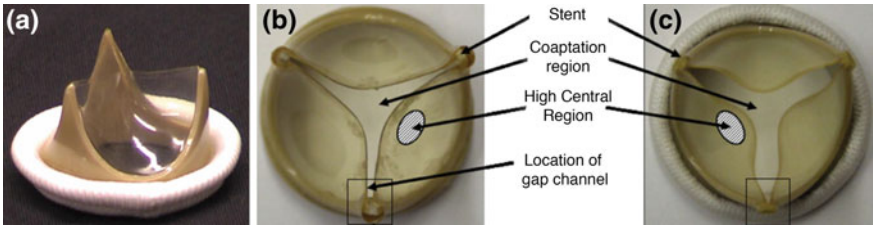

Fig. 3 **a** Ellipto-hyperbolic Estane® heart valve dip-coated on a PEEK frame and **b** Elast-Eon® valves with closed and open commissures (with permission: [2] and [71])

Lycra (a PEUU Du Pont), to later versions made from the more advanced Elast-Eon™ 3 (polysiloxane soft segment based polyurethanes (PSU) and polyurethane ureas (PSUU) with 40 % MDI based hard segment, Elastomedic/Aortech) [59–66]. Durability of more than 300 mc (12 Hz) achieved with ellipto-hyperbolic Estane valves [60] could be improved to over 450 million, with some valves achieving 800 mc (equivalent to 20 years), when changing to the diamine extended PEUU [59, 61, 64]. Leaflet thicknesses of 60–200 μm did not influence durability in PEU valves, but were directly related to durability of PEUU valves, with an optimum at 150 μm [59].

In vitro dynamic testing (in a fatigue tester) showed some calcification (similar levels for PEU and PEUU) of leaflets associated with tears at the free edge or commissures, degradation sites and sometimes with silicone present as additive or lubricant (in the materials or due to frame injection moulding) [60, 61]. Static in vitro and in vivo calcification assessment highlighted the effect of low molecular mass components in the polymers, as methanol and chloroform extracts and extracted polymers showed differential degrees of calcification. The low molecular mass extractables were generally shown to be accelerating factors in the calcification process [60, 61]. Hydrodynamic function tests in a simulated mitral position of a pulse duplicator demonstrated that the PU valves had similar mean pressure

drops to a bioprosthesis, and less reverse flow and energy losses than both the bioprosthetic and mechanical valve controls [64]. In the 6-month duration growing sheep mitral model the PU valves performed as well as the mechanical valve in terms of haemodynamics, while a porcine valve became compromised with time. Calcification of the PU valves was evident, and often associated with surface thrombus and degraded areas on the leaflets [66].

By the turn of the century, in a collaboration between the Universities of Leeds and Liverpool, the group proposed a new valve design with a conical attachment area and spherical upper/free edge are (henceforth termed the conico-spherical design (see Sect. 5.1). Original valves made from Tecothane (a PEU; Young's Modulus: E = 10 MPa; Thermedics) with 73–111 μm leaflets lasted for at least 360 mc, showed symmetrical opening and closing, and had superior EOA, lower regurgitant volume and lower energy losses than the single tilting disk mechanical and porcine bioprosthetic control valves used in the study [67]. Kinematic tests of similar valves with 150 μm leaflets showed the effect of cycle rate in accelerated testing, in that the leaflet kinematics, bending strains, the proportion of time fully open or closed, and the strain time integral were all dependent on cycle rate [68]. With valves of this geometry subsequently made from various grades of Elast-Eon™ 3 (E = 5–63.6 MPa and leaflets of 48–238 μm) the hydrodynamic function was not significantly affected by modulus, but significantly influenced by leaflet thickness [62]. PSU and PSUU based valves were implanted in the mitral position of young adult sheep for 6 months, after which the leaflets contained a fine surface proteinaceous layer, with no evidence of thrombus formation, fibrin deposition, calcification or thromboembolism [63, 65]. Although there was some evidence of surface enrichment of siloxane functional groups, the explanted leaflet materials differed little in appearance from their pre-implant state, were structurally intact, showed no degradation and exhibited retained mechanical properties [63]. There is some evidence, however, of degradation of PDMS soft segment polyurethanes with extended exposure to water, albeit at elevated temperatures, with possible site of hydrolysis being the carbamate groups adjacent to the PH(T)MO or PDMS chains [69].

Yoganathan's group in Atlanta studied three designs of Elast-Eon™ valves (Aortech Europe), namely ones with closed commissural design with those that had semi-open and open designs (Fig. 3b, c), in detail regarding the flow structure and its potential effect on thromogenicity [70, 71]. High shear and high velocities and thrombotic potential were identified at (i) the leakage jet at diastole, (ii) the trailing edge during peak forward flow, and (iii) the centre orifice jet downstream of the valve during peak forward flow.

In the interim, the Leeds group led by John Fisher also developed the alpha-rabola design valve made from thermoformed low modulus Eurothane 2003 (E = 6 MPa) to a leaflet thickness of 150–200 μm. The valves showed short term durability (100 mc), improved opening characteristics over spherical leaflets, as well as a clear effect of increasing opening pressures with thicker leaflets [72]. This design was used to compare two manufacturing methods, namely thermo-forming and dip-casting using IT C34 polyurethane (E = 7–10 MPa; both types

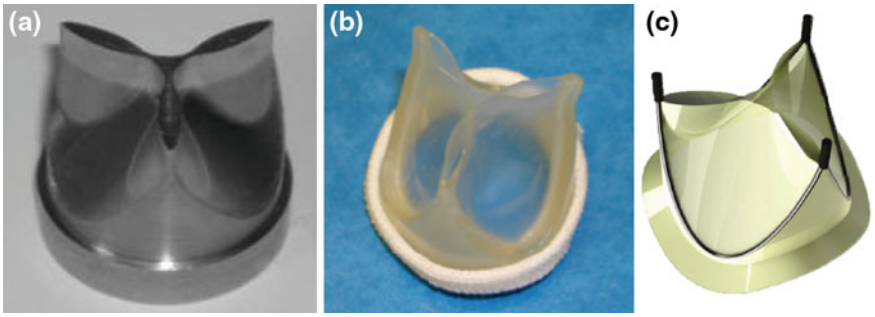

Fig. 4 POSS-PCU heart valve design (**a**) and prototype (**b**) developed by UCL [46]. Schematic representation (**c**) of the SSAV valve by the same group aimed at facilitating easy surgical procedure with minimal tissue damage and improved hemodynamic performance [77] (with permission from respective references given)

200 μm leaflet thickness) [73]. There was only a small difference in hemodynamic properties, but dip casting proved far superior in terms of durability, with at least 160 mc achieved compared to 100 million or less for the thermoformed valves. Finite element modelling of the alpharabola design showed reduction in principal tensile stress to 60 % of that of spherical leaflet geometry [74].

Nanocomposite POSS-PCU materials recently developed by the group of Alex Seifalian at University College London [75] showed improved mechanical properties over PCU controls and exhibited good surface properties and resistance to platelet adhesion [46]. A prototype heart valve made from this material is shown in Fig. 4a, b. In vitro assessment of a semi-stented surgical aortic valve (SSAV), 100, 150 and 200 μm leaflet valves based on this technology was performed and compared to control valves of similar size. The SSAV design (Fig. 4c) was shown to have improved performance over a conico-spherical design using finite element modelling and pulse duplication tests [76] and had lower transvalvular pressure drops, regurgitation and energy losses and a significantly increased calculated EOA than that control bioprosthetic valves [77].

2.4 Other Polymer Valves

A number of alternate polymers had been evaluated for use in flexible leaflet valves. During the late 1950s Roe et al. switched to silicone only after unsuccessful trials with polyvinyl alcohol, polyethylene and plasticized polyvinyl chloride (PVC, that lost flexibility after relatively short periods in the bloodstream due to loss of plasticizer in the case of PVC) [26].

Poly(styrene-b-isobutylene-b-styrene) (SIBS; Quatromer^{TM}, Innovia LLC), either as is or with polypropylene reinforcement fibres, has been proposed as a polymeric leaflet material due to its mechanical properties between that of silicone

and polyurethane, and its superior inertness due to its oxidation resistant Carbon–Carbon backbone [78, 79]. In addition to the percutaneous valve described in Sect. 4, the group also worked on surgically implantable valves. Early SIBS impregnated Dacron mesh valves (240 μm thickness) showed no significant difference to mechanical and bioprosthetic controls regarding thrombogenicity using a platelet activation state (PAS) assay in a VAD device [80]. Valves, with and without precoating with dimyristoyl phosphatidylcholine (DMPC), implanted for 20w in the sheep aortic position, failed due to stent deformation and cracks in the leaflets due to creep, with accompanying exposure of the PET fabric, with severe blood and tissue interactions, including extrinsic calcification [81]. A new SIBS valve design subsequently evaluated in vitro for thrombogenicity and platelet activation rates (PAR) was multiples lower than control bioprosthetic valves using the PAS assay and flow cytometry [82]. Innovia has also developed a thermoset crosslinked version of the material, dubbed xSIBS, to overcome creep problems associated with the non-crosslinked material, and to potentially make leaflets without the need for Dacron reinforcement [83]. The devices were recently optimised by the group at Stony Brook University (in collaboration with groups in Aachen and Arizona) for reduced stress, improved hemodynamics and reduced thrombogenicity using device thrombogenicity evaluation (DTE) [84, 85].

The group of Frank Baaijens in Eindhoven has been working on another olefinic material, namely crosslinked ethylene-propylene-dimer-monomer rubbers (EPDM; K520 from DSM), for the construction of heart valves. The valve comprises multiple layers of EPDM reinforced with wound fibres in a design that allows for the moulding of the leaflets (200 μm) as well as sinuses and part of the aortic root [86, 87].

Prototype heart valves have also been made from polyvinyl alcohol (PVA, a water soluble polymer) rendered insoluble by a one-piece cavity moulding/freeze thawing procedure (to form a so-called cryogel) using well-defined geometries discussed in Sect. 5 [88]. Devices were also fabricated from a combination of PVA with bacterial cellulose reinforcement to mimic the anisotropic mechanics of natural valve leaflets [89–91].

3 VAD/TAH Valves

Although some of the latest generation non-pulsatile centrifugal and axial flow VADs are also designed for (permanent) destination therapies (DT) [92], pulsatile VADs used in bridge to recovery (BTR) and/or bridge to transplant (BTT) treatments [93, 94] require valves that would function for a relatively short time. Reduced time of blood contact, reduced durability requirements and employment of systemic anticoagulation make the VAD market a logical entry point for polymeric valves, although the successful application of the device as a whole depends not only on the valve, but also on the large potentially thrombogenic blood-contact area of the pumping chamber.

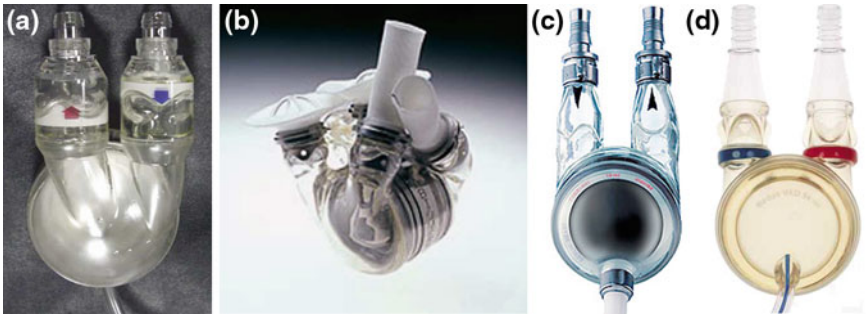

Fig. 5 Ventricular assist devices and total artificial heart using polyurethane flexible trileaflet valve: **a** Abiomed AB5000 VAD (with permission: [106]), **b** Abiomed Abiocor TAH (with permission: [103]), **c** Berlin Heart Excor VAD (courtesy of Marketing & Public Relations, Berlin Heart GmbH) and **d** Medos VAD III

The VAD examples mentioned below are paracorporeal devices that mostly use pneumatically driven pumping chambers and contain integrated trileaflet polyurethane valves that are of interest in this review, while the TAH devices are implantable. The Berlin Heart Excor (Fehling Medical AG, current owner Syscore GmbH) device is available in a variety of sizes and contains a trilayer pumping membrane with a graphite middle layer to minimize stresses (Fig. 5c). Although Sorin tilting disk valves are also used in larger models [95], all sizes are available with trileaflet PU valves [96]. The PU leaflet housings are non-bulbous to reduce dead volume and improve washout, and contain inclined cylindrical-section leaflets that are virtually leakproof. Both the pumping chamber and PU valves are treated with covalently attached heparin (Carmeda CBAS^{TM}) to reduce thrombogenicity [96]. The Berlin Heart has been used for biventricular support for children as young as 6 months [96] and several patients have been on biventricular support with this device for more than a year [95].

The MEDOS^{TM} VAD system (Fig. 5d), developed in the 1980s at the Helmholtz Institute Aachen (HIA) originally used mechanical valves, but these were replaced in the late 1980s by trileaflet polyurethane valves, followed by the acquisition of the device by Medos Medizintechnik AG in 1990 [97], and until recently made by Mecora® Medizintechnik Aachen [98]. The leaflets are set in a bulbous housing that resembles the aortic sinus to aid leaflet function and washing behind the valve structures. The devices are available for both the left and right heart in various pump sizes to cover paediatric and adult applications [99], and are configured for optimal outwash of both the pumping body and the valves. It is interesting to note the Berlin Heart and Medos systems have apparently opposing design features (non-bulbous vs. bulbous) to achieve the desired washout effect of the valve.

The Abiomed AB5000^{TM} (Fig. 5a, Abiomed Inc.) contains a drive membrane and trileaflet valves made from the company's proprietary Angioflex® PEU material [100]. The device has shown promising results in restoring haemodynamics and cardiac function in patients experiencing acute myocardial infarction

complicated by cardiogenic shock [101]. In addition to the VADs, the company had developed a total artificial heart designed to fit inside the body (Fig. 5b), which also made use of four polyurethane trileaflet valves [102, 103]. SynCardia use Medtronic-Hall mechanical valves in their Cardiowest TAH [104], but have signed a license agreement for the use of Elast-Eon polyurethane heart valve with AorTech for possible use in their pulsatile devices [105].

In a study by Zimmerman et al. where three of the above devices (plus 2 non-pulsatile device) were used in infants and children, no overall differences in the efficacy of devices were found, and the recommendation was to use the most practical system in terms of simplicity of implantation and mobility: (i) continuous flow for small children, (ii) pulsatile VADs for children >20 kg (gives mobility), and (iii) a TAH for large children [94].

Polyurethane (Cardiothane, a silicone-urethane copolymer/silicone homopolymer blend [107]) was also used in a novel jellyfish valve design by Imachi and colleagues in Tokyo for use in TAH devices, with the rationale that mechanical valves are very expensive to use sometimes for only a few days, and that thrombogenicity could be reduced by seamless integration. The valve went through a few design changes from prototype in 1988 [108] to successful 125 day implants in the early 1990s [109] and improved design/fabrication techniques after fracturing of the leaflet and finite element analysis to achieve a 10-fold increase in accelerated fatigue test durability [110]. Comparative results using this valve type on three different fatigue testers at different frequencies showed shorter lifetime with increased cyclic rate and different tear locations to those found in vivo [111].

As it does not make sense to use four expensive mechanical valves in an artificial heart that in many cases is used for only a few days, WJ Kolff used either Pellethane (a PEU) or Silastic HP-100 (Dow Corning) for making TAH valves [112]. Sacristan et al. revisited the use of silicone for the blood bag and valve of an experimental VAD in 2003 [113]. The valves were tested under static and pulsatile flow conditions, and although they had small transvalvular gradients [114], later MRI investigations showed limited hydrodynamic performance due to stenotic characteristics [115]. Another deviation from the polyurethane norm for VAD flexible valves was investigated by Kiraly et al. who compression moulded (a crosslinked polyolefin rubber) trileaflet valve in temporary blood pumps with good function and blood compatibility over three weeks [116].

4 Catheter-Based Valves

The history of catheter-mounted valves for relief of aortic insufficiency remarkably dates back to 1965, when Davies used a cone shaped parachute valve made by the US Catheter Company for temporary relief of aortic insufficiency. Although the material was not specified, it clearly appears to be of synthetic origin (Fig. 6). The design was subsequently improved upon in 1986 with an umbrella-shaped device placed in the aortic annulus of dogs [117].

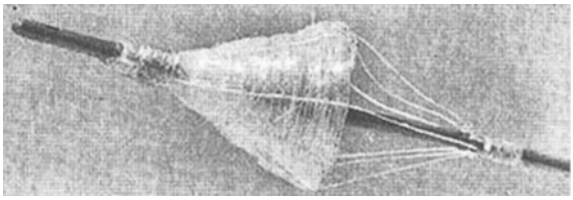

Fig. 6 First catheter-based valve described by Davies in 1965 (with permission: [117])

There are a number of reported designs of catheter based heart valves that use polyurethane materials in the construction of their leaflets/occluders. The first is a trileaflet valve in a stainless steel stent developed by Percutaneous Valve Technologies (PVT, NJ, USA, acquired by Edwards Lifesciences in 2004) [118], with good results in the sheep model. The company has subsequently switched to the pericardial tissue currently used in their SAPIEN® valves. Examples of the polymer valves can be see in [119].

A second is based on a traditional trileaflet design mounted in a Nitinol stent (24 mm diameter × 28 mm height). The valve (made by Mecora GmbH, Aachen) with 100–150 μm thick dip-coated leaflets fits into a very low-profile (14F) delivery device and showed competence after 1-month transfemoral implantation in the sheep pulmonary position by the group of Georg Lutter in Kiel (Fig. 7a) [120]. A more recent study by the same group in 9 sheep showed good opening and closing characteristics of the valves at 1 month, and no induration, macroscopic damage or inflammation [121].

Although the next two valves do not conform to the standard leaflet geometry, they are relevant in terms of containing flexible polyurethane occluders, and noteworthy in their design. The first is by Sochman et al. (Fig. 7b) using a self-expanding Interco Z-stent containing a collapsible polyurethane covered tilting disk with a mechanism to allow the disk to be snapped into place after deployment using a 10F catheter [122]. Implantation trials via the carotid artery in an acute (2–3 h) canine supra-coronary aortic model showed successful delivery, regular disk movement and short-term proof of principle.

A novel repositionable stent design comprising three Nitinol coils and locking wires, and a conical or umbrella-shaped polyurethane valve (Fig. 7c), was evaluated by Hashimoto et al. [123]. Acute implantation trials were performed via the common carotid artery in pigs with the valve in a sub-coronary position using a 10F introducer sheath. Valves were successfully placed, and although some regurgitation and thrombus formation was evident, excellent function and lack of coronary obstruction was observed. A fifth flexible leaflet transcatheter valve, developed by the group of Danny Bluestein at Stony Brook University comprised three SIBS/Dacron composite leaflets suspended in a self-expanding Nitinol stent (Fig. 7d). The valve was crimpable to less than 24F and was deployed and tested in a left heart simulator [124]. They have also described a synthetic leaflet version of the Edwards valve by using a modified Sapien-Cribier stent [124].

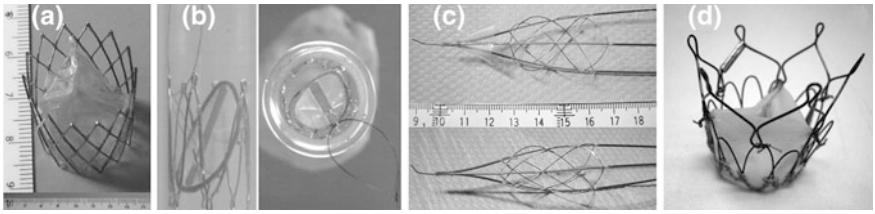

Fig. 7 Catheter deliverable polymeric heart valves, from *left* to *right*: **a** Mecora PU/Nitinol trileaflet design [120], **b** Tilting disk PU/Z-stent design by Sochman [122], **c** Hashimoto PU/Nitinol umbrella shaped valve [123], and **d** Claiborne SIBS/Dacron/Nitinol trileaflet valve [124] (with permissions)

Although these are early examples of attempts to produce catheter based valves from polymers as opposed to bioprosthetic tissue, the potential advantage of very small potential crimp sizes (10–14F vs. 18–19F for pericardial valves) is clear.

5 Valve Geometry

As the manufacture of polymeric valves provides greater freedom in design than is the case with pericardial valves (where leaflets are fashioned out of essentially flat sheets of tissue), a discussion on the geometry of the natural valve, and attempts to mimic it or provide other optimised geometries, is given in this section.

It is not surprising that the valves of the heart that are unsupported by cordae (and one that is) are of trileaflet design, as this configuration has been shown to be superior in stress distribution to bi- and quarto-leaflet analogues [125]. The central flow of the trileaflet design also has better mechanical efficiency, hydraulic characteristics and flow patterns that cause much less blood trauma than mechanical devices [126]. In trileaflet designs, the total free edge length of a closed leaflet (1x diameter) is very close to the cord that suspends the leaflet ($\pi D/3 \approx D$) with a planar free edge design thereby allowing greater opening area than in a bileaflet design, as pointed out by Roe et al. [26]. This is not to say that bi and quatro-leaflet designs cannot be successful, as seen with the bileaflet PU valve [57, 58] and quatrovalve bioprosthetic design [3].

The elliptical natural aortic sinuses [127] cause recirculating flow and provide rapid closure of leaflets with negligible backflow [38]. Aortic leaflets themselves have historically been considered to be portions of spherical surfaces, and described as *semilunar* by Philistion of Locri (ca. 427–ca. 347 BC), *sigmoid* by Erasistratus of Ceos (ca. 304–ca. 250 BC), as three adjacent hemispheres by Leonardo da Vinci (1452–1519) during the Renaissance, and by Retzius (in 1843) as three interlocking circles as seen from above [128]. More recently, Mercer (in 1973) approximated the leaflet shapes as *paraboloids of revolution* with foci at the base of the leaflets [72, 128], while Hamid and co-workers described the geometry as an elliptic paraboloid [129].

Chong et al. (1978) made careful measurements of an excised human aortic valve, and described the geometry in terms of parameters R_1, R_2, φ_1 and φ_2, where R_1 and R_2 are the principal radii of curvature and φ_1 and φ_2 the subtended angles [130, 131], whereas Thubrikar and others (1980s and 1990s) saw them as being *cylindrical* to slightly *conical* [50, 127, 132]. The valve in the latter case is defined by the radii at the base and commissures (R_b and R_c), the valve height (H), the bottom surface and free edge angles of the leaflets (α and φ), the commissure and sinus height (H_s and h_s), radius of the outermost wall sinus (d_s) and the coaptation height (C_c) [127]. Support for the cylindrical leaflet model comes from the description of homograft leaflet shape [133], and the fact that pericardial valves are often constructed using this geometry [134].

An interesting alternate way of describing the aortic leaflet geometry was introduced by Peskin and McQueen. The method, which determines the structure from the function (namely to support a uniform pressure load in the closed position), involves computation of the fractal structure of the reinforcing fibres assuming transfer of load to the aortic wall by a one-parameter family of fibres under tension [135].

Many researchers attempted to mimic nature's example for trileaflet valves by approximating leaflet shapes using swept conical sections, spheres and variable curvatures in addition to cylindrical sections, while others based and adapted their designs to reduce stresses and improve function and durability. In the majority of cases, the designs are qualitatively rather than quantitatively described, but where available, they are given in more detail. Other valve types that do not fall into the standard trileaflet paradigm are briefly described thereafter.

5.1 Trileaflet Valves

After various "flat", "nozzle" and windsock" designs had been evaluated and discarded, Roe et al. used "*cone-shaped*" trileaflet cusps as being more resistant to collapse than "*dome-shaped*" cusps [30, 34]. Similarly, Mohri et al. originally used *semi-domed* leaflet shapes, but abandoned them for more *triangular* shaped designs with the addition of a domed sinus, and finally settled on a preferred configuration without the sinus based on accelerated durability testing [36]. As the grade of silicone construction material was also changed, it is not clear whether shape or polymer had the biggest influence on the durability improvement. Wisman et al. produced hemicylindrical leaflets with a 10 mm diameter on polypropylene and polyacetal frames/stents using a multiple dipping technique of PU in DMAc with the aid of polished metal moulds [50].

A detailed description of a leaflet design that uses conic sections to describe its geometry, i.e. one that is elliptical in the radial direction and hyperbolic in the circumferential direction, is specified completely by the following four equations, [64], where E and H are the respective major and minor axes of the two conic sections as subscripted and E_0 and H_0 are the x-axis offsets (Fig. 8a).

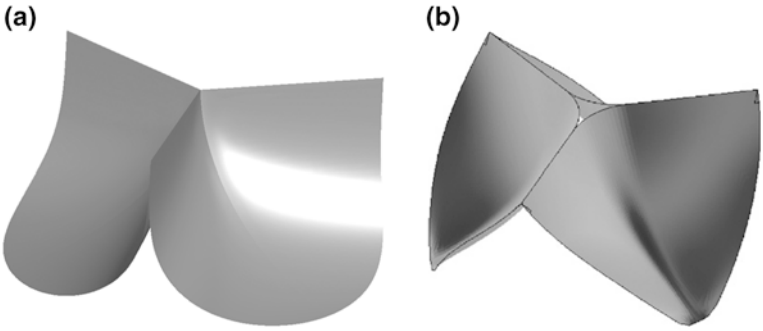

Fig. 8 **a** Ellipto-hyperbolic design described by Eqs. 1–4 and **b** Bezier drawn leaflet surface geometries (with permission: [136])

$$\left[(x - E_0)/E_{major}\right]^2 + [z/E_{minor}]^2 = 1 \tag{1}$$

$$\left[(x - H_0)/H_{major}\right]^2 - [y/H_{minor}]^2 = 1 \tag{2}$$

$$H_{major} = E_0 - (E_{major}[1 - (z/E_{minor})^2]^{1/2}) - H_0 \tag{3}$$

$$H_{minor} = H_{major} \cdot \tan 60^\circ \tag{4}$$

In apparent contrast, the group at the University of Leeds used a variable curvature or "alpharabola" shape for their polyurethane leaflets, defined by Eq. (5):

$$y^2 + z^2 = 2R_L(x - g) + \alpha(x - g)^2 \tag{5}$$

where z is the direction of flow, R_L is the minimum radius of curvature at the centre of the free edge, g is a small offset to position the leaflet and alpha is the shape parameter with a value between 0 and 1. When $\alpha = 1$, the radius of curvature is constant and a spherical leaflet with radius R_L ensues.

In fact, Leat's alpharabola design was shown, with some substitution of constants to be essentially a hyperboloid of revolution and thus similar to that of Wheatley (a spherico-hyperbolic as opposed to the elliptico-hyperbolic conicoid) and essentially equivalent to the hyperboloid of revolution (Fig. 9a) used by Jiang et al. to represent their polyvinyl alcohol valve geometry, as shown in Eq. (6), with z_0 the offset from the z coordinate [88].

$$\frac{x^2}{a^2} + \frac{y^2}{a^2} - \frac{(z - z_0)^2}{b^2} = -1 \tag{6}$$

The latter group also used an alternate geometry, namely that of a arc subtending two lines, which is rotated about an axis parallel to the x axis in order to form the three dimensional surface (Fig. 9b).

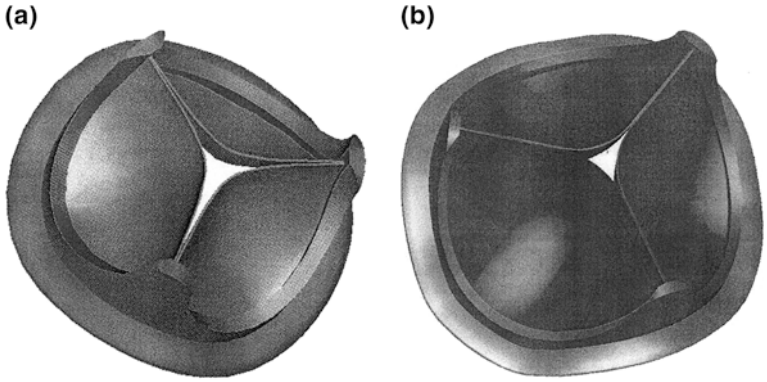

Fig. 9 CAD models of heart valves with leaflet geometries defined by (**a**) a hyperbola and (**b**) an arc subtending two straight lines. Use with permission from [88]

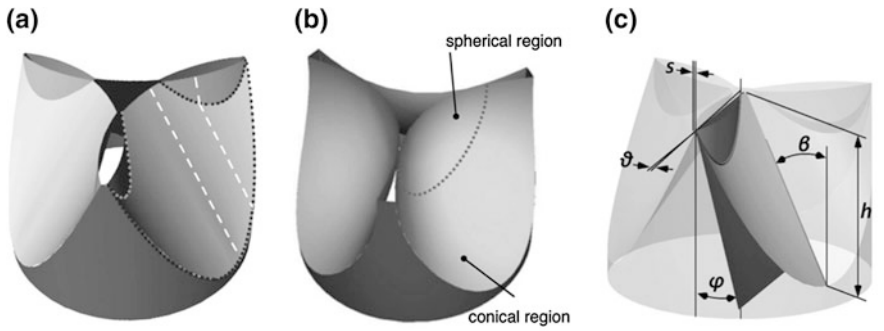

Fig. 10 Comparison of the UCL design (**a**) to the conico-spherical control valve (**b**), with dimensions defining the geometry in (**c**) [76] (with permission)

The leaflet geometry of the recently developed POSS-PCU valves [77] is given in detail in terms of ideal requirements, design principles and methodology by Burriesci et al. [76]. The leaflet is defined as a ruled surface between the intersection of the cylindrical stent with an inclined plane and an arc (normal to the axis) joining the commissures. The lateral portions of the leaflets are subsequently reflected through an inclined plane and the leaflet edge trimmed along a plane normal to the valve axis. This results in a leaflet defined by straight lines and the curvature described, as seen in Fig. 10a. The parameters (Fig. 10c) were subsequently optimized using finite element analysis of parametric models.

The interpretation of the Chong analysis of natural aortic valves and design criteria proposed by Ghista and Reul [52], i.e. smooth washout, minimal contact, minimal stress and pressure differential, led Kim et al. to suggest the ranges $0.87 < R_1/R_2 < 0.95$; $0.87 < R_2/R < 0.95$; $150 < \varphi_1 < 170$ and $85 < \varphi_2 < 100$, ad chose $R_1 = 10$ mm, $R_1 = R_2 = 0.9$, $\varphi_1 = 160$ and $\varphi_2 = 90$ for their Pellethane valve [131].

The SIBS percutaneous polymeric valve [124] used geometry based on the formula and constants proposed by Thubrikar [127], while the surgically implantable valve leaflets were originally of spherical and later cylindrical geometry, while the design was changed from a low to a medium profile [82, 137]. Further optimization using finite element analysis is described in two recent publications [84, 85].

Mohammadi et al. describe a novel way to simulate the natural aortic leaflets without the need for analytical description using conic sections or other geometries, although based on the elliptical paraboloid [129], by the use of Bezier curves using a limited number of control points and the de Casteljau algorithm to eliminate the gap between leaflets [90, 91, 136]. See Fig. 8b.

5.2 *Bileaflet Valves*

Interestingly, one of the first and also one of the most successful polymeric valves were of bileaflet design, and intended for the mitral position. The first comprised the PU-covered Dacron leaflets with attached Teflon cordae [27]. Arguably the most successful flexible leaflet polymeric heart valve (Fig. 2b), at least in terms of in vitro durability, is the bileaflet valve developed by ADIAM®. It is the only known design to have reached the 1 billion cycle mark (up to 26 years equivalent). The valve has a kidney-shaped stent with two asymmetrical struts supporting a large anterior and smaller posterior leaflet, thereby mimicking the natural mitral valve. This design creates natural flow patterns and vortices into the ventricle, prevents prolapse, and opening of the valve is facilitated by the suspension bridge design [58].

Another valve that could be considered a flexible bileaflet valve is a variation of the Jellyfish valve (see Sect. 5.3) that has its circular flexible disk attached to the frame along the diameter, as opposed to in its centre, thereby producing the two flaps. Regurgitation due to leaflet buckling was eliminated by increasing the thickness from 70 and 100 μm to 150 μm, but the valves had low durability (days to months equivalents) [138].

5.3 *Jellyfish Valves*

The jellyfish valve design by Imachi et al. in Tokyo for use in TAH devices is quite unique in that it has a flexible leaflet but is not of regular bi or tricuspid design. The original prototype comprised a brass disk with 8 circular perforations on top of which a thin (200 μm) membrane of cast polyurethane was screwed at its centre [108]. The disk was later changed to a 12-spoke design cast from polyurethane, with the membrane attached by gluing with the polymer solution [139].

6 Manufacturing Techniques

Various techniques have been used to process the polymers into the complex 3-dimensional leaflet shapes required. The first determinant of the technique available is the nature of the polymer used. Thermoplastic materials may be processed using heat and solvent processing (if the polymer is sufficiently soluble), whereas moulding techniques are required if the materials are thermosets.

Dipcasting is technologically one of the simplest techniques as it involves dipping a mould into a solution of the polymer, removing the mould such that a film of polymer solution adheres to the mould, and then evaporating the solvent to yield the desired structure. In practice, repeatability in obtaining the desired thicknesses and quality is not trivial. Solvent volatility, polymer concentration/viscosity, dipping number (single vs. multiple), technique and speed, drying position (upright, upside down, rotating), atmospheric conditions (pressure, temperature, gasses), and mould shape and surface properties all affect the distribution of material (leaflet thickness) and quality (surface morphology, uniformity, bubble formation/imperfections, durability and function (Fig. 11).

6.1 Polyurethane Valves

The J-3 polyurethane valve is interesting as it is manufactured in a half-open configuration. In order to achieve this, the top of the metal mould was flared so that the arms of the stent would be expanded between the minimal surface area leaflet surfaces. Dipcoating of leaflets and stent integration occurred in one step, using cleanroom conditions within a dry glove box, and the valve is tumbled in a controlled motion during drying to ensure even leaflet thicknesses [53, 54]. This method also avoids shape-memory effects, which can occur when leaflets are made in a precurved closed position.

ADIAM later improved the manufacturing technique by employing a combination of dipcoating and dropping techniques (Fig. 2c) of polymers of different hardnesses (soft outer layers and medium hardness core), whereby the polymer is applied in a controlled dropwise fashion in order to achieve accurate control over leaflet thickness (which is varied between 80 and 200 μm depending on position), the use of flexile stent posts to ensure proper closing, and the use of a precision laser to separate the leaflets [55, 56, 58]. The company also produced a scalloped bileaflet valve with large anterior and small posterior leaflets (varies between 100 and 300 μm thickness) specifically for the mitral position, and using sewing rings made from fleece-like sprayed PCU [55, 57, 58]. The Fraunhofer Institute in collaboration with Helmholtz Institute for Biomedical Engineering of RWTH Aachen University has recently also announced the very accurate production of small venous valves using the precise dropping techniques [140].

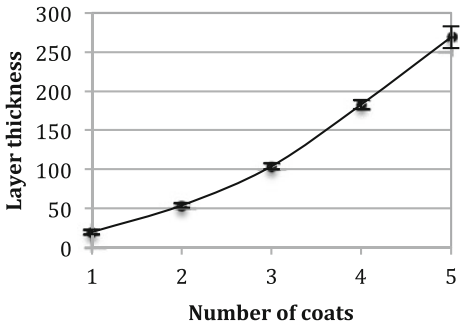

Fig. 11 Layer thickness as a function of number of coats for Avcothane®-51 polyurethane; 12.5 % solids by mass (adapted from [52])

Dip-coating onto injection moulded PU or machined PEEK frames fitted to metal forming mandrels (35–45 % Estane or Lycra in DMAc) was used by David Wheatley et al. to produce their ellipto-hyperbolic valves, with the solvent evaporated under slight positive pressure at 70–80 °C, vented into a water trap to ensure solvent evacuation [60, 61, 64]. Variations of this method when using Elast-Eon involved dipping and drying under inert atmosphere, and using single (1x 27 % PSUU in DMAc) and multiple (3x 15 % PSU in DMAc) coatings on pre-warmed steel former containing the PEEK frame [62, 63].

The alpharabola and spherical designs of the Leeds group were made by a combination of techniques. It comprised the solvent bonding (8 % PU in DMF) of leaflets cut from solvent cast films of PU to PU-dip-coated (250 μm layer) PEEK frames, and subsequent thermal forming of the leaflet geometries in custom-made metal moulds [72]. These valves were later compared to dipcoated valves, whereby stented mandrels were successively dipped in 25, 25 and 12 % (twice consecutively in 25 % then in 12 %) PU solutions in DMF followed by drying respectively in the upright, inverted (upside down) and upright positions (12 mm/min dipping; 75 °C drying for 1 h) [73]. Removal from the moulds was facilitated by extended immersion in water (12 h), and leaflets were cut using a sharp blade.

Alex Seifalian's group originally explored electro-hydrodynamic atomization (electrospraying) to make valves from their POSS-PCU material, but is now using a more established dip coating process [141]. The process comprises the repeated controlled dipping of a metal mandrel containing a contoured stent wire (0.5 mm titanium alloy) into the polyurethane solution (18 % w/v in DMAc) followed by drying (60 °C for 1 h) and trimming of the free edges [77].

6.2 Silicone Valves

Early silicone valves were cast in one piece (with a tubular root structure surrounding the leaflets) by compression moulding, heating the mould to 180 °C under high pressure and curing after removal from the die at 200 °C for 4 h [26, 30]. A similar process was followed 15 years later, using highly polished three-piece metal moulds into which the silicone was injected, from which excess air was removed

via a bleed screw, but in the latter case the valve was made on a three-posted metal stent to yield an integrated scalloped design [36]. With room temperature curing materials, the process can be simpler, as hand-made moulds from plaster and silicone can be used to form the desired shape by using centrifugation and/or evacuation to fill the cavity and allow sufficient time for the silicone to cure [38]. In order to make silicone valves for VAD devices at a fraction of the cost of mechanical or biological valves, one-piece devices (similar to those made by Roe et al.) were manufactured by injection moulding into 4-piece moulds [113]. This method resulted in an unexpected variability in leaflet thicknesses on the same valve as well as leaflets on different valves, but these differences were found not to affect the overall hemodynamic performance of the valves [142].

6.3 ePTFE Valves

Due to its high melt viscosity, PTFE requires different processing techniques than those used for conventional thermoplastics, and methods akin to those used for metals are often employed [143]. In terms of medical devices, the material is often used in an expanded form (expanded or ePTFE, e.g. Gore-Tex®) for the production of vascular grafts [144], although processing into fibres and subsequently into textile prostheses is also possible [145]. Early ePTFE valves were constructed from multiple layers of 3 μm thick (original thickness), 1 μm pore size (Gore-Tex®) sheets bonded together in diverse directions to achieve tensile strengths of 20x that of conventional PTFE. Composites containing various numbers of layers (4–15 layers, ranging from 8–31 μm total thickness) were then sewn to support stents after reinforcing the attachment zones with an additional 5–7 layers of material [146, 147]. More recently, Nistal et al. reported on valves comprised compact PTFE leaflets in a valve frame covered with ePTFE (and using ePTFE sutures) made by WL Gore & Associates [41]. The manufacturing technique, exact nature of the compact PTFE and whether it is similar to the composites used in the previously described valves are not clear. The manufacturing approach of the paediatric surgeons in Tokyo shows how innovative and simple designs can be very successful, albeit in the less demanding pulmonary position. The leaflets were hand made by folding a sheet of 100 μm in half, suturing the folded membrane to form three pockets, and then looping the ends around to form cylinders. The cylinders were then sewn into regular 12–28 mm Dacron (Haemashield, Boston Scientific Corp) vascular conduits and used with great success [42, 148] (see Fig. 12).

6.4 SIBS and EPDM Valves

SIBS percutaneous valves were made by impregnating Dacron fabric with the polymer dissolved in Toluene (15 % m/m) and air drying, forming a cylinder by stitching, stitching the cylinder to the Nitinol stent, and then annealing the leaflets

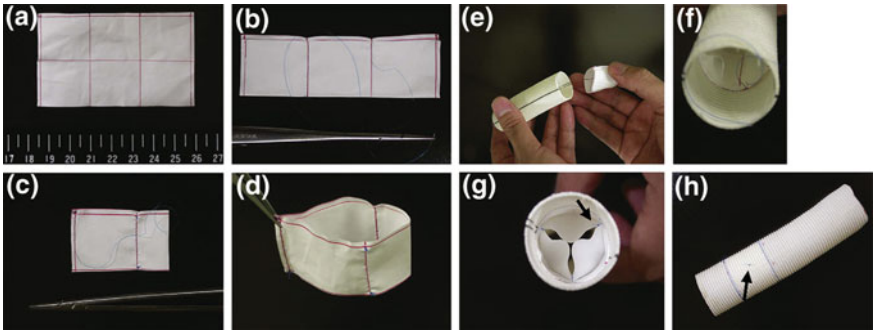

Fig. 12 Construction of Gore-Tex leaflet pouches (**a**–**d**) and insertion of the leaflets into the conduit to form the pulmonary valve (**e**–**h**) (with permission: [42])

into shape using three ball-bearings (9.5 mm) and a 19 mm aluminium cylinder [84, 124]. DTE optimised [85], surgically implantable valves were produced by filling 5-axis machined aluminum alloy molds (made by the collaborating Helmholtz Institute in Aachen) with raw 23 % styrene zSIBS, compressing to 1 ton of force and heating to 260 °C to effect the Diels-Alder crosslinking, as described in [84].

Other examples of SIBS valves made by different methods, from the use of dip-coating (with application of low density Dacron between coats) to compression moulding to solvent casting composite sheets and subsequently thermoforming the leaflets followed by solution bonding and suturing to the stent are shown in Fig. 13 [82, 137].

Valves made from the EPDM were manufactured by dipping rotating two piece moulds (one for leaflets, one that fits over the leaflet mould to produce the sinuses) into a 7.5 % solution of the material in xylene, combined and a fibre-winding machine that can be programmed to produce a variety of fibre orientations and patterns [86, 87].

6.5 PVA Valves

Dipcoating and film-fabricating technologies were, however, not considered suitable for the production of polyvinyl alcohol cryogel valves, as more constant dimensions and properties were expected from a cavity moulding process. Complex 4-axis-machined metal moulds comprising 9 parts were filled with hot PVA solutions by injection and pouring, and after closing of the mould, the whole assembly was subjected to freeze/thaw cycles in a water bath (−20 to +20 °C) [88]. The Ontario group subsequently developed anisotropic PVA cryogel valves by inclusion of a small percentage of bacterial cellulose, and straining the samples between cycles [90].

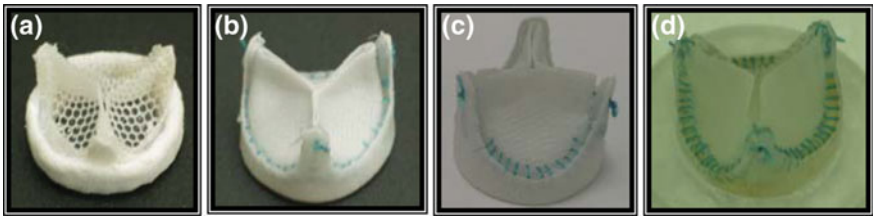

Fig. 13 SIBS valves made by dip-coating (**a**), dip-coating with thermal forming (**b**), compression moulding and thermal forming (**c**), and solvent casting/thermal forming (**d**) [137]

7 Surface/Bulk Treatments

A variety of surface and bulk treatments/compositions have been proposed for the reduction of thrombogenicity and calcification of polymeric valve leaflets, and for the maximization of durability. The main challenges facing these approaches are the limited surface area and volume of the leaflets and the sustained stability and activity of the treatments. This is especially demanding considering that about 6,000 litres of blood washes over the leaflets daily, so that active agents are readily depleted/overwhelmed even if they act in a catalytic manner.

Benson Roe was one of the first to attempt augmentation of the anticlotting properties of flexible leaflet valves by the surface bonding of graphite-benzalkonium-heparin [30, 149], but the contribution of the coating was unclear due to confounding factors, as valves failed for a variety of reasons, including thrombosis. Heparin, as well as taurine, aminosilane and polyethylene oxide (PEO) modification of PEU and PEUU valves did not affect leaflet thickness or hydrodynamic properties. When subjected to in vitro calcification in an accelerated tester, the PEO modification was detrimental to calcification and durability (155–200 down to 63–73 mc). The other three surfaces resulted in increased fatigue life; moderate in the case of the PEUU (155 to 180–320 mc) and marked in the case of the PEU (220 to 418–437 mc) [150]. In contrast, sulfonated PEO coupled to polyurethane heart valves and vascular grafts was shown in animal models to improve not only blood compatibility in terms of platelet adhesion and thrombus formation, but also to improve biostability and decrease calcification [151, 152].

Calcification is of course not only related to the surface of the leaflet, but also its composition. The mechanism of calcification of polyurethanes is not clear, but various have been proposed, including cation complexation by the polyether soft segment [60, 153] and chelation [154], or deposition of thrombi and cellular debris [49, 155], although calcification has been shown without the need for thrombus formation [156, 157]. Calcification has often also been shown to be associated with cracks or abrasions on leaflet surfaces, but it is not clear which causes which [156], while others have implicated the stresses and strains that leaflets undergo during cycling [158, 159].

Striking examples of treatments or formulations that result in reduced calcification are (i) the extraction of low molecular mass components from polyurethanes on calcification of leaflets in vitro [60, 61], (ii) the potential of nanocomposite formulations of PCA to decrease calcification [75], and (iii) the lack of degradation, calcification and thrombosis in leaflets made from Elast-Eon [63, 65].

Bisphosphonates are well known for their effect on mineralization [160], and derivatization of the hard segment of medical grade polyurethanes have been shown to decrease calcification in the rat subcutaneous model [161], as well as in the circulating sheep pulmonary valve cusp model without adverse effects on the polymers [157]. A summary of this group's work on anticalcification and antithrombotic treatments of polymeric materials can be found in [162].

Cholesterol modification of polyurethanes seems a very promising approach, as endothelial cell attachment and retention could be shown not only in vitro [163, 164], but also in vivo, employing pulmonary leaflet replacement with autologous endothelium-seeded polyurethane cusps [164].

Treatment of SIBS with dimyristoyl phosphatidylcholine (DMPC) did show promise in terms of decreased platelet adhesion, but calcification and degradation meant that the coatings did not have much effect when tested in a full-scale sheep valve model [81].

8 Summary and Conclusions

This review introduces the different types of replacement heart valves currently available, and identifies a need for alternate valves that would provide good long-term function and durability without the need for anticoagulation. Additionally, the unsolved need for inexpensive valves and replacement procedures for sufferers of rheumatic heart valve disease is highlighted. One alternative, namely the use of stable polymeric materials to fabricate the leaflets of heart valves, is reviewed and discussed in terms of application as surgically implantable valves, valves used in ventricular assist devices, and those that can be inserted via minimally invasive procedures.

In the case of surgical valves, polyurethanes were the most favoured polymer, with silicones and polytetrafluoroethylene being the next most prevalent materials, and polyolefins and cryogel polyvinyl alcohol materials making up the bulk of the remainder of research. Silicone valves produced in the 1960s could withstand accelerated testing of up to 700 mc, and 900 mc were achieved in the 1970s. In addition to animal studies, some of these valves were also implanted clinically, but failed due to surgical complications and thrombosis. Early PTFE fabric valves also failed when implanted into patients, as the materials stiffened, cracked, tore and even disintegrated. Handmade valves from expanded PTFE, on the other hand, were and are used with great success in a centre in Japan for pulmonary reconstruction after Ross procedures and complex congenital heart disease.

Polyurethane was used in the first mitral valve replacement in the early 1960s. Since then a myriad of polyurethane compositions has been used to fabricate more conventional trileaflet valve designs for use in aortic and other positions, but none have yet managed to overcome the three Achilles' heels of polyurethanes, namely degradation, calcification and thrombosis, in one design and formulation. By the late 1970s PU valves had attained durabilities of 400 mc, and up to 800 million and even a billion cycles could be realised by the turn of the century using diamine extended polyether and polycarbonate based urethanes, by groups in England and Germany respectively. Animal testing, however, showed combinations of calcification with accompanying degeneration/mechanical damage and/or thrombosis in most cases.

The development of silicone soft-segment polyurethanes held much promise for use in polymeric aortic valves, as they were initially shown to be resistant to oxidative and hydrolytic degradation. Animal studies using valves made from one of these materials also showed very encouraging results, in that no degradation, calcification or thrombosis was seen. A recent study, however, has observed in vitro hydrolytic degradation of two well-known examples of these materials.

Three current/recent ventricular assist devices use polyurethanes not only in construction of their valves, but also for the chambers and pumping membranes. As these devices are used for relatively short time periods, and patients are anticoagulated, the devices have been shown to be successful for up to a year without major complications.

Polyolefinic materials such as the SIBS copolymer do not contain labile groups in their backbones and are thus chemically stable, but they can suffer from other shortcomings, such as excessive creep leading to cracking and fabric reinforcement exposure. This prompted the users to develop crosslinked versions of the polymer to improve mechanical properties and reduce reliance on reinforcement. Crosslinked EPDM rubbers have also been proposed, most likely following the same arguments for the superiority of crosslinked hydrocarbons in terms of mechanics and chemical stability.

Minimally invasive, catheter based heart valves, even in their clinically approved designs featuring chemically fixed bioprosthetic tissue leaflets, are relatively new products. The use of polymeric materials for this application is thus represented by only a few examples. Three designs, namely a conventional trileaflet, a collapsible tilting disk, and an umbrella design are all made from polyurethane and have not undergone more than acute, or in the first case, one month of animal testing. The remaining example is also a trileaflet design in a Nitinol stent, is made from SIBS, and has been tested for deployment in a left heart simulator.

Although native aortic valves were designed by evolution rather than a geometer, the mathematical description of their shape has ranged from simple cylindrical surfaces, surfaces of constant curvature and paraboloids of revolution to elliptical paraboloids (with the exception of one group who followed the form follows function philosophy). It is thus not surprising that these, and other well described shapes such as spherico-hyperbolic, ellipto-hyperbolic and related alpharabola conicoids have been used to design polymeric leaflets that mimic their

natural counterparts. A valve mimicking the unsymmetric bileaflet shape of the mitral rather than the aortic valve, and the so-called jellyfish valve are two notable exceptions to the tricuspid design.

As silicone elastomers are crosslinked materials, compression moulding techniques have been most regularly employed to make heart valves. Early silicones were thermosetting in the strict sense of the word, and were thus heated in the moulds to effect the curing, and while the advent of room temperature curing ("vulcanisation") obviated the need for elevated temperatures, it seems that intra and intervalve consistency in terms of dimensions remains a challenge. PTFE, although defined as a thermoplastic, requires special sintering equipment to process, and valves were thus made from either PTFE fabric or pre-processed ePTFE membranes by conventional sewing techniques, while a variety of melt, heat and stitching combinations were employed to fabricate polyolefin valves such as the SIBS and EPDM prototypes mentioned above.

As the polyurethanes used for polymeric valves are thermoplastic and readily soluble in a range of solvents, both melt and solvent processing techniques have been employed. By far the simplest and most widely used method was the dip-coating technique, which requires nothing more than a few grams of polymer, a few decilitres of solvent, a scalloped frame and a positive cast of a mould shape to make a passable prototype valve. Despite its apparent simplicity, this method is also one of the most difficult to master, as the number of variables and tight control over them are numerous and difficult. Although relatively good control over leaflet thickness is attainable by optimising the dipping parameters for the particular polymer and geometry used, much more constant thicknesses may be achieved by using preformed polymer films that have either been extruded, melt pressed or solvent cast. The advantage gained in leaflet consistency is, however, lost to leaflet/frame (or stent) attachment strength, as secondary attachment methods are never as strong as in situ casting. As natural leaflets are not of constant thickness, it is clear that it is not constant thickness that is important, but rather control over thickness and thickness distribution that is critical. To this end, a method for the robotic dropwise placement of a polymer solution on a mould surface to controllably build the required profile was developed, and is currently being used to "print" small but very accurate venous valve prototypes. Whether this method is suitable for mass or large-scale production is not clear.

In attempts to overcome the degradation, calcification and thrombogenic shortcomings inherent in polyurethane formulations, numerous surface or bulk modification techniques have been investigated. Although many of these techniques resulted in improved properties in vitro or in short term in vivo experiments, they are all to be proven sufficient on/in actual polymeric valves in long-term implants. One of the most promising is the modification of polyurethanes with cholesterol for improved attachment and retention of endothelial cells that are seeded onto the surface.

Despite many years of progress and setbacks, research into the development of polymeric heart valves that can match or outperform existing bioprosthetic and mechanical counterparts continues. Whether the goal will eventually be reached

with continued incremental progress in the formulation of current materials, or whether a game-changing new polymer or process is required, remains a point for discussion. What is clear is that past attempts had failed, and that success will not only be a laudable scientific and technical achievement, but also a contribution to the well-being of those who suffer from a life threatening disease because they had strep throat and lacked a few dollars worth of antibiotics.

Acknowledgments The authors would like to thank Dr Art Coury for advice, suggestions and helpful discussions during the finalization of this review.

References

1. Yacoub, M.H., Takkenberg, J.J.: Will heart valve tissue engineering change the world? Nat. Clin. Pract. Cardiovasc. Med. **2**, 60–61 (2005)
2. Zilla, P., Brink, J., Human, P., Bezuidenhout, D.: Prosthetic heart valves: catering for the few. Biomaterials **29**, 385–406 (2008)
3. Butany, J., Fayet, C., Ahluwalia, M.S., Blit, P., Ahn, C., Munroe, C., et al.: Biological replacement heart valves. Identification and evaluation. Cardiovasc. Pathol. **12**, 119–139 (2003)
4. Kidane, A.G., Burriesci, G., Cornejo, P., Dooley, A., Sarkar, S., Bonhoeffer, P., et al.: Current developments and future prospects for heart valve replacement therapy. J. Biomed. Mater. Res. B Appl. Biomater. **88**, 290–303 (2009)
5. Butany, J., Ahluwalia, M.S., Munroe, C., Fayet, C., Ahn, C., Blit, P., et al.: Mechanical heart valve prostheses: identification and evaluation (erratum). Cardiovasc. Pathol. **12**, 322–344 (2003)
6. Chandran, K.B., Fatemi, R., Schoephoerster, R., Wurzel, D., Hansen, G., Pantalos, G., et al.: In vitro comparison of velocity profiles and turbulent shear distal to polyurethane trileaflet and pericardial prosthetic valves. Artif. Organs **13**, 148–154 (1989)
7. Senthilnathan, V., Treasure, T., Grunkemeier, G., Starr, A.: Heart valves: which is the best choice? Cardiovasc. Surg. **7**, 393–397 (1999)
8. Pibarot, P., Dumesnil, J.G.: Prosthetic heart valves: selection of the optimal prosthesis and long-term management. Circulation **119**, 1034–1048 (2009)
9. Rodes-Cabau, J.: Transcatheter aortic valve implantation: current and future approaches. Nat. Rev. Cardiol. **9**, 15–29 (2011)
10. Davidson, M.J., White, J.K., Baim, D.S.: Percutaneous therapies for valvular heart disease. Cardiovasc. Pathol. **15**, 123–129 (2006)
11. Ghanbari, H., Kidane, A.G., Burriesci, G., Bonhoeffer, P., Seifalian, A.M.: Percutaneous heart valve replacement: an update. Trends Cardiovasc. Med. **18**, 117–125 (2008)
12. Hollmer, M.: Edwards wins broader FDA approval for Sapien heart valve. Fierce Medical Devices, FierceMarkets (2012)
13. Award for TTK Chitra heart valve prosthesis. The Hindu (online) 15 May 2001. http://hindu.com/2001/05/15/stories/0615000b.htm Accessed 28 June 2013.
14. Raj, N.: Indigenous heart valve makes a difference. The Hindu (online) 2009. http://www.thehindu.com/opinion/op-ed/article69694.ece. Accessed 28 June 2013.
15. Indiamart. http://www.indiamart.com/ttkh-ltd/products.html. Accessed 28 June 2013.
16. Muralidharan, S., Muthubaskeran, V., Chandrasekar, P.: Ten years outcome of Chitra heart valves. Indian J Thorac Cardiovasc Surg. **27**, 24–27 (2011)
17. Sankarkumar, R., Bhuvaneshwar, G.S., Magotra, R., Muralidharan, S., Rajan, R.S., Saha, D., et al.: Chitra heart valve: results of a multicenter clinical study. J. Heart Valve Dis. **10**, 619–627 (2001)

18. Connell, J.: Medical Tourism. CABI (2011)
19. Lunt, N., Smith, R., Exworthy, M., Green, S., Horsfall, D., Mannion, R.: Medical Tourism: Treatments, Markets and Health System Implications: A Scoping Review. Organisation for Economic Co-operation and Development (OECD) (2011)
20. Filova, E., Straka, F., Mirejovsky, T., Masin, J., Bacakova, L.: Tissue-engineered heart valves. Physiol. Res. **58**(Suppl 2), S141–S158 (2009)
21. Schoen, F.J.: Heart valve tissue engineering: quo vadis? Curr. Opin. Biotechnol. **22**, 698–705 (2011)
22. Mendelson, K., Schoen, F.J.: Heart valve tissue engineering: concepts, approaches, progress, and challenges. Ann. Biomed. Eng. **34**, 1799–1819 (2006)
23. Fare, S., Brunella, M.F., Bruschi, G., Vitali, E.: Ex-vivo characterization of three Bjork-Shiley Delrin heart valves. J. Heart Valve Dis. **17**, 325–331 (2008)
24. Flege Jr, J.B., Melrose, D.G., Bentall, H.H.: Another prosthetic aortic valve. A preliminary report. Ann. Thorac. Surg. **2**, 623–625 (1966)
25. Akutsu, T., Dreyer, B., Kolff, W.J.: Polyurethane artificial heart valves in animals. J. Appl. Physiol. **14**, 1045–1048 (1959)
26. Roe, B.B., Moore, D.: Design and fabrication of prosthetic valves. Exp. Med. Surg. **16**, 177–182 (1958)
27. Braunwald, N.S., Cooper, T., Morrow, A.G.: Complete replacement of the mitral valve. Successful clinical application of a flexible polyurethane prosthesis. J. Thorac. Cardiovasc. Surg. **40**, 1–11 (1960)
28. Braunwald, N.S.: It will work: the first successful mitral valve replacement. Ann. Thorac. Surg. **48**, S1–S3 (1989)
29. Roe, B.B.: Late follow-up studies on flexible leaflet prosthetic valves. J. Thorac. Cardiovasc. Surg. **58**, 59–61 (1969)
30. Roe, B.B., Kelly Jr, P.B., Myers, J.L., Moore, D.W.: Tricuspid leaflet aortic valve prosthesis. Circulation **33**, I124–I130 (1966)
31. Van de Wal, H.J., Bennink, G.B., Haanschoten, M.C., Meijboom, E.J.: Autologous tissue cardiac valve: implantation in children. J. Thorac. Cardiovasc. Surg. **112**, 846–848 (1996)
32. Grabenwoger, M., Fitzal, F., Gross, C., Hutschala, D., Bock, P., Brucke, P., et al.: Different modes of degeneration in autologous and heterologous heart valve prostheses. J. Heart Valve Dis. **9**, 104–109; discussion 110–111 (2000)
33. Colas, A., Curtis, J.: Silicone biomaterials: history and chemistry. In: Rattner, B.D., Hoffman, A.S., Schoen, F.J., Lemons, J.E. (eds.) Biomaterials Science: An Introduction to Materials in Medicine, 2nd edn. Elsevier, San Diego (2004)
34. Roe, B.B., Owsley, J.W., Boudoures, P.C.: Experimental results with a prosthetic aortic valve. J. Thorac. Surg. **36**, 563–570 (1958)
35. Roe, B.B., Burke, M.F., Zebner Jr, H.: The subcoronary implantation of a flexible tricuspid aortic valve prosthesis. J. Thorac. Cardiovasc. Surg. **40**, 561–567 (1960)
36. Mohri, H., Hessel 2nd, E.A., Nelson, R.J., Anderson, H.N., Dillard, D.H., Merendino, K.A.: Design and durability test of Silastic trileaflet aortic valve prostheses. J. Thorac. Cardiovasc. Surg. **65**, 576–582 (1973)
37. Gerring, E.L., Bellhouse, B.J., Bellhouse, F.H., Haworth, W.S.: Long term animal trials of the Oxford aortic/pulmonary valve prosthesis without anticoagulants. Trans. Am. Soc. Artif. Intern. Organs **20**(B), 703–707 (1974)
38. Chetta, G.E., Lloyd, J.R.: The design, fabrication and evaluation of a trileaflet prosthetic heart valve. J. Biomech. Eng. **102**, 34–41 (1980)
39. Muller Jr, W.H., Warren, W.D., Dammann Jr, J.F., Beckwith, J.R., Wood Jr, J.E.: Surgical relief of aortic insufficiency by direct operation on the aortic valve. Circulation **21**, 587–597 (1960)
40. Braunwald, N.S., Morrow, A.G.: A late evaluation of flexible Teflon prostheses utilized for total aortic valve replacement. Postoperative clinical, hemodynamic, and pathological assessments. J. Thorac. Cardiovasc. Surg. **49**, 485–496 (1965)

41. Nistal, F., Garcia-Martinez, V., Arbe, E., Fernandez, D., Artinano, E., Mazorra, F., et al.: In vivo experimental assessment of polytetrafluoroethylene trileaflet heart valve prosthesis. J. Thorac. Cardiovasc. Surg. **99**, 1074–1081 (1990)
42. Ando, M., Takahashi, Y.: Ten-year experience with handmade trileaflet polytetrafluoroethylene valved conduit used for pulmonary reconstruction. J. Thorac. Cardiovasc. Surg. **137**, 124–131 (2009)
43. Chiappini, B., Sanchez, A., Noirhomme, P., Verhelst, R., Rubay, J., Poncelet, A., et al.: Replacement of chordae tendineae with polytetrafluoroethylene (PTFE) sutures in mitral valve repair: early and long-term results. J. Heart Valve Dis. **15**, 657–663; discussion 663 (2006)
44. Tomita, Y., Yasui, H., Iwai, T., Nishida, T., Tatewaki, H., Morita, S., et al.: Surgical application for a prolapse of the anterior mitral leaflet by replacing artificial chordae with polytetrafluoroethylene grafts. Surg. Today **35**, 812–818 (2005)
45. Coury, A., Slaikeu, P., Cahalan, P., Stokes, K.: Medical applications of implantable polyurethanes: current issues. Prog. Rubber Plast. Technol. **3**, 24–37 (1987)
46. Kidane, A.G., Burriesci, G., Edirisinghe, M., Ghanbari, H., Bonhoeffer, P., Seifalian, A.M.: A novel nanocomposite polymer for development of synthetic heart valve leaflets. Acta Biomater. **5**, 2409–2417 (2009)
47. Braunwald, E.: Nina Starr Braunwald: some reflections on the first woman heart surgeon. Ann. Thorac. Surg. **71**, S6–S7 (2001)
48. Boretos, J.W., Pierce, W.S.: Segmented polyurethane: a new elastomer for biomedical applications. Science **158**, 1481–1482 (1967)
49. Hilbert, S.L., Ferrans, V.J., Tomita, Y., Eidbo, E.E., Jones, M.: Evaluation of explanted polyurethane trileaflet cardiac valve prostheses. J. Thorac. Cardiovasc. Surg. **94**, 419–429 (1987)
50. Wisman, C.B., Pierce, W.S., Donachy, J.H., Pae, W.E., Myers, J.L., Prophet, G.A.: A polyurethane trileaflet cardiac valve prosthesis: in vitro and in vivo studies. Trans. Am. Soc. Artif. Intern. Organs **28**, 164–168 (1982)
51. Kütting, M., Roggenkamp, J., Urban, U., Schmitz-Rode, T., Steinseifer, U.: Polyurethane heart valves: past, present and future. Expert Rev. Med. Devices **8**, 227–233 (2011)
52. Ghista, D.N., Reul, H.: Optimal prosthetic aortic leaflet valve: design parametric and longevity analyses: development of the Avcothane-51 leaflet valve based on the optimum design analysis. J. Biomech. **10**, 313–324 (1977)
53. Jansen, J., Reul, H.: A synthetic three-leaflet valve. J. Med. Eng. Technol. **16**, 27–33 (1992)
54. Jansen, J., Willeke, S., Reiners, B., Harbott, P., Reul, H., Rau, G.: New J-3 flexible-leaflet polyurethane heart valve prosthesis with improved hydrodynamic performance. Int. J. Artif. Organs **14**, 655–660 (1991)
55. Daebritz, S.H., Fausten, B., Hermanns, B., Franke, A., Schroeder, J., Groetzner, J., et al.: New flexible polymeric heart valve prostheses for the mitral and aortic positions. Heart Surg. Forum **7**, E525–E532 (2004)
56. Daebritz, S.H., Fausten, B., Hermanns, B., Schroeder, J., Groetzner, J., Autschbach, R., et al.: Introduction of a flexible polymeric heart valve prosthesis with special design for aortic position. Eur. J. Cardiothorac. Surg. **25**, 946–952 (2004)
57. Daebritz, S.H., Sachweh, J.S., Hermanns, B., Fausten, B., Franke, A., Groetzner, J., et al.: Introduction of a flexible polymeric heart valve prosthesis with special design for mitral position. Circulation 108(Suppl 1):II134–II139 (2003)
58. Sachweh, J.S., Daebritz, S.H.: Novel "biomechanical" polymeric valve prostheses with special design for aortic and mitral position: a future option for pediatric patients? ASAIO J. **52**, 575–580 (2006)
59. Bernacca, G.M., Mackay, T.G., Gulbransen, M.J., Donn, A.W., Wheatley, D.J.: Polyurethane heart valve durability: effects of leaflet thickness and material. Int. J. Artif. Organs **20**, 327–331 (1997)
60. Bernacca, G.M., Mackay, T.G., Wilkinson, R., Wheatley, D.J.: Calcification and fatigue failure in a polyurethane heart value. Biomaterials **16**, 279–285 (1995)

61. Bernacca, G.M., Mackay, T.G., Wilkinson, R., Wheatley, D.J.: Polyurethane heart valves: fatigue failure, calcification, and polyurethane structure. J. Biomed. Mater. Res. **34**, 371–379 (1997)
62. Bernacca, G.M., O'Connor, B., Williams, D.F., Wheatley, D.J.: Hydrodynamic function of polyurethane prosthetic heart valves: influences of Young's modulus and leaflet thickness. Biomaterials **23**, 45–50 (2002)
63. Bernacca, G.M., Straub, I., Wheatley, D.J.: Mechanical and morphological study of biostable polyurethane heart valve leaflets explanted from sheep. J. Biomed. Mater. Res. **61**, 138–145 (2002)
64. Mackay, T.G., Wheatley, D.J., Bernacca, G.M., Fisher, A.C., Hindle, C.S.: New polyurethane heart valve prosthesis: design, manufacture and evaluation. Biomaterials **17**, 1857–1863 (1996)
65. Wheatley, D.J., Bernacca, G.M., Tolland, M.M., O'Connor, B., Fisher, J., Williams, D.F.: Hydrodynamic function of a biostable polyurethane flexible heart valve after six months in sheep. Int. J. Artif. Organs **24**, 95–101 (2001)
66. Wheatley, D.J., Raco, L., Bernacca, G.M., Sim, I., Belcher, P.R., Boyd, J.S.: Polyurethane: material for the next generation of heart valve prostheses? Eur. J. Cardiothorac. Surg. **17**, 440–448 (2000)
67. Butterfield, M., Wheatley, D.J., Williams, D.F., Fisher, J.: A new design for polyurethane heart valves. J. Heart Valve Dis. **10**, 105–110 (2001)
68. D'Souza, S.S., Butterfield, M., Fisher, J.: Kinematics of synthetic flexible leaflet heart valves during accelerated testing. J. Heart Valve Dis. **12,** 110–119; discussion 119–120
69. Chaffin, K., Buckalew, A., Schley, J., Chen, X., Jolly, M., Alketout, J., et al.: Influence of water on the structure and properties of PDMS-containing multiblock polyurethanes. Macromolecules **45**, 9110–9120 (2012)
70. Leo, H.L., Dasi, L.P., Carberry, J., Simon, H.A., Yoganathan, A.P.: Fluid dynamic assessment of three polymeric heart valves using particle image velocimetry. Ann. Biomed. Eng. **34**, 936–952 (2006)
71. Leo, H.L., Simon, H., Carberry, J., Lee, S.C., Yoganathan, A.P.: A comparison of flow field structures of two tri-leaflet polymeric heart valves. Ann. Biomed. Eng. **33**, 429–443 (2005)
72. Leat, M.E., Fisher, J.: A synthetic leaflet heart valve with improved opening characteristics. Med. Eng. Phys. **16**, 470–476 (1994)
73. Leat, M.E., Fisher, J.: The influence of manufacturing methods on the function and performance of a synthetic leaflet heart valve. Proc. Inst. Mech. Eng. H **209**, 65–69 (1995)
74. Clift, S.E., Fisher, J.: Finite element stress analysis of a new design of synthetic leaflet heart valve. Proc. Inst. Mech. Eng. H **210**, 267–272 (1996)
75. Ghanbari, H., Kidane, A.G., Burriesci, G., Ramesh, B., Darbyshire, A., Seifalian, A.M.: The anti-calcification potential of a silsesquioxane nanocomposite polymer under in vitro conditions: potential material for synthetic leaflet heart valve. Acta Biomater. **6**, 4249–4260 (2010)
76. Burriesci, G., Marincola, F.C., Zervides, C.: Design of a novel polymeric heart valve. J. Med. Eng. Technol. **34**, 7–22 (2010)
77. Rahmani, B., Tzamtzis, S., Ghanbari, H., Burriesci, G., Seifalian, A.M.: Manufacturing and hydrodynamic assessment of a novel aortic valve made of a new nanocomposite polymer. J. Biomech. **45**, 1205–1211 (2012)
78. Gallocher, S.L., Aguirre, A.F., Kasyanov, V., Pinchuk, L., Schoephoerster, R.T.: A novel polymer for potential use in a trileaflet heart valve. J. Biomed. Mater. Res. B Appl. Biomater. **79**, 325–334 (2006)
79. Pinchuk, L., Wilson, G.J., Barry, J.J., Schoephoerster, R.T., Parel, J.M., Kennedy, J.P.: Medical applications of poly(styrene-block-isobutylene-block-styrene) ("SIBS"). Biomaterials **29**, 448–460 (2008)
80. Yin, W., Gallocher, S., Pinchuk, L., Schoephoerster, R.T., Jesty, J., Bluestein, D.: Flow-induced platelet activation in a St. Jude mechanical heart valve, a trileaflet polymeric heart valve, and a St. Jude tissue valve. Artif. Organs **29**, 826–831 (2005)

81. Wang, Q., McGoron, A.J., Bianco, R., Kato, Y., Pinchuk, L., Schoephoerster, R.T.: In-vivo assessment of a novel polymer (SIBS) trileaflet heart valve. J. Heart Valve Dis. **19**, 499–505 (2010)
82. Claiborne, T.E., Girdhar, G., Gallocher-Lowe, S., Sheriff, J., Kato, Y.P., Pinchuk, L., et al.: Thrombogenic potential of Innovia polymer valves versus Carpentier-Edwards Perimount Magna aortic bioprosthetic valves. ASAIO J. **57**, 26–31 (2011)
83. Claiborne, T.E.: Optimization and Verification of a Novel Trileaflet Polymeric Prosthetic Heart Valve. Stony Brook University, Stony Brook (2012)
84. Claiborne, T.E., Sheriff, J., Kütting, M., Steinseifer, U., Slepian, M.J., Bluestein, D.: In vitro evaluation of a novel hemodynamically optimized trileaflet polymeric prosthetic heart valve. J. Biomech. Eng. **135**, 021021 (2013)
85. Claiborne, T.E., Xenos, M., Sheriff, J., Chiu, W.C., Soares, J., Alemu, Y., et al.: Toward optimization of a novel trileaflet polymeric prosthetic heart valve via device thrombogenicity emulation. ASAIO J. **59**, 275–283 (2013)
86. Cacciola, G., Peters, G.W., Baaijens, F.P.: A synthetic fiber-reinforced stentless heart valve. J. Biomech. **33**, 653–658 (2000)
87. Cacciola, G., Peters, G.W., Schreurs, P.J.: A three-dimensional mechanical analysis of a stentless fibre-reinforced aortic valve prosthesis. J. Biomech. **33**, 521–530 (2000)
88. Jiang, H., Campbell, G., Boughner, D., Wan, W.K., Quantz, M.: Design and manufacture of a polyvinyl alcohol (PVA) cryogel tri-leaflet heart valve prosthesis. Med. Eng. Phys. **26**, 269–277 (2004)
89. Mohammadi, H.: Nanocomposite biomaterial mimicking aortic heart valve leaflet mechanical behaviour. Proc. Inst. Mech. Eng. H **225**, 718–722 (2011)
90. Mohammadi, H., Boughner, D., Millon, L.E., Wan, W.K.: Design and simulation of a poly(vinyl alcohol)-bacterial cellulose nanocomposite mechanical aortic heart valve prosthesis. Proc. Inst. Mech. Eng. H **223**, 697–711 (2009)
91. Mohammadi, H., Mequanint, K.: Prosthetic aortic heart valves: modeling and design. Med. Eng. Phys. **33**, 131–147 (2011)
92. Thunberg, C.A., Gaitan, B.D., Arabia, F.A., Cole, D.J., Grigore, A.M.: Ventricular assist devices today and tomorrow. J. Cardiothorac. Vasc. Anesth. **24**, 656–680 (2010)
93. Garbade, J., Bittner, H.B., Barten, M.J., Mohr, F.W.: Current trends in implantable left ventricular assist devices. Cardiol. Res. Pract. **2011**, 290561 (2011)
94. Zimmerman, H., Covington, D., Smith, R., Copeland, J.: Mechanical support and medical therapy reverse heart failure in infants and children. Artif. Organs **34**, 885–890 (2010)
95. Drews, T., Loebe, M., Hennig, E., Kaufmann, F., Muller, J., Hetzer, R.: The 'Berlin Heart' assist device. Perfusion **15**, 387–396 (2000)
96. Hetzer, R., Alexi-Meskishvili, V., Weng, Y., Hubler, M., Potapov, E., Drews, T., et al.: Mechanical cardiac support in the young with the Berlin Heart EXCOR pulsatile ventricular assist device: 15 years' experience. Semin. Thorac. Cardiovasc. Surg. Pediatr. Card. Surg. Annu. **9**, 99–108 (2006)
97. Thuaudet, S.: The Medos ventricular assist device system. Perfusion **15**, 337–343 (2000)
98. Mecora® Medizintechnik Aachen. http://www.mecora.de/en/Produkte/Produkte.html Accessed 28 June 2013.
99. Arabia, F.A., Tsau, P.H., Smith, R.G., Nolan, P.E., Paramesh, V., Bose, R.K., et al.: Pediatric bridge to heart transplantation: application of the Berlin Heart, Medos and Thoratec ventricular assist devices. J. Heart Lung Transplant. **25**, 16–21 (2006)
100. Bermudez, C., Minakata, K., Kormos, R.: Options for advanced mechanical support for cardiogenic shock complicating cardiac reoperations. In: Schaff, H., Svenson, L., Machiraju, V. (eds.) Redo Cardiac Surgery in Adults, 2nd edn, pp. 73–74. Springer, New York (2012)
101. Anderson, M., Smedira, N., Samuels, L., Madani, M., Naka, Y., Acker, M., et al.: Use of the AB5000 ventricular assist device in cardiogenic shock after acute myocardial infarction. Ann. Thorac. Surg. **90**, 706–712 (2000)
102. Morris, R.J.: Total artificial heart—concepts and clinical use. Semin. Thorac. Cardiovasc. Surg. **20**, 247–254 (2008)

103. Gray Jr, N.A., Selzman, C.H.: Current status of the total artificial heart. Am. Heart J. **152**, 4–10 (2006)
104. Bernstein, O., Haddy, S.: Three-dimensional transesophageal echocardiography of a Medtronic Hall-type tilting disk valve. Echocardiography **29**, E129–E130 (2012)
105. Reuters.: UPDATE 1-Aortech licenses heart valve to SynCardia (2009)
106. Samuels, L.E., Holmes, E.C., Garwood, P., Ferdinand, F.: Initial experience with the Abiomed AB5000 ventricular assist device system. Ann. Thorac. Surg. **80**, 309–312 (2005)
107. Ward, R.S., Nyilas, E.: Production of biomedical polymers I: Silicone/urethane synergy in avcothane elastomers. In: Carraher, C.E. Jr. (ed.) Organometallic Polymers, pp. 219–222. Academic Press, Salt Lake (1978)
108. Imachi, K., Fujimasa, I., Mabuchi, K., Chinzei, T., Abe, Y., Maeda, K., et al.: A newly designed jellyfish valve for an artificial heart blood pump. ASAIO Trans. **34**, 726–728 (1988)
109. Imachi, K., Mabuchi, K., Chinzei, T., Abe, Y., Imanishi, K., Suzukawa, M., et al.: Blood compatibility of the jellyfish valve without anticoagulant. ASAIO Trans. **37**, M220–M222 (1991)
110. Iwasaki, K., Umezu, M., Imachi, K., Iijima, K., Fujimoto, T.: Design improvement of the jellyfish valve for long-term use in artificial hearts. Int. J. Artif. Organs **24**, 463–469 (2001)
111. Iwasaki, K., Umezu, M., Iijima, K., Imachi, K.: Implications for the establishment of accelerated fatigue test protocols for prosthetic heart valves. Artif. Organs **26**, 420–429 (2002)
112. Kolff, W.J., Yu, L.S.: The return of elastomer valves. Ann. Thorac. Surg. **48**, S98–S99 (1989)
113. Sacristan, E., Corona, F., Suarez, B., Rodriguez, G., Duenas, B., Gorzelewski, A., et al.: Development of a universal second generation pneumatic ventricular assist device and drive unit. In: Proceedings of the 25th Annual International Conference of the IEEE, pp. 427–430 (2003)
114. Garcia, J., Sacristan, E.: Trileaflet valve hydrodynamic resistance assessment. Conf. Proc. IEEE Eng. Med. Biol. Soc. **2008**, 1393–1396 (2008)
115. Garcia, J., Kadem, L., Pibarot, P.: Silicone rubber trileaflet valve assessment using cardiovascular magnetic resonance imaging. Conf. Proc. IEEE Eng. Med. Biol. Soc. **2010**, 5169–5172 (2010)
116. Kiraly, R., Yozu, R., Hillegass, D., Harasaki, H., Murabayashi, S., Snow, J., et al.: Hexsyn trileaflet valve: application to temporary blood pumps. Artif. Organs **6**, 190–197 (1982)
117. Hollman, A.: An early percutaneous catheter-mounted valve. Heart **97**, 1596 (2011)
118. Cribier, A.: Development of transcatheter aortic valve implantation (TAVI): a 20-year odyssey. Arch. Cardiovasc. Dis. **105**, 146–152 (2012)
119. Rowe, S., Bash, B.: Edwards in Israel: how it all began. Innovations in cardiovascular interventions. Tel Aviv, Israel (2012)
120. Attmann, T., Steinseifer, U., Cremer, J., Lutter, G.: Percutaneous valve replacement: a novel low-profile polyurethane valved stent. Eur. J. Cardiothorac. Surg. **30**, 379 (2006)
121. Metzner, A., Iino, K., Steinseifer, U., Uebing, A., de Buhr, W., Cremer, J., et al.: Percutaneous pulmonary polyurethane valved stent implantation. J. Thorac. Cardiovasc. Surg. **139**, 748–752 (2010)
122. Sochman, J., Peregrin, J.H., Pavcnik, D., Timmermans, H., Rosch, J.: Percutaneous transcatheter aortic disc valve prosthesis implantation: a feasibility study. Cardiovasc. Intervent. Radiol. **23**, 384–388 (2000)
123. Hashimoto, M., Kaminou, T., Ohuchi, Y., Nakamura, K., Sugiura, K., Adachi, A., et al.: Development of a re-positionable aortic stent-valve: a preliminary study in swine. J. Interv. Cardiol. **21**, 432–440 (2008)
124. Claiborne, T.E., Bluestein, D., Schoephoerster, R.T.: Development and evaluation of a novel artificial catheter-deliverable prosthetic heart valve and method for in vitro testing. Int. J. Artif. Organs **32**, 262–271 (2009)

125. Kuan, Y., Dasi, L., Yoganathan, A.P., Leo, H.: Recent advances in polymeric heart valve research. Int. J. Biomater. Res. Eng. **1**, 1–17 (2011)
126. Ghista, D.N.: Toward an optimum prosthetic trileaflet aortic-valve design. Med. Biol. Eng. **14**, 122–129 (1976)
127. Thubrikar, M.J.: The Aortic Valve. CRC Press, Boca Raton (1990)
128. Mercer, J.L., Benedicty, M., Bahnson, H.T.: The geometry and construction of the aortic leaflet. J. Thorac. Cardiovasc. Surg. **65**, 511–518 (1973)
129. Hamid, M.S., Sabbah, H.N., Stein, P.D.: Influence of stent height upon stresses on the cusps of closed bioprosthetic valves. J. Biomech. **19**, 759–769 (1986)
130. Chong, P., Wieting, D., Hwang, H., Kennedy, J.: Stress analysis of normal human aortic valve leaflets during diastole. Artif. Cells Blood Substit. Biotechnol. **1**, 307–321 (1973)
131. Kim, I., Kim, J., Jung, D., Kim, C.S., Min, B.G.: Development of polymer prosthetic heart valve—fabrication and in vitro test. Seoul J. Med. **32**, 35–42 (1991)
132. Lockie, K.J., Butterfield, M., Fisher, J., Juster, N.P., Watterson, K., Davies, G.A.: Geometry of homograft valve leaflets: effect of dilation of the aorta and the aortic root. Ann. Thorac. Surg. **56**, 125–130 (1993)
133. Swanson, M., Clark, R.E.: Dimensions and geometric relationships of the human aortic valve as a function of pressure. Circ. Res. **35**, 871–882 (1974)
134. Vesely, I.: The evolution of bioprosthetic heart valve design and its impact on durability. Cardiovasc. Pathol. **12**, 277–286 (2003)
135. Peskin, C.S., McQueen, D.M.: Mechanical equilibrium determines the fractal fiber architecture of aortic heart valve leaflets. Am. J. Physiol. **266**, H319–H328 (1994)
136. Mohammadi, H., Bahramian, F., Wan, W.: Advanced modeling strategy for the analysis of heart valve leaflet tissue mechanics using high-order finite element method. Med. Eng. Phys. **31**, 1110–1117 (2009)
137. Gallocher, S.: Durability Assessment of Polymer Trileaflet Heart Valves. Florida International University, Miami (2007)
138. Iwasaki, K., Umezu, M., Iijima, K., Inoue, A., Imachi, K., Ye, C.X.: Development of a polymer bileaflet valve to realize a low-cost pulsatile blood pump. Artif. Organs **27**, 78–83 (2003)
139. Imachi, K., Mabuchi, K., Chinzei, T., Abe, Y., Imanishi, K., Yonezawa, T., et al.: In vitro and in vivo evaluation of a jellyfish valve for practical use. ASAIO Trans. **35**, 298–301 (1989)
140. Smock, D.: Polycarbonate-urethane provides toughness for implanted valve. Plastics Today (2012)
141. Reade, L.: Nanocages for flexible heart valves. Materials World Magazine (2009)
142. Escobedo, C., Tovar, F., Vila, A., Garcia, J., Suarez, B., Corona, F., et al.: Hydrodynamic effects of the partial opening of a trileaflet valve. Conf. Proc. IEEE Eng. Med. Biol. Soc. **1**, 2896–2899 (2006)
143. Sperati, C.A.: Fluorocarbon polymers, polytetrafluoroethylene (PTFE). In: Rubin, I.I. (ed.) Handbook of Plastic Materials and Technology, pp. 117–129. Wiley, New York (1990)
144. Coury, A., Stokes, K., Cahalan, P., Slaikeu, P.: Biostability considerations for implantable polyurethanes. Life Support Syst. **5**, 25–39 (1987)
145. Bezuidenhout, D., Zilla, P.: Vascular grafts. In: Wnek, G., Bowlin, G. (eds.) Encyclopaedia of Biomaterials and Biomedical Engineering. Marcel Dekker, New York (2004)
146. Imamura, E., Kaye, M.P.: Function of expanded-polytetrafluoroethylene laminated trileaflet valves in animals. Mayo Clin. Proc. **52**, 770–775 (1977)
147. Imamura, E., Kaye, M.P., Davis, G.D.: Radiographic assessment of leaflet motion of Gore-Tex laminate trileaflet valves and Hancock xenograft in tricuspid position of dogs. Circulation **56**, 1053–1058 (1977)
148. Ando, M., Imai, Y., Takanashi, Y., Hoshino, S., Seo, K., Terada, M.: Fate of trileaflet equine pericardial extracardiac conduit used for the correction of anomalies having pulmonic ventricle-pulmonary arterial discontinuity. Ann. Thorac. Surg. **64**, 154–158 (1997)

149. Whiffen, J.D., Young, W.P., Gott, V.L.: Stability of the thrombus-resistant graphite-benzalkonium-heparin surface in an anti-heparin environment. J. Thorac. Cardiovasc. Surg. **48**, 317–322 (1964)
150. Bernacca, G.M., Wheatley, D.J.: Surface modification of polyurethane heart valves: effects on fatigue life and calcification. Int. J. Artif. Organs **21**, 814–819 (1998)
151. Han, D.K., Park, K., Park, K.D., Ahn, K.D., Kim, Y.H.: In vivo biocompatibility of sulfonated PEO-grafted polyurethanes for polymer heart valve and vascular graft. Artif. Organs **30**, 955–959 (2006)
152. Kim, Y.H., Han, D.K., Park, K.D., Kim, S.H.: Enhanced blood compatibility of polymers grafted by sulfonated PEO via a negative cilia concept. Biomaterials **24**, 2213–2223 (2003)
153. Pedersen, C.: Cyclic polyethers and their complexes with metal salts. J. Am. Chem. Soc. **89**, 7017–7036 (1967)
154. Hamon, R.F., Khan, A.S., Chow, A.: The cation-chelation mechanism of metal-ion sorption by polyurethanes. Talanta **29**, 313–326 (1982)
155. Harasaki, H., Gerrity, R., Kiraly, R., Jacobs, G., Nose, Y.: Calcification in blood pumps. Trans. Am. Soc. Artif. Intern. Organs **25**, 305–310 (1979)
156. Alferiev, I., Stachelek, S.J., Lu, Z., Fu, A.L., Sellaro, T.L., Connolly, J.M., et al.: Prevention of polyurethane valve cusp calcification with covalently attached bisphosphonate diethylamino moieties. J. Biomed. Mater. Res. A **66**, 385–395 (2003)
157. Alferiev, I., Vyavahare, N., Song, C., Connolly, J., Hinson, J.T., Lu, Z., et al.: Bisphosphonate derivatized polyurethanes resist calcification. Biomaterials **22**, 2683–2693 (2001)
158. Whalen, R.L., Snow, J.L., Harasaki, H., Nose, Y.: Mechanical strain and calcification in blood pumps. Trans. Am. Soc. Artif. Intern. Organs **26**, 487–492 (1980)
159. Imachi, K., Chinzei, T., Abe, Y., Mabuchi, K., Matsuura, H., Karita, T., et al.: A new hypothesis on the mechanism of calcification formed on a blood-contacted polymer surface. J. Artif. Organs **4**, 74–82 (2001)
160. Levy, R.J., Wolfrum, J., Schoen, F.J., Hawley, M.A., Lund, S.A., Langer, R.: Inhibition of calcification of bioprosthetic heart valves by local controlled-release diphosphonate. Science **228**, 190–192 (1985)
161. Joshi, R.R., Frautschi, J.R., Phillips Jr, R.E., Levy, R.J.: Phosphonated polyurethanes that resist calcification. J. Appl. Biomater. (an official journal of the Society for Biomaterials) **5**, 65–77 (1994)
162. Vyavahare, N., Chen, W., Joshi, R., Lee, C.-H., Hirsch, D., Levy, J.G., et al.: Current progress in anticalcification for bioprosthetic and polymeric heart valves. Cardiovasc. Pathol. **6**, 219–229 (1997)
163. Stachelek, S.J., Alferiev, I., Choi, H., Kronsteiner, A., Uttayarat, P., Gooch, K.J., et al.: Cholesterol-derivatized polyurethane: characterization and endothelial cell adhesion. J. Biomed. Mater. Res. A **72**, 200–212 (2005)
164. Stachelek, S.J., Alferiev, I., Connolly, J.M., Sacks, M., Hebbel, R.P., Bianco, R., et al.: Cholesterol-modified polyurethane valve cusps demonstrate blood outgrowth endothelial cell adhesion post-seeding in vitro and in vivo. Ann. Thorac. Surg. **81**, 47–55 (2006)

Aortic Biological Prosthetic Valve for Open-Surgery and Percutaneous Implant: Procedure Simulation and Performance Assessment

Ferdinando Auricchio, Michele Conti and Simone Morganti

Abstract Valvular heart disorders represent a remarkable contribution to cardiovascular diseases; in fact, more than 300,000 heart valve surgical operations were performed in 2006 worldwide. Such a huge social and economical problem calls for a dedicated multidisciplinary research, integrating different scientific fields, from medicine to engineering, along the various clinical steps, from diagnosis to treatment strategy. In particular, new manufacturing technologies and advanced materials are contributing to innovative devices for the replacement of aortic valves through minimally-invasive procedures, emerging as a valid alternative to classical open-chest surgery. Design, development and performance assessment of such devices are the natural field of application of computational biomechanics, which investigates the mechanical behaviour of biological systems and their interaction with artificial implants through the principle of mechanics. Moving from such considerations, we discuss from a biomechanical perspective the *biological* prostheses replacing the native aortic valve and implanted either through open-surgery or percutaneous procedures. Consequently, we focus on the use of patient-specific finite element analysis (FEA) to assess the structural performance of (i) a stentless biological prosthesis used for aortic valve replacement (AVR) and (ii) a transcatheter aortic valve implant (TAVI), where a biological valve sewn inside a stent, is crimped and properly placed in the patient's heart by means of an endovascular procedure. From a more general point of view, our contribution underlines the potential role of computational biomechanics and realistic computer-based simulations in the surgical procedure planning, moving through a new paradigm in medicine which aims at reinforcing "diagnosis" with "prediction".

F. Auricchio · M. Conti · S. Morganti (✉)
Department of Civil Engineering and Architecture, Pavia University,
Via Ferrata 3, 27100 Pavia, Italy
e-mail: simone.morganti@unipv.it

Stud Mechanobiol Tissue Eng Biomater (2014) 15: 131–168
DOI: 10.1007/8415_2013_161

Published Online: 7 July 2013

1 Introduction

Cardiovascular diseases (CVDs) is the generic name given to dysfunctions of the cardiovascular system such as hypertension, coronary heart disease, heart failure or stroke. CVDs are the leading cause of death in Western countries; a recent report of American Heart Association [93] states that an estimated 82,600,000 American adults (>1 in 3) have 1 or more types of CVDs. This well explains the high incidence of such pathologies, which lead to high social and economical costs; for example, the estimated direct and indirect cost of CVDs for 2007 was $286.6 billions [111].

Even though often underestimated, valvular heart disorders represent a remarkable contribution to CVDs: nearly 30 % of all adults over 65 have a sclerotic aortic valve (AV), 10 % of which having accompanying stenosis [81]. More than 300,000 heart valve surgical operations were performed in 2006 worldwide [83]. Such a huge social and economical problem calls for a dedicated multidisciplinary research integrating different scientific fields, from medicine to engineering, along the various clinical steps, from the diagnosis to treatment strategy. This observation is particularly meaningful if we consider the influence of emerging technologies in both diagnosis and treatment of CVDs; modern techniques for generation and analysis of medical images allows accurate 3D reconstruction of several organs, the use of innovative materials to design miniaturized devices increases the number of interventional options adding new minimally-invasive procedures to classical open-heart surgery. Design, development and performance assessment of the devices used in these procedures are natural fields of application of computational biomechanics. The evolution of computational science has enabled the study of biomedical problems and structures, which are characterized by complex geometries, heterogeneous materials and whose functionality is determined by multiple concomitant factors. All these aspects may contribute to progressive advances in medicine enabling a change in its paradigm.

In fact, although surgeon's experience is still the key factor for disease classification and treatment planning, statistics is the principal way to establish whether a specific medical remedy is appropriate or not for a given case; the high inter-variability requires specific surgical procedures and prosthetic devices tailored to each specific patient, especially in pathologic situations where physiological and morphological alterations are severe. For example, Tyrone-David, one of the most well-known expert of AV surgery and father of the AV sparing technique, stated that like most reconstructive procedures in cardiac surgery, the actual performance of the operation remains "more art than science" [30]. In this context, surgeon skills could be supported by predictive information and data derived by dedicated computational analyses. This concept can be referred to as *predictive* medicine in which realistic computer-based simulations are performed both to evaluate the efficacy of different possible treatments and to tailor surgical

solutions based on patient-specific data, leading to a new paradigm in medicine which aims at reinforcing diagnosis with prediction.

Obviously, in order to achieve such a challenging goal, a multidisciplinary approach, derived from a close collaboration between engineers and physicians, is necessary.

In this chapter we expand on the previous considerations through the biomechanical analysis of the *biological* prostheses used for the replacement of native AV either through open-surgery or percutaneous procedures. In particular, we focus on the use of patient-specific finite element analysis (FEA) to assess the structural performance of (i) stentless biological prosthesis used for aortic valve replacement (AVR) and (ii) transcatheter aortic valve implant (TAVI).

Before discussing these specific applications, we briefly review the biomechanical features of the aortic root, proposing also an overview of the past finite element studies addressing the AV structural mechanics from different points of view.

2 Aortic Valve Mechanics

Realistic computer-based simulations require an understanding of the AV structure. In fact, it is well-recognized that AV function depends on complex relationship of AV and root, as demonstrated by Kunzelman et al. [67], who examined the AV structure in cryo-preserved normal adult human specimens. For this reason, the study of both valve histology, from a micro-structural point of view, and anatomy, from a macro-structural point of view, as well as the study of valve physiology and pathology, are basic requirements for a computational investigation of AV functions.

2.1 Structure

From a macro-functional point of view, heart and large blood arteries can be over simplified into two serial elements, the pulmonary circulatory system and the systemic circulatory system, driven respectively by the right ventricle and the left ventricle acting as pumps. Hidden behind such an apparent simplicity, the micro-functionality of each component is extremely sophisticated. In particular, the aortic root is a complex body region where anatomical structures and physiology are related. In terms of basic functional elements [97], the aortic root is composed by:

- sinotubular junction (STJ);
- Valsalva sinuses;
- interleaflet triangles;
- ventriculoaortic junction (VAJ);
- leaflets and commissures.

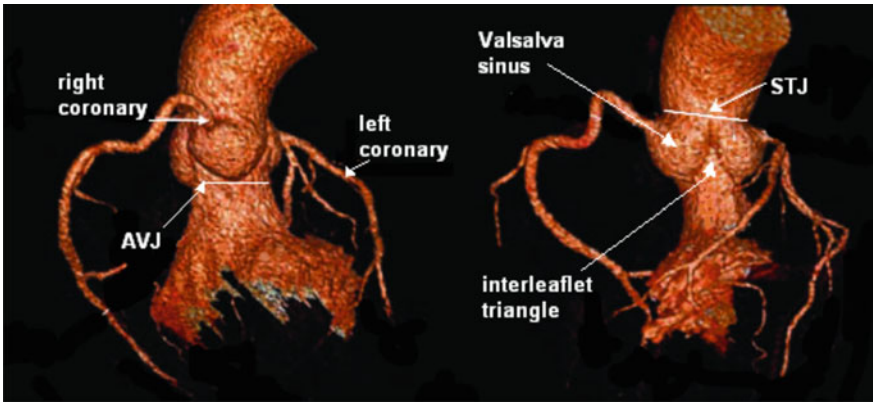

Fig. 1 Two different view of the 3D anatomy of the aortic root reconstructed from CTA and highlighting its main functional elements (adapted from [97])

In the following, we discuss each functional element highlighting its biomechanical role within the aortic root functionality.

2.1.1 Sinotubular Junction

The sinotubular junction (STJ) is a circular ring which separates the tubular portion of the ascending aorta from the aortic root (see Fig. 1). It lies at the level of the commissural apices and provides most of the support for the valve cusps and commissures. For this reason, its integrity is essential for the proper function of the valve as demonstrated by Thubrikar et al. [114].

STJ is a circular structure of primarily elastic composition, but with important collagenous supports for the valvar leaflets [110]. It has been demonstrated that STJ has a key-role in normal aortic valve behavior and that its pathological dilation significantly compromise aortic valve performance [114].

2.1.2 Valsalva Sinuses

Blood is supplied to the heart by its own vascular system, called coronary circulation; the right and left coronary arteries originate from two of the three Valsalva sinuses, which are dilations just above the AV. They are named, as the leaflets, according to the coronary arteries: left coronary, right coronary and noncoronary. In fact, the inlets to the coronary artery system can be found within the sinuses of Valsalva, superior to the leaflet attachments and inferior to the STJ. The two openings in the aortic sinus that mark the origin of the (left and right) coronary arteries are named ostia.

The Valsalva sinuses play a key role in the local hemodynamic forces that exert their effects on both leaflet motion and coronary flow; they generate a cavity behind the open leaflets preventing occlusion of the coronary orifices. Such a cavity favours the generation of "eddy currents", described first by Leonardo da Vinci and additionally supported by Henderson and Johnson [58]. The sinuses are also important in transmitting the stress from the leaflets to the aortic wall [112].

The histological composition of Valsalva sinuses resembles the structure of large arteries: the *intima* is made up of the endothelium attached to a basement membrane and a thin layer of connective tissue; the *media* is formed by layers of smooth muscle cells scattered with elastic lamellae; the *adventitia* consists mainly of loose connective tissue with some smooth muscle cells.

The biomechanical properties of Valsalva sinuses remain largely unknown, especially due to the fact that measuring their behavior is more challenging due to the non-planar nature of the tissue. Only recently, Martin et al. (2011) tested human aortic sinuses and compared their behavior with the one exhibited by porcine specimens [78]. As the AV leaflets, the Valsalva sinuses show a nonlinear stress-strain behavior in the circumferential and longitudinal directions.

2.1.3 Interleaflet Triangles

Beneath the apices formed by the lines of attachment of the leaflets to the aortic wall, the fibrous components of the aortic root exist. Although these areas are unequivocally a part of the aortic root, they are triangular extensions of the left ventricle outflow tract. Such areas, bounded by the semilunar attachments of the leaflets, are named interleaflet triangles, which have different characteristics from a microscopic point of view [97]:

- the triangle between the left and right coronary cusps is partially constituted of myocardial tissue;
- the triangle between the right coronary and noncoronary cusps is composed of a fibrous tissue and contains the atrioventricular bundle of the conduction axis;
- the triangle between the noncoronary and left cusps is only made of fibrous tissue.

2.1.4 Ventriculoaortic Junction

Ventriculoaortic junction (VAJ) is composed of the cusp bases and the interleaflet triangles; the planar line passing through the inferior point of the attachment line of each leaflet and through the basis of each interleaflet triangle represents the ideal ring that is considered the so-called *aortic annulus*, routinely measured by imaging techniques. All structures that are distal (with reference to the heart) to the aorto-ventricular junction are subjected to arterial pressures, whereas those that are

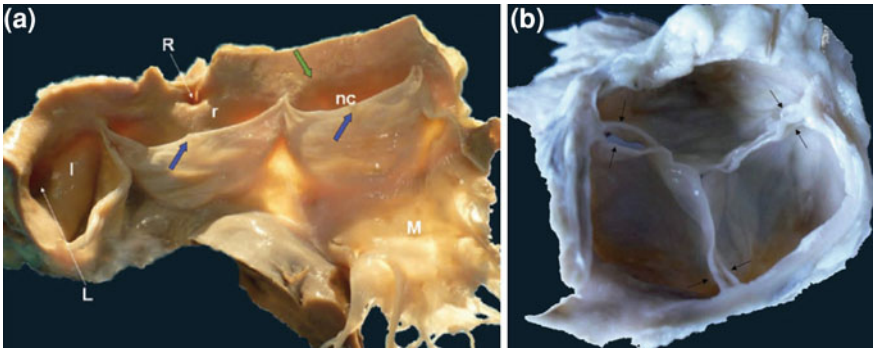

Fig. 2 Aortic leaflets: **a** The aortic root cut between the noncoronary sinus (nc) and the left coronary sinus (l). *Blue arrows* indicate the Arantius nodulus; *green arrow* indicates how the sinotubular ridge appears on the internal face of the root. **b** View of the aortic root from the ascending aorta. The picture highlights the coaptation between of leaflets avoiding the regurgitation during the diastolic phase; *arrows* indicate commissures. Both pictures are adapted from [97]

proximal are subjected to ventricular loads. Regarding the histology of the VAJ, collagen is dense at the hinge point that constitutes the semilunar contour of the leaflet attachment.

2.1.5 Leaflets and Commissures

Normal aortic valves have three semilunar leaflets (or cusps) (see Fig. 2a), which are the most mobile parts of the valve since they open and close during the cardiac cycle. They are very thin and flexible so that they may come together to seal the valve orifice during diastole and avoid retrograde blood flow from the aorta to the ventricle. During the diastolic phase, each leaflet coapts against the other two leaflets; the area of the cusps in contact is called *coaptation area* which should not be considered redundant since it does bear a load. The only free boundary of the leaflet, which is also the distal boundary of the coaptation surface, is called *free margin* or *free edge* of the leaflet, clearly visible in Fig. 2b.

The free margin of each cusp shows a central corpus called *nodule of Arantius*. The aortic leaflets are named in relation to the coronary arteries: left coronary, right coronary and noncoronary. The latter is usually larger than the other two cusps.

The aortic leaflets are composed of three layers, the *ventricularis* and the *fibrosa* separated by a gelatinous *spongiosa* (see Fig. 3a). The ventricularis faces the left ventricular chamber and it is composed of radially aligned elastin fibers and collagen fibers randomly distributed. The spongiosa mainly consists of glicosaminoglycans, proteoglycans and mucopolysaccharides that give it a soft consistency together with loosely arranged collagen fibers. Finally, the fibrosa consists of

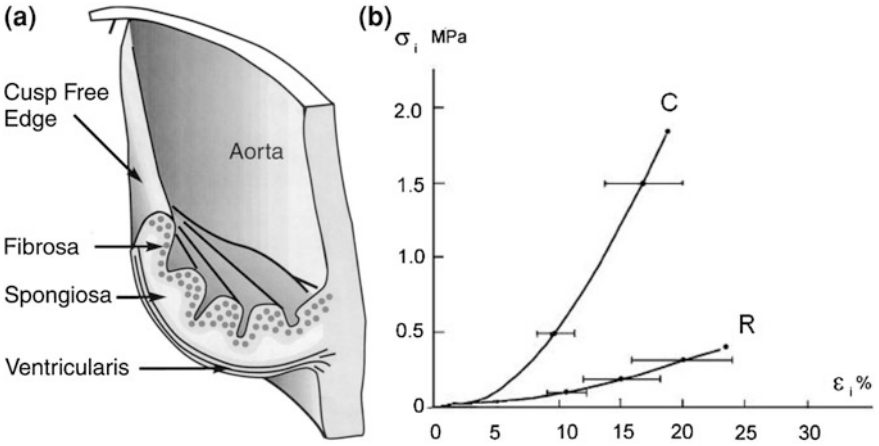

Fig. 3 Aortic leaflets: **a** a cutaway view of the three layers (adapted from [120]); **b** mechanical behavior of aortic leaflets: the stress-strain curve obtained by testing human specimens in circumferential (C) and radial (R) direction is represented (adapted from [106])

collagen fibers embedded in an elastin matrix and highly oriented in the circumferential direction, i.e., parallel to the annulus. Such a structural arrangement makes the fibrosa considerably stiffer in the circumferential direction giving to the leaflet the ability to withstand high cyclic mechanical loads [33]. The fibrosa and ventricularis are preloaded by virtue of their attachment to each other; the fibrosa under compression and the ventricularis under tension [120]. In general, the valve cusps contain about 50 % collagen and only 13 % elastin by dry weight [11]. Even though this would suggest that, with respect to collagen, the contribution of elastin to valve leaflet mechanics is minimal, during diastolic loading, there is considerable realignment of collagen fibers as the cusps extend beyond 50 % strain and recoil elastically. Since collagen on its own is not highly elastic, it has been hypothesized that AV elastin is responsible for their elastic recoil. This implies that collagen extends passively through most of its elongation phase.

Most of biomechanical measurements of the heart valve leaflets have been performed by means of uniaxial tests. However, biaxial tests are preferable since the effects of multiaxial collagen fiber distributions remain intact and testable. Generally, AV cusps show non-linear behavior, different in circumferential and radial directions. In Fig. 3b, the mechanical behavior of human aortic leaflet tissue is represented in terms of stress-strain relationship [106]. At the beginning of the loading of samples at low stress, the tissue extends very compliantly. During loading the wavy structure of the tissue becomes straight, more fibers are recruited and, with increasing stress, the strain of the tissue decreases drastically. The high compliance at low strains and the high stiffness at high strains enables the tissue to be optimally flexible during systole and rigid during diastole [17].

Leaflet commissures are formed by the mural regions where two leaflets insert side by side along parallel lines [112] (see Fig. 2). Hence, the commissures are the zones of apposition between the leaflets of the AV [110].

2.2 Dynamics

The complex structure of the aortic root is always in motion due to the pumping action of the heart. The AV opens during systole, when the ventricle is contracting and, then, closes during diastole, as the ventricle relaxes. During such motion, the leaflets are not the only actors but all the surrounding structures and valvular components interact in a complex but functionally efficient manner.

AV dynamics has been studied using different techniques: either injecting a radiopaque dye and visualizing the movement under X-ray [104] or by means of two-dimensional echocardiography [49] or using marker-fluoroscopy technique [113]. Moreover, valve motion has been also studied *in vitro* using pulse-duplicator systems [79]. AV opens rapidly at the beginning of systole and closes rapidly at the end of systole. The consecutive phases of AV motion during a cardiac cycle can be summarized as follows: a sudden opening of the valve, just a little movement while the valve remains open, a sudden closure of the valve and almost no movement while the valve remains closed (see Fig. 4).

Although the leaflets are the most flexible and dynamic parts, the motions of the other components of the AV are also important. Thubrikar et al. (1986) studied the movement of the commissures in dogs by placing radiopaque markers at appropriate positions of the aortic root and recording their movement under X-ray [113]. The commissures move outward during systole and inward during diastole. As depicted in Fig. 5, the commissure motion follows the aortic pressure curve closely. They measured the perimeter of a triangle formed by the commissural markers, recording an increase from diastole to systole of about 12 %. During the cardiac cycle, the AV annulus expands and contracts, too; both echocardiographic and angiographic images show that the base of the aortic valve changes diameter and dimensions during the cardiac cycle. It is maximally dilated during valve opening and maximally contracted at the time of valve closure; the percentage of change in base perimeter is approximately 20 %.

2.3 Pathologies

As previously mentioned, AV function has been shown to depend on the complex anatomic and dynamic relationship of aortic valve and root. As a consequence, any morphological, structural and histological alterations of valve components may lead to valve dysfunction. Even though there are several diseases which can cause malfunctioning of aortic valves, we distinguish two main families of

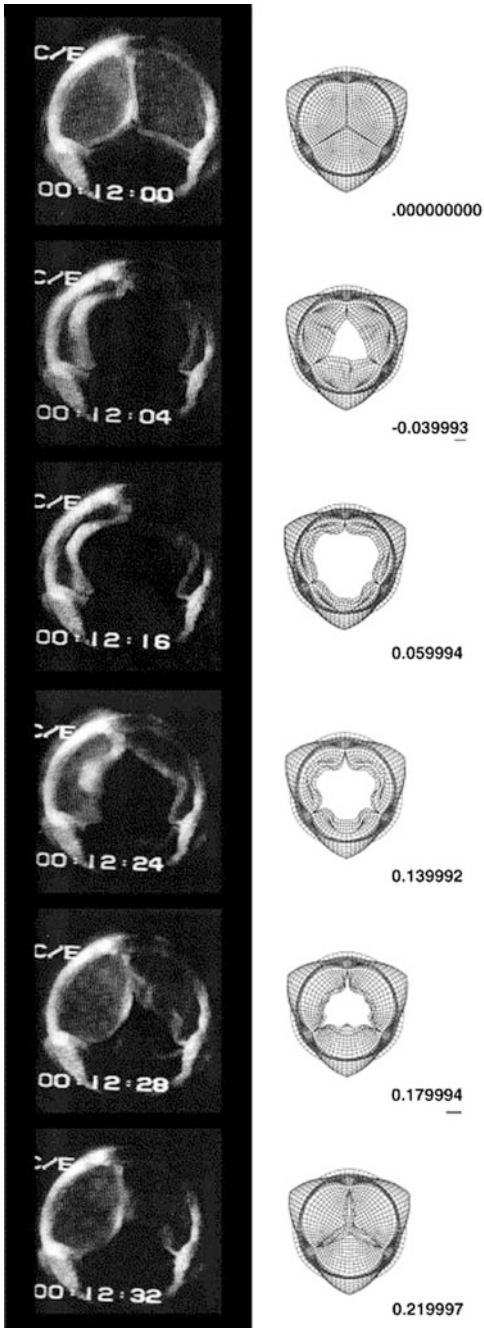

Fig. 4 Sequence of snapshots of a human aortic valve displacements at selected instants in the cardiac cycle (adapted from [20])

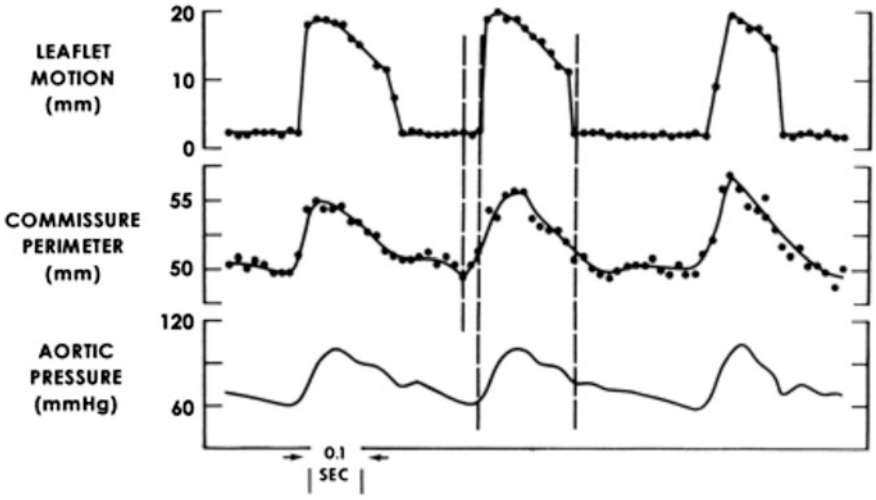

Fig. 5 Aortic valve dynamics: plot of the leaflet motion, commissural perimeter and pressure in the ascending aorta (adapted from [112])

AV pathologies: (i) stenosis, i.e., restricted opening, producing pressure overloading and (ii) regurgitation, i.e., inadequate valve closure inducing volume overloading.

2.3.1 Aortic Valve Stenosis

Aortic stenosis refers to an obstruction of flow at the level of the AV; in particular, there are mainly three causes of stenosis: (i) calcifications related to atherosclerosis, which can be roughly defined as an inflammatory disease impairing valve patency; (ii) endocarditis, that is an infection caused by the presence of bacteria in the bloodstream and bacterial vegetations on valve leaflets; (iii) congenital diseases and, in particular, bicuspid aortic valve, which consists in the fusion of two leaflets.

Congenital bicuspid aortic valve and calcific aortic occlusion account for the majority of aortic stenosis cases [63, 111]. Bicuspid valves are characterized by the fusion of two of the three leaflets, most commonly the left and right, and they present raphe, leaflet doming and eccentric closure under echocardiography; its incidence varies from about 0.4 to 2.25 % [59]. According to the work by Stewart et al. (1997), calcific aortic stenosis, usually referred to as "degenerative" pathology, affects, approximately 25 % of the population older than 65. For these patients, echocardiography showed leaflet thickening or calcification, or both, and the prevalence increased with advancing age [105].

In this case, aortic valve replacement through open-surgery represents the most common surgical remedy; either biological valves or mechanical valves may be used to replace the stenotic native valve; for elderly patients, innovative

transcatheter aortic valves, which do not require open-heart surgery and cardiopulmonary bypass, may be implanted.

2.3.2 Aortic Valve Regurgitation

Aortic regurgitation is defined by AV incompetence, in which a retrograde blood flow from the aorta to the left ventricle originates during diastole. Infective endocarditis involving the aortic valve as well as rheumatic fever associated with chronic inflammatory aortic valve disease may result in aortic regurgitation because of loss of coaptation, leaflet retraction, or perforation. Even though aortic stenosis is only related to diseased valve leaflets, aortic regurgitation may depend either on valve leaflets or on other components of the aortic root. In particular, pathologic dilations of the aortic annulus or of the Valsalva sinuses, or both, as well as an abnormal enlargement of the STJ (see Sect. 2.1) may cause aortic regurgitation.

All of these morphological alterations of the aortic root may be related either to atherosclerotic and/or hypertensive damage of the aortic wall or to heritable connective tissue disease (like Marfan syndrome or Loeys-Dietz syndrome).

In presence of aortic insufficiency, a volume overloading of the left ventricle occurs which may increase slowly and may be well tolerated for long periods. The consequences of aortic insufficiency include left ventricular dilation and hypertrophy, with remodeling of the left ventricle [76].

Severe aortic regurgitation generally requires surgical treatments. In particular, if the native aortic leaflets are healthy, aortic valve sparing techniques (which are cardiac surgical procedures involving replacement of the aortic root without replacement of the aortic leaflets) may be adopted [31, 61]. Otherwise, the whole aortic root can be substituted with biological or mechanical valves sewn into appropriate grafts [14].

2.4 Surgical Treatments

The classification of aortic valve surgery procedures is not trivial, given the wide range of available treatment options; in the following, we decided to split them with respect to the related interventional strategy, i.e., traditional open heart surgery or minimally-invasive.

2.4.1 Open Heart Surgery

Different surgical treatments are adopted to restore valve functionality. In the literature many techniques for aortic root reconstruction are described, either sparing the valve leaflets [41, 98] or involving the use of mechanical [92], stented

[86, 115] or stentless biological prostheses [45] as well as homograft and allograft valves [43, 125] which means that the tissue graft is obtained from an organism of the same species as the recipient; they can be either stented or stentless.

If the aortic root wall does not show any remarkable pathological dilation so that the valvular leaflets can be considered as the principal cause of disease, AV is replaced by means of mechanical or biological valves as discussed in many comparative studies, reported in the literature [1, 101, 103].

On the one hand, mechanical prostheses assure a long-term solution due to an excellent durability [66], on the other hand, they are associated with a greater incidence of hemorrhage than bioprostheses since they do not avoid the use of anticoagulants. Moreover, bioprostheses are associated with more physiological hemodynamics as well as a minor trombogeneticity [88]; accordingly, especially for elderly patients, biological valves assure greater performances than mechanical ones and, in particular, stentless valves are preferable than stented ones, representing an "excellent option for aortic valve replacement" [84].

The use of stentless valves, in fact, appears to potentially increase the long-term survival when compared to stented ones due to improved ventricular reverse remodeling [13]. At the same time, the hemodynamics is closer to physiologic behavior; additionally, the use of a continuous suture technique reduces the cross-clamp times and cardiopulmonary bypass.

However, open heart surgery with cardiopulmonary bypass is not always recommended: in presence of coexisting conditions such as advanced age, congestive heart failure, coronary artery disease, lung disease and renal insufficiency, the surgical risk becomes very high and, in some cases, unsustainable [28, 80].

2.4.2 Minimally-Invasive Surgery

In 1986 Cribier et al. [28] introduced percutaneous transluminal valvuloplasty to reduce the aortic valvular gradient and improve left ventricular ejection; unfortunately, such a treatment provided very poor mid and long-term outcomes [74] and the associated risks and follow-up events have been subject of concern because the incidence of restenosis has been found approximately 50 % at 6–12 months [60].

New developments in cardiothoracic surgery have led to innovative minimally-invasive devices for the treatment of aortic stenosis in patients associated with potential high surgical risk. In 2002, Cribier performed the first clinical implant of a percutaneous balloon-expandable aortic valve at the level of the native valve [29] while, in 2004, Grube implanted for the first time a self-expandable transcatheter valve [55].

In the last decade, different devices have been designed and submitted to clinical evaluation confirming that, on one hand, such an innovative technique represents a promising solution for aortic stenosis even though, on the other hand, at present, it is still an immature procedure due to limited follow-up data and durability evaluation. The two transcatheter devices, which are currently available,

Fig. 6 Transcatheter aortic valve prostheses currently used in clinical practice: the Medtronic CoreValve (*left*) and the Edwards SAPIEN XT (*right*)

consist of either a stainless steel (or cobalt chromium, since the very last prosthetic devices, named SAPIEN XT, are made of an innovative cobalt chromium alloy) balloon-expandable (Edwards Sapien) or nitinol self-expandable stent (Medtronic CoreValve), see Fig. 6.

In both cases, a tri-foliate bovine/porcine pericardium heart valve is attached inside the cylindrical metallic frame. Prosthesis placement can be achieved by either a trans-femoral or trans-apical access. In the first case, the prosthetic device is inserted through the femoral artery and passes retrogradely through the aorta until the aortic root is reached [122] while, in the second case, it is placed directly through the apex of the heart [73]. Once the valve has been positioned, in case of balloon-expandable devices, a balloon inflation leads to the valved stent expansion which excludes and compresses the native diseased leaflets.

Self-expandable valve placement procedure is very similar to the supra-mentioned procedure except that self-expandable prostheses automatically open through a step-wise deployment when gradually extracted from the delivery catheter: they do not need the help provided by a balloon expansion due to the peculiar properties of their constitutive material.

Particular attention must be devoted to positioning, which is crucial since it affects post-operative performance: on one hand, the implanted valve must guarantee regular flow through the coronaries while, on the other hand, the prosthesis should not overlap and crush the left bundle branch [89] to avoid is a cardiac conduction abnormality.

3 Structural Modeling of Aortic Valve: A Brief Review

Before discussing the simulation of two specific surgical strategies to treat aortic valve stenosis, we would like to provide a brief overview about the use of structural FEA to investigate either aortic valve biomechanics in both healthy and diseased conditions or to design and evaluate prosthetic devices.

The first engineering and mathematical studies on the aortic valve date back to the 1970s with the pioneering works by a group of the Washington University that first characterized the mechanics of human aortic valve by computing the stress/strain distribution throughout the leaflet structure [23, 24, 47] and by creating specific mathematical models of the valve leaflets [21, 48].

During the 1980s a great contribution to the investigation of AV mechanics has been given by several authors. In 1983, Sauren developed a theoretical model to gain insights into the factors which govern the mechanical behavior of the natural aortic valve during diastole [99], while other researchers focused on the modeling of bioprostheses by a geometrical and constitutive point of view. Christie and Medland (1982) performed non-linear finite element stress analyses of bioprosthetic heart valves [22] while Sabbah et al. (1985, 1986) employed a finite element model of a porcine trileaflet bioprosthesis, paying particular attention to stress localization and its correlation with calcifications [95, 96]. Rousseau et al. [94] included viscoelastic material properties into their closed bioprosthetic model.

In 1990, Thubrikar published a book [112], which is a milestone for the analysis of aortic valve, in which the author proposed a geometrical model of the valve and also deepened other different aspects such as valve physiology, dynamics and pathology. Attention to valve design has been payed also by Clift et al. (1996) who focused on synthetic leaflets [25] while Knierbein et al. used finite element models to improve the design of polyurethane valves [64].

From 2000, the interest in aortic valve is further increased; many other experimental and numerical studies addressing several aspects of the aortic valve modeling, ranging from its geometrical description to the constitutive modeling, have appeared.

On the material modeling side, since Billiar and Sacks [15], who have highlighted the highly non-linear and anisotropic behavior of aortic leaflets through specialized biaxial testing techniques, many biomechanical studies have addressed this issue. Driessen et al. [34–36] proposed a numerical representation of mechanically-induced collagen fiber architectures in aortic leaflet tissue while Freed et al. [42] developed a transverse isotropic non-linear constitutive model which takes into account the experimentally-observed dispersion of collagen fibers. The effects of anisotropy have been also studied to evaluate leaflet stress distribution in polymer composite prostheses [75], while, Mohammadi et al. [82] developed a new high-order element using p-type finite element formulation to implement anisotropic material properties similar to those of the heart valve leaflet tissue in only one single element. In 2010, Koch et al. performed static FEA of the whole aortic root in diastolic configuration to investigate the influence of non-

linear and anisotropic material properties [65]. Moreover, dedicated FEA-based investigations have shown that orthotropy has to be considered during the manufacturing process of *bioprosthetic devices* since it can negatively affect both the displacements of the leaflets and their stress distribution [3]. More recently a simplified version of Fung's elastic constitutive model for skin, developed by Sun and Sacks [107], was implemented using FEA and applied to the modelling of bovine and kangaroo pericardium to evaluate the design of percutaneous aortic valve as function of different leaflet material, fiber orientation and abnormal valve dilation on the valve [102].

In dealing with the *geometrical modeling* of the human trileaflet aortic valve, Labrosse et al. (2006) proposed a new approach to accommodate the wide dimensional variety observed in normal human aortic valves based on fully 3D analyses [68]; according to this study, a finite element model of the native aortic valve is developed implementing anisotropic hyperelastic material properties for the leaflets and aortic tissues, starting from the unpressurized geometry [69]. More recently, Haj-Ali and colleagues [56] proposed a general mathematical description for the complex 3D geometry of the native tricuspid aortic valve including the cusps, commissures and sinuses; the needed parameters to construct the curves defining the 3D model are obtained from echocardiographic measurements. In this context, it is worth mentioning that dedicated algorithms to elaborate novel medical imaging, such as 4D CTA, allows to quantify morphological and functional aspects of the so-called aortic valve complex [54, 62].

Computer-based simulations have been also adopted to study *pathologies* of the aortic valve. In particular, we quote the works by Grande-Allen et al. [51, 52] who used MRI-derived models to associate aortic root dilation with valve incompetence, stating that dilation leads to higher values of stress and strain in the leaflets. They also investigated the effects of normal aging by increasing both the thickness and the stiffness of the aortic structure, showing that it may result in valvular regurgitation [50]. Conti et al. [26] demonstrated by means of a finite element model that bicuspid geometry per-se entails abnormal leaflet stress which may play a role in tissue degeneration, while Auricchio et al. [5] developed a computer-based procedure to reproduce the aortic root pathologic dilation on the basis of experimentally measured parameters.

The *dynamical behavior* of the aortic valve throughout the cardiac cycle has been investigated using numerical models by Gnyaneshwar (2002) who simulated the whole cardiac cycle to analyze the interaction between the aortic root and the leaflets [46]. Dynamic finite element analysis has been performed by Conti et al. (2010) who obtained leaflet stretches, leaflet coaptation lengths and commissure motions, as well as the timings of aortic leaflet closure and opening, all matching with the experimental findings reported in the literature [27].

Finally, FEA has been adopted to predict the outcomes of *aortic valve surgery*. In particular, the aortic valve sparing technique has received a lot of attentions: Grande-Allen et al. (2001) discussed the influence of graft shape and stiffness on post-operative valve performance concluding that the optimization of both graft shape and material design may result in improved longevity of the spared valve

[53]. Ranga et al. (2006) evaluated aortic reconstruction following valve-sparing operation and validated the simulation results with MRI in-vivo data [90]. In Soncini et al. (2009), the aortic root performance after valve sparing procedure is estimated by means of a comparative finite element analysis, while more recently, Totaro et al. evaluated the potential of a preoperative prediction of the optimal graft size, using FEA, proving that the virtual simulation of the AVS procedure could be useful in predicting the post-operative physiology of the aortic root [116, 117].

Labrosse et al. [70] created a finite element model with the ability to simulate physiologic function in normal valves, and aortic insufficiency due to leaflet prolapse in asymmetric, diseased or sub-optimally repaired valves. More recently, Votta et al. have extended in-vitro investigation of the neo-chordae technique via finite element models to systematically assess the acute effects of changing neo-chordae features, i.e., length, opening angle, asymmetry and insertion on the aorta. Furthermore, Xiong et al. highlighted the importance of leaflet geometry for stentless pericardial aortic valves [124]. Moreover, Hammer et al. [57] used a structural finite element model to explore how a pericardial leaflet graft of various sizes interacts with two native leaflets when the valve is closed and loaded.

In the following section we discuss two applicative examples of using realistic simulations to investigate two different AVR procedures: (i) open-surgery implant of stentless biological prosthesis; (ii) transcatheter implant of stented valves.

4 Patient-Specific Simulation of Aortic Valve Replacement: Applicative Examples

As stated in the Introduction, the clinical outcomes of AVR are related to an appropriate choice of both prosthesis size and replacement technique. At present, the performance of the surgical operation is strictly dependent on surgeon's expertise, especially in consideration of the fact that the technique is non-trivial. Hence, all these aspects make AVR a strongly surgeon-dependent procedure. Moving from such considerations, in this section we propose a patient-specific approach to optimize prosthesis placement and sizing during the pre-operative planning considering both an open-surgery intervention and a minimally-invasive procedural option.

4.1 Open-Surgery Implant of Stentless Biological Prosthesis

4.1.1 Clinical Procedure and Simulation Strategy

The surgical approach to stentless valve implant can be summarized in three main operative steps [45]:

1. after transecting the ascending aorta for exposure, the diseased valve is excised;
2. the aortic annulus is sized with a dedicated aortic valve sizer;
3. stay sutures are placed and, subsequently, the valve is lowered: the prosthesis takes its position supra-annularly.

On the basis of the operative steps of the real procedure, we adopted a simulation strategy which can be described in four principal steps:

1. a parametric CAD model of the supra-annular prosthesis is properly created;
2. the CAD model of the aortic root is obtained from DICOM images of contrast-enhanced computed tomography-angiography (CT-A) through dedicated image processing;
3. the AVR operation is mimicked by positioning the stentless tissue valve inside the aortic root through a placement simulation;
4. finally, a second simulation considering both aortic root and valve is performed to evaluate valve competence during diastole.

In particular, we simulate the implant of three different sizes of the Freedom Solo (Sorin Biomedica Cardio, Saluggia, Italy) stentless valve, starting from a single patient-specific aortic root model. In the following, we discuss each of listed operative steps, while more details are reported in [6].

4.1.2 Stentless Prosthesis Model

As stated by Xiong et al. (2010), the prosthetic leaflet geometry plays a key-role for efficacy and durability in AVR procedures and, for this reason, it is important to accurately reproduce it in order to predict the realistic valve behavior. In our case, given the lack of specific technical data from the manufacturer, we generate the model of the stentless valve assuming that the three leaflets to be implanted in the patient's aortic root have the same geometrical features as a healthy native AV [9].

Even though modeling the stentless prosthesis simply respecting the geometrical properties of healthy valves does not allow very accurate reconstructions of the prosthetic device, we believe that this simplifying assumption does not affect the methodological approach we would like to discuss herein. Indeed, at the same time, we think that future developments to achieve more precise geometrical models of the prosthesis have to be addressed to obtain simulation results closer to reality.

Herein, for the sake of simplicity, the Labrosse's geometrical guidelines are adopted to define the model [68] hence our model of the prosthetic leaflets is completely described by the following five parameters [5] (see Fig. 7):

- diameter of the annulus, D_a;
- diameter of the top of the commissure, D_c;
- valve height, H;
- leaflet free margin length, L_{fm};
- leaflet height, L_h.

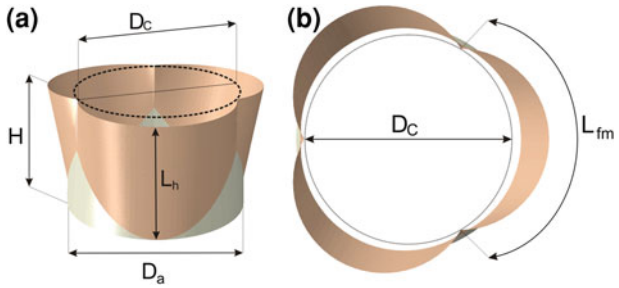

Fig. 7 Geometric model of the valve by Labrosse et al. [68]: **a** the *perspective view* shows parameters D_a, D_c, H and L_h; **b** the *top view* highlights L_{fm} and, again, D_c

Table 1 Set of the chosen parameters highlighted in Fig. 7 adopted to model the stentless prostheses

Prosthesis ID	D_a (mm)	D_c (mm)	H (mm)	L_{fm} (mm)	L_h (mm)
SIZE 25	25	23	17	31	17
SIZE 27	27	25	18	33	18
SIZE 29	29	27	19	36	19

The subcommissural triangles are properly removed and three different model variants characterized by different sizes are created based on product specifications of the Freedom Solo prosthesis [6]. In particular, the dimensions reported in Table 1 have been considered.

The leaflets are meshed within Abaqus v6.10 (Simulia, Dassáult Systems, Providence, RI, USA) using 4,200 four node membrane elements M3D4R with 0.5 mm uniform thickness [12].

4.1.3 Materials

The stentless valve is made of two bovine pericardial sheets without any fabric reinforcement.

In the last decades, there has been a quite long diatribe about whether the prosthetic valve after the fixation process behaves more as an homogeneous isotropic material [72, 118] or as an anisotropic material [3, 71]. Even though some recent studies confirm an anisotropic response of treated pericardium [16], for the sake of simplicity, we take into account the simplifying assumption of isotropic material.

Consequently, an incompressible isotropic hyperelastic Mooney-Rivlin model is adopted for the stentless valve leaflets [39, 91]. However, it is worth noting that material modeling of fixed pericardium is still a matter of debate as detailed in Sect. 4.1.

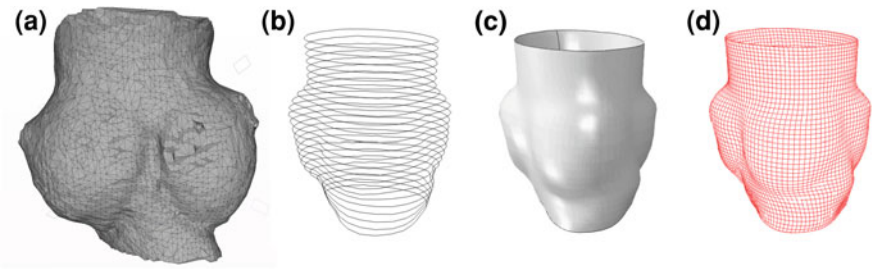

Fig. 8 Creation of aortic root model: **a** an STL file is extracted from medical images by appropriate processing; **b** a series of splines identifying the aortic root wall are obtained elaborating the STL file; **c** a CAD model of the aortic root is obtained through lofting; **d** a structured mesh is derived from the CAD model

4.1.4 Patient-Specific Model of the Aortic Root

CT-A examination allows accurate 3D reconstructions of anatomical regions and, even though it is not used for all patients due to its high cost in terms of X-ray doses, it is frequently adopted for imaging diagnosis of aortic valve pathologies. For this reason, we base the aortic root model on DICOM images of a cardiac CT-A performed using a iodinate contrast die on a 46 year-old male patient performed at IRCCS Policlinico San Matteo, Pavia, Italy, using a SOMATOM Sensation Dual Energy scanner (Siemens Medical Solutions, Forchheim, Germany). The scan data are characterized by the following features: slice thickness: 0.6 mm; slice width $\times$ height: 512 $\times$ 512; pixel spacing: 0.56 mm.

We process the resulting DICOM images using ITK-SNAP v2.0.0 [126] in order to firstly enhance the contrast die, then extract a confined region of interest from the whole reconstructed body and, finally, apply an automatic segmentation procedure based on the *snake evolution* methodology to obtain a stereolithographic (STL)—(see Fig. 8a)—description of the anatomical region of interest. The STL file is processed within Matlab (Natick, Massachusetts, U.S.A.) to define a set of splines identifying the cross sectional contours of the aortic bulb volume (Fig. 8b). The CAD model is then obtained by means of a lofting procedure from the spline curves imported in Abaqus CAE (Fig. 8c). Finally, the model is meshed with 43,260 linear quadrilateral shell elements S4R (Fig. 8d).

For the sake of simplicity, the same material properties already adopted for the prosthetic tissue valve are used also for the aortic root wall [91]. It is worth stating that such an assumption has been recently removed by considering a fiber-reinforced material model [7].

4.1.5 Prosthesis Placement

The prosthesis implant is simulated by constraining the attachment lines of prosthesis leaflets to overlap the so-called “suture-lines”, defined on our patient-specific aortic root model trough the following three steps:

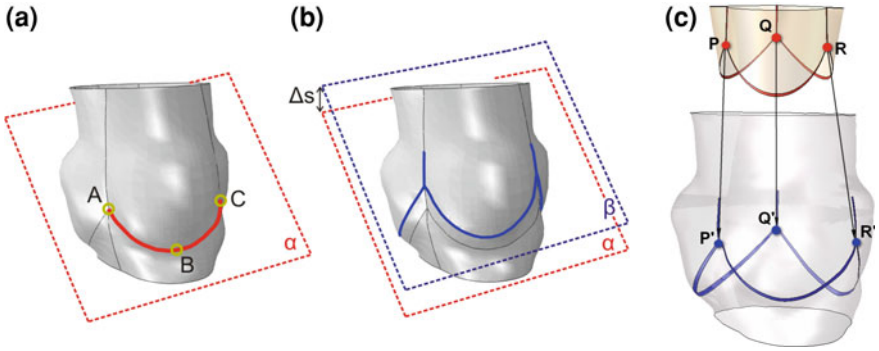

Fig. 9 Definition of the suture lines: **a** the plane α containing the native line of attachment and passing through the points A, B and C is created; **b** the plane β is obtained translating α vertically; the line of attachment of the prosthesis leaflet is defined by the intersection of α with the sinus. The *blue lines* represent the whole set of attachment lines where the nodes of the prosthesis are tied with the nodes of the sinuses; **c** simulation strategy for the prosthesis placement: the *black arrows* represent the displacements to be computed and applied to the nodes of the prosthesis line of attachment

- definition of the plane α passing through the reference points A, B, C and containing the line of the native leaflet attachment (see Fig. 9a);
- definition of the plane β, obtained with a Δs vertical translation of the plane α;
- definition of the supra-annular suture-line from the intersection of β with the patient-specific CAD model of the Valsalva sinuses (see Fig. 9b).

This sequence of geometrical operations is repeated for each Valsalva sinus to obtain the whole set of suture-lines. Subsequently, a quasi-static FEA of the prosthesis placement is performed using Abaqus Explicit solver; precomputed displacements are imposed to the nodes of the prosthesis attachment line (see Fig. 9c). Inertial forces do not dominate the analysis since the ratio of kinetic energy to internal energy remains less than 5 %. For quasi-static simulations involving rate-independent material behavior, the natural time scale is in general not important. For this reason, a mass scaling strategy, i.e., an artificial increase of the mass of the model, is used to reduce computational costs.

To evaluate the behavior of the valve implanted in different positions, different values of Δs (0.5, 2 and 5 mm) associated with three different labels, i.e., suture-line 1, 2 and 3, respectively, are taken into consideration.

4.1.6 Prosthesis Closure

To evaluate the performance of prosthetic valve after the replacement procedure as a function of each combination of prosthesis size and suture-line position, we simulate the diastolic phase of the cardiac cycle. Because CT-A data adopted

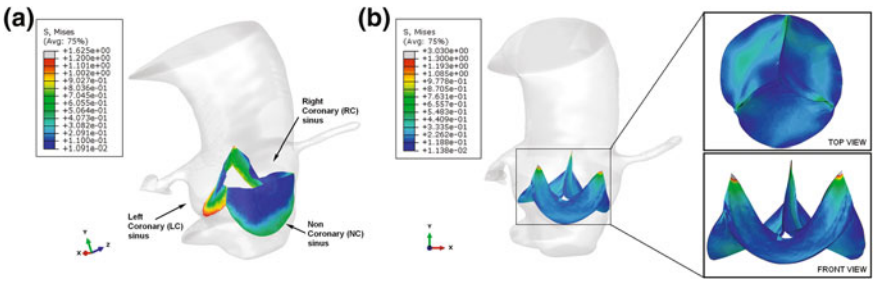

Fig. 10 Simulation results: **a** the von Mises stress contour plot, outcome of the simulation of prosthesis implant on a given the suture-line is represented—Non Coronary (NC), Left Coronary (LC) and Right Coronary (RC) sinuses; **b** prosthesis placed on a given suture-line at the end of diastole: due to the asymmetry of the patient-specific sinuses, the non-coronary leaflet of the virtually implanted symmetric valve closes below the other two leaflets. A central gap is highlighted from the *front view* which means that the replacement solution fails

to generate the geometrical model of the aortic root wall have been obtained at end-diastole, a uniform pressure, $p = 80$ mmHg, is gradually applied on the leaflets, while the pressure acting on the internal wall of the sinuses is for simplicity assumed equal to zero. The nodes belonging both to the top and to the bottom of the aortic root model are confined to the plane of their original configuration.

The numerical analysis of the prosthesis closure is a non-linear problem involving large deformation and contact. For this reason, Abaqus Explicit solver is used to perform large deformation analyses; also in this case a quasi-static simulation is performed.

4.1.7 Results of Prosthesis Placement

We evaluate the positioning of three different sizes of stentless tissue valves in one aortic root model. Each prosthesis is placed along three different supra-annular suture-lines, defining thus nine different scenarios.

The FEA of the stentless valve implantation into the patient-specific aortic bulb provides the tensional state of each leaflet. As depicted in Fig. 10a, the results of the prosthesis placement in one particular case are reported in terms of von Mises stress pattern. It is possible to note that the stress distribution is not the same for each leaflet; this is due to the asymmetric morphology of the host aortic bulb, while the stentless valve has a symmetric shape. To highlight this aspect we compute the von Mises stress averaged over the leaflets domain, σ_{av}, defined to neglect peak values of the stress due to local concentration.

4.1.8 Results of Prosthesis Closure

Once the prosthesis is implanted and sutured inside the aortic root, a uniform pressure is applied on the leaflets to evaluate the performance of the surgical

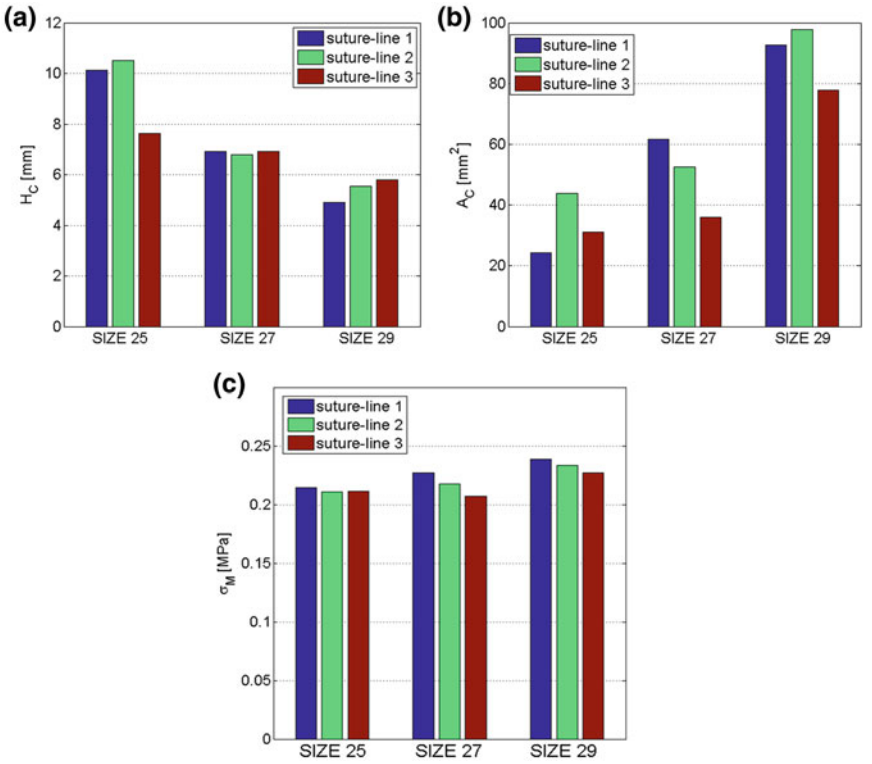

Fig. 11 Trend of the coaptation measures and of the tensile state: **a** the coaptation height, H_C, **b** the coaptation area, A_C and **c** the average von Mises stress, σ_{av}, are evaluated as a function of the prosthesis size and the suture-line position

solution under consideration. In Fig. 10b, the SIZE 25 valve placed along suture-line 1 is represented at the end of the diastolic phase; the von Mises stress distribution is highlighted. Two basic parameters are measured to evaluate the prosthesis physiology: the coaptation area, A_C, defined as the total area of the elements in contact, and the coaptation height, H_C, defined as the distance between the plane containing the annulus and the point where the coaptation occurs. The bar graphs depicted in Fig. 11a, b show the impact of both prosthesis size and suture-line position on the coaptation measurements. In particular, Fig. 11a suggests that the increase of prosthesis size leads to the decrease of H_C, while the suture-line position does not affect significantly the coaptation height.

On the contrary, both the coaptation area, A_C, and the average stress, σ_{av}, increase with the prosthesis size while the suture-line site has a minor impact on such values (see Fig. 11b, c). Moreover, the valve closure results show that the coaptation of the three leaflets is not perfectly symmetric due to the physiological asymmetry of the aortic sinuses. For this reason, during the diastolic phase, a central gap is observable (see Fig. 10b, front view) which implies insufficiency of

the virtually implanted valve. Consequently, we can speculate that the replacement solution under investigation could fail.

In conclusion, the results indicate an uneven distribution of stresses on the three leaflets underlying the impact of the anatomical asymmetry of the native aortic bulb where the prosthesis is placed. Consistently, the simulation of valve closure displays a non-uniform coaptation of the leaflets during the diastolic phase, which means a potential incompetence of the substituted valve. It is also worth underlining that such considerations are consistent with the results presented by Sun et al. [108] who studied the implications of an asymmetric trans-catheter aortic valve deployment. Moreover, our findings highlight the relevance of prosthesis size as to both the coaptation area, i.e., the performance of the prosthetic valve, and the stress distribution over the leaflets, i.e., the durability of the prosthesis, whereas no significant impact has been shown by the suture-line site. This observation underlines importance of the choice of prosthesis size while it seems that suturing the valve in a position slightly more distal or more proximal with respect to conventional suture sites (i.e., at 2–3 mm from the host annulus of each sinus [45]) does not affect significantly the procedure outcome.

4.1.9 Impact of Material Modeling

Event though it is well accepted that bovine pericardium is an anisotropic material, there is no unique opinion on the glutaraldehyde-treated pericardium. In fact, the chemical fixation process makes it behave like an isotropic material [72, 118], while others claim that it maintains its original anisotropic characteristics even after the fixation procedure [3, 71]. For this reason, we have analysed the differences of considering an isotropic (Fig. 12a) or a fibre-reinforced anisotropic (Fig. 12b) model for the valve leaflets [7].

First of all, we may observe that the maximum principal stress distribution on the closed valve leaflets is less uniformly aligned in case of isotropic material model (see Fig. 12c) with respect to an anisotropic model (see Fig. 12d). We may conclude that the fibres drive the stress distribution predominantly in the direction of their alignment (i.e., circumferentially). This aspect also leads to the reduced stress values obtained adopting an anisotropic material model with respect to an isotropic model as also highlighted by a previous study [65]. Moreover, the performed simulations confirm that anisotropic leaflets have a significantly greater coaptive area exhibiting a smoother closure. It is observed that at the end of diastole, the isotropic leaflets exhibit many non-physiological foldings and wrinkles, particularly close to the commissures, which are not present in the closed configuration of the anisotropic leaflets. Furthermore, the coaptation length increases while the coaptation height decreases when moving from an isotropic to an anisotropic model. Also this indication is in agreement with previously published studies [65], confirming that the introduction of anisotropy in the leaflet model leads to both an increased compliance in the radial direction and an improved coaptation. These findings suggest that the choice of material model

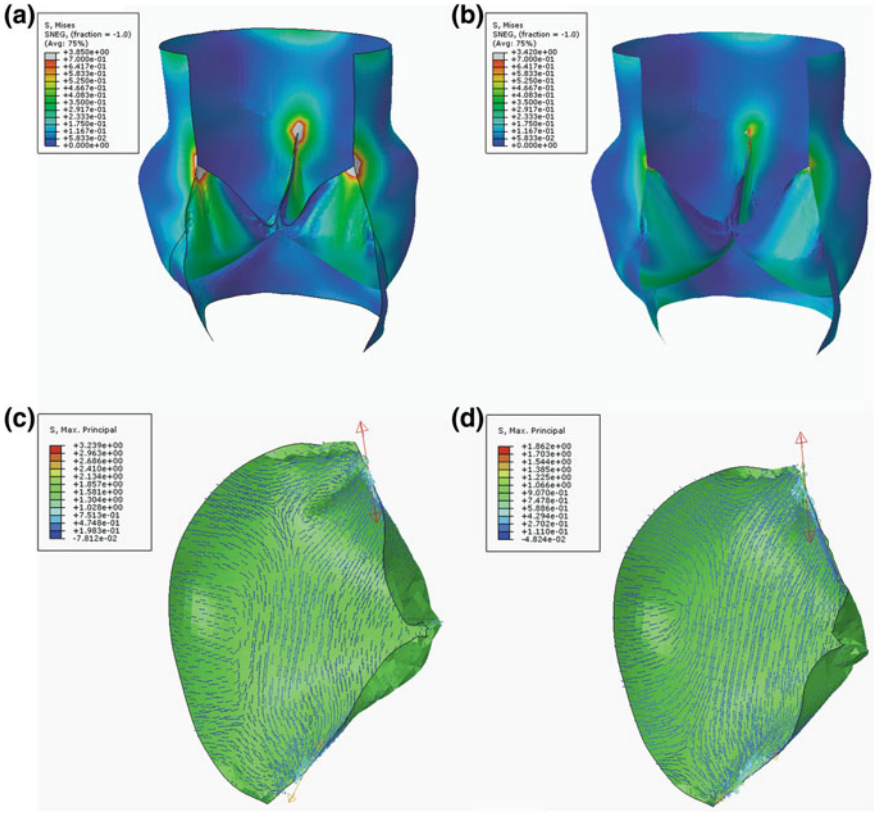

Fig. 12 von Mises stress pattern at the end of diastole: **a** isotropic material model; **b** fibre-reinforced model. A *cut view* is adopted to highlight the coaptation. Vector plot of the maximum principal stress of the closed leaflets at the end of diastole: **c** isotropic material model; **d** anisotropic Holzapfel material model. The *bigger arrows* close to the commissures show a stress concentration in that region

significantly influences the performance of the implanted valve and, therefore, it represents a crucial issue when performing numerical simulations.

4.2 Transcatheter Aortic Valve Implant

4.2.1 Clinical Procedure and Simulation Strategy

In this section we focus on one of the currently available percutaneous aortic valve prosthesis, i.e., the balloon expandable Edwards Lifescience Sapien valve which is basically composed of three flexible biological leaflets sutured on a stainless steel balloon-expandable stent. Sapien placement can be achieved by either a

trans-femoral or trans-apical access. In the first case, the prosthetic device is inserted through the femoral artery and passes retrogradely through the aorta until the aortic root is reached [122] while, in the second case, it is placed directly through the apex of the heart [73]. Once the device has been positioned, balloon inflation leads to the valved stent expansion which excludes and compresses the native diseased leaflets.

Few studies have already used FEA to develop new concepts for different percutaneous aortic leaflet geometries [102] or to better understand the mechanics and hemodynamics of TAVI device [108, 121]. Moreover, Schievano et al. [100] and Capelli et al. [18] proposed a FEA-based methodology to provide information and help clinicians during percutaneous pulmonary valve implantation planning, while a more recent study deals with the deployment of Sapien within several patient specific aortic root models [19]. Structural analysis has been also used to assess the impact of design features on the radial force transmitted by the stent to the aortic root [119].

Within this context, given the TAVI procedural phases, our simulation approach results in the following steps:

1. creation of transcatheter prosthesis (stent and prosthetic valve);
2. simulation of stent crimping;
3. simulation of balloon inflation and stent expansion;
4. simulation of valve closure.

Clearly, the simulation of stent apposition accounts for a patient-specific aortic root model, which is basically created as described in Sect. 4.1. However, if, on one hand, a very accurate model of the aortic root is considered, on the other hand, the native calcified leaflets are not taken into account representing a significant simplifying assumption for the simulation of prosthesis expansion and anchoring. In the following, each of the previously listed steps is detailed.

4.2.2 Stent Model

In absence of both a device sample and design data from the manufacturer, we base the creation of the stent geometry on the few data and pictures available on the official web-site of the Edwards Lifesciences company [38]. For the sake of simplicity, as previously mentioned in Sect. 4.1 when discussing the model creation of biological stentless valves, assumptions are made about the geometry of the prosthesis which do not affect the intention of this chapter, i.e., proposing a methodological approach to reproduce aortic valve diseases and related treatments. We firstly create the unfolded geometry of the stent using Rhinoceros software v.4.0 (McNeel & associates, Seattle, WA, USA) observing that it is made of a primitive geometry, mirrored and replicated. Once the unfolded geometry of the stent has been created, we mesh it using Abaqus software v6.10 (Simulia, Dassault Systéms, Providence, RI, USA) obtaining a list of nodes and elements. To such

nodes we can assign proper polar coordinates easily computed from their original cartesian coordinates to obtain the folded geometry.

4.2.3 Prosthetic Valve Model

The prosthetic valve model is generated through a lofting procedure starting from the circular line of the bottom and the peculiar line of the top of the valve extracted from the real device picture. The two closed lines have to be concentric and, in particular, the top line has to be inscribed into the circular base whose radius is equal to the inner radius of the stent.

In dealing with the material, the valve leaflets are made of glutaraldehyde-treated bovine pericardium. Therefore, they are modeled following the considerations discussed in Sect. 4.1. In particular, in this case, we chose to adopt an isotropic relation to model the leaflets mechanical behavior [124].

4.2.4 Stent Crimping

A cylindrical catheter is gradually crimped leading to stent deformation: the initial diameter of the catheter is 28 mm while the final diameter is 7 mm in agreement with the work of Capelli et al. [18]. A quasi-static simulation is performed using Abaqus/Explicit; the kinetic energy is monitored to ensure that inertial effects do not affect the results. The catheter is meshed using 403 4-node surface elements with reduced integration (SFM3D4R) and it is modeled as a rigid material; the stent has been discretized using 90,279 solid elements with reduced integration (C3D8R). The material used for the balloon-expandable stent is the low carbon 316L stainless steel, whose behavior is described by an elastoplastic model according to the work of Auricchio et al. [4]. A frictionless general contact is used to handle the interactions between the catheter and the stent.

4.2.5 Simulation of Balloon Inflation and Stent Expansion

The simulation of stent apposition is performed assembling (i) the crimped stent, whose tensional state is imported from the crimping simulation and it is assumed as a predefined field, (ii) the balloon modeled as a cylindrical folded body with two conical tapered ends and (iii) the patient-specific aortic root.

The balloon model is discretized with 13,680 3-node membrane elements (M3D3); the Duralyn material properties are assigned [32].

Once the balloon-stent system has been properly placed inside the aortic root model (excluding, for the sake of simplicity, the native aortic leaflets which can not be modeled by processing CT images), Abaqus/Explicit solver is again used to perform the expansion simulation: a uniform pressure of 1 MPa (75 mmHg) is gradually applied to the inner surface of the balloon while its fixation to the

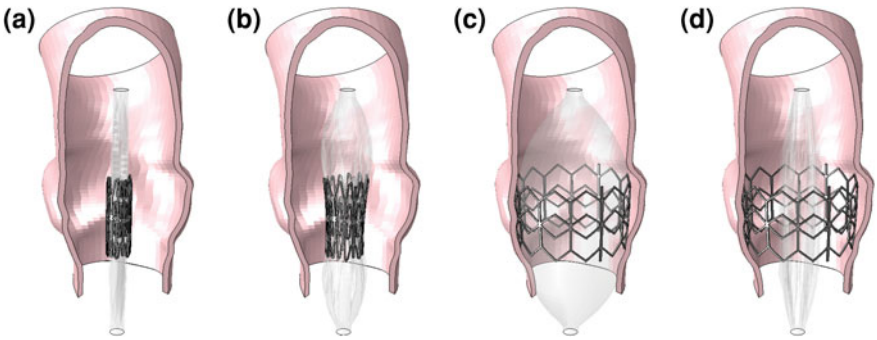

Fig. 13 Different frames of balloon expansion and stent apposition: **a** initial configuration; **b** the balloon starts to deploy the stent; **c** the balloon is fully expanded and the stent is fully deployed; **d** final configuration after balloon deflation

catheter is virtually reproduced by constraining the displacements in each direction of the proximal and distal balloon tips. Since the compliant chart of the Edwards SAPIEN balloon is not available, a reasonable pressure value which leads to a smooth stent expansion has been used.

The complex contact problem of the balloon interacting with itself and the stent is described by a Coulomb friction model with a friction coefficient of 0.2. The whole assembly and the result of the simulation of balloon inflation and stent expansion is shown in Fig. 13.

4.2.6 Simulation of Valve Closure

Once the simulation of balloon expansion has been completed and the stent is placed within the aortic root, we perform a quasi-static simulation to map the valve onto the implanted stent. In particular, we compute the displacement field of two different sets of valve nodes: (i) the nodes lying on the line of attachment with the stent and (ii) the nodes of the circular base of the valve, which are, in the real device, sewn onto a cylindrical fabric skirt attached to the stent. Finally, the overlapping nodes of the stent-valve system are tied together.

The last step of the procedure to simulate TAVI consists in the simulation of valve closure with the aim of evaluating its performance. The diastolic phase of valve closure has been reproduced by gradually applying a uniform pressure of 0.01 MPa to the leaflets. The nodes of the VAJ and of the STJ belonging to the patient-specific aortic root model have been constrained; the displacements of the nodes at the base of the valve are constrained as well.

4.2.7 Results

The described simulation procedure has been performed in two different cases to evaluate the impact of positioning on the post-implant device behavior: moving

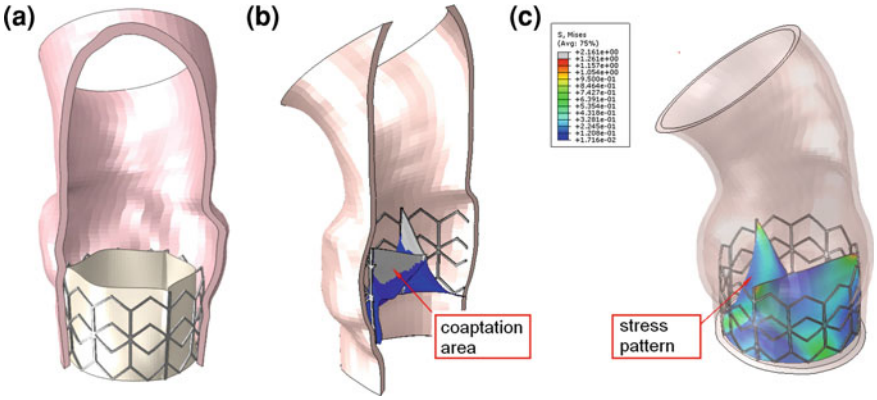

Fig. 14 Simulation results: **a** the coaptation area is highlighted; **b** the leaflet tensional state (MPa) is reported

from the same patient-specific aortic root model, we have in fact simulated TAVI with a distal positioning, i.e., immediately below the coronary ostia and, with a proximal positioning, i.e, 7 mm below the distal position.

The inclusion within the simulation framework of the biological valve prosthesis, sewn onto the metallic frame (see Fig. 14a), allows to compute the post-implant valve performance, evaluated in terms of coaptation area (see Fig. 14b) and stress/strain field (see Fig. 14c). The former gives a direct indication of the efficacy of the non-invasive repair procedure while the latter highlights localized stresses/strains on the prosthesis, identifying the weakest point of the implanted device. Consequently, we measure a coaptation area of 340.5 mm^2 for the closed valve placed in the proximal position while the valve positioned distally shows a reduced coaptation area of 258.2 mm^2. In this case, we register a 24.2 % decrease from the proximal implant to the distal one. Finally, the stress induced by balloon inflation both on the stent structure and on the aortic root wall has been analyzed.

The obtained values of σ_{av} in the proximal position are equal to 229 kPa while in the distal position are equal to 260 kPa, which means that moving from a proximal implant approach to a distal one, a 13.5 % increase of σ_{av} can be observed. The maximum predicted von Mises stress values are equal to 2.32 MPa (proximal configuration) and 2.16 MPa (distal), both below the ultimate stress of bovine pericardium [109].

These results suggest that, for the specific considered case, there are not significant differences in placing the valved stent either proximally or distally. Nevertheless, we can speculate that the proximal implant should be preferable because it leads to a greater coaptation area, preventing retrograde blood flow, and a lower stress, indicating thus a minor tensional state which can be correlated to prosthesis failure. The end-diastolic average stress on valve leaflets results to be in good agreement with correspondent stress values on bovine pericardium leaflets presented in other works [5, 6, 102].

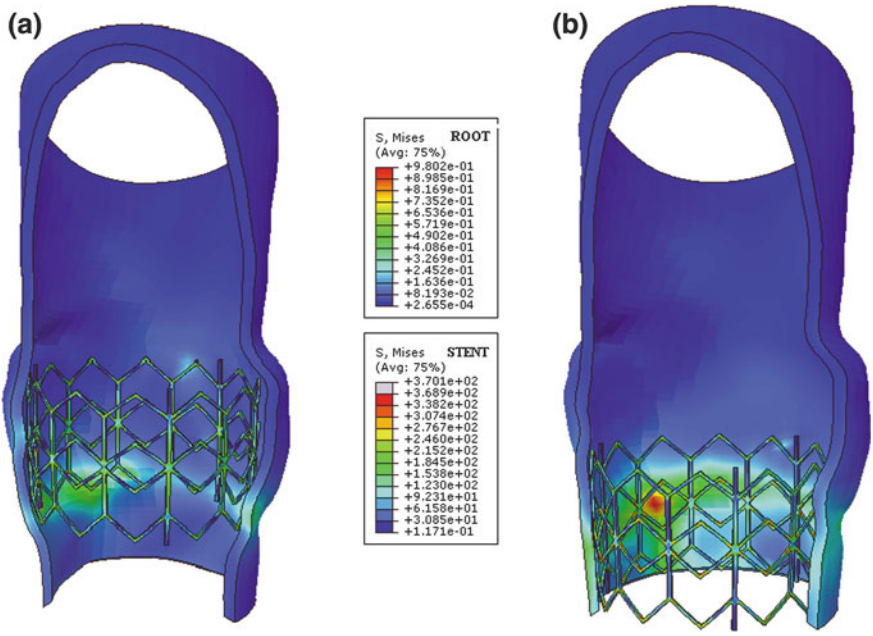

Fig. 15 Simulation results: the von Mises stresses on the aortic root wall and stent struts are represented: **a** after the distal positioning; **b** after the proximal positioning

Clearly, the simulation of TAVI allows to evaluate the impact of the prosthesis on the aortic root and the related stress distribution along the vessel wall as depicted in Fig. 15. We can observe that a different positioning procedure leads to different tensional state on the vessel wall which means different potential injury induced by the stent on the aortic root tissue. In particular, the distal positioning leads to reduced stresses on the aortic root wall if compared with the proximal positioning (−22.4 %). The obtained stress values are slightly higher than values reported by Capelli et al. [19] and comparable with the results reported by Wang et al. [121]; obviously, such a difference could be mainly attributable to the different constitutive model assigned to the aortic root.

The analysis of von Mises stress distribution along the prosthesis metallic frame confirms the results reported by Capelli et al. [19]; the final open configuration of the stent is guaranteed by material yielding occurring in correspondence to strut junctions. Moreover, the ultimate stress value for of the low carbon 316L stainless steel was not reached, confirming the low risk of acute structural failure after the deployment, although long-term stent failure due to the pulsatile loading conditions during the cardiac cycle cannot be underestimated. Despite the discussed computational framework already resembles the complexity of the real TAVI procedure, several steps have to be done to approach the challenge of predicting the clinical outcomes using computer-based simulations as discussed in the following.

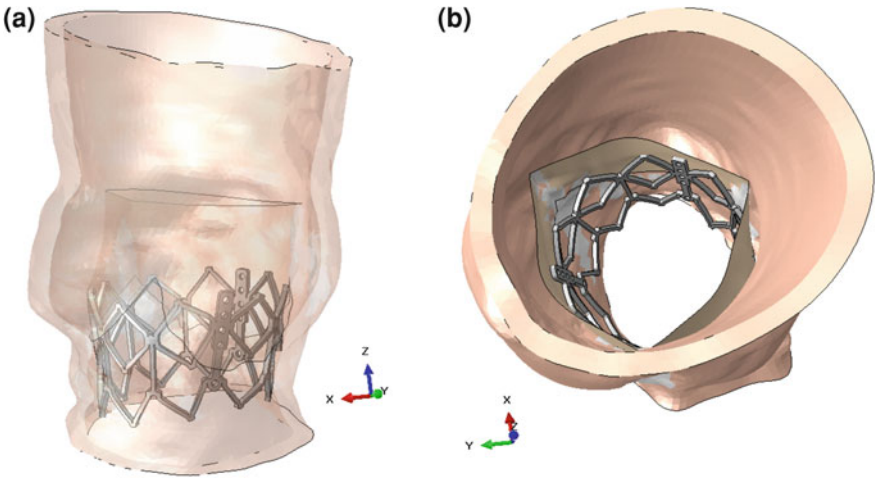

Fig. 16 Simulation of the prosthesis apposition in a patient-specific root model including the calcific leaflets: **a** *lateral view* depicting the stent model resembling the real device structure based on high-resolution micro-CT; **b** *top view* of the simulation results where *grey regions* are the element sets referred to the calcification

On one hand, a more accurate models of the aortic root could be created; in particular, the simulation could take into account the native leaflets which will be crushed and compressed by the valved stent. Moreover, the valve model can embed the calcifications because most of the candidate patients for TAVI are often shown highly calcified leaflets with a variability in the bulkiness of the calcific nodules [85]. Both Wang et al. [121] and Capelli et al. [19] have proposed a possible modeling for this issue but, certainly, the limit amount of data in literature regarding aortic valve calcification material limits the modeling reliability.

We also know that the generation of the aortic root model directly from CT-A, recorded under physiological pressure, requires to take into account the related pre-tensional state. Despite different approaches have been proposed [2, 19, 44, 121], it is not clear how to account for heterogeneity of the vessel wall tissue due to presence of calcification. A successful approach could exploit 4D images, linking thus configuration and loading change during the cardiac cycle [87].

On the other hand, a more accurate model of the Sapien device accounting for all its structural and geometrical details, can be derived from micro-CT imaging of a real device. Finally, a dedicated validation of the numerical outcomes with respect to *in-vitro* and *in-vivo* data (i.e., simulation vs. post-operative or follow-up images) will certainly enhance the reliability of the proposed computer-based tools.

The preliminary results of such modeling improvements are depicted in Fig. 16: the model of the aortic root includes also the calcified leaflets and the model of Edwards Sapien is created from high resolution micro-CT scan of the size-23 real prosthesis.

It is also worth underlining that structural analysis can be a preliminary step to further investigations addressing the assessment of post-implant hemodynamics and associated migration forces as shown in several recent studies [10, 37, 102].

In conclusion, percutaneous devices are now under constant development and FEA represents a valuable computational technique being not only an integral part of the design process, but also a predictive tool able to anticipate the area of localized stress, the post-operative coaptation as well as possible modes of failure, thus representing, also for this recent application, a support to clinicians during the decision-making process [40].

5 Conclusions and Further Directions

The main goal of the present chapter is to highlight the potential impact and importance of computational biomechanics and realistic computer-based simulations in the surgical procedure planning for aortic valve replacement, moving through a new paradigm in medicine which aims at reinforcing diagnosis with prediction. In fact, the constant technological advancement of medical imaging and computational mechanics and their appropriate combination allows to overcome past modeling limitations leading to new models which can replicate the physio-pathological problems in a more accurate manner.

Certainly, the use of computational biomechanics to study the aortic valve is far from being exhausted. Highly-impact results will certainly come up in the next future from the numerous research fields addressing the aortic root mechanics.

Dedicated fluid structure interaction analyses including a compliant root and valve coaptation using physiologically realistic conditions may certainly provide a better insight into the aortic root dynamics [77].

Moreover, the improvement of dedicated constitutive material models allows for the inclusion of several complexities of the valve tissue and material models embedded within commercial finite element software certainly enhance their applicability [8].

Nevertheless, the development of multiscale models is also enhancing the capability of computational studies to analyze the impact of mechanical effects on the cellular or tissue level opening the doors to further understanding of diseased conditions such as calcified aortic stenosis [123].

Finally, it is clear that all these research directions have to be coordinated and integrated through a consistent multidisciplinary approach based on a closer interaction between clinical reality and engineering science.

Acknowledgments The work presented within this book chapter reflects a research activity which has been partially funded by Cariplo Foundation through the Project no. 2009.2822, partially by the European Research Council through the Project no. 259229 entitled 'ISOBIO: Isogeometric Methods for Biomechanics' and partially by the Ministero dell'Istruzione, dell'Universitàà e della Ricerca through the project n. 2010BFXRHS.

The authors would acknowledge also Dr. M. Aiello of IRCCS Policlinico San Matteo, Pavia, Italy, and Prof. S. Petronio of Ospedale di Cisanello, Pisa, Italy, for their support on medical

aspects related to the present work, and Dr. A. Valentini of IRCCS Policlinico San Matteo, Pavia, Italy, for support to the imaging aspects of the study.

References

1. Aboud, A., Breuer, M., Bossert, T., Gummert, J.: Quality of life after mechanical vs. biological aortic valve replacement. Asian Cardiovasc. Thorac. Ann. **17**, 35–38 (2010)
2. Alastrue, V., Garia, A., Pena, E., Rodriguez, J., Martinez, M., Doblare, M.: Numerical framework for patient-specific computational modelling of vascular tissue. Int. J. Numer. Methods Biomed. Eng. **26**, 35–51 (2010)
3. Arcidiacono, G., Corvi, A., Severi, T.: Functional analysis of bioprosthetic heart valves. J. Biomech. **38**, 1483–1490 (2005)
4. Auricchio, F., Di Loreto, M., Sacco, E.: Finite element analysis of a stenotic artery revascularization through a stent insertion. Comput. Methods Biomech. Biomed. Eng. **4**, 249–263 (2001)
5. Auricchio, F., Conti, M., Demertzis, S., Morganti, S.: Finite element analysis of aortic root dilation: a new procedure to reproduce pathology based on experimental data. Comput. Methods Biomech. Biomed. Eng. **14**(10), 875–882 (2011). doi:10.1080/10255842.2010.499867
6. Auricchio, F., Conti, M., Morganti, S., Totaro, P.: A computational tool to support pre-operative planning of stentless aortic valve implant. Med. Eng. Phys. **33**(10), 1183–1192 (2011). doi:10.1016/j.medengphy.2011.05.006
7. Auricchio, F., Conti, M., Ferrara, A., Morganti, S., Reali, A.: Patient-specific simulation of a stentless aortic valve implant: the impact of fibres on leaflet performance. Comput. Methods Biomech. Biomed. Eng. **0**(0), 1–9 (2012). doi:10.1080/10255842.2012.681645
8. Auricchio, F., Ferrara, A., Morganti, S.: Comparison and critical analysis of invariant-based models with respect to their ability in fitting human aortic valve data. Ann. Solid Struct. Mech. **4**, 1–14 (2012)
9. Aymard, T., Eckstein, F., Englberger, L., Stalder, M., Kadner, A., Carrel, T.: The Sorin Freedom SOLO stentless aortic valve: technique of implantation and operative results in 109 patients. J. Thorac. Cardiovasc. Surg. **139**, 775–777 (2010)
10. Azadani, A., Jaussaud, N., Matthews, P., Ge, L., Chuter, T., Tseng, E.: Transcatheter aortic valves inadequately relieve stenosis in small degenerated bioprostheses. Inter. Cardiovasc. Thorac. Surg. **11**, 70–77 (2010)
11. Bashey, R., Torii, S., Angrist, A.: Age-related collagen and elastin content of human heart valves. J. Gerontol. **20**, 203–208 (1967)
12. Beck, A., Thubrikar, M., Robicsek, F.: Stress analysis of the aortic valve with and without the sinuses of valsalva. J. Heart Valve Dis. **10**, 1–11 (2001)
13. Beholz, S., Dushe, S., Konertz, W.: Continuous suture technique for freedom stentless valve: reduced crossclamp time. Asian Cardiovasc. Thorac. Ann. **14**, 128–133 (2006)
14. Bentall, H., Bono, A.D.: A technique for complete replacement of the ascending aorta. Thorax **23**, 338–339 (1968)
15. Billiar, K.L., Sacks, M.S.: Biaxial mechanical properties of the natural and glutaraldehyde treated aortic valve cusp—Part I: Experimental results. J. Biomech. Eng. **122**, 23–30 (2000)
16. Borgognoni, C., Maizato, M., Leirner, A., Polakiewicz, M.B., Higa, O., Pitombo, R.: Effect of freeze-drying on the mechanical, physical and morphological properties of glutaraldehyde-treated bovine pericardium: evaluation of freeze-dried treated bovine pericardium properties. J. Appl. Biomater. Biomech. **8**, 186–190 (2010)
17. Butcher, J., Mahler, G., Hochaday, L.: Aortic valve disease and treatment: the need for naturally engineered solutions. Adv. Drug Deliv. Rev. **63**, 242–268 (2011)

18. Capelli, C., Taylor, A., Migliavacca, F., Bonhoeffer, P., Schievano, S.: Patient-specific reconstructed anatomies and computer simulations are fundamental for selecting medical device treatment: application to a new percutaneous pulmonary valve. Phil. Trans. R. Soc. **368**, 3027–3038 (2010)
19. Capelli, C., Bosi, M., Cerri, E., Nordmeyer, J., Odenwald, T., Bonhoeffer, P., Migliavacca, F., Taylor, S., Schievano, A.M.:Patient-specific simulations of transcatheter aortic valve stent implantation. Med. Biol. Eng. Comput. **368**, 183–192 (2012)
20. Carmody, C., Burriesci, G., Howard, I., Patterson, E.: An approach to the simulation of fluid–structure interaction in the aortic valve. J. Biomech. **39**, 158–169 (2006)
21. Cataloglu, A., Gould, P., Clark, R.: Validation of a simplified mathematical model for the stress analysis of human aortic heart valves. J. Biomech. **8**, 347–348 (1975)
22. Christie, G., Medland, I.: Finite Element in Biomechanics. Wiley, New York (1982)
23. Clark, R.: Stress-strain characteristics of fresh and frozen human aortic and mitral leaflets and chordae tendineae. J. Thorac. Cardiovasc. Surg. **66**, 202–208 (1973)
24. Clark, R., Butterworth, G.: Characterization of the mechanics of human aortic and mitral valve leaflets. Surg. Forum **22**, 134–136 (1971)
25. Clift, S., Fisher, J.: Finite element stress analysis of a new design of synthetic leaflet heart valve. In: Proceedings of the Institution of Mechanical Engineers—Part H, vol. 210, pp. 267–272 (1996)
26. Conti, C., Della Corte, A., Votta, E., Del Viscovo, L., Bancone, C., De Santo, L., Redaelli, A.: Biomechanical implications of the congenital bicuspid aortic valve: a finite element study of aortic root function from in vivo data. J. Thorac. Cardiovasc. Surg. **140**, 890–896 (2010)
27. Conti, C., Votta, E., Della Corte, A., Del Viscovo, L., Bancone, C., Cotrufo, M., Redaelli, A.: Dynamic finite element analysis of the aortic root from MRI-derived parameters. Med. Eng. Phys. **32**, 212–221 (2010)
28. Cribier, A., Saoudi, N., Berland, J., Savin, T., Rocha, P., Letac, B.: Percutaneous transluminal valvuloplasty of acquired aortic stenosis in elderly patients: an alternative to valve replacement. The Lancet **327**, 63–67 (1986)
29. Cribier, A., Eltchaninoff, H., Bash, A., Borenstein, N., Tron, C., Bauer, F., Derumeaux, G., Anselme, F., Laborde, F., Leon, M.: Percutaneous transcatheter implantation of an aortic valve prosthesis for calcific aortic stenosis: first human case description. Circulation **106**, 3006–3008 (2002)
30. David, T.: Aortic valve sparing operations. Ann. Thorac. Surg. **73**, 1029–1030 (2002)
31. David, T.E.: Aortic valve haemodynamics after aortic valve-sparing operations. Eur. J. Cardio-Thorac. Surg. **41**(4), 788–789 (2012). doi:10.1093/ejcts/ezr119
32. De Beule, M.: Finite element stent design. Ph.D. Thesis, University of Ghent (2007/2008)
33. de Hart, J., Cacciola, G., Schreurs, P., Peters, G.: Collagen fibers reduce stresses and stabilize motion of aortic valve leaflets during systole. J. Biomech. **31**, 629–638 (1998)
34. Driessen, N., Boerboom, R., Huyghe, J., Bouten, C., Baaijens, F.: Computational analyses of mechanically induced collagen fiber remodeling in the aortic heart valve. J. Biomech. Eng. **125**, 549–557 (2003)
35. Driessen, N., Bouten, C., Baaijens, F.: Improved prediction of the collagen fiber architecture in the aortic heart valve. J. Biomech. Eng. **127**, 329–336 (2005)
36. Driessen, N., Bouten, C., Baaijens, F.: A structural constitutive model for collagenous cardiovascular tissues incorporating the angular fiber distribution. J. Biomech. Eng. **127**, 494–503 (2005)
37. Dwyer, H., Matthews, P., Azadani, A., Ge, L., Guy, T.S., Tseng, E.: Migration forces of transcatheter aortic valves in patients with noncalcific aortic insufficiency. J. Thorac. Cardiovasc. Surg. **138**, 1227–1233 (2009)
38. Edwards Lifesciences web-page (last access on April 2011) The Edwards SAPIEN valve. http://www.edwards.com
39. Einstein, D., Reinhall, P., Nicosia, M., Cochran, R., Kunzelman, K.: Dynamic finite element implementation of nonlinear, anisotropic hyperelastic biological membranes. Comput. Methods Biomech. Biomed. Eng. **6**, 33–44 (2003)

40. Fann, J., Chronos, N., Rowe, S., Michiels, R., Lyons, B., Leon, M., Kaplan, A.: Evolving strategies for the treatment of valvular heart: preclinical and clinical pathways for percutaneous aortic valve replacement. Cathet. Cardiovasc. Intervent. **71**, 434–440 (2008)
41. Feindel, C., David, T.E.: Aortic valve sparing operations: basic concepts. Int. J. Cardiol. **97**, 61–66 (2004)
42. Freed, A., Einstein, D., Vesely, I.: Invariant formulation for dispersed transverse isotropy in aortic heart valves. Biomech. Model. Mechanobiol. **4**, 100–117 (2005)
43. Ganguly, G., Akhunji, Z., Neethling, W., Hodge, A.: Homograft aortic valve replacement: the experience of one unit. Heart Lung Circul. **13**, 161–167 (2004)
44. Gee, M., Forster, C., Wall, W.: A computational strategy for prestressing patient-specific biomechanical problems under finite deformation. Int. J. Numer. Methods Biomed. Eng. **26**, 52–72 (2010)
45. Glauber, M., Solinas, S., Karimov, J.: Technique for implant of the stentless aortic valve Freedom Solo. Multimed. Man. Cardiothorac. Surg. **13**, 161–167 (2007)
46. Gnyaneshwar, R., Kumar, R., Balakrishnan, K.: Dynamic analysis of the aortic valve using a finite element model. Ann. Thorac. Surg. **73**, 1122–1129 (2002)
47. Gould, P., Cataloglu, A., Dhatt, G., Chattophadyay, A., Clark, R.: Stress analysis of the human aortic valve. Comput. Struct. **3**, 377–384 (1973)
48. Gould, P., Cataloglu, A., Clark, R.: Mathematical modelling of human aortic valve leaflets. Appl. Math. Model. **1**, 33–36 (1976)
49. Gramiak, R., Shah, P.: Echocardiography of the normal and diseased aortic valves. Radiology **96**, 1–8 (1970)
50. Grande, K., Cochran, R., Reinhall, P., Kunzelman, K.: Mechanisms of aortic valve incompetence in aging: a finite element model. J. Heart Valve Dis. **8**, 149–156 (1999)
51. Grande, K., Cochran, R., Reinhall, P., Kunzelman, K.: Mechanisms of aortic valve incompetence: finite element modeling of aortic root dilatation. Ann. Thorac. Surg. **69**, 1851–1857 (2000)
52. Grande, K., Cochran, R., Reinhall, P., Kunzelman, K.: Mechanisms of aortic valve incompetence: finite element modeling of Marfan syndrome. J. Thorac. Cardiovasc. Surg. **122**, 946–954 (2001)
53. Grande-Allen, K.J., Cochran, R., Reinhall, P., Kunzelman, K.: Finite-element analysis of aortic valve-sparing: Influence of graft shape and stiffness. IEEE Trans. Biomed. Eng. **48**, 647–659 (2001)
54. Grbic, S., Ionasec, R., Vitanovski, D., Voigt, I., Wang, Y., Georgescu, B., Navab, N., Comaniciu, D.: Complete valvular heart apparatus model from 4d cardiac CT. Medical Image Anal. **16**(5), 1003–1014 (2012). doi:10.1016/j.media.2012.02.003
55. Grube, E., Laborde, J., Gerckens, U., Felderhoff, T., Sauren, B., Buellesfeld, L., Mueller, R., Menichelli, M., Schmidt, T., Zickmann, B., Iversen, S., Stone, G.: Percutaneous implantation of the CoreValve self-expanding valve prosthesis in high-risk patients with aortic valve disease: the Siegburg first-in-man study. Circulation **114**, 1616–1624 (2006)
56. Haj-Ali, R., Marom, G., Zekry, S.B., Rosenfeld, M., Raanani, E.: A general three-dimensional parametric geometry of the native aortic valve and root for biomechanical modeling. J. Biomech. **45**(14), 2392–2397 (2012). doi:10.1016/j.jbiomech.2012.07.017
57. Hammer, P.E., Chen, P.C., del Nido, P.J., Howe, R.D.: Computational model of aortic valve surgical repair using grafted pericardium. J. Biomech. **45**(7), 1199–1204 (2012). doi:10.1016/j.jbiomech.2012.01.031
58. Henderson, Y., Johnson, F.: Two modes of closure of heart valves. Heart **4**, 69–82 (1912)
59. Hoffman, J., Kaplan, S.: The incidence of congenital heart disease. J. Am. Coll. Cardiol. **39**, 1890–900 (2002)
60. Holmes, D., Nishimura, R., Feeder, G.: In-hospital mortality after balloon aortic valvuloplasty: frequency and associated factors. J. Am. Coll. Cardiol. **17**, 189–192 (1991)

61. Hopkins, R.: Aortic valve leaflet sparing and salvage surgery: evolution of techniques for aortic root reconstruction. Eur. J. Cardio-Thorac. Surg. **24**, 886–897 (2003)
62. Ionasec, R., Voigt, I., Georgescu, B., Wang, Y., Houle, H., Hornegger, J., Navab, N., Comaniciu, D.: Personalized modeling and assessment of the aortic-mitral coupling from 4d TEE and CT. In: Yang, G.Z., Hawkes, D., Rueckert, D., Noble, A., Taylor, C. (eds) Medical Image Computing and Computer-Assisted Intervention—MICCAI 2009, Lecture Notes in Computer Science, vol. 5762, pp. 767–775. Springer, Berlin (2009)
63. Iung, B., Baron, G., Butchart, E., Delahaye, F., Gohlke-Barwolf, C., Levang, O., Tornos, P., Vanoverschelde, J.L., Vermeer, F., Boersma, E., Ravaud, P., Vahanian, A.: A prospective survey of patients with valvular heart disease in Europe: the Euro heart survey on valvular heart disease. Eur. Heart J. **24**, 1231–1243 (2003)
64. Knierbein, B., Mohr-Matuschek, U., Rechlin, M., Reul, H., Rau, G., Michaeli, W.: Evaluation of mechanical loading of a trileaflet polyurethane blood pump valve by finite element analysis. Int. J. Artif. Organs **13**, 307–315 (1990)
65. Koch, T., Reddy, B., Zilla, P., Franz, T.: Aortic valve leaflet mechanical properties facilitate diastolic valve function. Comput. Methods Biomech. Biomed. Eng. **13**, 225–234 (2010)
66. Kulik, A., Bedard, P., Lam, B.K., Rubens, F., Hendry, P., Masters, R., Mesana, T., Ruel, M.: Mechanical versus bioprosthetic valve replacement in middle-aged patients. Eur. J. Cardio-Thorac. Surg. **30**, 485–491 (2006)
67. Kunzelman, K., Grande, K., David, T., Cochran, R., Verrier, E.: Aortic root and valve relationships: impact on surgical repair. J. Thorac. Cardiovasc. Surg. **107**, 162–170 (1994)
68. Labrosse, M., Beller, C., Robicsek, F., Thubrikar, M.: Geometric modeling of functional trileaflet aortic valves: development and clinical applications.. J. Biomech. **39**, 2665–2672 (2006)
69. Labrosse, M.R., Lobo, K., Beller, C.J.: Structural analysis of the natural aortic valve in dynamics: from unpressurized to physiologically loaded. J. Biomech. **43**(10), 1916–1922 (2010). doi:10.1016/j.jbiomech.2010.03.020
70. Labrosse, M.R., Boodhwani, M., Sohmer, B., Beller, C.J.: Modeling leaflet correction techniques in aortic valve repair: a finite element study. J. Biomech. **44**(12), 2292–2298 (2011). doi:10.1016/j.jbiomech.2011.05.032
71. Langdon, S., Chernecky, R., Pereira, C., Abdulla, D., Lee, J.M.: Biaxial mechanica/ structural effects of equibiaxial strain during crosslinking of bovine pericardial xenogrfat materials. Biomaterials **20**, 137–153 (1999)
72. Lee, J., Haberer, S.A., Boughner, D.R.: The bovine pericardial xenograft: I. Effects of fixation in aldehydes without constraints on the tensile viscoelastic properties of bovine pericardium. J. Biomed. Mater. Res. **23**, 457–475 (1989)
73. Lichtenstein, S., Cheung, A., Ye, J., Thompson, C., Carere, R., Pasupati, S., Webb, J.: Transapical transcatheter aortic valve implantation in humans: initial clinical experience. Circulation **114**, 591–596 (2006)
74. Lieberman, E., Bashore, T., Hermiller, J., Wilson, J., Pieper, K., Keeler, G., Pierce, C., Kisslo, K., Harrison, J., Davidson, C.: Balloon aortic valvuloplasty in adults: failure of procedure to improve long-term survival. J. Am. Coll. Cardiol. **26**, 1522–1528 (1995)
75. Liu, Y., Kasyanov, V., Schoephoerster, R.: Effect of fiber orientation on the stress distribution within a leaflet of a polymer composite heart valve in the closed position. J. Biomech. **40**, 1099–1106 (2007)
76. Lorell, B., Carabello, B.: Left ventricular hypertrophy: pathogenesis, detection, and prognosis. Circulation **102**, 470–479 (2000)
77. Marom, G., Haj-Ali, R., Raanani, E., Schafers, H.J., Rosenfeld, M.: A fluid-structure interaction model of the aortic valve with coaptation and compliant aortic root. Med. Biol. Eng. Comput. **50**, 173–182 (2012)
78. Martin, C., Pham, T., Sun, W.: Significant differences in the material properties between aged human and porcine aortic tissues. Eur. J. Cardio-Thorac. Surg. **40**, 28–34 (2011)
79. Martin, T., Palmer, J., Black, M.: A new apparatus for the in vitro study of aortic valve mechanics. Eng. Med. **7**, 229–230 (1978)

80. McKay, M.: The mansfield scientific aortic valvuloplasty registry: overview of acute hemodynamic results and procedural complications. J. Am. Coll. Cardiol. **17**, 189–192 (1991)
81. Messika-Zeitoun, D., Bielak, L., Peyser, P., Sheedy, P., Turner, S., Nkomo, V., Breen, J., Maalouf, J., Scott, C., Tajik, A., Enriquez-Sarano, M.: Aortic valve calcification : determinants and progression in the population. Arterioscl. Thromb. Vasc. Biol. **27**, 642–648 (2007)
82. Mohammadi, H., Bahramian, F., Wan, W.: Advanced modeling strategy for the analysis of heart valve leaflet tissue mechanics using high-order finite element method. Med. Eng. Phys. **31**, 1110–1117 (2009)
83. Nkomo, V.T., Gardin, J.M., Skelton, T.N., Gottdiener, J.S., Scott, C.G., Enriquez-Sarano, M.: Burden of valvular heart diseases: a population-based study. The Lancet **368**, 1005–1011 (2006)
84. Oses, P., Guibaud, J., Elia, N., Dubois, G., Lebreton, G., Pernot, M., Roques, X.: Freedom SOLO valve: early- and intermediate-term results of a single centre's first 100 cases. Eur. J. Cardio-Thorac. Surg. (2010). doi:10.1016/j.ejcts.2010.04.038
85. Padala, M., Sarin, E., Willis, P., Babaliaros, V., Block, P., Guyton, R., Thourani, V.: An engineering review of transcatheter aortic valve technologies. Cardiovasc. Eng. Technol. **1**, 77–87 (2010)
86. Pavoni, D., Badano, L., Musumeci, S., Frassani, R., Gianfagna, P., Mazzaro, E., Livi, U.: Results of aortic valve replacement with a new supra-annular pericardial stented bioprosthesis. Ann. Thorac. Surg. **82**, 2133–2138 (2006)
87. Perego, M., Veneziani, A., Vergara, C.: A variational approach for estimating the compliance of the cardiovascular tissue: an inverse fluid-structure interaction problem. SIAM J. Sci. Comput. **33**, 1181–1211 (2011)
88. Peterseim, D., Cen, Y., Cheruvu, S., Landolfo, K., Bashore, T., Lowe, J., Wolfe, W., Glower, D.: Long-term outcome after biologic versus mechanical aortic valve replacement in 841 patients. J. Thorac. Cardiovasc. Surg. **117**, 890–897 (1999)
89. Piazza, N., de Jaegere, P., Schultz, C., Becker, A., Serruys, P., Anderson, R.: Anatomhy of the aortic valvar complex and its implications of transcatheter implantation of the aortic valve. Circul. Cardiovasc. Intervent. **1**, 74–81 (2008)
90. Ranga, A., Bouchot, O., Mongrain, R., P, U., R, C.: Computational simulations of the aortic valve validated by imaging data: evaluation of valve-sparing techniques. Inter. Cardiovasc. Thorac. Surg. **5**, 373–378 (2006)
91. Ranga, A., Mongrain, R., Biadilah, Y., Cartier, R.: A compliant dynamic FEA model of the aortic valves. In: Proceedings of 12th IFToMM World Congress, Besancon (2007)
92. Remadi, J., Marticho, P., Nzomvuama, A., Degandta, A.: Preliminary results of 130 aortic valve replacements with a new mechanical bileaflet prosthesis: the Edwards MIRA valve. Inter. Cardiovasc. Thorac. Surg. **2**, 80–83 (2003)
93. Roger, V.L., Go, A.S., Lloyd-Jones, D.M., Adams, R.J., Berry, J.D., Brown, T.M., Carnethon, M.R., Dai, S., de Simone, G., Ford, E.S., Fox, C.S., Fullerton, H.J., Gillespie, C., Greenlund, K.J., Hailpern, S.M., Heit, J.A., Ho, P.M., Howard, V.J., Kissela, B.M., Kittner, S.J., Lackland, D.T., Lichtman, J.H., Lisabeth, L.D., Makuc, D.M., Marcus, G.M., Marelli, A., Matchar, D.B., McDermott, M.M., Meigs, J.B., Moy, C.S., Mozaffarian. D., Mussolino, M.E., Nichol, G., Paynter, N.P., Rosamond, W.D., Sorlie, P.D., Stafford, R.S., Turan, T.N., Turner, M.B., Wong, N.D., Wylie-Rosett, J.: Heart disease and stroke statistics—2011 update. Circulation **123**(4):e18–e209 (2011). doi:10.1161/CIR.0b013e3182009701
94. Rousseau, E., van Steenhoven, A., Janssen, J., Huysmans, H.: A mechanical analysis of the closed hancock heart valve prosthesis. J. Biomech. **21**, 545–562 (1988)
95. Sabbah, H., Hamid, M., Stein, P.: Estimation of mechanical stresses on closed cusps of porcine bioprosthetic valves: effects of stiffening, focal calcium and focal thinning. Am. J. Cardiol. **55**, 1091–1096 (1985)
96. Sabbah, H., Hamid, M., Stein, P.: Mechanical stresses on closed cusps of porcine bioprosthetic valves: correlation with sites of calcification. Ann. Thorac. Surg. **42**, 93–96 (1986)

97. Saremi, F., Achenbach, S., Arbustini, E., Narula, J.: Revisiting Cardiac Anatomy: A Computed-Tomography Based Atlas and Reference. Wiley-Blackwell, New York (2011)
98. Sarsam, M., Yacoub, M.: Remodeling of the aortic valve anulus. J. Thorac. Cardiovasc. Surg. **105**, 435–438 (1993)
99. Sauren, A.: The mechanical behavior of the aortic valve. Ph.D. Thesis, Technische hogeschool Eindhoven (1983)
100. Schievano, S., Taylor, A., Capelli, C., Lurz, P., Nordmeyer, J., Migliavacca, F., Bonhoeffer, P.: Patient specific finite element analysis results in more accurate prediction of stent fractures: application to percutaneous pulmonary valve implantation. J. Biomech. **43**(4), 687–693 (2010)
101. Sedrakyan, A., Hebert, P., Vaccarino, V., Paltiel, A., Elefteriades, J., Mattera, J., Lin, Z., Roumanis, S., Krumholz, H.: Quality of life after aortic valve replacement with tissue and mechanical implants. J. Thorac. Cardiovasc. Surg. **128**, 266–272 (2004)
102. Smuts, A., Blaine, D., Scheffer, C., Weich, H., Doubell, A., Dellimore, K.: Application of finite element analysis to the design of tissue leaflets for a percutaneous aortic valve. J. Mech. Behav. Biomed. Mater. **4**, 85–98 (2011)
103. Stassano, P., Di Tommaso, L., Monaco, M., Iorio, F., Pepino, P., Spampinato, N., Vosa, C.: Aortic valve replacement: a prospective randomized evaluation of mechanical versus biological valves in patients ages 55 to 70 years. J. Am. Coll. Cardiol. **54**, 1862–1868 (2009)
104. Stein, P., Munter, W.: New functional concept of valvular mechanics in normal and diseased aortic valves. Circulation **44**, 101–108 (1971)
105. Stewart, B., Siscovick, D., Lind, B., Gardin, J., Gottdiener, J., Smith, V., Kitzman, D., Otto, C.: Clinical factors associated with calcific aortic valve disease. J. Am. Coll. Cardiol. **29**, 630–634 (1997)
106. Stradins, P., Lacis, R., Ozolanta, I., Purina, B., Ose, V., Feldmane, L.: Comparison of biomechanical and structural properties between human aortic and pulmonary valve. Eur. J. Cardio-Thorac. Surg. **26**, 634–639 (2004)
107. Sun, W., Sacks, M.: Finite element implementation of a generalized Fung-elastic constitutive model for planar soft tissues. Biomech. Model. Mechanobiol. **4**, 190–199 (2005)
108. Sun, W., Li, K., Sirois, E.: Simulated elliptical bioprosthetic valve deformation: implications for a symmetric transcatheter valve deployment. J. Biomech. **43**, 3085–3090 (2010)
109. Sung, H.W., Chen, W.Y., Chiu, C.T., Chen, C.N., Liang, H.C.: Crosslinking characteristics and mechanical properties of a bovine pericardium fixed with a naturally occurring crosslinking agent. J. Biomed. Mater. Res. **47**, 116–126 (1999)
110. Sutton, J., Ho, S., Anderson, R.: The forgotten interleaflet triangles: a review of the surgical anatomy of the aortic valve. Ann. Thorac. Surg. **59**, 419–427 (1995)
111. AHA Committee: Heart disease and stroke statistics 2010 update: a report from the American heart association. Circulation **121**, e46–e215 (2010)
112. Thubrikar, M.: The Aortic Valve. CRC Press, Boca Raton (1990)
113. Thubrikar, M., Nolan, S., Aouad, J., Deck, J.: Stress sharing between the sinus and leaflets of canine aortic valves. Ann. Thorac. Surg. **42**, 434–440 (1986)
114. Thubrikar, M.J., Labrosse, M.R., Zehr, K.J., Robicsek, F., Gong, G.G., Fowler, B.L.: Aortic root dilatation may alter the dimensions of the valve leaflets. Eur. J. Cardio-Thorac. Surg. **28**, 850–856 (2005)
115. Totaro, P., Degno, N., Zaidi, A., Youhana, A., Argano, V.: Carpentier-Edwards PERIMOUNT Magna bioprosthesis: a stented valve with stentless performance?. J. Thorac. Cardiovasc. Surg. **130**, 1668–1674 (2005)
116. Totaro, P., Morganti, S., Auricchio, F., Vigano, M.: Computer-based analysis to optimize prosthesis sizing during aortic valve surgery. Int. J. Cardiol. **151**(2), 253–254 (2011). doi:10.1016/j.ijcard.2011.06.079

117. Totaro, P., Morganti, S., Ngo ~ Yon, C.L., Dore, R., Conti, M., Auricchio, F., Vigano, M.: Computational finite element analyses to optimize graft sizing during aortic valve-sparing procedure. J. Heart Valve Dis. **21**(2), 141–147 (2012)
118. Trowbridge, E.A., Black, M.M., Daniel, C.L.: The mechanical response of glutaraldehyde fixed bovine pericardium to uniaxial load. J. Mater. Sci. **20**, 114–140 (1985)
119. Tzamtzis, S., Viquerat, J., Yapc, J., Mullenc, M., Burriesci, G.: Numerical analysis of the radial force produced by the Medtronic-CoreValve and Edwards-Sapien after transcatheter aortic valve implantation (TAVI). Med. Eng. Phys. **35**, 125–130 (2012) doi:10.1016/j.medengphy.2012.04.009
120. Vesely, I.: The role of elastin in aortic valve mechanics. J. Biomech. **31**, 115–123 (1998)
121. Wang, Q., Sirois, E., Sun, W.: Patient-specific modeling of biomechanical interaction in transcatheter aortic valve deployment. J. Biomech. **45**(11), 1965–1971 (2012)
122. Webb, J., Chandavimol, M., Thompson, C., Ricci, D., Carere, R., Munt, B., Buller, C., Pasupati, S., Lichtenstein, S.: Percutaneous aortic valve implantation retrograde from the femoral artery. Circulation **113**, 842–850 (2006)
123. Weinberg, E., Shahmirzadi, D., Mofrad, M.: On the multiscale modeling of heart valve biomechanics in health and disease. Biomech. Model. Mechanobiol. **9**, 373–387 (2010)
124. Xiong, F., Goetz, W., Chong, C., Chua, Y., Pfeifer, S., Wintermantel, E., Yeo, J.: Finite element investigation of stentless pericardial aortic valves: relevance of leaflet geometry. Ann. Biomed. Eng. **38**, 1908–1918 (2010)
125. Yap, C.H., Yii, M.: Allograft aortic valve replacement in the adult: a review. Heart Lung Circul. **13**, 41–51 (2004)
126. Yushkevich, P., Piven, J., Hazlett, H., Smith, R., Ho, S., Gee, J., Gerig, G.: User-guided 3D active contour segmentation of anatomical structures: significantly improved efficiency and reliability. Neuroimage **31**(3), 1116–1128 (2006)

Cardiac Restraint and Support Following Myocardial Infarction

Samantha A. Clarke, Ravi K. Ghanta, Gorav Ailawadi and Jeffrey W. Holmes

Abstract Myocardial infarction occurs when blood supply to a region of the myocardium is interrupted or eliminated, leading within seconds to loss of active contraction in the affected region and within minutes to cardiomyocyte death. Unable to contract, the infarct stretches passively each time the heart generates pressure, creating an immediate mechanical disadvantage and, if the infarct is large, triggering a cascade of pathological ventricular remodeling that eventually leads to heart failure. Therefore, a variety of therapies have been explored to mechanically reinforce the infarcted heart in the hopes of improving cardiac function and limiting adverse remodeling. This chapter will discuss two major strategies for mechanical support post-MI: globally restraining one or both ventricles, or locally reinforcing only the infarct area. Several ventricular restraint devices and a variety of local reinforcement approaches are compared and evaluated for their ability to reduce left ventricular remodeling and improve cardiac function following myocardial infarction. A variety of metrics used to quantify cardiac function are discussed, including limitations of frequently used functional indices. Differences in efficacy between synthetic and cell-seeded or tissue engineered patches for local reinforcement are investigated, followed by a brief discussion of the importance of patch material properties. Finally, methods for

S. A. Clarke · G. Ailawadi · J. W. Holmes (✉)
Department of Biomedical Engineering, University of Virginia, Charlottesville, Virginia, US
e-mail: holmes@virginia.edu

R. K. Ghanta · G. Ailawadi
Department of Surgery, University of Virginia, Charlottesville, VA, US

J. W. Holmes
Robert M. Berne Cardiovascular Research Center, University of Virginia, Charlottesville, VA, US

J. W. Holmes
Department of Medicine, University of Virginia, Health System, 800759 Charlottesville, VA 22908, US

Stud Mechanobiol Tissue Eng Biomater (2014) 15: 169–206
DOI: 10.1007/8415_2013_163

Published Online: 5 June 2013

optimizing the type and degree of reinforcement are presented, including both experimental and computational approaches.

1 Mechanics of Myocardial Infarction

Each year, over 1 million Americans will suffer a new or recurrent heart attack, or myocardial infarction (MI) [1]. An MI most commonly occurs when a coronary artery becomes occluded, cutting off blood flow to the area of myocardium supplied by that vessel (Fig. 1). Within minutes, the ischemic region becomes passive and non-contractile. Since the mechanical properties of the infarct still closely mirror those of normal, passive myocardium, the diastolic filling phase of the cycle remains unaffected [2]. However, during systole the infarct stretches and bulges outward while the rest of the heart is contracting and moving inward. As a result, the mechanical efficiency of the heart as a pump and the volume of blood the heart is able to eject with each beat are decreased, leading to a series of short and long term compensatory changes [3]. Diastolic pressure and volume rise, leading to enhanced contractility of the viable myocardium through the Frank-Starling mechanism [4]. Reflex activation of the sympathetic nervous system can also help preserve cardiac output (CO) by enhancing contractility and increasing heart rate (HR). This sympathetic stimulation helps to limit the severity of functional depression acutely post-MI, but becomes problematic in the long term; prolonged sympathetic activation is frequently associated with progression of chronic heart failure (CHF) [5, 6].

After several hours of occlusion, the passive properties of the nonviable myocardium do start to change, with clear infarct stiffening by 6 hr post-occlusion [7, 8]. The first week following MI is dominated by processes of inflammation and necrosis, and although infarct stiffening is observed, the scar is also most prone to rupture during this time [9]. In this week, necrotic muscle is being degraded with limited deposition of new collagen, which in combination with the infarct expansion and thinning that is also likely to occur, leaves the infarct area mechanically compromised. However, by the end of the first week post-MI, fibroblasts rapidly infiltrate the infarct scar and subsequent deposition of new collagen fibers by these fibroblasts rises quickly [10]. Over the course of the next few weeks, infarct stiffness rises with increasing collagen content, but the mechanical behavior of the scar that forms also depends heavily on the structure of the collagen fibers that constitute it. In some infarcts, parallel collagen fibers give rise to an anisotropic scar that is much stiffer in the fiber direction, while randomly oriented collagen fibers in others result in an isotropic scar that exhibits the same stiffness in both the fiber and cross-fiber directions [11–13]. Different animal models have been shown to form different scar structures, as have different infarct locations in the same animal model; we recently showed that patterns of stretch in the scar during healing correlate with scar structure across these animal models

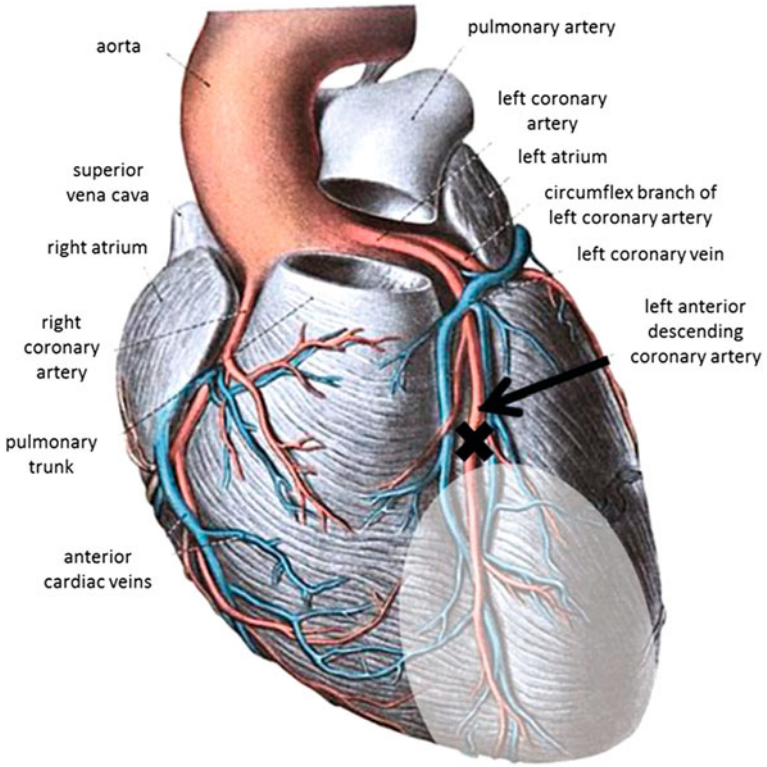

Fig. 1 A myocardial infarction (MI) occurs when a coronary artery, here the *left* anterior descending (LAD) artery (marked by the *black arrow*), becomes occluded, leaving the myocardium normally perfused by that vessel (shaded in *light gray*) without blood supply (adapted from [70])

and proposed that mechanical guidance of scar formation could explain much of the reported variation [14, 15].

After several weeks of healing, the infarct is stiffer than normal myocardium and remains so indefinitely. Scar compaction is observed in some animal models (especially dogs), resulting in a smaller, denser scar [16]. The left ventricle (LV) continues to remodel for several months, and in the case of small infarcts LV function generally improves throughout the healing process [17]. Unfortunately, the opposite is observed for large infarcts where dysfunction is too severe; compensatory mechanisms are insufficient and pathological remodeling processes dominate [18, 19]. As opposed to compacting, the infarct gradually becomes larger and thinner, compromising the mechanical integrity of the scar and exacerbating contractile dysfunction in the borderzone myocardium. In these cases, continuing dilation of the entire ventricle leads to increased wall stresses and further dilation, creating a positive feedback loop that ultimately leads to heart failure (HF).

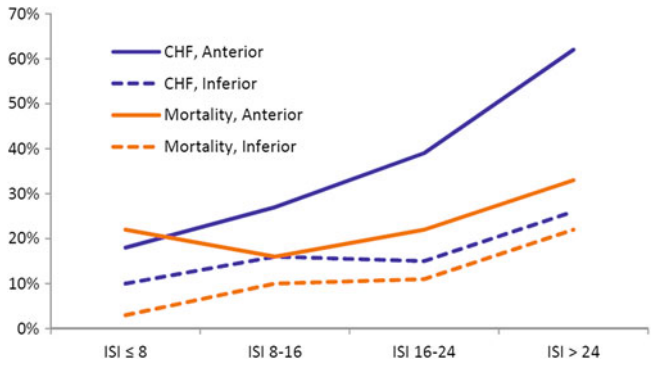

Fig. 2 Prevalence of CHF and mortality in human MI patients. Data were collected over an average follow-up period of 30.8 months post-MI and are stratified by infarct size (*ISI* = infarct size index) and location (based on data from [20])

1.1 Rationale for Mechanical Reinforcement of the Left Ventricle Post-MI

As discussed above, myocardial dysfunction in the infarct area triggers a series of compensatory mechanisms that can ultimately lead to heart failure. Patients who suffer a large MI on the anterior wall [arising from occlusion of the left anterior descending coronary artery (LAD)] are especially at risk, and exhibit HF and cardiac mortality rates more than double those for patients with infarcts in other locations [20]. When stratified by infarct size, 62 % of hearts in the largest anterior infarct quartile developed CHF over an average of 30.8 months post-MI (Fig. 2) [20]. Therefore, preventing or slowing the development of HF is a central therapeutic goal in treating patients who survive an infarction. Current pharmacologic therapies aim to reduce both LV dilation (angiotensin converting enzyme inhibitors) and sympathetic activation (beta-adrenergic blockers). In addition, a number of mechanical reinforcement strategies have been proposed. This chapter will review and discuss those mechanical reinforcement strategies, and is organized roughly in the order these approaches appeared in the literature. Work in this area began with efforts to restrain and stimulate the failing heart by wrapping the epicardium with the latissimus dorsi muscle and stimulating the skeletal muscle wrap to contract [21, 22]. However, later clinical studies showed that the passive restraint effect of the wrap was the principal source of its efficacy, and the procedure was subsequently abandoned because of its complexity [23]. Building on the promising results of passive restraint, devices were then developed to treat end-stage HF by physically restraining the LV, and use of these devices was later extended from treatment of HF to prevention of LV dilation post-MI. Next, several groups considered whether localized mechanical restraint of the infarct could similarly limit LV dilation. More recently, a number of variants on local restraint—including tissue-engineered or cell-seeded patches and anisotropic

reinforcement—aim to prevent the progression to HF by improving LV function early after infarction, instead of or in addition to physically preventing dilation.

1.2 Metrics for Measuring and Reporting Improvements in Pump Function

There are many metrics that are used to compare cardiac function across treatment groups or experimental states. The slope of the end-systolic pressure–volume relationship (ESPVR) and the peak rate of systolic pressure generation, (dp/dt) are fairly reliable indicators of systolic contractility, although simultaneous changes in diastolic function can potentially offset systolic improvements. By contrast, many studies of cardiac reinforcement and restraint report recovery of systolic function assessed by ejection fraction (EF), systolic wall thickening (WT), or fractional shortening (FS), all of which must be interpreted with caution in the post-MI or failing heart.

EF reflects the volume of blood that the heart is able to eject with each beat, or stroke volume (SV), as a percentage of the end-diastolic volume (EDV):

$$EF = \frac{SV}{EDV}$$

Although it is the most commonly reported functional measure, EF is particularly difficult to interpret in the setting of post-infarction remodeling, for two reasons. First, because the heart compensates for infarction using the Frank-Starling mechanism, changes in SV are difficult to interpret unless end-diastolic pressure (EDP) is also measured. For example, in the setting of a large acute infarct, SV typically changes little while LV EDP increases dramatically; the combination of unchanged SV and increased EDP clearly indicate reduced pumping capacity, while the isolated fact that SV is unchanged could be easily misinterpreted. Changes in HR due to sympathetic activation can similarly confound interpretation of SV. Second, once the heart begins to dilate, changes in the denominator of the EF calculation can also be misleading. EDV can change due to growth and remodeling of the heart as well as due to changes in preload, causing changes in EF that may be unrelated to actual pump function. In order to fully understand and separate functional and geometric changes during post-infarction remodeling and therapy, it is important to assess function by comparing Starling curves (plots of CO as a function of LV EDP), or at least hemodynamics at matched pressures. A similar logic applies to changes in LV EDV and end-systolic volume (ESV) from a pre-intervention baseline commonly used to evaluate the degree of LV cavity dilation as the ventricle remodels. Because both remodeling and changes in hemodynamics will affect these volumes, it is important to assess diastolic and systolic volumes at matched pressures, or even better over a range of pressures (i.e., comparing pressure–volume relationships).

Local metrics used to assess function include infarct or borderzone FS, which describe the percent decrease in LV short axis diameter from end-diastole (ED) to end-systole (ES), and systolic WT, which describes the percent increase in wall thickness from ED to ES. As will be described in the CorCap restraint section, extensive mechanical coupling between the infarct and borderzone allows transmission of abnormal motion from the scar to the surrounding myocardium. Tethering to an excessively compliant or stiff scar can directly cause functional impairment of the adjacent viable and otherwise normal myocardium. Therefore, differences in systolic FS or WT may be partially reflective of changes in scar mechanical properties or in mechanical coupling between the muscle and scar. Additionally, both of these indices assume that radial wall motion implies active contraction, yet we know that both coupling to adjacent myocardium and prominent shearing can decouple WT from active shortening in healing infarcts. For example, using implanted radiopaque markers filmed with high-speed cineradiography, we observed apparently normal levels of WT in the center of 3-week-old porcine infarcts, despite the fact that on histology these infarcts contained >60 % collagen and no apparently viable myocytes [13]. Because so few studies of infarct mechanics and post-infarction therapy have measured both regional and global function over a range of preloads, the relationship between regional shortening or thickening in the infarct and border zone and global pump function remains unclear, suggesting caution should be used in drawing conclusions about global function from regional measures.

2 Bi-Ventricular Restraint

This section will discuss several devices that have been used to restrain one or both ventricles following MI. Although most ventricular restraint devices were developed and designed to support the failing heart, their use has been extended to include reinforcement of the compromised (including post-MI) heart. The rationale for total ventricular restraint in HF is to limit further dilation of the ventricle, and potentially even reverse some of the dilation that has already occurred. Restraint following MI has the same objective, although if the device is applied early enough post-MI, it can also serve to prevent significant cavity dilation before it occurs. We limit our discussion here to four well studied reinforcement devices that illustrate the overall approach.

2.1 Acorn CorCap

The Acorn Corcap cardiac support device (CSD) is a mesh-like device that surrounds the heart, covering both the left and right ventricles (Fig. 3). The knitted polyester construction makes the device fairly compliant, although it is designed to provide diastolic support that is greater in the circumferential direction than in the

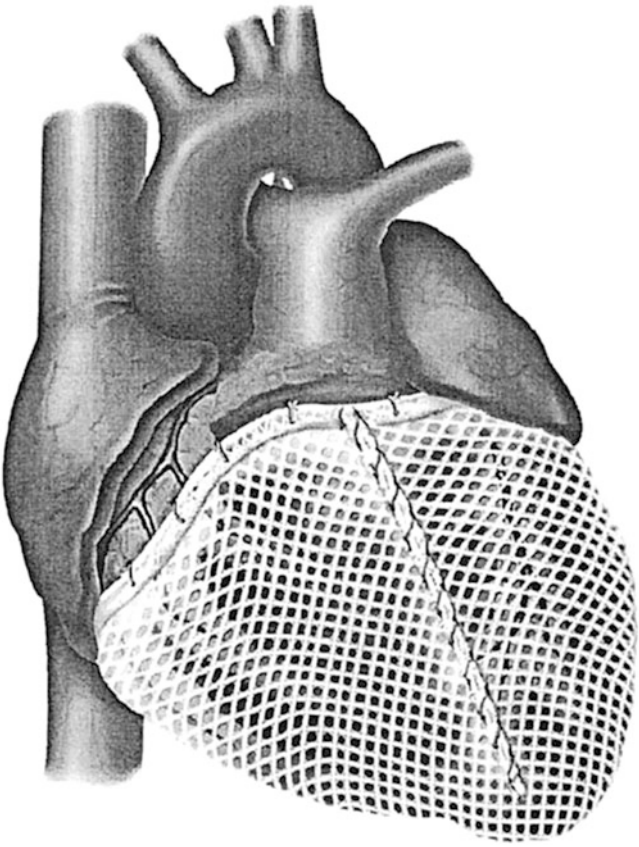

Fig. 3 Acorn CorCap cardiac restraint device (reproduced with permission from [71])

apex-base direction [24]. Prior to implantation, the most appropriate CSD is chosen from 6 available sizes. The CSD is first attached to the epicardium with a ring of sutures around the base of the heart. The two abutting edges of the CSD are then drawn together and sutured, creating a seam on the anterior wall. By controlling the amount of mesh drawn into the anterior seam, the surgeon can further adjust the CSD fit and can also generate substantial amounts of circumferential tension in the device [24]. When properly positioned and tightened, the device is intended to bear enough of the end-diastolic load to reduce the degree of stretching and the magnitude of wall stress.

2.2 Animal Studies of the Acorn CorCap in Heart Failure

Prior to testing the ability of the CorCap to prevent pathological remodeling post-MI, its efficacy to reduce or reverse the progression of heart failure was

established. Power and colleagues studied the effects of CorCap implantation in an ovine model [25]. HF was induced in 12 sheep through rapid pacing of the right ventricle over 21 days. After completion of the initial pacing regimen, animals were surgically instrumented with the Acorn CSD, which was retained in half of the animals and subsequently removed before closing in the remaining half of the animals (sham procedure). Rapid pacing was then resumed for another 28 days following the implant procedure. Left ventricular cavity dimensions were measured using echocardiography and hemodynamics were measured with an LV pressure catheter and aortic flow probe. A baseline study was performed prior to the first round of pacing, a HF baseline after the first 3 weeks of pacing, and a final study 4 weeks after CSD implantation with continued pacing. At the completion of the study, the CorCap group showed significantly smaller LV cross-sectional area than the sham group, although areas in both groups were more than double those at baseline. LV FS also decreased from baseline in both groups, although the CorCap group showed significantly greater preservation of shortening compared to sham. Few hemodynamic differences between the treatment and control groups were observed at the final time point, although minimum LV pressure was found to be significantly lower in the CSD group. SV, CO, and dP/dt were all similar between the two groups at the completion of the study.

The CorCap was also tested in a large animal model of heart failure resulting from global ischemia rather than rapid pacing. [26]. Intracoronary microembolization, in which sequential injections of latex microspheres into the coronary arteries lead to myocardial necrosis and depressed function, was used to induce HF in dogs. An average total of 6.4 microembolizations, each spaced by 1–3 weeks, were required to produce enough dysfunction to reach an EF within the target range of 30–40 %. Two weeks after the last microembolization, 6 dogs were surgically instrumented with the Acorn CSD while another 6 served as unoperated controls. Hemodynamic, angiographic, echocardiographic, and histological data were collected at the completion of the study, 3 months post-implantation. Comparisons between pre and 3 months post-implantation revealed a reversal in the progression of dilation as measured by LV EDV, which increased over the time course of the experiment in the control group but decreased in the CSD treatment group. In addition, the LV fractional area of shortening and LV sphericity index both increased in the treatment group with a concurrent decrease in the control group. Failing hearts tend to exhibit left ventricles that are more spherically shaped than normal, which is indicated by a decrease in the sphericity index, defined as the ratio of the lengths of the major axis/minor axis of the LV, where a value of 1 indicates a perfect sphere. Therefore, Chaudry and colleagues proposed that an increase in the sphericity index in the treatment group signified a reversal in the trend towards pathological remodeling seen in the control group [26]. Finally, on a cellular level, myocyte cross sectional areas were found to be smaller in the CorCap animals than in the control animals at study completion, indicating attenuation of hypertrophy with CSD treatment.

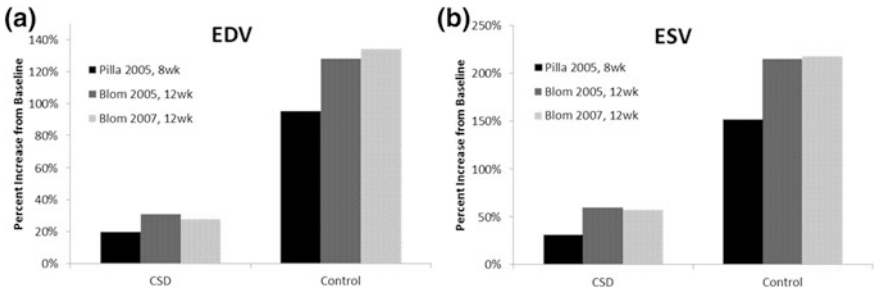

Fig. 4 Changes in end-diastolic **a** and end-systolic **b** LV volumes following post-infarction CorCap reinforcement. Volumes at the final time point for the CorCap CSD and control groups are represented as the percent increase from the pre-MI baseline value (based on data from [27–29])

2.3 Animal Studies of Acorn CorCap Implantation Following Myocardial Infarction

Once the Acorn CorCap was shown to be promising for the treatment of heart failure, investigations of the device were expanded to include studies of its ability to prevent dilation following myocardial infarction. One group has conducted several studies in sheep to examine the effects of CorCap implantation following MI [27–29]. In each study, the infarct was created by permanently ligating all of the diagonal branches of the left anterior descending (LAD) coronary artery. One week post-MI, half of the animals underwent CSD implantation while the other half served as MI-only controls. MRI data in all studies from either 8 weeks, 12 weeks, or 3 months post-MI showed smaller EDV and ESV in the CSD group compared to control, indicating attenuation of LV dilation, although in all studies the final LV volumes in the treatment groups were still significantly higher than the pre-MI baseline (Fig. 4) [27–29]. Interestingly, inconsistent changes in infarct size were observed in two studies from the same group. Using the same final time point of 12 weeks post-MI, one of the studies found that reinforced infarcts were smaller in area than unreinforced infarcts, while the other showed infarct sizes were similar between the two groups [27, 28]. In both studies, the CorCap group exhibited higher EF than the control group, although SV in the two groups was similar [27, 28]. Compared to control animals, the CSD group also showed greater preservation of percent systolic WT and radial strain in the borderzone, which was defined to start at the infarct boundary and span 20° in the direction of the septum [27, 28]. This result highlights the impact of mechanical coupling between the non-contractile infarct and the surrounding, viable myocardium. The ability of the borderzone to contract normally can be inhibited by its tethering to the infarct at any stage of healing, whether by the stretching and bulging of an acute infarct or the presence of a very stiff, collagenous scar. These data suggest that mechanical reinforcement can act to ameliorate this transmitted dysfunction.

2.4 Clinical Trials of Acorn CorCap Implantation for Heart Failure in Humans

The Acorn Corcap CSD was first implanted in 32 patients in Germany and Australia in 1999 [30]. This initial safety study demonstrated improvements in New York Heart Association (NYHA) classification and LV size, with no device-related morbidity at 2 years post-implant [31]. In 2004, the pivotal Acorn Trial was initiated to test the hypothesis that the Acorn CSD would improve a composite score of survival, NYHA functional status, and freedom from cardiac procedures in patients with HF [32]. This prospective, multi-center, randomized trial enrolled 300 HF patients at 29 centers in the United States and Canada. Enrolled patients had NYHA class III-IV HF of either ischemic or nonischemic etiology. Patients were between ages 18 and 80 years, with an LV EF less than 35 % and LV end-diastolic diameter (EDD) greater than 60 mm. The trial design was complex, as it included patients with significant mitral regurgitation (MR) who required a mitral valve repair or replacement (MVR). Patients who required an MVR were randomized to MVR plus CSD (91 patients) or MVR alone (102 patients). Patients who did not require an MVR were randomized to CSD (57 patients) or control (50 patients). The primary outcome was a composite score based on survival, change in NYHA classification, and freedom from major cardiac procedures. Secondary outcomes included mortality, hospitalization, LV size, and quality of life. Patients were followed up at 3, 6, and 12 months and then annually for 5 years.

The initial operative mortality was 7.8 % (4/51) in CSD only patients and 2.2 % (2/91) in CSD plus MVR patients [33]. At 1 and 5 years there were no significant differences in adverse events between CSD and non-CSD patients [33–35]. Importantly, there were no cases of pericardial constriction—an often cited concern about the CSD. The Acorn trial confirmed that ventricular restraint reduced LV size. When averaged over 5 years, LV EDV in the CSD group was 28.9 ml less than in the control group ($p = 0.029$) [35]. In the MVR patients, LV EDV decreased by 75 ml in patients who underwent MVR alone, but an additional 16.5 ml incremental reduction was seen with MVR plus CSD [34]. In addition, the heart assumed a more ellipsoid shape, especially in the MVR patients. LV EF improved by 6 % in the MVR group, but there was no difference between the MVR and MVR plus CSD patients and no improvement in LV EF in the non-MVR patients.

These improvements in LV size and shape were secondary endpoints of the study; the primary endpoints of survival, improvement in NYHA classification, and freedom from major cardiac procedures were not as conclusive. There was a significant improvement in the composite primary endpoint at 1 year, but not at 5 years [34, 35]. In addition, no survival benefit was seen with the CSD. In logistic regression analysis, more patients improved by at least 1 NYHA classification in the CSD group than the control group ($p = 0.0005$). No significant benefit in freedom from cardiac procedures was reported. Thus, although the 5 year results of the study demonstrated sustained improvements in LV size and shape, the primary endpoints were not achieved. However, a subgroup analysis found that

patients with an LV EDV indexed to body surface area greater than 30 mm/m^2 and less than 40 mm/m^2 did have a benefit in the primary endpoint of the trial. The implication of this is that the CSD may be of greater benefit in patients with a moderate degree of dilation, who are not too advanced towards end-stage HF. A second-generation CSD that can be implanted through a minimally invasive approach in this focused cohort of patients with LV EDV between 30 mm/m^2 and 40 mm/m^2 is currently under investigation.

There have been numerous criticisms of the Acorn trial [36]. The complex design of the Acorn trial by inclusion of MVR and non-MVR strata made the data difficult to interpret. The challenges of follow-up in this patient population with four different sub-groups led to small patient numbers at 5 years. The patients in the study had primarily non-ischemic HF, whereas the majority of HF patients have ischemic HF. For these reasons and the relatively high observed operative mortality (7.8 %), the United States Food and Drug Administration (FDA) did not approve the device primarily over concerns of safety and efficacy. The device thus remains investigational.

2.5 Paracor HeartNet

The Paracor HeartNet cardiac support device is another passive, bi-ventricular restraint device that wraps around the epicardium of both the left and right ventricles (Fig. 5). The HeartNet consists of a wire mesh made of Nitinol, a nickel and titanium alloy. The device is designed to be flexible and elastic, so that a snug fit is achieved around the heart (if the appropriate device size is chosen pre-procedure) without making further adjustments like those required to implant the CorCap. Also unlike the CorCap and unlike native pericardium, stretch in the Paracor CSD has been shown to vary linearly with increasing pressure, and the HeartNet exhibits much greater compliance at high pressures than either of the other two (Fig. 6) [37].

One benefit of the HeartNet is the inclusion of a delivery system that makes the implantation procedure less invasive than for other CSDs. A small incision is made to allow access to the apex of the heart and an introducer port is inserted through the hole. The delivery system is then used to grasp the apex while the HeartNet is passed through the channel and deployed (Fig. 7) [38]. The elastic behavior of the mesh allows the device to conform to the shape of the epicardium and helps anchor the device in place.

2.6 Animal Studies of the Paracor HeartNet in Heart Failure

The effects of HeartNet implantation in heart failure have been examined using a similar canine microembolization model as described previously for the CorCap [39]. HF was induced in 10 dogs through daily embolization with small polymer

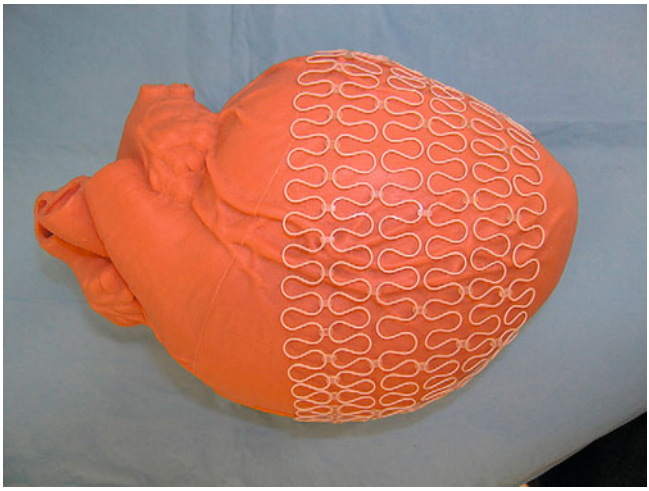

Fig. 5 Paracor HeartNet cardiac restraint device (reproduced with permission from [38])

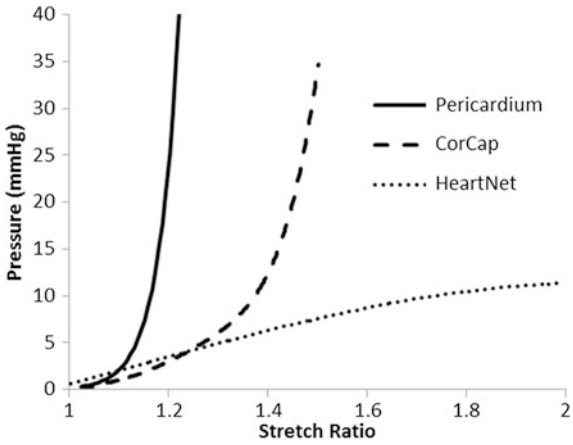

Fig. 6 Stiffnesses of the Acorn CorCap and Paracor HeartNet compared to that of normal pericardium (replotted from [37])

beads over an average of 6 weeks. The HeartNet was then implanted in 5 animals, while the remaining 5 underwent sham surgery. By 8 weeks after CSD implantation, the treatment group exhibited decreases in EDV and ESV from the pre-implantation HF state, compared to further increases in the control group volumes. PV loops shifted dramatically rightward and decreased in height between baseline and development of CHF, reflecting the increased volumes and reduced ability to generate systolic pressure in the dilated heart. Without reinforcement, PV loops in the control animals continued to shift rightward over the course of 8 weeks as the ventricle continued to dilate and systolic function progressively declined. By contrast, HeartNet reinforcement caused PV loops to shift leftward, back towards the pre-HF baseline.

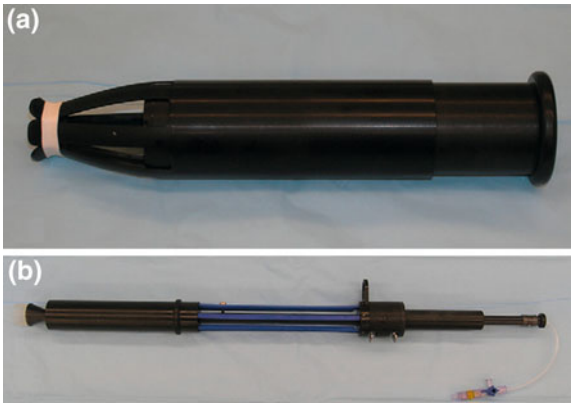

Fig. 7 Introducer sheath **a** delivery system **b** HeartNet implantation (reproduced with permission from [38])

2.7 Animal Studies of Paracor HeartNet Implantation Following Myocardial Infarction

The Paracor has also been studied in large animal models for post-MI reinforcement. One such study used an ovine model of coronary ligation similar to those in the CorCap studies, although this model employed permanent ligation of the main LAD as opposed to the diagonal branches [40]. Also unlike the studies described previously, infarction and reinforcement were performed as a single surgical procedure, with HeartNet implantation immediately following ligation in 7 of 14 animals. At 6 weeks post-MI, CSD animals exhibited smaller increases in LV mass, EDV, and ESV (all normalized to body surface area) compared to control animals. However, this apparent prevention of dilation did not seem to translate to improved function, as no differences in EF, SV or CO were found between the groups at the end of the study.

2.8 Clinical Trials of Paracor HeartNet Implantation for Heart Failure in Humans

The Paracor HeartNet device was initially implanted in 21 patients in the United States in 2007 [38]. Initial clinical safety and feasibility data demonstrated low complication rates in these 21 patients with nonischemic NYHA class II and III HF. Following this, a non-randomized, multi-institutional study of 51 patients demonstrated improvements in LV EDV, LV ESV, 6 min walk test, and Minnesota Living with Heart Failure (MLWHF) questionnaire at 6 months, with no device morbidity [38]. Based on these promising results, a randomized, multi-institutional trial [Prospective Evaluation of Elastic Restraint to Lessen the Effects of Heart Failure (PEERLESS-HF)] was then initiated to enroll 274 patients at 35

sites in the United States and Canada [41]. Enrolled patients had ischemic or nonischemic dilated cardiomyopathy requiring HF treatment for at least 3 months, LV EF less than 35 %, and LV EDD less than 85 mm. In addition, patients were required to attain a 6 min walk (6 MW) of 150–450 m with a peak VO2 of 10.0–20.0 ml/kg/min for males and 9.0–18.0 ml/kg/min for females. The primary safety outcome was all-cause mortality. The primary efficacy outcomes were improvement in peak VO2, 6 MW, and MLHWF score.

All-cause mortality at 12 months was similar between the HeartNet and control groups. At 6 months, the HeartNet group did have a greater decrease in LV mass ($p = 0.032$) and LV EDV ($p = 0.031$), compared to controls [41]. The peak VO2, which is a measure of exercise capacity and a strong predictor of survival in HF patients, was deemed an essential outcome by the FDA for evaluation of the device. At 6 months, an interim analysis revealed futility to achieve the peak VO2 endpoint, leading to suspension of the trial. Thus, like the Acorn Corcap device, despite sustained improvements in LV size, the primary outcome of the trial was not achieved. Subsequent subgroup analysis showed that the HeartNet device may have an enhanced benefit (decreased mortality, cardiac procedure, HF hospitalization) in patients receiving cardiac resynchronization therapy (CRT). A new study with the HeartNet device has been initiated in patients receiving CRT.

3 Left Ventricular Restraint Devices

In contrast to the sock-like structure of the Acorn and Paracor devices, which wrap around both ventricles, the Myocor Coapsys (Myosplint) and the CardioClasp interact with the LV only and take a different approach to modifying the shape of the heart. Also unlike the CorCap and HeartNet, the Coapsys and CardioClasp have not been well studied as post-MI therapies. Since implantation of both the Coapsys and CardioClasp may involve placing instrumentation directly into or over only part of the ischemic area (as opposed to reinforcing the entire infarct), it is possible that these devices have not been explored as post-MI treatments due to concerns regarding the potential for concentration of stresses within an already weakened acute infarct. Nevertheless, their efficacy as treatments for HF (both ischemic and nonischemic) has been evaluated through animal studies, clinical trials, and finite element modeling. Therefore, a brief discussion of each device has been included to illustrate these alternative mechanisms of generating LV restraint and to highlight the computational tools that have been used to evaluate them.

3.1 Myocor Coapsys (Myosplint)

The Myocor Coapsys has been referred to as the Myosplint in animal studies of the device but has been primarily called the Coapsys in human clinical trials.

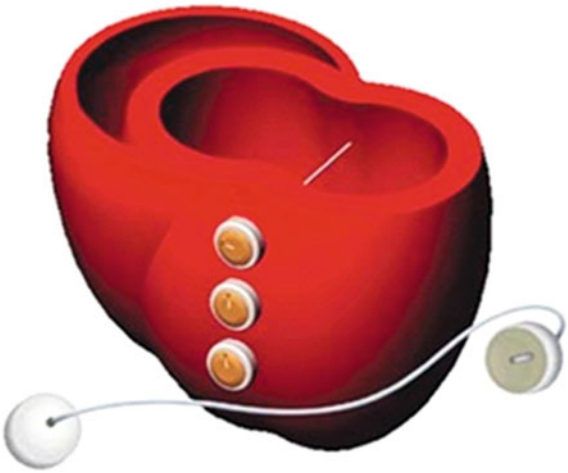

Fig. 8 Myocor Coapsys (Myosplint) left ventricular support device. Epicardial pads connected by tension members threaded through the LV cavity create a bilobular ventricle (reproduced with permission from [72])

The Coapsys is placed on the epicardium of the LV and consists of two rigid pads connected through the cavity. The pads are first positioned on opposing surfaces of the LV, one on the anterior and the other on the posterior wall, and then drawn together by the tension member, which is fed through the LV cavity (Fig. 8). Increasing the tension between the two epicardial pads reshapes the enlarged LV, creating a bilobular ventricle with decreased chamber radius [42]. Typically 3 Myosplints are used, aligned in a longitudinal (apex-base) line on the LV, and tension is adjusted until the radius of each new lobe is approximately 80 % of the radius of the un-reinforced LV cavity.

3.2 Animal Studies of the Myocor Coapsys in Heart Failure

The effects of Coapsys reinforcement were studied in a canine model of rapid pacing heart failure [42]. HF was established over an average of 27 days of rapid pacing in 20 animals, after which 3 Myosplints were implanted in each of 9 animals, while another 8 underwent sham surgery to serve as controls. At the end of the 4 week post-implantation follow-up period, CSD treated animals had significantly reduced EDV and ESV and increased EF compared to both the control group at 4 weeks and to the baseline, HF values (pre-implantation). However, despite dramatic attenuation of dilation, no major functional improvements were observed; SV, HR, CO, EDP and end-systolic pressure (ESP) were all similar between the 4 week treatment and control groups.

3.3 Computational Modeling of the Myocor Coapsys in Heart Failure

Up to this point in the chapter, all of the studies presented have been *in vivo*, large animal experiments or clinical studies. Another strategy that has been employed to explore the acute effects of mechanical reinforcement is computational modeling of restraint devices. Computational models have the potential advantage of allowing the investigator to explore many variants of a particular reinforcement strategy (different levels of restraint, different mechanical properties of a particular device, etc.) in order to select the combinations most likely to produce the desired result. These models also provide estimates of quantities that might be of interest but are difficult to measure directly, such as local changes in wall stress. Guccione et al. used a finite element model (FEM) to simulate the changes that occur immediately following Coapsys implantation in a failing heart [43]. First, an FEM of a globally dilated heart was generated to represent the HF state. Application of 3 Myosplints was simulated by modifying the mesh assuming a 25 % reduction in end-diastolic LV diameter at each attachment site. Not surprisingly, EDV and ESV were found to be reduced when the Coapsys model was inflated to the same EDP and ESP as the HF model. Starling curves for the pre- and post-operative models were almost identical, indicating that no functional improvement was generated by Coapsys restraint. However, dramatic reductions in average fiber stresses throughout the myocardium at both ED and ES were observed in the Coapsys FEM, suggesting potential for this type of reinforcement to retard or prevent further pathological remodeling in the compromised heart.

3.4 Clinical Trials of Myocor Coapsys (Myosplint) Implantation in Patients with Mitral Regurgitation

The Myocor Coapsys system was initially implanted in 34 patients with moderate or greater ischemic MR in 2003 in India [44]. Initial results were encouraging, demonstrating decreased MR with no device related adverse events. This led to the initiation of the Randomized Evaluation of Surgical Treatment for Off-Pump Repair of the Mitral Valve (RESTOR-MV) trial [45]. This randomized, multi-center trial enrolled 165 patients undergoing coronary artery bypass grafting (CABG) with moderate or greater ischemic MR. Patients were first divided based on candidacy for MVR. In the non-MVR group, patients were randomized to CABG only (8 patients) and CABG plus Coapsys (8 patients). In the MVR group, patients were randomized to CABG plus MVR (75 patients) and CABG plus Coapsys (74 patients). The primary outcomes were all-cause mortality, adverse events (stroke, myocardial infarction, reoperation, device failure), and decrease in MR.

Unfortunately the RESTOR-MV trial was terminated prematurely for financial reasons. An intention to treat analysis was performed on 2 year follow-up data

[45]. Overall survival was improved in patients who received the Coapsys versus control (89 versus 76 %; Hazard Ratio 0.421; $p = 0.038$). Overall freedom from adverse events was also improved in patients who received the Coapsys versus control (76 versus 63 %; Hazard Ratio 0.461; $p = 0.022$). The degree of reduction in MR was greater with CABG plus MVR (2.54–0.35) in comparison to CABG plus Coapsys (2.40–0.97), but LV EDD decreased more with CABG plus Coapsys (6.0–5.4 cm) than CABG plus MVR (5.9–5.6 cm).

In summary, Myocor Coapsys (Myosplint) demonstrated promising results in the RESTOR-MV trial with improved survival and decreased adverse events compared to standard surgical therapy. Coapsys also decreased MR, although not to the extent of standard surgical techniques. The survival advantage with Coapsys over standard surgery may be due to the additional effects of ventricular reshaping and reduction of wall stress with the Coapsys device. The future application of this device remains uncertain as the intellectual property rights for the device are being transitioned to new ownership, although new studies are anticipated.

3.5 CardioClasp

The final ventricular restraint device to be discussed in this chapter is similar in structure and design to the Coapsys. The CardioClasp CSD consists of two rigid bars connected through the LV cavity by an adjustable tether. The long, thin bars are designed to mimic the natural contours of the heart, and are attached to the epicardial surface via contact pads that are flexible along their length but not across their width. The bars are aligned longitudinally on the anterior and posterior walls, in a very similar configuration to the one used for placement of Myosplints. Following implantation, the tension in the tether is adjusted to draw the anterior and posterior bars together until an approximate 30 % reduction in the end-diastolic anterior-posterior dimension is observed [46]. The CardioClasp reinforcement scheme follows the same principle as described for Coapsys restraint: use anterior-posterior tension to reshape the LV cavity and create two lobes of smaller diameter in the hopes of reducing LV wall stresses and adverse remodeling.

Kashem et al. conducted a series of large animal studies on the acute effects of CardioClasp reinforcement in the canine rapid-pacing HF model [46–48] with CardioClasp reinforcement. Overall, they found an increase in fractional area of contraction, a decrease in ED and ES LV cavity area, and a decrease in estimated LV wall stress with CardioClasp reinforcement [46, 47]. Pressure–volume loop analysis revealed an increase in slope of ESPVR with CardioClasp implantation, indicating increased systolic contractility (Fig. 9) [47]. They saw similar increases in the slope of the systolic curves of pressure-area loops and pressure-segment length (in the anterior-posterior and septal-free wall directions) loops, which also shifted leftward [46, 48]. Despite changes in geometry and hemodynamics, EDP, ESP, CO and dP/dt all remained unchanged from their baseline HF values [46, 48].

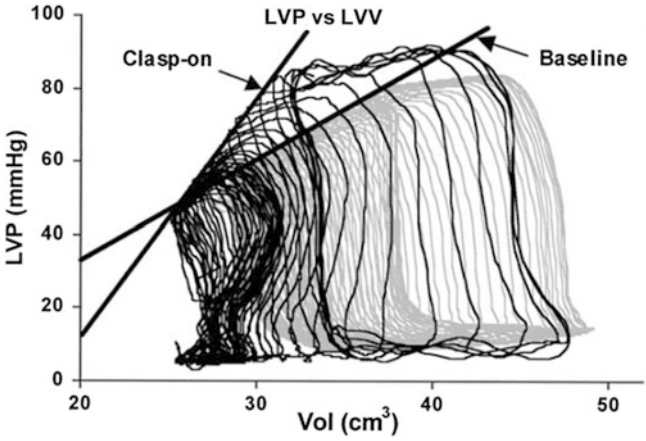

Fig. 9 Acute effects of CardioClasp implantation on the ESPVR of dogs with CHF. *Gray lines* are pre-implantation, *black lines* are post-implantation (reproduced with permission from [47])

4 Ventricular Restraint Limits Dilation, But Functional Changes Remain Unclear

A prominent theme that emerges from studies investigating the effects of cardiac restraint device implantation in HF or post-MI is that ventricular restraint reduces LV cavity size and decreases the severity of dilation. Therefore, these global approaches to ventricular reinforcement hold promise for preventing the development or reversing the progression of HF. However, multiple clinical trials have failed to demonstrate clear improvements in functional outcomes, and changes in functional indices employed in many animal studies are difficult to interpret (Table 1). Although most of the studies discussed in this chapter showed decreased LV volumes with mixed changes in functional metrics, there were some studies in which no functional differences at all were observed between the treatment and control groups. For example, Magovern et al. measured reductions in LV volume after HeartNet implantation but saw no changes in EF, SV or CO compared to control [40]. In general, studies of CorCap reinforcement showed increases in EF and systolic FS or WT, but no changes in SV, CO, or dP/dt. Therefore, it is possible that the device is producing improvements in systolic function, but as discussed in the beginning of this chapter, concurrent geometric and material changes in the heart also affect these indices (EF and FS/WT) and make it impossible to draw definitive conclusions from these values. Similar to the CorCap, mixed results were also obtained in studies of the other three ventricular restraint devices. Coapsys reinforcement increased EF without affecting SV or CO, while CardioClasp increased the fractional area of contraction (FAC) without changing CO or dP/dt. However, studies of both devices also showed increases in the slope of the systolic pressure–volume, pressure-short axis area, or pressure-segment length curves. Therefore, due

to the inconsistencies in the functional changes observed in the studies discussed and the difficultly in interpreting some of the indices used, the true effects of total ventricular restraint on cardiac function remain unclear. The final two studies listed in Table 1 will be discussed in the Optimizing Restraint section.

4.1 Limitations of Whole Ventricle Restraint

Although they have been shown to limit progression toward dilated heart failure following MI, there are still significant limitations associated with CSD use. A prominent drawback is the invasiveness of the procedures that are required to implant most of the devices. The risks of performing an open chest procedure on a patient who recently had a large MI make these devices unattractive as post-infarction therapies. Their clinical relevancy has been limited to patient subpopulations that are already scheduled to undergo an open chest procedure for a concurrent pathology, such as a coronary artery bypass or mitral valve repair. Another potential drawback of the total ventricular restraint approach for post-MI reinforcement is the possibility of interference with the normal myocardium. For example, implanting a globally stiff CSD may work well to reinforce a bulging infarct scar, but may also inhibit diastolic filling throughout the ventricle. Although several of the commercialized restraint devices (Acorn CorCap and Paracor HeartNet) have been shown to be much less stiff than the native pericardium that surrounds the heart, these devices have also been consistently shown to affect LV volumes. While long-term reductions in LV volumes can be indicative of attenuation of dilation, studies showing decreases in EDV during acute reinforcement suggest that global filling is immediately affected upon implantation. Local restraint approaches have attempted to address this issue by reinforcing only the nonviable infarct scar, and several variations of local restraint will be discussed in the following sections.

5 Local Restraint: Cardiac Patches

Once the idea of physically preventing post-infarction remodeling was established, it was natural to explore whether global restraint of the infarcted left ventricle is really necessary, or whether local restraint of the infarct region might be sufficient. Cardiac patches intended for local, post-infarction application have taken a variety of forms, from synthetic to cell-seeded to completely tissue engineered. Some aim to mechanically reinforce the infarct, while others are intended primarily to deliver growth factors or cells to the damaged region. An extensive summary of materials that have been used in the construction of cardiac patches can be found in Rane and Christman 2011 [49]. Although a multitude of tissue engineered and cell-seeded patches have been fabricated and tested, we will limit our discussion in

Table 1 Summary of ventricular restraint device studies

Reference	Animal	Infarct/HF model	Restraint device	EDV	ESV	EF	SV	CO	FS/FAS/WT	dP/dt	ESPVR
Power 1999	Sheep	Rapid pacing	CorCap				↔	↔	↑FS	↔	
Chaudry 2000	Dog	Micro-embolization	CorCap	↓					↑FAS		
Pilla 2005	Sheep	LAD ligation	CorCap	↓	↓				↑WT in BZ		
Blom 2005	Sheep	LAD ligation	CorCap	↓	↓	↑	↔				
Blom 2007	Sheep	LAD ligation	CorCap	↓	↓	↑			↑RS in BZ		
George 2007	Dog	Micro-embolization	HeartNet	↓	↓						
Magovern 2006	Sheep	LAD ligation	HeartNet	↓	↓	↔	↔	↔			
McCarthy 2001	Dog	Rapid pacing	Coapsys	↓	↓	↑	↔	↔			
Guccione 2003	Human	FEM	Coapsys	↓	↓			↔			↑ESPVR
Kashem 2002	Dog	Rapid pacing	Cardio-clasp						↑FAC		↑ESPSLR
Kashem 2003b	Dog	Rapid pacing	Cardio-clasp	↓ED CSA	↓ES CSA						↑ESPVR
Kashem 2003a	Dog	Rapid pacing	Cardio-clasp					↔		↔	↑ESPAR
Ghanta 2007	Sheep	LAD diag. ligation	Optimized QVR	↓		↑					
Lee 2012	Sheep	LAD diag. ligation	AMVR versus. static	↓	↓	↑					

HF = heart failure, *EDV* = end-diastolic volume, *ESV* = end-systolic volume, *EF* = ejection fraction, *SV* = stroke volume, *CO* = cardiac output, *FS* = fractional shortening, *FAS* = fractional area shortening, *FAC* = fractional area of contraction, *WT* = wall thickening, *RS* = radial strain, dP/dt = rate of systolic pressure generation, *ESPVR* (*ESPAR*, *ESPSLR*) = slope of the end-systolic pressure–volume (pressure-area, pressure-segment length) relationship, *BZ* = borderzone, *CSA* = cross-sectional area, *LAD* = left anterior descending coronary artery, *FEM* = finite element model, *QVR* = quantitative ventricular restraint, *AMVR* = adjustable and measureable ventricular restraint

this chapter to those that are attached to the epicardium of the heart in a manner that would allow the patch to have a mechanical effect. For example, regardless of the mechanical properties of the construct, a tissue engineered patch that is attached to the epicardium by a single suture in the center of the infarct will not be under tension and will not reduce the load placed on the scar.

5.1 Synthetic Patch Application Pre or Post-MI Reduces LV Dilation and Preserves LV Shape

Early studies of local restraint showed that placing synthetic patches over the anticipated infarct region prior to inducing MI could reduce infarct expansion and LV dilation. Kelley et al. used the ovine MI model of permanent LAD ligation to investigate the effects of patch application pre-MI [50]. A polypropylene mesh patch was sutured onto the epicardium of the expected ischemic area (determined by temporary LAD occlusion) 10–14 days prior to ligation. By 8 weeks post-MI (10 weeks after patch implantation), patch animals exhibited lower EDV and ESV, and higher CO, SV, EF, and SW compared to control, although hemodynamic measurements were not compared at matched EDP (Fig. 10). Patched ventricles also showed greater preservation of wall thickness in the infarcted apex. Moainie et al. used the same timeline of patch implantation and MI induction, only this time for an infarct arising from permanent ligation of the left circumflex (LCx) coronary artery instead of the LAD [51]. In contrast to the antero-apical infarcts that form in response to LAD occlusion, LCx infarcts develop on the posterior wall, closer to the base. In this study, implantation of a polypropylene patch 10–14 days prior to LCx ligation was unable to produce the hemodynamic benefits observed using the same patch prior to LAD ligation. At 8 weeks post-MI, no significant differences were observed in CO, SV or EF between the patch and control groups. However, both global and local measures showed significant attenuation of infarct expansion and LV cavity dilation with reinforcement. Infarct segment length at ED, EDV and ESV all rose substantially in control animals, while increases in patch animals were significantly less dramatic.

Because local restraint is intended to prevent infarct expansion, much of which occurs in the first few days after infarction, it seems logical to expect application of local patches to provide diminishing returns with increasing time after MI. A recent study by Liao and colleagues that showed significant geometric and hemodynamic benefits of local reinforcement 8 weeks after infarction was therefore very surprising [52]. Infarction was induced through embolization of the LCx, followed by implantation of a multi-layered, polypropylene and polytetrafluoroethylene patch at 8 weeks post-MI. At the 20 week post-MI endpoint, the patch reinforcement animals had greater preservation of wall thickness, higher EF, smaller EDV and ESV, lower EDP and higher peak systolic pressure than control animals.

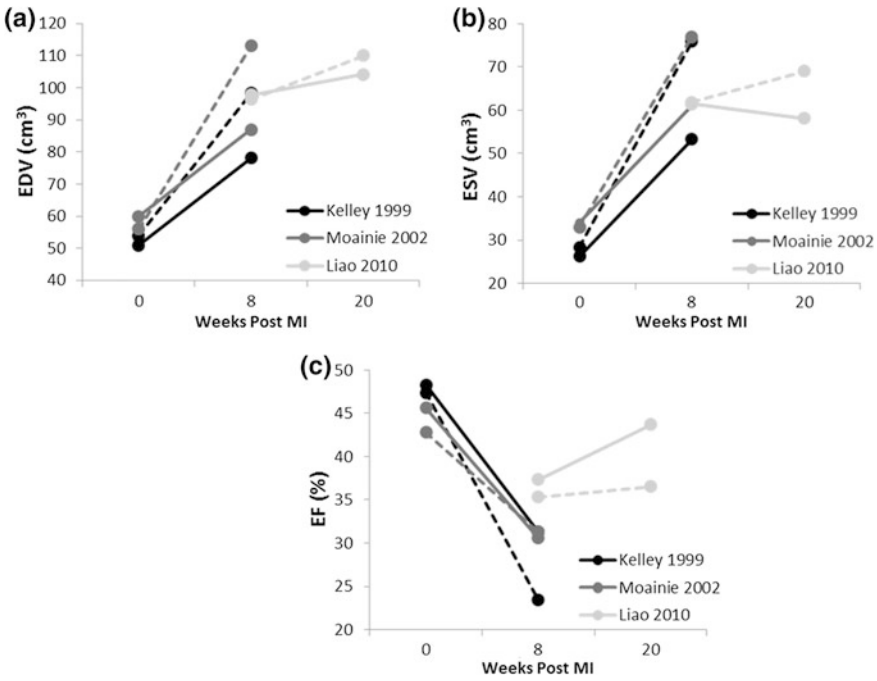

Fig. 10 Changes in LV end-diastolic **a** and end-systolic **b** volumes and EF **c** following local patch reinforcement. *Dotted lines* indicate changes in the control group, *solid lines* indicate changes in the patch reinforcement group (based on data from [50–52])

Fujimoto et al. also demonstrated remodeling benefits of post-infarction local reinforcement, suturing polyester urethane urea patches to the epicardium 2 weeks after LAD ligation in rats [53]. Unlike the polypropylene meshes, these patches were designed to be elastic and biodegradable, with erosion occurring over the course of several weeks. By 10 weeks post-MI (8 weeks after patch implantation surgery), the degradable patches were observed to be significantly absorbed and well integrated with the ventricle wall, leading to better preservation of infarct wall thickness in patch animals. ED LV cavity area (calculated from a short axis image) was maintained near its baseline value and FAC improved in the reinforcement group, compared to an increase in area and decrease in FAC in control animals. Infarct compliance measured during passive inflation of the LV showed that native 8 week infarct scars were stiffer than reinforced scars in both the circumferential and longitudinal directions (Fig. 11a, b). Overall, these results suggest that the biodegradable patches used in this study could have modulated the biology of infarct healing in addition to or instead of infarct mechanics; developing patches that provide a combination of mechanical support and biologic effects is one of the most exciting current areas of research in novel post-infarction therapies.

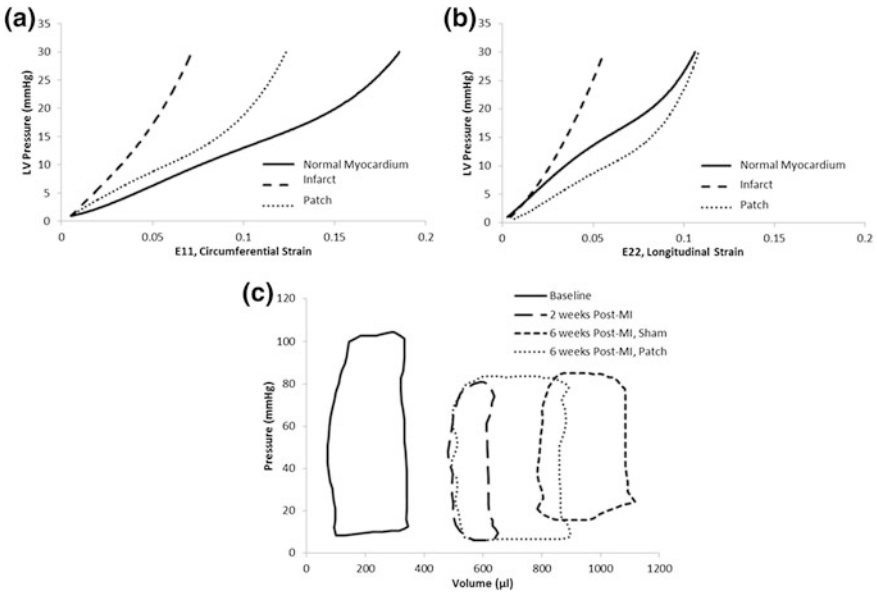

Fig. 11 Effects of local infarct reinforcement in rats. Comparison of compliance between normal myocardium, polyester urethane urea patched infarcts, and unpatched infarcts in the circumferential **a** and longitudinal **b** directions (replotted from [53]). Pressure–volume loops **c** following infarction and reinforcement with a viable engineered heart tissue patch (replotted from [56])

5.2 Cell Seeded and Tissue Engineered Patches: Better Than Synthetic?

In an attempt to combine reinforcement with regeneration, numerous studies have sought to determine whether infarct restraint with tissue engineered patches, or combined therapies in which cells are seeded in a biological or synthetic matrix, offer greater benefit than synthetic reinforcement alone. Findings on functional improvement with regenerative approaches have been mixed, with some studies suggesting enhanced benefit over infarct reinforcement alone and others suggesting minimal difference in efficacy between the two approaches. In one of the studies that offered the most support for combining mechanical reinforcement with cell therapy, Liu and colleagues used a fibrin matrix seeded with autologous mesenchymal stem cells (MSC) to reinforce acute infarcts in pigs [54]. After 60 min of LAD occlusion followed by reperfusion, a fibrin gel solution containing MSCs was placed onto the epicardium and allowed to polymerize into a semi-solid matrix. Terminal studies at 18–21 days post-MI revealed pronounced differences in systolic WT within the reperfused infarct, with active WT in seeded patch animals and passive stretching and wall thinning in both unpatched and unseeded patch animals. Kellar et al. also showed enhanced benefit using a cell-seeded patch compared to unseeded [55]. Permanent LAD ligation was used to infarct severe

combined immunodeficient (SCID) mice, followed by immediate application of a poly (lactic-*co*-glycolic) acid mesh patch seeded with either viable or non-viable human dermal fibroblasts. At 2 weeks post-MI, EF and SV were higher in animals whose patches contained viable fibroblasts compared to the non-viable patch group. However, CO, EDP, ESP, EDV, and ESV were not observed to depend on cell viability and were similar between the two patch groups. Compared to control animals with unpatched infarcts, both patch groups showed improved EF, increased wall thickness, and lower EDP at 2 weeks post-MI.

Despite the evidence described above suggesting that combined reinforcement and regenerative therapies are superior to reinforcement alone, numerous other studies have shown minimal added benefit using cell seeded or tissue engineered patches when compared to the corresponding unseeded or non-viable construct. Zimmermann et al. examined implantation of heart tissue grafts made from neonatal rat cardiac cells over the infarct area 2 weeks after LAD ligation in rats [56]. By 6 weeks post-MI (4 weeks after grafting), not only were LV volumes, pressures, CO, SV, EF, FS and dP/dt all similar between the viable graft and non-cardiomyocyte graft groups, but the viable graft group also failed to show significant improvements in these metrics compared to the unpatched sham group, even though shifts in the pressure–volume behavior of the groups were observed (Fig. 11c). Using the same animal model, immediate application of a human MSC seeded collagen scaffold to the infarct area led to improved FS and a smaller increase in ED and ES cavity dimension at 4 weeks post-MI compared to both the unseeded scaffold and the control groups [57]. However, no differences in EDP, ESP or dP/dt were observed among the three experimental groups. In a similar study, infarcts created in rats by 5 h of LAD occlusion were reinforced at 1 week post-MI with a poly(glycolide-*co*-caprolactone) scaffold seeded with bone marrow derived mononuclear cells (BMC) [58]. 5 weeks post-MI, both BMC seeded and unseeded patch animals showed smaller ED and ES LV cavity dimensions, higher percentage of FS, greater preservation of wall thickness, and lower EDP than control animals. Over a much longer follow-up period, Giraud et al. used the rat LAD ligation model to compare the effects of seeded patches, unseeded patches and cell injection on long-term healing [59]. At 2 weeks post-MI, animals were randomized to receive implantation of a polyurethane patch seeded with rat skeletal myoblasts, implantation of an unseeded patch, or injection of skeletal myoblast suspension. One year after induction of MI, no differences in dP/dt or EDP were observed between the groups. Interestingly, percent change in FS compared to pre-treatment baseline showed a delayed decrease in the seeded patch group (the first significant decrease in FS in this group was observed at 12 months compared to at 6 or 9 months in the other experimental groups), although this delayed decrease was so dramatic that the seeded patch group had the worst FS of all groups at the final time point.

Despite mixed conclusions regarding the potential of post-MI therapies that combine reinforcement with cell therapies to produce greater benefit than mechanical reinforcement alone, one fairly consistently finding across many studies is that mechanical therapy is superior to cell therapy when both are used in

isolation. Several studies that have sought to compare various methods of cell delivery to an infarct have found greater remodeling benefits when cells are implanted with a scaffold or patch than when cells are injected into the infarct site. Godier-furnémont et al. used a rat LAD ligation model to show that immediate reinforcement with a decellularized human myocardium and fibrin hydrogel patch seeded with human mesenchymal progenitor cells reduced LV cavity dimensions at ED and ES and increased FS at 4 weeks post-MI to a greater degree than immediate injection of cells alone [60]. Chachques et al. examined the effects of cell injection versus cell injection with cell seeded patch implantation in a clinical feasibility trial [61]. Out of 20 patients who presented with post-ischemic scars in the LV and indication for coronary artery bypass surgery, half received injection of autologous BMCs while the remaining half received BMC injection in conjunction with application of a BMC seeded collagen patch. At the end of the 10 month follow up period, the combined injection and patch group showed enhanced attenuation of pathological LV remodeling, exhibiting greater preservation of infarct wall thickness and larger magnitudes of reduction in EDV and ESV.

6 Patch Restraint Post-MI Produces Mixed Changes in Both LV Volumes and Function

Strikingly similar to the changes observed following total ventricular reinforcement with CSDs, the reports on whether a cardiac patch of any type actually improves pump function after a heart attack are mixed. As discussed in the beginning of the chapter, there are several metrics that are commonly used to quantify cardiac function with varying degrees of validity. To reiterate, evaluating shifts in CO versus LV EDP curves or calculating CO at matched values of LV EDP across different treatment conditions are the best methods to separate changes in pump function from the concurrent hemodynamic and geometric changes and make reliable conclusions about changes in cardiac function. Although EF and systolic FS or WT may reflect changes in active pumping capability, it is impossible to draw definitive conclusions from these values alone, because they are also sensitive to changes in cavity geometry, infarct mechanical properties, coupling between the infarct and the surrounding myocardium, and the amount of transmural shearing during contraction. Therefore, comparing cardiac function across unreinforced and reinforced states requires careful attention to the variety of geometric and hemodynamic changes during remodeling and cautious interpretation of the metrics used to make conclusions about functional improvements.

Although the studies discussed in this section all employ local reinforcement to restrain a large infarct, this seemingly similar mechanical intervention leads to widely varying reported changes in volume and function (Table 2). While a slight majority of studies do show a decrease in LV volume, diameter, or cross-sectional area, there are several cases in which patch reinforcement fails to reduce dilation, suggesting that it may be more difficult to limit LV dilation with patch restraint as

opposed to ventricular restraint. In addition to the increased variability observed in volume changes, there is also slightly more variability in the reported functional changes following local versus global reinforcement. For example, Kelley et al. showed that patch reinforcement of an LAD infarct could reduce LV volumes and improve EF, SV, CO, and ESPVR slope, but using the same patch to reinforce an LCx infarct failed to improve any of these parameters compared to the control group [50, 51]. In addition, Zimmermann et al. found that reinforcing an LAD infarct with a different type of patch produced no changes in LV volumes, EF, SV, CO, FAS or dP/dt [56]. With the exception of one report of worsened dilation and FS following seeded patch application, most of the other studies discussed showed decreases in LV volumes and improvements in EF or FS.

When looking at the patch studies discussed in this chapter as a whole, somewhat consistent reductions in both LV EDV and ESV are observed. Reminiscent of global restraint, however, the metrics used to evaluate changes in LV function make it difficult to distinguish geometric changes from actual improvements in pumping. Additionally, as discussed in the beginning of this chapter and above, the two most consistently reported improved indices (EF and FS) are difficult to interpret due to their dependence on geometry and material properties. Across studies, consistent increases in EF and FS, FAC or WT are unaccompanied by increases in SV, CO, or dP/dt. However, as seen in Table 2, few studies actually measured more than one or two indices, so it is possible that there are true functional changes occurring that are not being captured simply because they aren't being measured. Comparing the pool of local reinforcement studies described here to the global restraint studies discussed earlier, it appears that patch restraint can successful generate similar geometric and contractile changes to global restraint, although with slightly less consistency. However, since nearly every patch study described used a different type of patch material and attachment scheme, while global reinforcement studies employed commercialized devices with standard implantation procedures, it is not at all surprising that we see significantly more variability in the results of the patch studies.

6.1 Importance of Patch Material Properties

The studies reviewed above used patches with a variety of material properties, applied under different degrees of tension, and exerting a variable degree of biologic influence on infarct healing, in addition to direct mechanical effects. As a result, it is very difficult to distill conclusions about how these individual variables affect remodeling and function, or to articulate clear design goals for the next generation of patches. However, some consensus is beginning to emerge regarding the impact of one key variable, the mechanical properties of the patch itself.

Early computational models that simulated the functional impact of changes in infarct material properties over the time course of healing found an interesting trade-off between the effect of scar stiffening on systolic versus, diastolic function

Table 2 Summary of local reinforcement studies

Reference	Animal	Infarct/HF model	Patch material	EDV	ESV	EF	SV	CO	FS/FAS/WT	dP/dt	ESPVR
Kelley 1999	Sheep	LAD ligation	PP	↓	↓	↑	↑	↑			↑ESPVR
Moainie 2002	Sheep	LCx ligation	PP	↔	↔	↔	↔	↔			
Fujimoto 2007	Rat	LAD ligation	PEUU	↔ED CSA					↑FAC		
Liao 2010	Pig	LCx emboli-zation	PP + PTFE	↓	↓	↑					
Liu 2004	Pig	60 min LAD occlusion	Fibrin Matrix + MSC						↑WT in infarct*		
Kellar 2005	Mice	LAD ligation	PLGA + Fibroblast		↓	↑[a]	↔	↔			↔ESPVR
Zimmer-mann 2006	Rat	LAD ligation	EHTG	↔	↔	↔	↔	↔	↔FAS	↔	
Simpson 2007	Rat	LAD ligation	Collagen + MSC	↓EDD[a]	↓ESD[a]				↑FS[a]	↔	
Piao 2007	Rat	5 h LAD occlusion	PGCL + BMCs	↓EDD	↓ESD				↑FS		
Giraud 2010	Rat	LAD ligation	PU + MyoB	↑EDD[a]					↓FS	↔	
Godier-furnemont 2011	Rat	LAD ligation	Myocardium + Fibrin + MSC	↓EDD	↓ESD				↑FS		
Chachques 2008	Human	Post-isch. LV scars	Collagen + BMCs	↓	↓						
Fomovsky 2012	Dog	LAD ligation	Anisotropic dacron		↓			↑			

LCx = left circumflex coronary artery, *EDD* = end-diastolic diameter, *ESD* = end-systolic diameter, *PP* = polypropylene, *PEUU* = polyester urethane urea, *PTFE* = polytetrafluoroethylene, *MSC* = mesenchymal stem cells, *PLGA* = poly (lactic-*co*-glycolic) acid, *EHTG* = engineered heart tissue graft, *PGCL* = poly (glycolide-*co*-caprolactone), *PU* = polyurethane, *MyoB* = myoblasts, See Table 1 caption for list of other relevant abbreviations

[a] indicates a significant difference from control in the seeded patch or viable construct group only, no symbol indicates a significant difference from control in all patch groups (seeded + unseeded/viable + non-viable)

[2, 62]. Simulating acute infarcts as noncontractile regions with material properties identical to passive myocardium predicted normal diastolic behavior (reflected in an unchanged end-diastolic pressure–volume relationship, EDPVR) but severely depressed systolic function (altered end-systolic function pressure volume relationship, ESPVR), in agreement with experiments. Increasing infarct stiffness in the model improved systolic function as expected, shifting the predicted ESPVR back towards baseline. However, hearts with a stiffer infarct also displayed impaired filling, reflected in a left-shifted EDPVR, and reduced filling exactly offset improved ejection, producing no overall change in predicted CO at matched pressures (Fig. 12). These early models made a number of simplifications, particularly assuming that scar is mechanically isotropic (having the same properties when stretched in any direction), but recent modeling studies using much more sophisticated and better-validated finite element models reached similar conclusions. We found that isotropically stiffening a large anterior infarct in a model of an infarcted dog heart reduced both systolic and diastolic volumes at matched pressures, producing no net benefit in overall pump function [63]. Similarly, Dang et al. studied the impact of the stiffness of an isotropic patch applied in a simulated Surgical Anterior Ventricular Restoration (SAVER) operation, and found that increasing patch stiffness reduced systolic and diastolic volumes at matched pressures, but actually decreased SV—in this setting, stiffer patches impaired filling more than they improved ejection [64]. Overall, these computational studies are remarkably consistent with the majority of the functional evidence reviewed above for both global and local infarct reinforcement. We conclude that stiffer patches or restraints are likely to be more effective in reducing or limiting LV size, but that isotropic patches are unlikely to directly improve LV pump function, regardless of stiffness.

6.2 Anisotropic Infarct Reinforcement

We recently proposed one idea for finessing the trade-off between systolic and diastolic function apparent in the studies discussed above. Inspired by the fact that some of the infarct scars we have studied are highly anisotropic (much stiffer in some directions than others [13]), we tested whether any choice of material properties in the circumferential and longitudinal directions could significantly enhance predicted pump function in an FEM of a dog heart with a large anterior infarct [63]. Those simulations suggested that an infarct that is quite stiff in the longitudinal direction (the apex-base direction) but as compliant as passive myocardium in the circumferential direction would have the best pump function; this suggested to us that selective longitudinal reinforcement of an acute anterior infarct could significantly improve LV pump function.

We tested this hypothesis directly by ligating the LAD in open-chest anesthetized dogs and reinforcing the resulting acute infarcts with a modified Dacron patch that was inextensible in the longitudinal direction but free to deform in the

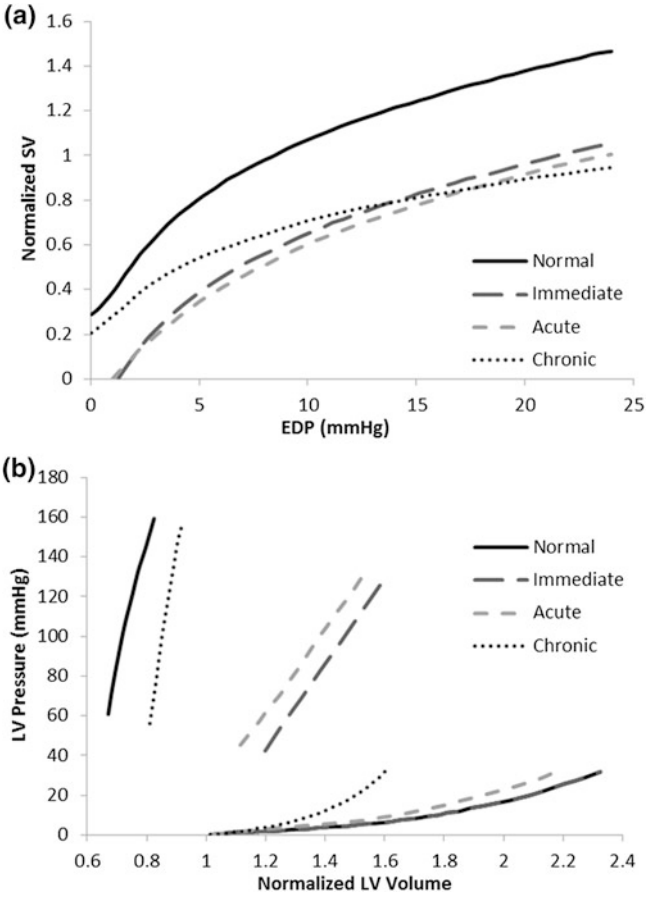

Fig. 12 Computationally generated LV pressure–volume loops **a** and Starling curves **b** for normal myocardium and three stages of infarct healing. Normalized volumes are relative to the initial reference volume in the simulation (replotted from [2])

circumferential direction (Fig. 13a) [65]. Comparison of hemodynamics immediately before and after reinforcement revealed that the anisotropic patch dramatically improved pump function, as indicated by an upward shift in the Starling curve, in the direction of the baseline curve (Fig. 13c). Calculating CO values at a matched EDP (the EDP value observed in the pre-MI baseline state) revealed that anisotropic reinforcement was able to restore half of the CO deficit that had developed between the baseline and acute MI states (Fig. 13d). Additionally, pressure–volume analysis showed that the anisotropic patch caused a leftward shift in the ESPVR, indicating enhanced contractile capability, while the EDPVR remained unchanged, signifying minimal change in the passive behavior of the scar and therefore minimal interference with diastolic filling of the LV (Fig. 13b). The ability of this anisotropic patch to produce dramatic restoration of systolic

function without depression of diastolic filling makes anisotropy a promising avenue for exploration, not only for local reinforcement but possibly in total ventricular restraint as well.

6.3 Limitations of Patch Restraint

Although local restraint devices are applied to the infarct area and do not generally extend very far beyond the infarct borders, these patch approaches still hold some potential to influence contraction and affect motion in the borderzone and surrounding myocardium. However, wall motion at the infarct border, where passive scar intersects with contractile myocardium, is complex and underexplored. Locally reinforcing these tissues only increases the complexity of borderzone function, making the effects of local infarct reinforcement on the surrounding myocardium very difficult to decipher. Further investigation will be required before the effects of these local approaches on function in the borderzone and remote myocardium can be distinguished.

7 Optimizing Restraint

As discussed above for both global and local cardiac restraint, there are numerous sources of variability in studies of infarct and cardiac restraint, including the location of the infarct, the material properties of the CSD or patch, the technique used to apply it to the heart, the timing of reinforcement following infarction, and the degree of tension under which the restraint is applied, which likely all play a role in determining the efficacy of the therapy. In an attempt to address some of these factors, investigators have explored both experimental and computational approaches to optimizing post-infarction restraint. Computational models are often powerful tools for refining and optimizing experiments. Designing experiments *in silico* can dramatically reduce the time, number of animals, and costs that would be required to perform the same experiment *in vivo*. The following section will discuss methods that have been used to identify the best type or magnitude of reinforcement for a given infarct model and restraint approach (local or global).

7.1 Optimizing Global Restraint

Optimization of bi-ventricular restraint has been performed using a technique called Quantitative Ventricular Restraint (QVR) [66]. In this method, a half-ellipsoidal polyurethane balloon is implanted around both ventricles and is inflated to generate restraint. Fluid can be added to or withdrawn from the lumen to vary

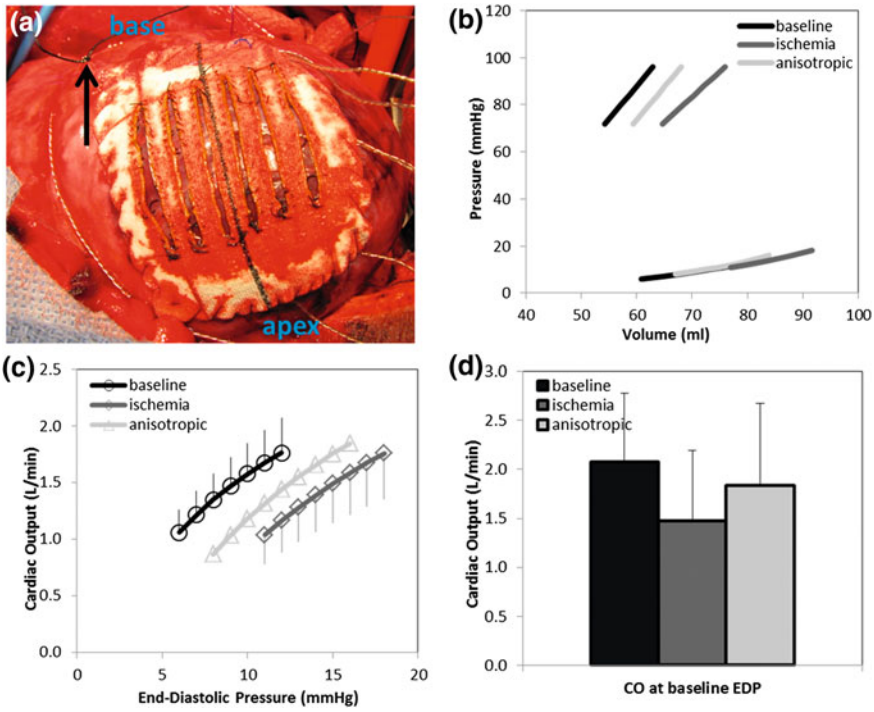

Fig. 13 **a** Image of modified Dacron patch providing longitudinal reinforcement to an acute antero-apical infarct in a canine. The black arrow marks the site of LAD ligation. **b** Comparison of ESPVR and EDPVR between pre-MI baseline, acute ischemia, and acute longitudinal reinforcement. **c** Starling curves showing functional improvement immediately following longitudinal reinforcement. **d** CO calculated at a matched EDP (pre-MI baseline EDP value), showing 50 % recovery of the functional deficit due to MI following longitudinal reinforcement (images B-D adapted from [65])

the inflation pressure and subsequent degree of restraint via an external access line. Ghanta et al. applied several restraint levels in an ovine coronary ligation model of ischemic HF [66]. Investigation of the acute hemodynamic effects of each of the restraint levels revealed a monotonic decrease in both SV and CO and an increase in EDP with increasing QVR pressure (Fig. 14). The optimum restraint level was selected to be one of the intermediate values, based on the criteria of maximizing the reductions in transmural myocardial pressure and myocardial oxygen consumption while minimizing the deleterious hemodynamic effects. After 2 months of reinforcement at this optimized level, QVR animals showed an increase in EF and decrease in EDV from the pre-treatment baseline, while control animals showed opposite changes in both parameters. Interestingly, restraint level was found to decrease over time as the LV cavity reverse remodeled, to the point where there was no longer any restraint pressure being applied at the conclusion of the experiment. In a follow-up study, the same group examined the effects of several

levels of adjustable and measurable ventricular restraint (AMVR) on long-term LV remodeling [67]. Both the low level and high level restraint groups showed decreases in LV volumes and an increase in EF from pre-treatment to 2 months post-treatment while control animals showed opposite changes. Changes in each metric were consistently of greater magnitude in the high restraint than in the low restraint group, and the speed of reverse remodeling was shown to be significantly accelerated in the high restraint group. In the second part of the study, the researchers used the AMVR device to compare the effects of static and adjustable restraint, in which fluid was added to the balloon lumen to maintain a constant restraint pressure over the course of the 2 month remodeling period. Although adjustable restraint enhanced reductions in LV volumes, no significant differences were observed in EF, SV or CO after 8 weeks of either static or adjustable restraint.

Jhun et al. used a computational approach to study how different levels of global passive epicardial restraint affect pump function and wall stress in the dilated left ventricle [68]. In agreement with the experimental studies reviewed above, they found that increasing levels of pressure applied to the epicardium gradually reduced SV and CO. Their model data suggest that epicardial restraint restricts filling more than it improves systolic function, depressing the Starling curve despite reducing systolic wall stress. The same group has used computational models to explore how the effects of Coapsys depend on the pre-implantation systolic and diastolic material properties [43].

7.2 Optimizing Local Restraint

As discussed above, we employed computational modeling to determine the optimum mechanical properties for a patch to reinforce acute antero-apical infarcts (arising from LAD occlusion) in dogs [63]. An FEM was used to simulate a large MI, followed by imposition of varying magnitudes of local isotropic, circumferential, and longitudinal infarct reinforcement. Based on the hemodynamic results of each simulation, the optimum patch was determined to be very stiff longitudinally and very compliant circumferentially. This infarct reinforcement strategy was then tested *in vivo* in dogs, where longitudinal reinforcement was shown to produce dramatic improvement in pump function (as described in the Anisotropic Infarct Reinforcement section) [65]. However, it is not safe to assume that longitudinal reinforcement is the optimal approach for every infarct. In our discussion of local infarct reinforcement, it was noted that implantation of the same patch into the same animal model improved function for one infarct location but failed to do so for another, suggesting that the optimal patch configuration for the two locations may differ [50, 51]. Other groups have used computational modeling to optimize other potential local post-infarction therapies, such as selecting patterns of polymer injection (discussed in a separate chapter of this book) [69].

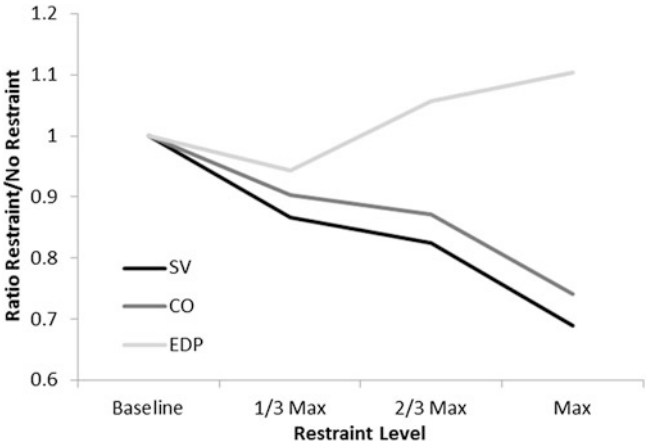

Fig. 14 Acute hemodynamic changes with increasing levels of passive restraint (based on data from [66])

8 Future Directions

Despite the progress that has been made in exploring the utility of mechanical reinforcement to improve and restore cardiac function following MI, there are still many unanswered questions surrounding the use of these therapies. One such question is the level of individualization needed to optimally apply restraint therapies. As discussed earlier, there is likely a need for infarct location-specific optimization of reinforcement strategies, but will this optimal therapy be the same for every patient? Or will differences in individual heart geometry and dynamics make it necessary to optimize reinforcement therapies on a patient-specific rather than infarct-specific basis? The studies reviewed in this chapter also reveal many trade-offs that may have long-term consequences we do not fully understand. For example, computational models suggest that global restraint depresses pump function but lowers wall stress—is that a trade we should make? Lower wall stresses could lead to lower levels of hypertrophy and adverse LV remodeling, but current models generally predict only acute effects of various therapies and devices. Computational models that can simulate not only the acute effects of reinforcement but also the resulting chronic effects on long-term LV remodeling, scar healing, and sympathetic activation will be invaluable. Such models would allow exploration of not only the best treatment to achieve a desired goal, but also the optimal time post-MI to apply the treatment. In addition to determining the best therapy, there is also a need for less invasive implantation procedures for many of the therapies described. The open chest procedures required to implant most of the current mechanical reinforcement therapies are too invasive to be feasible in many post-infarction patients. Therefore, minimally invasive

implantation procedures will need to be developed before these therapies can be clinically relevant for the majority of the patient population.

References

1. Roger, V.L., Go, A.S., Lloyd-Jones, D.M., et al.: Heart disease and stroke statistics–2012 update: a report from the American Heart Association. Circulation **125**, e2–e220 (2011). doi:10.1161/CIR.0b013e31823ac046
2. Bogen, D.K., Rabinowitz, S.A., Needleman, A., et al.: An analysis of the mechanical disadvantage of myocardial infarction in the canine left ventricle. Circ. Res. **47**, 728–741 (1980)
3. Holmes, J.W., Borg, T.K., Covell, J.W.: Structure and mechanics of healing myocardial infarcts. Annu. Rev. Biomed. Eng. **7**, 223–253 (2005). doi:10.1146/annurev.bioeng.7.060804.100453
4. Nieminen, M., Heikkilä, J.: Echoventriculography in acute myocardial infarction. II: monitoring of left ventricular performance. Brit. Heart J. **38**, 271–281 (1976)
5. Bristow, M.R., Ginsburg, R., Minobe, W., et al.: Decreased catecholamine sensitivity and B-adrenergic-receptor density in failing human hearts. New England J. Med. **307**, 205–211 (1982)
6. Thomas, J.A., Marks, B.H.: Plasma norepinephrine in congestive heart failure. Am. J. Cardiol. **41**, 233–243 (1978)
7. Pirzada, F.A., Ekong, E.A., Vokonas, P.S., et al.: Experimental myocardial infarction. XIII. Sequential changes in left ventricular pressure-length relationships in the acute phase. Circulation **53**, 970–975 (1976). doi:10.1161/01.CIR.53.6.970
8. Vokonas, P.S., Pirzada, F.A., Hood, W.B.: Experimental myocardial infarction: XII. Dynamic changes in segmental mechanical behavior of infarcted and non-infarcted myocardium. Am. J. Cardiol. **37**, 853–859 (1976)
9. Birnbaum, Y., Chamoun, A.J., Anzuini, A., et al.: Ventricular free wall rupture following acute myocardial infarction. Coron. Artery Dis. **14**, 463–470 (2003). doi:10.1097/01.mca.0000085885.61165.f9
10. Fishbein, M.C., Maclean, D., Maroko, P.R.: The histopathologic evolution of myocardial infarction. Chest **73**, 843–849 (1978). doi:10.1378/chest.73.6.843
11. Fomovsky, G.M., Holmes, J.W.: Evolution of scar structure, mechanics, and ventricular function after myocardial infarction in the rat. A. J. Physiol. Heart Circu. Physiol. **298**, H221–H228 (2010). doi:10.1152/ajpheart.00495.2009
12. Gupta, K.B., Ratcliffe, M.B., Fallert, M.A., et al.: Changes in passive mechanical stiffness of myocardial tissue with aneurysm formation. Circulation **89**, 2315–2326 (1994)
13. Holmes, J.W., Nuñez, J.A., Covell, J.W.: Functional implications of myocardial scar structure. Am. J. Physiol. 272 Heart Circ. Physiol. **41**, H2123–H2130 (1997)
14. Fomovsky, G.M., Rouillard, A.D., Holmes, J.W.: Regional mechanics determine collagen fiber structure in healing myocardial infarcts. J. Mol. Cell. Cardiol. **52**, 1083–1090 (2012). doi:10.1016/j.yjmcc.2012.02.012
15. Rouillard, A.D., Holmes, J.W.: Mechanical regulation of fibroblast migration and collagen remodeling in healing myocardial infarcts. J. Physiol. **18**, 4585–4602 (2012). doi:10.1113/jphysiol.2012.229484
16. Jugdutt, B.I., Amy, R.W.M.: Healing after myocardial infarction in the dog: changes in infarct hydroxyproline and topography. J. Am. Coll. Cardiol. **7**, 91–102 (1986). doi:10.1016/S0735-1097(86)80265-0

17. Kupper, W., Bleifeld, W., Hanrath, P., et al.: Left ventricular hemodynamics and function in acute myocardial infarction: studies during the acute phase, convalescence and late recovery. Am. J. Cardiol. **40**, 900–905 (1977)
18. Pfeffer, J.M., Pfeffer, M.A., Fletcher, P.J., Braunwald, E.: Progressive ventricular remodeling in rat with myocardial infarction. Am. J. Physiol. 260 Heart Circu. Physiol. **29**, H1406–H1414 (1991)
19. Pfeffer, M., Pfeffer, J., Fishbein, M., et al.: Myocardial infarct size and ventricular function in rats. Circ. Res. **44**, 503–512 (1979)
20. Stone, P.H., Raabe, D.S., Jaffe, A.S.: Prognostic significance of location and type of myocardial infarction: independent adverse outcome associated with anterior location. J. Am. Coll. Cardiol. **11**, 453–463 (1988)
21. Chachques, J.C., Grandjean, P., Schwartz, K., et al.: (1988) Effect of latissimus dorsi dynamic cardiomyoplasty on ventricular function. Circulation **78**(5 Pt. 2), 203–216
22. Lee, K.F., Dignan, R.J., Parmar, J.M., et al.: (1991) Effects of dynamic cardiomyoplasty on left ventricular performance and myocardial mechanics in dilated cardiomyopathy. J. Thorac. Cardiovasc. Surg. **102**(1), 124–131
23. Grandjean, P.A., Austin, L., Chan, S., et al.: Dynamic cardiomyoplasty: clinical follow-up results. J. Cardiac. Surg. **6**(1 Suppl), 80–88 (1991)
24. Oz, M.C., Konertz, W.F., Kleber, F.X., et al.: Global surgical experience with the Acorn cardiac support device. J. Thorac. Cardiovasc. Surg. **126**, 983–991 (2003). doi:10.1016/S0022-5223(03)00049-7
25. Power, J.M., Raman, J., Dornom, A., et al.: Passive ventricular constraint amends the course of heart failure: a study in an ovine model of dilated cardiomyopathy. Cardiovasc. Res. **44**, 549–555 (1999)
26. Chaudhry, P.A., Mishima, T., Sharov, V.G., et al.: Passive epicardial containment prevents ventricular remodeling in heart failure. Ann. Thorac. Surg. **70**, 1275–1280 (2000)
27. Blom, A.S., Mukherjee, R., Pilla, J.J., et al.: Cardiac support device modifies left ventricular geometry and myocardial structure after myocardial infarction. Circulation **112**, 1274–1283 (2005). doi:10.1161/CIRCULATIONAHA.104.499202
28. Blom, A.S., Pilla, J.J., Arkles, J., et al.: Ventricular restraint prevents infarct expansion and improves borderzone function after myocardial infarction: a study using magnetic resonance imaging, three-dimensional surface modeling, and myocardial tagging. Ann. Thorac. Surg. **84**, 2004–2010 (2007). doi:10.1016/j.athoracsur.2007.06.062
29. Pilla, J.J., Blom, A.S., Gorman III, J.H., et al.: Early postinfarction ventricular restraint improves borderzone wall thickening dynamics during remodeling. Ann. Thorac. Surg. **80**, 2257–2262 (2005). doi:10.1016/j.athoracsur.2005.05.089
30. Konertz, W.F., Shapland, J.E., Hotz, H., et al.: Passive containment and reverse remodeling by a novel textile cardiac support device. Circulation **104**, I270–I275 (2001). doi:10.1161/hc37t1.094525
31. Oz, M.C., Konertz, W.F., Raman, J., Kleber, F.X.: Reverse remodeling of the failing ventricle: surgical intervention with the Acorn cardiac support device. Congest. Heart Fail. **10**, 96–104 (2004)
32. Mann, D.L., Acker, M.A., Jessup, M., et al.: Rationale, design, and methods for a pivotal randomized clinical trial for the assessment of a cardiac support device in patients with New York health association class III-IV heart failure. J. Cardiac Fail. **10**, 185–192 (2004). doi:10.1016/j.cardfail.2003.10.007
33. Speziale, G., Nasso, G., Piancone, F., et al.: One-year results after implantation of the CorCap for dilated cardiomyopathy and heart failure. Ann. Thorac. Surg. **91**, 1356–1362 (2011). doi:10.1016/j.athoracsur.2011.02.006
34. Acker, M.A., Jessup, M., Bolling, S.F., et al.: Mitral valve repair in heart failure: five-year follow-up from the mitral valve replacement stratum of the Acorn randomized trial. J. Thorac. Cardiovasc. Surg. **142**, 569–574 (2011). doi:10.1016/j.jtcvs.2010.10.051

35. Mann, D.L., Kubo, S.H., Sabbah, H.N., et al.: Beneficial effects of the CorCap cardiac support device: five-year results from the Acorn trial. J. Thoracic. Cardiovasc. Surg. **143**, 1036–1042 (2012). doi:10.1016/j.jtcvs.2011.06.014
36. Kwon, M.H., Cevasco, M., Schmitto, J.D., Chen, F.Y.: Ventricular restraint therapy for heart failure: a review, summary of state of the art, and future directions. J. Thorac. Cardiovasc. Surg. **144**, 771–777 (2012). doi:10.1016/j.jtcvs.2012.06.014
37. Gummert, J.F., Rahmel, A., Bossert, T., Mohr, F.W.: Socks for the dilated heart: does passive cardiomyoplasty have a role in long-term care for heart failure patients? Zeitschrift für Kardiologie **93**, 849–854 (2004). doi:10.1007/s00392-004-0160-7
38. Klodell, C.T., Aranda, J.M., McGiffin, D.C., et al.: Worldwide surgical experience with the Paracor HeartNet cardiac restraint device. J. Thorac. Cardiovasc. Surg. **135**, 188–195 (2008). doi:10.1016/j.jtcvs.2007.09.034
39. George, I., Cheng, Y., Yi, G.-H., et al.: Effect of passive cardiac containment on ventricular synchrony and cardiac function in awake dogs. Eur. J. Cardio Thorac. Surg **31**, 55–64 (2007). doi:10.1016/j.ejcts.2006.09.024
40. Magovern, J.A., Teekell-Taylor, L., Mankad, S., et al.: Effect of a flexible ventricular restraint device on cardiac remodeling after acute myocardial infarction. Am. Soc. Artif. Intern. Organs J. **52**, 196–200 (2006). doi:10.1097/01.mat.0000199751.51424.78
41. Costanzo, M.R., Ivanhoe, R.J., Kao, A., et al.: Prospective evaluation of elastic restraint to lessen the effects of heart failure (PEERLESS-HF) trial. J. Cardiac Fail. **18**, 446–458 (2012). doi:10.1016/j.cardfail.2012.04.004
42. McCarthy, P.M., Takagaki, M., Ochiai, Y., et al.: Device-based change in left ventricular shape: a new concept for the treatment of dilated cardiomyopathy. J. Thorac. Cardiovasc. Surg. **122**, 482–490 (2001). doi:10.1067/mtc.2001.115240
43. Guccione, J.M., Salahieh, A., Moonly, S.M., et al.: (2003) Myosplint decreases wall stress without depressing function in the failing heart: a finite element model study. Ann. Thorac. Surg. **76,** 1171–80 (discussion 1180)
44. Mishra, Y.K., Mittal, S., Jaguri, P., Trehan, N.: Coapsys mitral annuloplasty for chronic functional ischemic mitral regurgitation: 1-year results. Ann. Thorac. Surg. **81**, 42–46 (2006). doi:10.1016/j.athoracsur.2005.06.023
45. Grossi, E.A., Patel, N., Woo, Y.J., et al.: Outcomes of the RESTOR-MV trial (randomized evaluation of a surgical treatment for off-pump repair of the mitral valve). J. Am. Coll. Cardiol. **56**, 1984–1993 (2010). doi:10.1016/j.jacc.2010.06.051
46. Kashem, A., Santamore, W.P., Hassan, S., et al.: CardioClasp : a new passive device to reshape cardiac enlargement. Am. Soc. Artif. Intern. Organs J. **48**, 253–259 (2002)
47. Kashem, A., Hassan, S., Crabbe, D.L., et al.: Left ventricular reshaping: effects on the pressure-volume relationship. J. Thorac. Cardiovasc. Surg. **125**, 391–399 (2003). doi:10.1067/mtc.2003.4
48. Kashem, A., Santamore, W.P., Hassan, S., et al.: CardioClasp changes left ventricular shape acutely in enlarged canine heart. J. Card. Surg. **18**, S49–S60 (2003)
49. Rane, A.A., Christman, K.L.: Biomaterials for the treatment of myocardial infarction: a 5-year update. J. Am. Coll. Cardiol. **58**, 2615–2629 (2011). doi:10.1016/j.jacc.2011.11.001
50. Kelley, S.T., Malekan, R., Gorman III, J.H., et al.: Restraining infarct expansion preserves left ventricular geometry and function after acute anteroapical infarction. Circulation **99**, 135–142 (1999). doi:10.1161/01.CIR.99.1.135
51. Moainie, S.L., Guy, T.S., Gorman III, J.H., et al.: Infarct restraint attenuates remodeling and reduces chronic ischemic mitral regurgitation after postero-lateral infarction. Ann. Thorac. Surg. **74**, 444–449 (2002)
52. Liao, S.-Y., Siu, C.-W., Liu, Y., et al.: Attenuation of left ventricular adverse remodeling with epicardial patching after myocardial infarction. J. Cardiac Fail. **16**, 590–598 (2010). doi:10.1016/j.cardfail.2010.02.007
53. Fujimoto, K.L., Tobita, K., Merryman, W.D., et al.: An elastic, biodegradable cardiac patch induces contractile smooth muscle and improves cardiac remodeling and function in subacute

myocardial infarction. J. Am. Coll. Cardiol. **49**, 2292–2300 (2007). doi:10.1016/j.jacc.2007.02.050
54. Liu, J., Hu, Q., Wang, Z., et al.: Autologous stem cell transplantation for myocardial repair. Am. J. Physiol. Heart Circu. Physiol. **287**, H501–H511 (2004). doi:10.1152/ajpheart.00019.2004
55. Kellar, R.S., Shepherd, B.R., Larson, D.F., et al.: Cardiac patch constructed from human fibroblasts attenuates reduction in cardiac function after acute infarct. Tissue Eng. **11**, 1678–1687 (2005). doi:10.1089/ten.2005.11.1678
56. Zimmermann, W.-H., Melnychenko, I., Wasmeier, G., et al.: Engineered heart tissue grafts improve systolic and diastolic function in infarcted rat hearts. Nat. Med. **12**, 452–458 (2006). doi:10.1038/nm1394
57. Simpson, D., Liu, H., Fan, T.-H.M., et al.: A tissue engineering approach to progenitor cell delivery results in significant cell engraftment and improved myocardial remodeling. Stem Cells **25**, 2350–2357 (2007). doi:10.1634/stemcells.2007-0132
58. Piao, H., Kwon, J.-S., Piao, S., et al.: Effects of cardiac patches engineered with bone marrow-derived mononuclear cells and PGCL scaffolds in a rat myocardial infarction model. Biomaterials **28**, 641–649 (2007). doi:10.1016/j.biomaterials.2006.09.009
59. Giraud, M.-N., Flueckiger, R., Cook, S., et al.: Long-term evaluation of myoblast seeded patches implanted on infarcted rat hearts. Artif. Organs **34**, E184–E192 (2010). doi:10.1111/j.1525-1594.2009.00979.x
60. Godier-Furnémont, A.F.G., Martens, T.P., Koeckert, M.S., et al.: Composite scaffold provides a cell delivery platform for cardiovascular repair. Proc. Natl. Acad. Sci. U.S.A. **108**, 7974–7979 (2011). doi:10.1073/pnas.1104619108/DCSupplemental.www.pnas.org/cgi/doi/10.1073/pnas.1104619108
61. Chachques, J.C., Trainini, J.C., Lago, N., et al.: Myocardial assistance by grafting a new bioartificial upgraded myocardium (MAGNUM trial): clinical feasibility study. Ann. Thorac. Surg. **85**, 901–908 (2008). doi:10.1016/j.athoracsur.2007.10.052
62. Janz, R.F., Waldron, R.J.: Predicted effect of chronic apical aneurysms on the passive stiffness of the human left ventricle. Circ. Res. **42**, 255–263 (1978). doi:10.1161/01.RES.42.2.255
63. Fomovsky, G.M., Macadangdang, J.R., Ailawadi, G., Holmes, J.W.: Model-based design of mechanical therapies for myocardial infarction. J. Cardiovasc. Trans. Res. **4**, 82–91 (2011). doi:10.1007/s12265-010-9241-3
64. Dang, A.B.C., Guccione, J.M., Zhang, P., et al.: Effect of ventricular size and patch stiffness in surgical anterior ventricular restoration: a finite element model study. Ann. Thorac. Surg. **79**, 185–193 (2005). doi:10.1016/j.athoracsur.2004.06.007
65. Fomovsky, G.M., Clark, S.A., Parker, K.M., et al.: Anisotropic reinforcement of acute anteroapical infarcts improves pump function. Circu. Heart Fail. (2012). doi:10.1161/CIRCHEARTFAILURE.111.965731
66. Ghanta, R.K., Rangaraj, A., Umakanthan, R., et al.: Adjustable, physiological ventricular restraint improves left ventricular mechanics and reduces dilatation in an ovine model of chronic heart failure. Circulation **115**, 1201–1210 (2007). doi:10.1161/CIRCULATIONAHA.106.671370
67. Lee, L.S., Ghanta, R.K., Mokashi, S.A., et al.: Optimized ventricular restraint therapy: adjustable restraint is superior to standard restraint in an ovine model of ischemic cardiomyopathy. J. Thorac. Cardiovasc. Surg. **145**(3), 824–831 (2012). doi:10.1016/j.jtcvs.2012.05.018
68. Jhun, C.-S., Wenk, J.F., Zhang, Z., et al.: Effect of adjustable passive constraint on the failing left ventricle: a finite-element model study. Ann. Thorac. Surg. **89**, 132–137 (2010). doi:10.1016/j.athoracsur.2009.08.075
69. Wenk, J.F., Wall, S.T., Peterson, R.C., et al.: A method for automatically optimizing medical devices for treating heart failure: designing polymeric injection patterns. J. Biomech. Eng. **131**, 121011–121017 (2009). doi:10.1115/1.4000165

70. Sobotta, J.: Atlas and Text-Book of Human Anatomy: Volume III, Vascular System, Lymphatic System, Nervous System and Sense Organs, p. 21. W.B. Saunders Company, Philadelphia (1907)
71. Saavedra, W.F., Tunin, R.S., Paolocci, N., et al.: Reverse remodeling and enhanced adrenergic reserve from passive external support in experimental dilated heart failure. J. Am. Coll. Cardiol. **39**, 2069–2076 (2002)
72. Raman, J.: Management of heart failure, Vol. 2. Surgical, Fig 17.3. Springer, New York (2008)

In Vivo Mechanical Loading Conditions of Pectorally Implanted Cardiac Pacemakers

Thomas Franz, Michael Hamman de Vaal, James Neville, Jacques Scherman, Micah Litow and Peter Zilla

Abstract With technological progress enabling new patient populations and smaller devices, detailed data on mechanical in vivo loads become increasingly important to ensure reliability of implantable medical devices. Employing a system for remote measurement of in vivo mechanical loadings on fully implantable pacemaker, pre-clinical investigations on in-line force and transverse reaction force of the *Pectoralis major* were conducted in the *Chacma* baboon. Based on an intra-species correlation derived from these investigations, a simplified physiological model and a mechanical equivalent model were developed for a sub-muscular pectoral device implant considering the *Pectoralis major*, *Pectoralis minor* and rib cage. By assessing the morphometric and mechanical parameters of these musculoskeletal structures and associated model parameters, the intra-species correlation was shown to exhibit robustness for a larger intra-species subject population and a linear scale variance allowing the application to humans under consideration of the inter-species difference of the attachment angles of the *Pectoralis major*. The transfer function provides a basis for the prediction of patient-specific maximum mechanical loadings on a sub-muscular pectoral cardiac pacemaker implant through non- or minimal invasive measurements on the patient. This study

T. Franz (✉) · M. H. de Vaal · J. Scherman · P. Zilla
Cardiovascular Research Unit, Chris Barnard Department of Cardiothoracic Surgery, University of Cape Town, Observatory, South Africa
e-mail: Thomas.Franz@uct.ac.za

T. Franz
Programme for the Enhancement of Research Capacity, Research Office, University of Cape Town, Mowbray, South Africa

T. Franz
Centre for Research in Computational and Applied Mechanics, University of Cape Town, Rondebosch, South Africa

J. Neville
Cardiac Rhythm Disease Management, Medtronic Inc, Minneapolis, MN, USA

M. Litow
Neuromodulation Division, Medtronic Inc, Minneapolis, MN, USA

Stud Mechanobiol Tissue Eng Biomater (2014) 15: 207–237
DOI: 10.1007/8415_2013_160

Published Online: 16 May 2013

demonstrated the feasibility of the approach for assessment of in vivo mechanical loading conditions of implantable pacemakers.

Notations

a_i	Coefficients of inter-species transfer function for i = 1 to 5
F_{IL}	In-line force generated in the sternal *Pectoralis major*
F_T	Transverse force acting on the IPM/pectoral implant
k_r	Transverse stiffness coefficient of the rib cage
k_{t1}	Transverse stiffness coefficient of the *Pectoralis major*
k_{t2}	Transverse stiffness coefficient of the *Pectoralis minor*
L_f	Muscle fibre length
$L_{f,opt}$	Optimal muscle fibre length
L_m	Length of the sternal *Pectoralis major* along the estimated line of action
L_r	Characteristic length of the rib cage determined by the rib geometry and curvature
M_b	Body mass of subject
M_m	Mass of the entire *Pectoralis major*
N	Number of subjects
Q_{IL}	Uniformly distributed in-line force along the width of the *Pectoralis major* over the pectoral implant
t_m	Thickness of the sternal *Pectoralis major* at the location of the IPM/pectoral implant
$t_{m,cb}$	Thickness of the sternal *Pectoralis major* at crossbar of the buckle force transducer
t_{mu}	Thickness of the *Pectoralis minor* at the location of the IPM implant
V_m	Volume of the entire *Pectoralis major*
w_m	Width of the *Pectoralis major* over the IPM/pectoral implant
$w_{m,cb}$	Width of the *Pectoralis major* at the cross bar of the buckle transducer
ψ_1	Angle of attachment of the *Pectoralis major* at its origin
$\bar{\psi}_1$	Mean angle of attachment of the *Pectoralis major* at its origin for n subjects
ψ_2	Angle of attachment of the *Pectoralis major* at its insertion
$\bar{\psi}_2$	Mean angle of attachment of the *Pectoralis major* at its insertion for n subjects
θ	Pennation angle of the skeletal muscle fibres
ρ_m	Material density of *Pectoralis major*
σ_m	Axial stress in the *Pectoralis major* during contraction
σ_{mu}	Axial stress in the *Pectoralis minor* during contraction

Subscripts

B Baboon
H Human

1 Introduction

Implantable cardiac rhythm assist devices have been used extensively for the therapy of patients with cardiac arrhythmias. These devices have been shown to reduce mortality in high-risk patient populations [27] and to significantly increase clinical benefits for the treatment of cardiac arrhythmias compared to purely pharmacological therapy [7]. The two main groups of assist devices are implantable pulse generators (IPG), i.e., pacemakers, and implantable cardioverter defibrillators (ICD).

The implantable parts of an IPG or ICD system comprise a housing that contains the generator, battery and control circuitry, and the transvenous leads. Implantation sites include the abdominal, the retro-mammary and the pectoral regions. The abdominal region is mostly used when the physical conditions of the pectoral region are inappropriate. The retro-mammary position is preferred in female patients mainly for cosmetic considerations [21]. Pectoral implants have been shown to cause fewer complications compared to devices in abdominal positions [24]. Hence, the pectoral region has been utilized more frequently as implant site. Here, the housing is placed in a tissue pocket either sub-cutaneously, resting on the *Pectoralis major*, or sub/intra-muscularly between the *Pectoralis major* and the *Pectoralis minor* and rib cage, respectively [22].

In recent years, several factors emerged that indicate an increase in the mechanical demands placed on implanted pacemakers. Technological advances have made it possible to reduce the size, in particular the thickness, of pacemakers [16, 27, 34]. This development, in combination with clinical advances, has increased the feasibility of implantable pacemaker technology for use in younger patients [1, 15, 16] which are generally more active than the adult patients traditionally receiving pacemakers. In order to ensure structural integrity, mechanical longevity and device reliability, increased mechanical demands resulting from physically more active recipients need to be considered during the development stage of new devices in particular when reduced device dimensions are targeted. Mechanical loads on pacemaker housing associated with daily living activities do not seem to present potential for device failure. However, detailed quantitative knowledge of the mechanical use conditions of implantable pacemakers becomes imperative for the design process in view of increased patient activity and smaller implants.

While IPG and ICD leads have received extensive attention with respect to reliability [14, 18, 24, 29] and in vivo mechanics [2, 43, 44], research on the in vivo mechanical loading of pacemaker housing has not been reported previous to the studies described here. The characterization of mechanical loading conditions of pectoral pacemaker implants may potentially be studied in cadaver tests. Such tests can, however, represent the in vivo conditions only partially. The main limiting factors of cadaver tests are the exclusively passive movements of the upper extremities, differences in tissue properties, the absence of conscious muscle tone and breathing loads as well as the lack of fibrous encapsulation of the implant

as part of the biological healing process. These physiological differences may be less limiting in certain situations, e.g., for the testing of mechanical loading on the implanted device in a simulated vehicle crash where inertial and external forces are likely to dominate. For musculoskeletal, i.e. 'internal', loading conditions associated with day-to-day activities of the recipients, these differences appear to limit the efficacy of such data more significantly.

This chapter is based on a series of research studies. The first study was concerned with the assessment of a system for the measurement of in vivo loading conditions of an implanted pacemaker housing [9]. The study utilized a non-human primate model (*Chacma* baboon) due to the anatomical similarity of the pectoral and upper thoracic region to that of a human. Most importantly, the existence of the clavicle in the baboon qualified this animal model over other mammalians, e.g., hoofed species such as sheep, which lack the clavicle and demonstrate a considerably difference in locomotion pattern of the upper extremities. The study facilitated a small cohort of test subjects and was not primarily designed to provide data with statistical significances.

The focus of the second study was the investigation of a relationship between the force of the *Pectoralis major* muscle in line of its action, i.e., in-line force, and the transverse force exerted on a pacemaker housing implanted in the sub-muscular position [10]. The in-line force of the *Pectoralis major* muscle can be assessed with surface-based measurement techniques such as electro-myography. A correlation between in-line and transverse force of the *Pectoralis major* may as such allow for the non-invasive characterization of in vivo mechanical conditions of pacemaker implants in volunteers, as opposed to requiring invasive measurements of the in vivo mechanical loadings on pacemakers with the system evaluated in the first study.

The third study dealt with the development of a transfer function that entails the extension of an intra-species relationship for in-line and transverse force of the *Pectoralis major* in baboons to humans [8]. The proposed transfer function may provide the basis for the clinical quantification of mechanical forces on pacemaker implants by measuring the in-line force of the *Pectoralis major* in patients using non- or minimally invasive methods such as electro-myography.

2 In Vivo Assessment of Mechanical Loadings on Pectoral Pacemaker Implants

2.1 Measurement System

The principal components of the in vivo measurement system comprised an implantable instrumented pacemaker (IPM), a wireless radio-frequency (RF) data logging system and a synchronous video capture system. The IPM (dimensions: 64 × 61 × 11 mm, volume: 29 cm^3) was equipped with six custom manufactured contact force sensors with optimal compressive force range of 18–36 N (Tekscan,

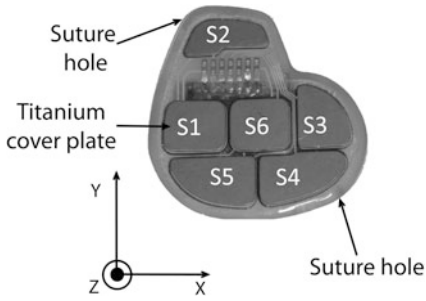

Fig. 1 Implantable instrumented pacemaker with Titanium cover plates of six contact forces sensors (S1–S6) visible. Two suture holes served for fixation of the device to surrounding tissue in order to prevent migration of the implant

Boston, MA), one three-axis accelerometer (±10 g full scale per axis, Freescale Semiconductor, Tempe, AZ) as well as a RF transceiver, micro-controller, real-time clock and high energy lithium battery. These components were embedded in a medical grade epoxy cast to a shape resembling a typical commercial pacemaker housing (Fig. 1).

The force sensors were distributed across one principal surface of the device and assembled with custom-made Titanium cover plates according to the specifications of the sensor manufacturer. The RF data control and logging system comprised a custom built RF transceiver, a PC laptop (Dell Latitude, Dell, Round Rock, TX) and control software developed using LabVIEW (National Instruments Corp, Austin, TX). The transceiver and PC laptop were connected through a serial RS232 connection. RF data transmission with a 10-bit data resolution at a maximum frequency of 1000 Hz (signal quality dependent) was utilized for the remote activation of the IPM and the acquisition of data from the force sensors and accelerator of the IPM. The force sensors and accelerometers had a maximum response time of 5 μs and 1 ms, respectively. By default, the IPM was dormant to preserve battery power. In order to record and transmit data, the IPM was remotely activated for a user-defined period after which it returned automatically into dormant mode. Data transmitted from the IPM was received with the second transceiver and stored on the PC laptop for subsequent analysis. The synchronous video monitoring system comprised a Basler A602f 1/2" CMOS camera (Basler, Ahrensburg, Germany) with Navitar DOZ-6X8.5 zoom lens (Navitar Inc, Rochester, NY). The camera was connected to and operated from the Dell PC laptop using a custom LabVIEW code. Recorded video data, interlaced with the associated synchronous data from the contact force sensors, was stored on the PC laptop.

After assembly and prior to implantation, the force sensors of each IPM were preconditioned for 4 weeks with a mild static compression load in a moist environment at 37 °C simulating in vivo conditions at rest. During preconditioning, two IPMs were assembled with the force sensing surfaces facing each other, separated by a 6.4 mm thick sheet of static dissipating polyurethane foam (McMaster-Carr, Elmhurst, IL). The assembly was fixed with two rubber bands so as to create a slight compressive load on the force sensing surfaces, wrapped in wet paper tissue, placed in a sealed bag and stored at 37 °C.

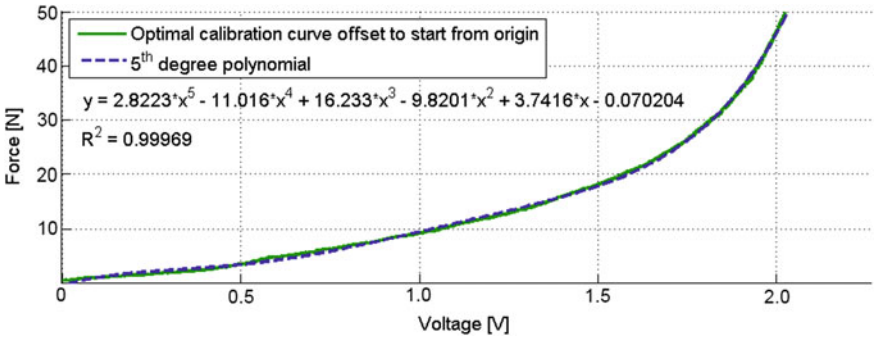

Fig. 2 Example of a calibration curve of a force sensor fitted with a 5th degree polynomial function

The IPM force sensors were calibrated repeatedly throughout the precondition procedure, prior to and after sterilization, and after explantation in order to monitor a change of sensitivity over time. The calibration performed within 4 h after IPM explantation served as reference for the data analysis. The calibrations were performed on an Instron 5544 universal testing machine with a 500 N load cell and Merlin software (Instron Corp, Norwood, MA). The IPM was placed in a custom-build fixture. After activating the data acquisition and transmission of the IPM, a compressive force (0–44.5 N, cross-head speed: 0.254 mm/min) was applied with a stainless steel pin (diameter 9.5 mm, flat end) to each sensor cover plate individually. The Instron force data and corresponding sensor voltage data were correlated to create sensor-specific calibration curves, see Fig. 2, using a customized code in MATLAB (MathWorks Inc., Natick, MA).

2.2 Measurements of in Vivo Loadings and Morphometric Parameters

All experiments were approved by the research ethics committee of the University of Cape Town and animal care was in accordance with institutional guidelines. Three senescent *Chacma* baboons (implant body mass: 20.6 ± 1.15 kg) received one IPM implant unilaterally in the upper pectoral region (alternating left and right side) under full anaesthesia. The devices were placed in the sub-muscular position with the force-sensing surface facing outwards and secured in place with two sutures. The procedures were performed using standard surgical techniques for the implantation of cardiac pacemakers. A healing period of 8 weeks was allowed to ensure fibrous encapsulation of the implants before the commencement of in vivo measurements.

Using the measurement system described above, in vivo loadings on the implanted IPM devices associated with activities of the animals were recorded in daily sessions of between 5 and 15 min duration for up to 6 days. The measurements were performed during periods of elevated levels of physical activity of the animals prior to the routine feeding. The activities of the animals included vertical movement in the cages, pulling and pushing at cage walls and ceiling using the upper extremities and single-arm striking. Physical activities of the subjects associated with the loading events were recorded with synchronized video. In vivo loading data associated with physiological range of motion (ROM) of the upper extremities was acquired in experiments on anesthetized animals. The arm/shoulder complex of the respective implant side was moved so as to separately simulate adduction/abduction, circumduction and elevation (rotation of the arm predominantly in the axial, coronal and sagittal plane, respectively). Subsequently, the animals were euthanized under full anaesthesia and IPM implants retrieved. Post-mortem, the length, L_m, along the estimated line of action and the thickness, t_m, at the location of the IPM of the *Pectoralis major* muscle were measured in situ using a ruler and caliper, respectively. Following excision, the mass, M_m, and volume, V_m, of the excised muscle were measured with a scale and by fluid displacement method, respectively. The fibrotic capsule formed around the implant and adjacent muscles tissue underwent paraffin histology and staining for Haematoxylin and Eosin and fluorescent CD68 to assess fibrotic tissue formation and inflammatory response.

Data of the IPM force sensors was processed using customized software routines in MATLAB (MathWorks Inc, Natick, MA). The raw voltage data was subjected to a median filter ($n = 7$) to reduce noise levels. In absence of a true and common in vivo reference value, the voltage at rest, V_{rest}, of the conscious animals was used as reference for voltage-force conversion algorithm. The sensor calibration curves obtained within 4 h after device explantation were identified to closest approximate the sensor sensitivity during the in vivo experiments and used for the data conversion. Assuming an equal distribution over the principal IPM surface, the transverse force F_T acting on the IPM was determined from the sum of the individual forces of the six sensors, F_{Si}, and the ratio of the total area of the IPM principal surface A_T to the sum of the areas of the sensor cover plates, A_{Si}:

$$F_T = \frac{A_T}{\sum_{i=1}^{6} A_{Si}} \sum_{i=1}^{6} F_{Si} \tag{1}$$

A custom peak detection algorithm in MATLAB was employed to filter the force data and to obtain a single maximum force value associated with distinct movement events. The algorithm was based on the comparison of the force value of two adjacent data points. A threshold value of $\Delta F_T = 0.25$ N was found to be suitable to prevent loss of significant features.

2.3 In Vivo Loading Conditions During Voluntary Activities

For implants 447 and 449, 20 and 19 data acquisition sessions were conducted with a total duration of 77 and 78 min, respectively, while 10 data acquisition sessions of 38 min in total were employed for implant 575. The contact force sensors used yielded good repeatability evident from the low variation of between 3.8 ± 4.0 % and 4.7 ± 2.1 % for the reference measurements at rest. Histograms of the compressive force F_T measured during all experiments for each implant are presented in Fig. 3.

The F_T events recorded with the different IPMs were of similar Gauss-type distribution of the force amplitude with a gradual tail towards the maximum forces. The majority of F_T events were close to the resting force whereas events with maximum F_T amplitude occurred very infrequently. For all three implants, 95 % of the F_T data was found to lie between a lower limit (P2.5) of approximately 0.8 $F_{T,rest}$ and an upper limit (P97.5) of approximately 1.2 $F_{T,rest}$. The maximum amplitude of F_T was found to be between two and five fold of $F_{T,rest}$ for the different IPM implants. The comparison of $F_{T,max}$ between the different implants was somewhat restricted due to the fact that maximum voluntary contraction, generally used in experiments with human volunteers, could not be confirmed in these experiments on animals. However, a strong correlation of $F_{T,rest}$ with the volume V_m of the *Pectoralis major* ($R^2 = 0.99$, $p = 0.008$) in combination with the uncontrolled movements of the animals justified the variation of $F_{T,max}$ between the three IPMs.

The maximum and median of the compressive force, F_T, for all three IPMs were 77.2 ± 54.6 N and 22.1 ± 7.0 N, respectively (see Fig. 4). With the animals at rest, the force on the IPM was on average 22.2 ± 7.3 N (14.3, 23.7 and 28.7 N for implants 447, 449 and 575). For the 30 highest force values measured, the associated movements of the upper extremities were identified from the synchronous video data of each implant. The typical movements were pushing (against cage wall, weight bearing, landing from vertical movement), pulling (at cage walls and foraging objects), stretching (adduction, abduction and raising of arms without resistance) and striking (fast movement of arm without resistance) while some force events remained unidentified, see Table 1. Although the intensity of movements determined loading on the device, a clear ranking of movement type (e.g., pushing, pulling, etc.) with respect to force amplitude could not be ascertained from the results obtained from the conscious baboons.

2.4 In Vivo Loadings During Range of Motion and Morphometric Measurements

In the anaesthetized animals, the force on the IPM at rest was $F_{T,rest}$ = 13.4 ± 3.3 N (9.8, 16.3 and 14.1 N for implants 447, 449 and 575) with the arm

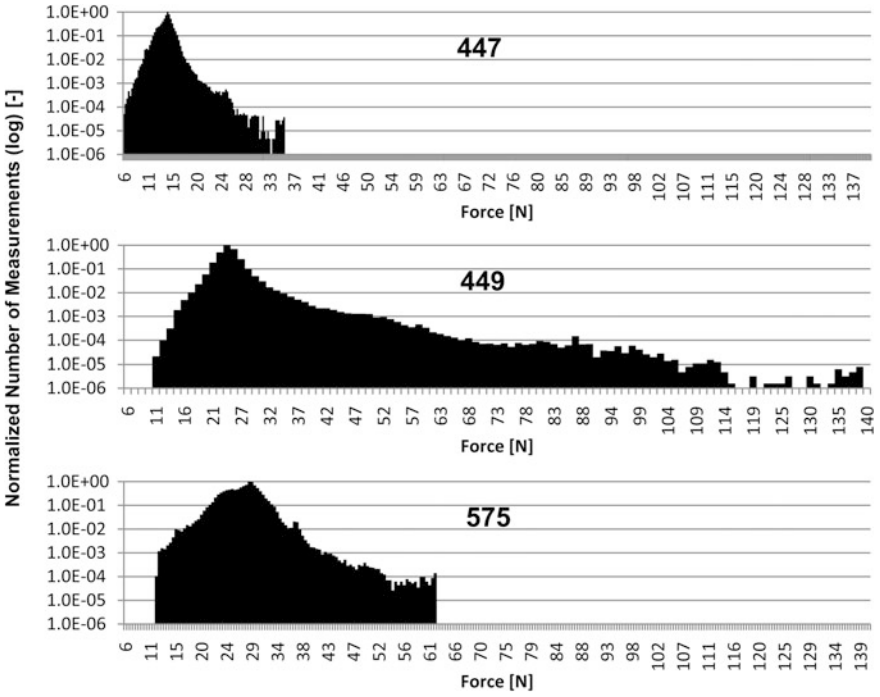

Fig. 3 Histograms of force F_T measurements for the IPM implants. The number of measurements was normalized in order to account for the different durations of the experiments for the three implants

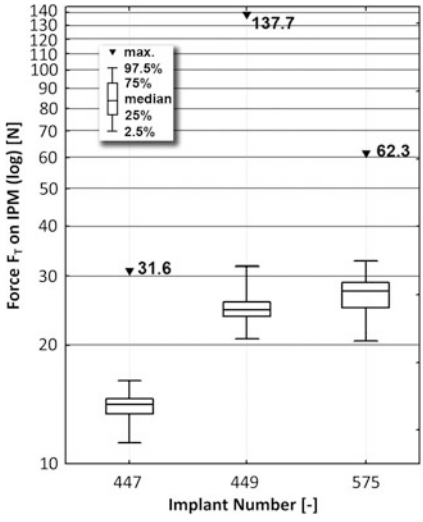

Fig. 4 Median and maximum in vivo forces on implanted IPM devices during voluntary activities of the animals

Table 1 Normalized force $F_T/F_{T,rest}$ on IPM implants associated with movements inducing high levels of loads

Movement	$F_T/F_{T,rest}$			
	447	449	575	Mean
Pushing	1.9 ± 0.2	4.0 ± 0.0	1.8	2.1 ± 0.7
Pulling	1.7 ± 0.0	4.2 ± 0.9	1.7 ± 0.3	2.5 ± 1.7
Stretching	1.9 ± 0.3	–	–	–
Striking	1.7 ± 0.0	–	–	–
Unidentified	1.8 ± 0.2	3.8 ± 0.3	1.6 ± 0.0	2.3 ± 1.1

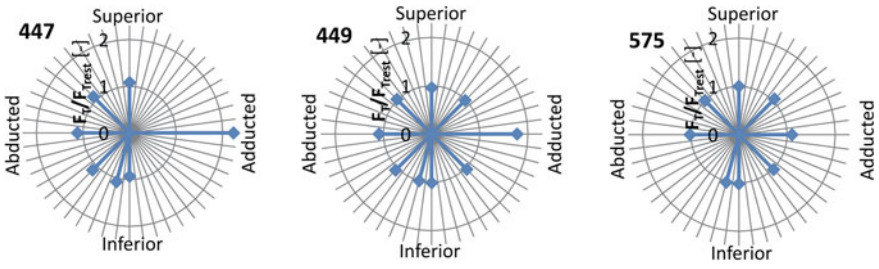

Fig. 5 Polar graphs of the normalized force $F_T/F_{T,rest}$ acting on the IPM versus position of the upper limb obtained in range of motion experiments

ipsilateral to the implant and positioned in the anatomical position. The maximum force recorded during the range of motion movements was 34.6 ± 15.7 N. For most of the positions of the arm, the forces on the IPM were only marginally larger than the force at rest, indicated by values of the ratio $F_T/F_{T,rest}$ close to unity (see Fig. 4). For two implants, a marked increase of the force on the IPM (to 4.0 and 2.9 fold of $F_{T,rest}$) was recorded in the adduction position of the arm while a other arm positions did not cause considerable changes in the force on the implant.

The force exerted on the implanted IPM was caused by a combination of tension in and compression by the surrounding anatomical structures; and more specifically, (1) the extreme position of the arm that generated tension in the fibrous encapsulation of the chronically implanted IPM and (2) the strength of *Pectoralis major* contraction. This finding was supported by results from the ROM experiments, which yielded peak forces caused by the muscle being stretched and compressed, respectively (Fig. 5). However, not all extreme arm positions caused these peak forces, e.g., circumduction of the arm caused a fluctuating, rather than continuous F_T response. This was interpreted as an effect of the fusion of the fibrotic encapsulation to the surrounding anatomical structures.

The effect of the muscle tone present in conscious subjects was evident from an decrease in resting force $F_{T,rest}$ of between 31 and 51 % between conscious and anaesthetized animals. This outcome indicated the effect of muscle tone on in vivo

Table 2 Body mass (M_b) of the animals and morphometric parameters of the *Pectoralis major* muscles of baboons and human

Parameter	Baboon implant no.				Baboon overall[a]	Human
	447C	447A	449C	449A		
M_b (kg)	24.7	24.7	23.0	23.0	23.9 ± 1.2	~90[b]
M_m (g)	82	154	125	166	131.8 ± 37.4	716.8[c]
V_m (cm^3)	70	135	120	150	118.8 ± 34.7	676.4[d]
ρ_m (g/cm^3)	1.171	1.141	1.042	1.107	1.115 ± 0.055	1.060[e]
$t_{m,cb}$ (mm)	5	4	4	6.5	4.9 ± 1.2	–[f]
$w_{m,cb}$ (mm)	42.5	60	47.5	50	50.0 ± 7.4	–[f]
$w_{m,IPM}$ (mm)	92.5	95	90	80	89.4 ± 6.6	–[f]
L_m (mm)	150	150	170	180	163 ± 15	–[f]
PCSA[g] (cm^2)	7.7	14.8	11.6	13.7	12.0 ± 3.1	18.3[h]

The length along the estimated line of action (L_m), thickness and width at the crossbar of the buckle force transducer ($t_{m,cb}$, $w_{m,cb}$), and width over the IPM implant ($w_{m,IPM}$) were measured with a ruler and caliper, respectively. After excision, the mass (M_m) and volume (V_m) of the muscle were recorded using a scale and a fluid displacement method, respectively

[a] Mean ± standard deviation

[b] From Spitzer et al. [35]

[c] $M_m = \rho_m V_m$

[d] From Garner and Pandy [17]

[e] From Ward and Lieber [40]

[f] To be measured

[g] With the assumption of $L_f/L_{f,opt} = 1$

[h] From Chang et al. [6]

forces on implants which typically can in fact not be captured in cadaver experiments.

Results of morphometric measurements of the *Pectoralis major* muscles are summarized in Table 2.

3 Correlation of In-Line and Transverse Force of the *Pectoralis major*

3.1 Measurement of Transverse and In-Line Muscle Force

The transverse force of the *Pectoralis major* was measured employing the wireless in vivo measurement system described in Sect. 2.1. For the measurement of the in-line force of the *Pectoralis major* associated with muscle contraction, a custom-made stainless steel buckle transducer with closed rectangular frame (66 × 100 mm, 4 × 4 mm cross-section), removable cross bar (semi-circular cross section: R = 2 mm) and two linear foil strain gauges (EA DY 125BT 350, Vishay Micro Measurements Group, Malvern, PA) (Fig. 6a) were utilized [10].

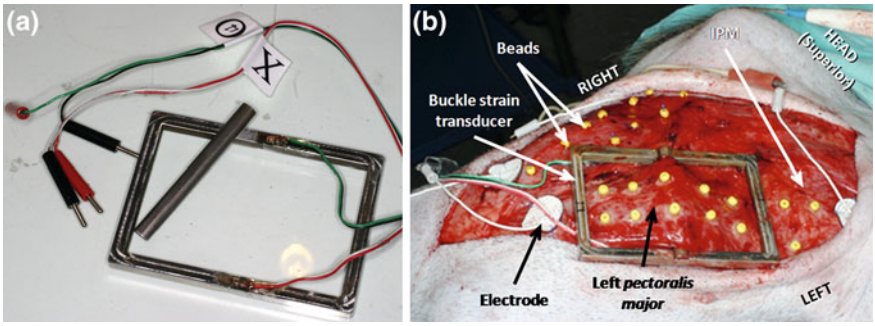

Fig. 6 Custom-made buckle force transducer with foil strain gauges for the measurement of in-line force of the *Pectoralis major* (**a**) and exposed *Pectoralis major* muscle with attached buckle force transducer and electrodes for electrical stimulation experiments (**b**) (The beads attached to the muscle were used for an unrelated study.)

All experiments were approved by the research ethics committee of the University of Cape Town. In connection with the first study described above, two senescent *Chacma* baboons (implant body mass: 23.9 ± 1.2 kg) received one IPM unilaterally in the upper pectoral region (left side: one animal, right side: one animal) under full anaesthesia. The IPM was implanted in the sub-muscular position with the force-sensing surface facing outwards and secured in place with two sutures. The procedures were performed using standard surgical techniques for the implantation of cardiac pacemakers.

Ten weeks after implantation, with the IPM implants having obtained fibrous encapsulation, the *Pectoralis major* muscle was exposed by removing overlying skin with the animals under full anaesthesia. The muscle was isolated from surrounding soft tissue. To attach the buckle force transducer, two incisions were made in the fibre direction of the muscle extending from the IPM implant towards the insertion of the muscle. The frame of the buckle transducer was positioned over the muscle section between the incisions and secured in place with the crossbar (Fig. 6b). Pre-gelled disposable adhesive surface electrodes (Model 9013S0211, Medtronic Inc, Minneapolis, MN) were attached to the exposed *Pectoralis major* muscle near its origin and insertion for electrical stimulation. At the same occasion, identical procedures were performed on the alternate pectoral side without chronic IPM implant for both animals. The alternate pectoral side received, however, an acute IPM implant for the force measurement procedure.

Constant frequency train (CFT) stimulation of the *Pectoralis major* was performed using a PULSAR 6 bp bipolar stimulator (FHC Inc, Bowdoinham, ME) and pre-gelled surface electrodes. The exposed and isolated muscle received trains of electrical current of constant, discrete amplitude of 3, 5, 7, 9, 11, 15, 17, 21, 23, 27, 31, 33, and 35 mA in one of two pre-determined randomly ordered sets. Each train comprised 2000 pulses with pulse duration of 53 μs and pulse interval of 203 μs. The selected amplitude range of the current and the randomization aimed at reaching maximum activation and minimizing fatigue, respectively, of the

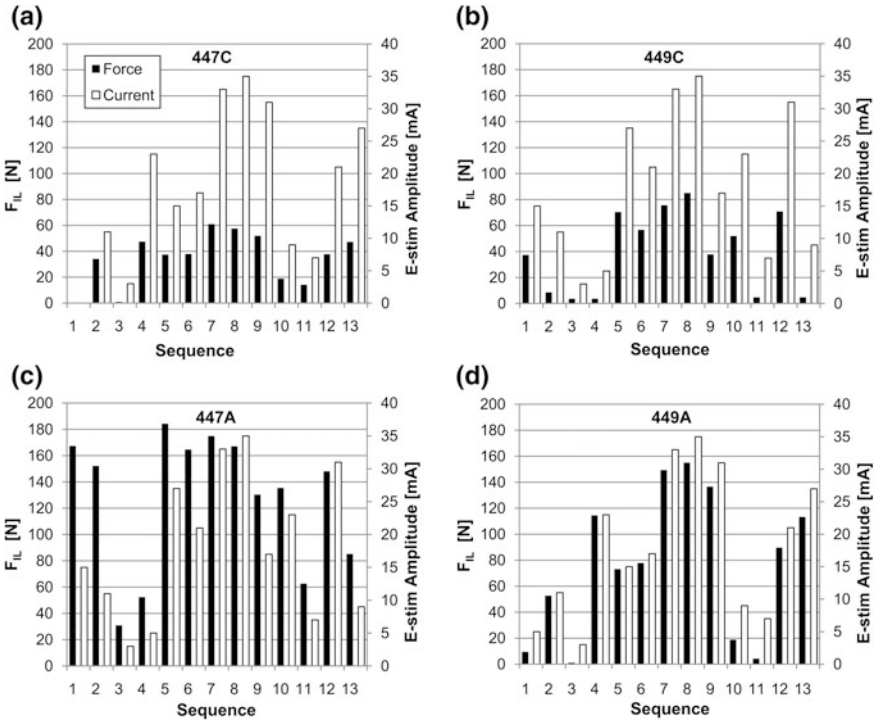

Fig. 7 In-line force F_{IL} of *Pectoralis major* (*solid bars*) and associated amplitude of electrical current (*open bars*) during the 13 pulse trains of the electrical stimulation for various implants: **a** chronic implant 447C, **b** chronic implant 449C, **c** acute implant 447A and **d** acute implant 449A. (For experiment 447C, the first data pair is not included due to a malfunction of the in-line force measurement during the stimulation with current amplitude of 5 mA.)

muscle. The arm of the baboon was constrained in the anatomical position whereas the shoulder complex was left to move freely, which led to the generation of a concentric (non-isometric) contraction of the muscle. The contractile force F_{IL} developed in the stimulated muscle was measured with the buckle force transducer. The transverse force F_T of the contracting muscle was measured with the implanted IPM and data transmitted via the wireless acquisition system. The maximum forces F_T and F_{IL} were identified for each stimulation train.

The in-line force F_{IL} of the *Pectoralis major* recorded during each set of electrical stimulations for all four experiments are illustrated in Fig. 7. The in-line force F_{IL} varied in the ranges of 0.9–60.9 N (447C) and 3.6–85.0 N (449C) for the chronic IPM implants whereas the force ranges were larger for the acute implants with 30.9–184.3 N (447A) and 1.1–155.1 N (449A). The maximum force was observed for the maximum level of stimulation current for two implants, 449C and 449A, only. For the implants 447C and 447A, the maximum force activation was obtained at sub-maximal current levels prior to maximum stimulation.

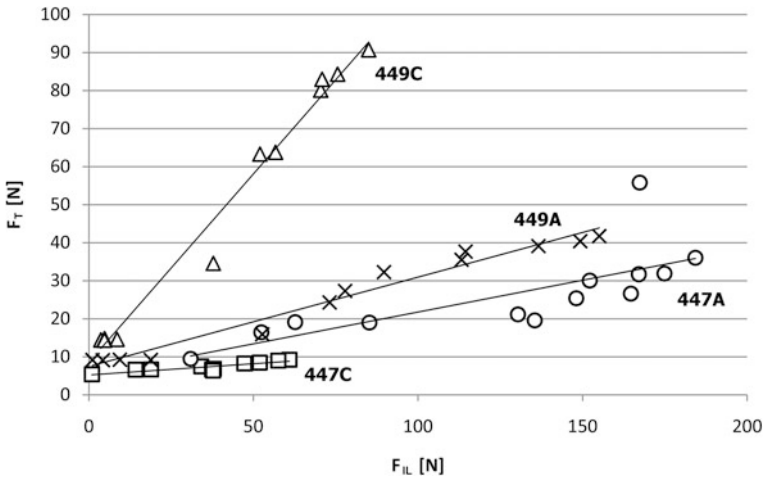

Fig. 8 Transverse force F_T acting on the IPM implant versus in-line force F_{IL} of the *Pectoralis major* during the electrical stimulation experiments for the two chronic and two acute implants. The trend lines were obtained with simple linear regression

The transverse force F_T of the *Pectoralis major* associated with the in-line force F_{IL} during electrical stimulation is illustrated in Fig. 8 for all four implants. The transverse force was measured in the following ranges: 5.4–9.2 N (447C), 9.2–41.7 N (449A), 9.5–55.8 (447A) and 14.3–90.7 N (449C). While there was a distinct difference with regards to the maximum F_{IL} between chronic (low F_{IL}) and acute implants (high F_{IL}), this was not the case for the transverse force.

3.2 Correlation of In-Line Force and Transverse Force of the Pectoralis Major

Simple and multiple linear regression (SLR and MLR) analyses were performed to evaluate the relationship between the in-line force F_{IL} and the transverse force F_T of the *Pectoralis major* muscle and to identify significant parameters of this relationship.

The approach of forward-stepwise multiple linear regression involves (i) identifying an initial model, (ii) iteratively "stepping," that is, repeatedly altering the model at the previous step by adding or removing a predictor variable in accordance with the "stepping criteria," and (iii) terminating the search when stepping is no longer possible, or when a specified maximum number of steps has been reached. The forward-stepwise method employs a combination of forward entry and backward removal methods. At the first step, the procedure of forward entry is performed. At any subsequent step where two or more effects have been selected for entry into the model, forward entry is performed if possible, and backward removal is performed if possible, until both procedures cannot be performed and stepping is

terminated. In forward entry, the effect with the largest value on the entry statistic is entered into the model whereas the effect with the smallest value on the removal statistic is removed from the model in backward removal [19].

The transverse force F_T and the relative transverse force $\Delta F_T = F_T - F_{T,Rest}$ were alternatively defined as response. The in-line force F_{IL} and the morphometric parameters of the *Pectoralis major*, L_m, $t_{m,cb}$, $w_{m,cb}$, $w_{m,IPM}$, M_m, and V_m, were regarded as input parameters (regressors). Although not measured directly, two additional regressors were considered; the physiological cross-sectional area (PCSA) [20] defined as

$$PCSA = \frac{V_m}{L_m} \cdot \frac{L_f}{L_{f,opt}}, \tag{2}$$

where L_f and $L_{f,opt}$ were the muscle fibre length and optimal muscle fibre length, respectively, and the stress σ_m in the *Pectoralis major*

$$\sigma_m = \frac{F_{IL}}{PCSA} \tag{3}$$

The PCSA was included as it scaled proportionately with, and as such related to, the maximum isometric force of a muscle, $F_{IL,opt}$, at optimal muscle fibre length, $L_{f,opt}$. The muscle fibre length and the optimal muscle fibre length was assumed to be similar, and the ratio $L_f/L_{f,opt}$ to be unity, for all *Pectoralis major* muscles of the two animals. The muscle stress σ_m was considered in the analyses since it was a unique interpretable parameter combining force and a morphometric parameter of the muscle.

The correlation results obtained from multiple regression analyses were evaluated for model misspecification by observing the distribution of residuals, as well as the correlation between regression-obtained coefficients. The significance of a correlation was evaluated by calculating the non-directional probability of the correlation coefficient, R, using t-statistics with $t = R/\sqrt{(1 - R^2)/(N - 2)}$ where N is the sample size. An adjusted coefficient of determination, R^2_{adj}, was employed where required to account for the increase of the degree of freedom associated with the addition of regressors in an MLR analysis [38]. R^2_{adj} indicates a genuine improvement in of correlation as compared to an apparent improvement associated with an increased value for the non-adjusted coefficient of determination R^2. Statistical significance was assumed for $p < 0.05$.

3.2.1 Subject-Specific Correlation

SLR analyses of the corresponding $F_T - F_{IL}$ data indicated significant correlation ($p < 0.05$) between the transverse force and in-line force for each *Pectoralis major* muscle and IPM implant, respectively. The subject-specific linear regression, indicated by the trend lines in Fig. 8, yielded the following relationships between the in-line force F_{IL} and the transverse force F_T both for the chronic and acute IPM implants:

Table 3 Significances of individual regressors, normal and adjusted coefficients of determination and correlation significance obtained in linear regression analyses for various combinations of experimental parameters with response F_T and ΔF_T, respectively, indicated in the second column. The first column provides the case indicator

		Individual significance (p) of correlation for regressors									Results		
		F_{IL}	$t_{m,cb}$	L_m	$w_{m,IPM}$	$w_{m,cb}$	V_m	M_m	PCSA	σ_m	R^2	R^2_{adj}	p
A	F_T	0.0028									0.17	0.15	0.0028
B	F_T	$<10^{-7}$	n	$<10^{-7}$	$<10^{-7}$	0.0014	n	n			0.69	0.66	$<10^{-7}$
C	F_T	0.0545	n	$<10^{-7}$	$<10^{-7}$	n	n	n	n	0.0004	0.71	0.68	$<10^{-7}$
D	ΔF_T	0.0007									0.21	0.19	0.0007
E	ΔF_T	$<10^{-7}$	n	$<10^{-7}$	$<10^{-7}$	0.0010	n	n			0.63	0.60	$<10^{-7}$
F	ΔF_T	n	0.0371	0.0076	0.0175	n	n	n	n	$<10^{-7}$	0.65	0.62	$<10^{-7}$

n Regressor used but no correlation indicated

- 447C: $F_T = 0.06\ F_{IL} + 5.24$, $R^2 = 0.80$;
- 449C: $F_T = 0.99\ F_{IL} + 8.63$, $R^2 = 0.97$;
- 447A: $F_T = 0.17\ F_{IL} + 5.03$, $R^2 = 0.56$; and
- 449A: $F_T = 0.23\ F_{IL} + 7.47$, $R^2 = 0.96$.

The subject-specificity of this relationship was confirmed by a poor generalized correlation between F_{IL} and F_T ($R^2 = 0.17$) when data of all implants was included (case A, Table 3).

3.2.2 Generalized Correlation

The generalized intra-species correlation was evaluated by performing SLR and MLR analyses on the entire data set of F_T and F_{IL} ($n = 51$) from all four experiments (447C, 447A, 449C and 449A). The SLR with F_T and ΔF_T, respectively, as response and F_{IL} as single regressor indicated poor correlation with R^2 of 0.17 and 0.21 (Table 3, cases A and D).

Employing a forward-stepwise MLR approach, the two strongest correlations were obtained when all considered regressors were included in the analysis, see Table 3, cases C and F. The overall strongest intra-species correlation was found between transverse force F_T and in-line force F_{IL} of the *Pectoralis major* ($R^2 = 0.71$, $p < 0.001$) with additional regressors of stress σ_m in the *Pectoralis major*, originating from the in-line force F_{IL}, the length L_m of the muscle and the width of the muscle over the IPM, $w_{m,IPM}$ (case C). This correlation yielded following regression equation:

$$F_T = -1055.78 - 0.24\ F_{IL} + 3.24\ L_m + 5.95\ w_{m,IPM} + 434.62\ \sigma_m. \quad (4)$$

Although F_{IL} marginally failed to reach significance ($p = 0.055$), it was included in the regression equation since it (a) constituted one of the two principal parameters of interest of this study, F_T and F_{IL}, and (b) was measured experimentally, unlike σ_m which was a derived parameter (see Eq. 3). Figure 9 illustrates

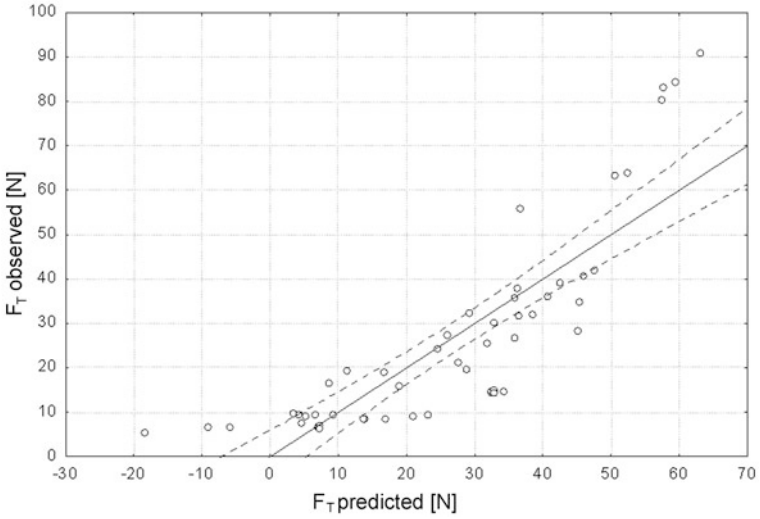

Fig. 9 Observed versus predicted transverse force F_T of the *Pectoralis major* in the baboon. The prediction was obtained from the intra-species correlation equation established (Eq. 4). The dashed lines indicate the 95 % confidence interval

the relationship between the predicted F_T, using Eq. (4), and the measured values of F_T.

The strength of the intra-species correlation was not affected by the estimation of the parameters $L_f/L_{f,opt}$ and cos θ, both of which were considered to be unity for all subjects. These assumptions were deemed reasonable since the animals used in the study were of the same species, same gender and similar body masses. The variation of the fibre length, L_f, and the optimal fibre length, $L_{f,opt}$, of a muscle has been reported to remain minimal when scaling these parameters with respect to body mass in different test subjects of the same species [12]. While the uncertainty of these parameters may have affected the predicted magnitude of F_T, the specific formulation of the linear regression relationships ensured that the correlation of response and regressors was not affected [38].

For the chronic implants (447C, 449C), the maximum in-line force $F_{IL,max}$ was significantly lower than for the acute implants (447A, 449A): 73.0 ± 17.0 N versus 169.7 ± 20.6 N, $p = 0.036$. Differences of the morphometric parameters of the *Pectoralis major*, determined post-mortem (Table 2), such as mass M_m, volume V_m and physiological cross-sectional area PCSA, could however not be established. It is suggested that the strength of the intra-species F_T-F_{IL} correlation will improve beyond the value of $R^2 = 0.71$ obtained when the analysis is limited to chronic implants only. Due to the feasibility character of the presented study with two animals and two implants per group (chronic and acute), this separation was not meaningful. Despite the fact that the significant difference between chronic and acute implants observed for $F_{IL,max}$ did not extend to the maximum transverse force $F_{T,max}$, these results are seen as a strong indication for the benefit

of this in vivo study, and presented method, over cadaver studies; namely the ability to capture the effect of fibrous encapsulation on the in vivo biomechanics of the implant.

It remained uncertain whether maximum levels of F_{IL} and F_T, respectively, were reached during the electrical stimulation experiments. The maximum electrical current did not always yield the maximum magnitude of the in-line force F_{IL} (Fig. 7). Accelerated muscle fatigue due to the CFT stimulation compared to variable frequency train (VFT) stimulation [4] may have played a role. However, the CFT stimulation was chosen in this study as this method is used in most current systems for functional electrical stimulation [11] and generally provides a more physiological stimulation pattern. A further influencing factor may have been the potential differences in the maximum levels of F_{IL} due to concentric, isometric and eccentric contractions [32].

The definition of the PCSA (Eq. 2) [20] used in this study did not account for the pennation angle θ of the muscle fibres as compared to a more comprehensive formulation of the PCSA that considers this parameter [33]. This simplification was based on the assumption that the pennation angle of the *Pectoralis major* muscle did neither differ between the bilateral sides of each subject nor between subjects of this study.

With the motivation for this study to quantify in vivo forces on pacemaker devices implanted sub-muscularly in the pectoral region, the established intra-species relationship may offer potential towards gaining new insights in biomechanics of such implants in patients. One requirement is a more detailed assessment of the proposed relationship with regards to the distinctiveness and the precision of individual parameters and the robustness of the relationship based on a larger subject cohort. Furthermore, inter-species differences will need to be considered in an extended and more comprehensive relationship as considered in the following section.

4 Inter-Species Transfer Function for the Patient-Specific Prediction of Intrinsic Mechanical Loadings on Sub-Muscular Pectoral Pacemaker Implants

4.1 Assessment of Pectoral Anatomy in Baboon and Human

After conclusion of abovementioned study [10], two *Chacma* baboons ($M_b = 23.9 \pm 1.2$ kg) with pectoral sub-muscular implants of instrumented pacemakers (IPM) underwent imaging of the thoracic region with computed tomography (Aquilion 4, Toshiba Medical Systems, Zoetermeer, Netherlands) within 2 h of euthanasia. Subsequently, the *Pectoralis major* was dissected and morphometric details were recorded as described by de Vaal [10]: length along the estimated line of action L_m, thickness and width at the crossbar of the buckle force

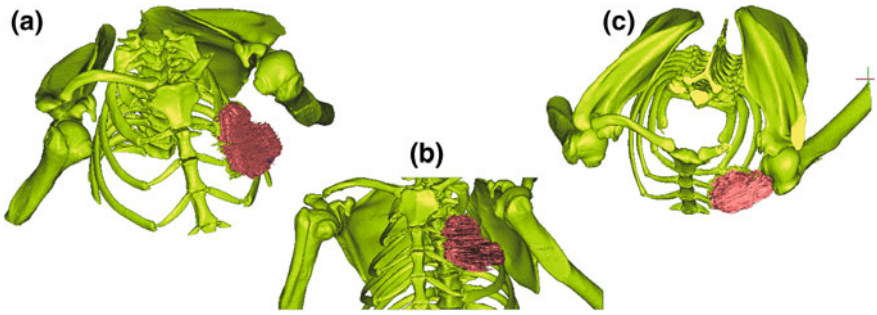

Fig. 10 Three-dimensional reconstruction of baboon thoracic skeletal structures (in *green*) and pectoral IPM implant (in *purple*) from CT data: **a** isometric view, **b** frontal view and **c** top view (Imaging artefacts in the CT data were responsible for the poor resolution of the implant compared to the skeletal structures)

transducer $t_{m,cb}$ and $w_{m,cb}$, and width over the IPM implant w_m. After excision, mass M_m and volume V_m of the muscle were recorded.

Using Mimics® (Materialise BV, Leuven, Belgium), the location of the IPM and surrounding musculoskeletal structures were reviewed in axial and sagittal cross-sectional views of baboon and human CT imaging data. The latter were obtained from the Virtual Human Male (VHM), Visible Human Project, National Library of Medicine National Institutes of Health, Bethesda, MD, USA [17, 35]. In VHM images, the position of a pectoral sub-muscular pacemaker implant was estimated according to Brinker and Midei [5]. Comparative anterior-posterior and lateral measurements for baboon and human were obtained from axial views. A 3D representation of skeletal anatomy of one baboon with IPM implant was obtained by reconstruction from a CT image set using thresholding operations (Mimics®).

The baboon morphometric data are summarized in Table 2. The position of a sub-muscular pectoral IPM implant in one baboon is illustrated in Fig. 10. Cross-sectional views of the pectoral region of baboon and human are shown in Fig. 11. The anterior-posterior and lateral (humerus-to-humerus) distances are indicated in an axial section at the middle of the sternum and corresponding sagittal section at the medial third of the clavicle is shown. The ratio of lateral to anterior-posterior distance was 15 % larger in the baboon compared to the human.

4.2 Simplified Model of Sub-Muscular Pectoral Implant

A simplified representation of a sub-muscular pacemaker implant was proposed to facilitate the evaluation of influence of individual parameters on the mechanical loading on the implant. The representation was limited to the instance of the muscle contraction. This limitation was deemed sufficient for quasi-static loading, disregarding mass or damping effects, based on two assumptions. The IPM was exposed to a load at rest, i.e., the muscle was compressed prior to contraction.

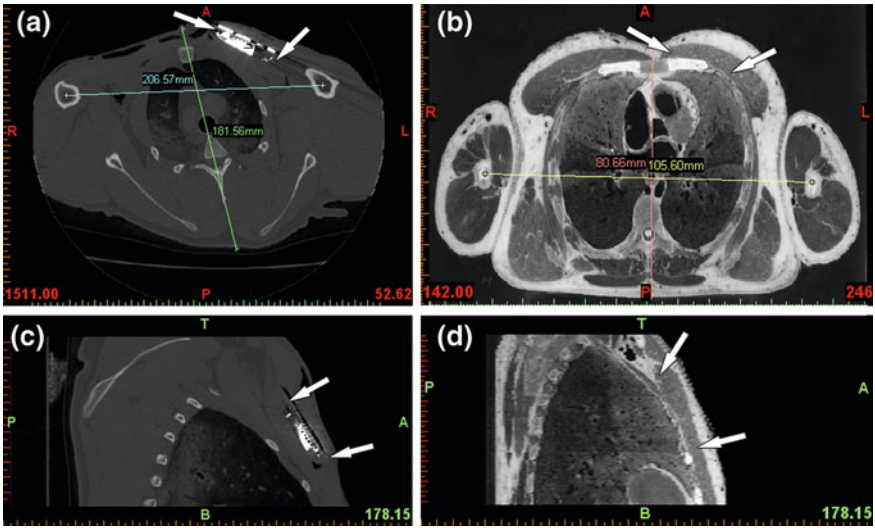

Fig. 11 Cross sectional views of the pectoral region of the baboon and human [35]. The anterior-posterior (front-to-back) and lateral (femur-to-femur) distances are indicated in axial section at the middle of the sternum for baboon (**a**) and human (**b**). The corresponding sagittal section at medial third of the clavicle is shown for baboon (**c**) and human (**d**). Axial distances were not according to same scale for baboon and human; however only the ratios of measured values were used. The position of the IPM implant in the baboon is indicated with *white arrows* (**a**, **c**). For human (**b**, **d**), the estimated position is indicated [5]

In addition, the effects of load rate and fibre orientation on the viscoelastic behaviour of passive muscle under compression [36] can be neglected since, in our experiments, the muscle was active with increased stiffness compared to passive state and the compression acted in cross-fibre direction with lower stiffness compared to the fibre direction. The muscle contraction was sustained for approximately 0.5 s only [10] and the compression rate was similar to that for contraction of a relaxed muscle to maximum level of 200 s^{-1} [42]. This value was considerably higher than the rate reported by Van Locke et al. [36] for which they reported that the reaction of passive muscle to compression was devoid of viscous effects for instantaneous loadings.

Figure 12 illustrates a simplified physiological model: The IPM resting on *Pectoralis minor*, supported by rib cage, is compressed by the *Pectoralis major*.

The mechanically equivalent model is illustrated in Fig. 13 indicating parameters considered to affect the normal force F_T in the two-dimensional case: in-line force F_{IL} generated in the *Pectoralis major*, material properties of the anatomical structures surrounding the IPM, and angles of attachment of the *Pectoralis major* from the IPM location to origin and insertion of the muscle, ψ_1 and ψ_2, respectively. In the three-dimensional case, the interplay between width of the *Pectoralis major* over the implant, w_m, and the force uniformly distributed along this width, Q_{IL}, with

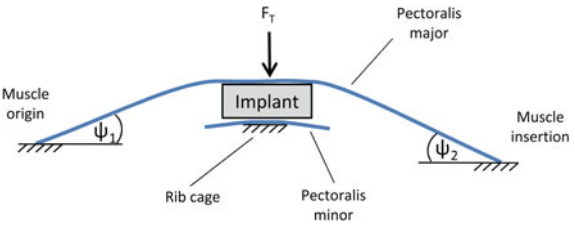

Fig. 12 Simplified physiological representation of a sub-muscular pectoral pacemaker implant situated between the *Pectoralis major* and the *Pectoralis minor* resting on the rib cage

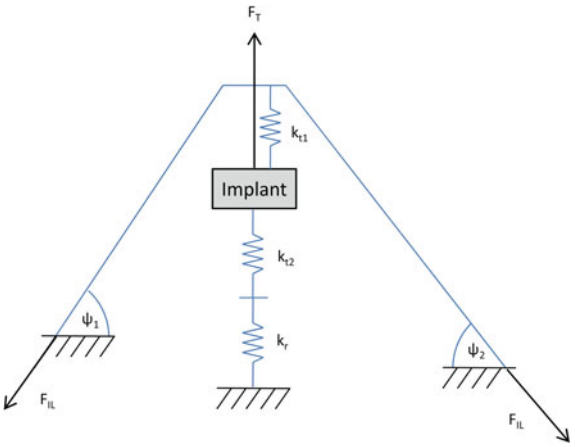

Fig. 13 Mechanical equivalent of the simplified physiological model of a sub-muscular pectoral implant indicating the transverse force F_T on the implant and parameters that affect the magnitude of F_T

$$Q_{IL} = \frac{dF_{IL}}{dw_m}, \tag{5}$$

was assumed to affect F_T due to the muscle contraction causing a concentrated muscle mass around the line of action. The IPM was considered to be a rigid structure. The transverse viscoelastic properties of *Pectoralis major* and *Pectoralis minor* [36] were simplified as transverse stiffness k_{t1} and k_{t2}, respectively. The transverse stiffness of the rib cage [37] was simplified as transverse stiffness k_r.

The experimental measurement of in-line force F_{IL} and transverse force F_T of the *Pectoralis major sternum* in the baboon in a related study has been described in Sect. 3 above.

4.3 Assessment of the Robustness of the Baboon Intra-Species Correlation

Due to the small sample size used to establish the intra-species correlation in the baboon, Eq. (4), in Sect. 3 above, it was desirable to assess the robustness of these findings for larger sample sizes in terms of subjects' body mass M_b. Since the established intra-species correlation is a linear relationship between causative

Table 4 Causative parameters and corresponding parameters of the simplified physiological model included in the robustness assessment of the intra-species correlation in baboons

Case	Causative parameter	Model parameter(s)	Relationship
A	F_{IL}	F_{IL}	Linear
B	L_m	F_{IL}	Linear
C	w_m	w_m	Linear
D	σ_m	F_{IL}	Linear
E	σ_m	k_{t1}	Negligible

A linear relationship between the causative factor and model parameter supported robustness of the intra-species correlation

parameters (morphometric and mechanical parameters) and response (F_T), the correlation was considered robust if proportionality, i.e., a linear relationship, existed between causative parameters and the corresponding parameters of the simplified physiological model. Only causative parameters shown to have a significant effect on F_T, i.e., those captured in Eq. (2), were included in the robustness assessment. The relationship between causative parameters and corresponding model parameters was evaluated presuming that all other model parameters remained constant. The assessment incorporated the simplified physiological cross-sectional area (PCSA) defined by Holzbaur et al. [20] as

$$\mathrm{PCSA} = \frac{V_m}{L_m} \cdot \frac{L_f}{L_{f,opt}} \tag{6}$$

and the relationship for the axial stress in the *Pectoralis major*

$$\sigma_m = \frac{F_{IL}}{\mathrm{PCSA}} \tag{7}$$

In contrast to more comprehensive definitions of the PCSA [33], Eq. (6) did not account for the pennation angle of the muscle fibres. This was based on the assumption that the pennation angle of the *Pectoralis major* did not differ between subjects [10]. The assessment also considered that the mechanical properties (i.e., density, constant stress and strain) of vertebrate species' skeletal muscles are generally scale-invariant whereas parameters involved in force generating scale proportionally to scale-variant changes in muscle fibre cross-sectional area and are therefore related to the PCSA [3, 26, 28]. From the latter it follows that the maximum muscle force scales linearly with the muscle's PCSA.

The outcomes of the robustness assessment of the intra-species correlation and the basis for establishing the relationship between causative and model parameters are summarized in Table 4. The proportionality of morphometric parameters F_{IL} and w_m with each acting as its own model parameter was trivial (cases A and C). The linear relationship of the length of the *Pectoralis major* along the line of action L_m and axial stress σ_m, respectively, with the in-line force F_{IL} as model parameter (cases B and D) was based on the proportionality (a) between L_m and PCSA according to Eq. (2) and (b) between PCSA and the maximum isometric

force of a muscle. Proportionality between the tensile stress σ_m and model parameters k_{t1} (case E) could not be ascertained. This case was subsequently neglected since the effect of the transverse stiffness k_{t1} of the *Pectoralis major* on the transverse force F_T was small compared to the effect of the stress σ_m on F_T.

With proportionality for four out of the five significant pairs of morphometric and model parameter and one pair deemed negligible, the intra-species correlation in the baboon was considered sufficiently robust and valid for larger sample sizes, in terms of a wider range of body mass M_b, under similar conditions. Physiological parameters not included in Eq. (4) had a negligible effect on F_T and thus did not affect the robustness of the intra-species correlation.

4.4 Intra-Species and Inter-Species Evaluation of Model Parameters

The intra-species correlation of morphometric parameters and F_{IL} with the transverse force on the pacemaker, F_T, was derived and formulated in Eq. (4) as follows:

$$F_T = -1055.78 - 0.24\, F_{IL} + 3.24\, L_m + 5.95\, w_m + 434.62\, \sigma_m$$

The difference of morphometric and mechanical parameters between subjects and the influence of the model parameters on F_T were evaluated intra-specifically (between baboons) and inter-specifically (between baboons and humans). The following subject populations were considered:

- Baboons: adult males, $M_b \approx 24$ kg [10],
- Humans: adult males, $M_b \approx 90$ kg [35].

Musculoskeletal material parameters were comparable between baboons and humans based on similarity of mammalian musculoskeletal tissue [3]. The evaluation of each model parameter for the intra-species and inter-species effect on F_T was conducted by assuming that all model parameters, except the one under evaluation, remained constant, and ascertaining whether the influence of the variance of this parameter within the subject population had a strong (significant) or weak (insignificant) effect on the magnitude of F_T.

For the intra-species baboon case, the strength of the effect (weak or strong) of a parameter on F_T was based on: (a) whether or not it was represented in Eq. (4), (b) experimental findings and/or (c) data from literature. For model parameters not studied in our intra-species MLR analysis [10], weak intra-species influence on F_T was assigned based on the following considerations:

- t_{mu} and σ_{mu}: Due to the non-linear elastic properties of passive muscle and $F_{Trest} > 0$, a sufficiently high stiffness k_{t2} was assumed, minimizing a change of t_{mu} during contraction of *Pectoralis major*. Combined with the indication that

Table 5 The intra-species and inter-species difference of parameters of the simplified physiological model and the strength of their effect on the transverse force F_T

Model parameter	Morphometric and mechanical parameters				
	Governing parameter	Availability of data		Effect on F_T	
		Baboon	Human[a]	Intra-species	Inter-species
F_{IL}	F_{IL}	x		Strong	Strong
F_{IL}	PCSA	x	x	Strong	Strong
k_{t1}	$t_{m,cb}$	x		Weak	Weak
k_{t1}	σ_m	x		Strong	Strong
k_{t2}	t_{mu}			Weak	Weak
k_{t2}	σ_{mu}			Weak	Weak
k_r	L_r			Weak	Weak
ψ_1, ψ_2	ψ_1, ψ_2			Weak	Strong
w_m	w_m	x		Strong	Strong
Q_{IL}	F_{IL}, t_m, w_m			Weak	Weak

For each model parameter, the governing morphometric and mechanical parameters and the availability of data for baboon and human is indicated

[a] VHM [17]. Obtaining additional morphometric measurements from the raw VHM data set was beyond the scope of this study

$t_{m,cb}$ had no intra-species effect on F_T, see Eq. (4), and $t_{mu} < t_{m,cb}$, a weak influence of t_{mu}, and similarly of σ_{mu}, on F_T was assumed.

- k_r: Based on high values of stiffness and damping of the human chest [37], a weak influence on F_T was assumed for k_r. For baboons, this was supported by the fact that the shoulder was allowed to move freely during electrical stimulation [10], causing a lower compression on the ribs compared to an isometric contraction (with shoulder and sternum fixed).
- ψ_1 and ψ_2: Since F_T and F_{IL} were evaluated only at maximum level of contraction and the shoulder complex was free to move during electrical stimulation, subject-specific differences for ψ_1 and ψ_2 in the contracted muscle state were assumed to be negligible.
- Q_{IL}: The uniform distribution of F_{IL} throughout the muscle cross-section over the IPM, based on an uniform distribution of motor units within the cross section of the activated muscle region [23] was assumed to have a weak influence on F_T.

Adopting the reasoning for the intra-species case, parameters with weak intra-species effect on F_T were also assumed to exhibit a weak inter-species effect on F_T. Due to the considerable difference in the torso geometry between baboon and human, a strong inter-species influence on F_T was, however, assumed for ψ_1 and ψ_2.

For each parameter of the simplified physiological model of a pectoral implant, the size of intra-species and inter-species effect on F_T is given in Table 5. The governing morphometric parameter(s) and availability of data for baboon and human is indicated for each model parameter. A strong inter-species influence on F_T was indicated for *Pectoralis major* model parameters, namely F_{IL}, k_{t1}, ψ_1, ψ_2,

and w_m. Weak inter-species effect was indicated for Q_{IL} and parameters of *Pectoralis minor* and rib cage.

4.5 Assessment of Suitability of Baboon Intra-Species Correlation for Humans

The intra-species correlation established for baboons was considered to be suitable for humans if the differences of morphometric and mechanical parameters between baboons and humans were proportional to differences of the corresponding model parameters. The assessment included causative parameters with

(a) significant intra-species effect on F_T, see Eq. (4), and
(b) unknown effect on F_T, namely PCSA, $t_{m,cb}$, t_{mu}, σ_{mu}, ψ_1 and ψ_2.

The type of relationship (linear or non-linear) between causative and model parameters established for the intra-species correlation in the robustness assessment (Sect. 4.3) was considered equally applicable for the inter-species correlation due to the similarity of the musculoskeletal material properties between baboon and human [3] and the self-similarity of the cursorial upper limbs [39]. Morphometric parameters without significant intra-species effect on F_T according to our previous MLR analysis [10] were considered to have a negligible effect on F_T for the inter-species correlation. To account for the geometrical differences between the two species, the effect of the *Pectoralis major* attachment angles were employed utilizing a relationship derived from the mechanically equivalent simplified model, Fig. 13:

$$F_T = F_{IL}(\cos\,\psi_1 + \cos\,\psi_2). \tag{8}$$

Assuming that F_{IL} did not depend on ψ_1 and ψ_2, a relationship for inter-species differences can be derived from Eq. (8):

$$F_{T,H} = F_{T,B}\frac{(\cos\,\psi_1 + \cos\,\psi_2)_H}{(\cos\,\psi_1 + \cos\,\psi_2)_B}. \tag{9}$$

The outcomes of the suitability assessment are summarized in Table 6. Proportionality between causative and model parameter was indicated for F_{IL}, L_m, w_m, and σ_m (cases A–E) based on the results of the robustness assessment (Supplement). PCSA and $t_{m,cb}$ were negligible based on their insignificant effect on F_T despite potential intra-specific variation in the baboon (cases F and G). The parameters t_{mu} and σ_{mu} were deemed negligible based on the assumptions that the *Pectoralis minor* had a negligible effect on F_T (cases H and I). The attachment angles ψ_1 and ψ_2 exhibited non-linear relationships to the associated model parameter F_T according to Eq. (8) (case J). Whereas cases A–I supported the suitability, i.e., linear scale variance, of the intra-species correlation for inter-species correlation, case J imposed a limitation that required inclusion of a corrective term.

Table 6 Causative parameters and associated model parameters included in assessment of the suitability of the baboon intra-species correlation (Eq. 4) for humans and the type of their inter-species relationship

Case	Causative parameter	Model parameters	Included in intra-species MLR analysis[a]	Inter-species relationship
A	F_{IL}	F_{IL}	Yes	Linear
B	L_m	F_{IL}	Yes	Linear
C	w_m	w_m	Yes	Linear
D	σ_m	F_{IL}	Yes	Linear
E	σ_m	k_{t1}	Yes	Negligible
F	PCSA	F_{IL}	Yes	Linear
G	$t_{m,cb}$	k_{t1}	Yes	Negligible
H	t_{mu}	k_{t2}	No	Negligible
I	σ_{mu}	k_{t2}	No	Negligible
J	ψ_1, ψ_2	ψ_1, ψ_2, F_T	No	Nonlinear

It is also indicated whether a combination of causative and model parameter was included in the intra-species regression analysis [10]. A linear inter-species relationship supported suitability of the baboon intra-species correlation for humans

[a] Described in Sect. 3 and in de Vaal et al. [10]

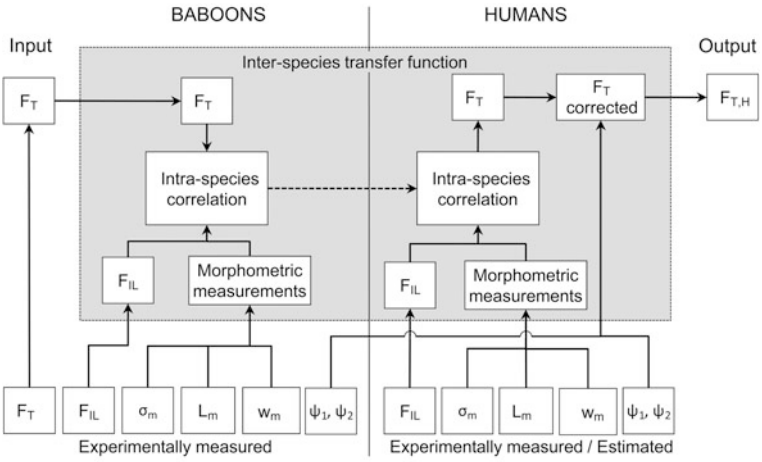

Fig. 14 Diagram illustrating the inter-species transfer function for the correlation of the transverse force F_T on a sub-muscular pectoral pacemaker implant in baboons and humans

4.6 Inter-Species Transfer Function

The concept of the inter-species transfer function to obtain maximum mechanical loads due to muscle contraction on a sub-muscular pectoral device implant is illustrated in Fig. 14. The principal steps of the transfer function are:

1. Experimental acquisition of *Pectoralis major* morphometric parameters (L_m, w_m and σ_m), F_{IL} and F_T in baboons;
2. Attainment of intra-species correlation between morphometric parameters, F_{IL} and F_T from baboon data using linear regression analysis;
3. Acquisition of *Pectoralis major* morphometric parameters and F_{IL} for a human subject;
4. Calculation of uncorrected F_T for human subject using intra-species correlation (step 2) with human data;
5. Correction for nonlinear relationship of ψ_1 and ψ_2 with F_T using Eq. (4).

The inter-species transfer function can be derived from Eqs. (4) and (9) as:

$$F_{T,H} = \frac{(\cos\psi_1 + \cos\psi_2)_H}{(\cos\psi_1 + \cos\psi_2)_B} \cdot (a_1 + a_2 F_{IL} + a_3 L_m + a_4 w_m + a_5 \sigma_m), \qquad (10)$$

where $\bar{\psi}_1$ and $\bar{\psi}_2$ are the average attachment angles of the *Pectoralis major* for baboons with

$$\bar{\psi}_1 = \sum_1^n \psi_1/n \text{ and } \bar{\psi}_2 = \sum_1^n \psi_2/n$$

for n subjects. The initial coefficients values were $a_1 = -1055.78$, $a_2 = -0.24$, $a_3 = 3.24$, $a_4 = 5.95$ and $a_5 = 434.62$ according to Eq. (4). (Note: Eq. (10) requires the parameters to be specified in the following unit: F_{IL} in N, L_m and w_m in mm, and σ_m in N/mm^2).

5 Discussion

Due to the presence of a clavicle, that is absent in all other mammalian animals, the *Chacma* baboon was the most suitable animal model for the inter-species assessment of the in vivo mechanical loading on a pectoral pacemaker implant in humans. This essential resemblance to humans enabled similar movements of the upper limb not found in other laboratory animals [39]. The pectoral implantation site in the baboons compared very well to those of humans, relative to surrounding anatomical structures. The material density of the *Pectoralis major* in baboons of 1.115 ± 0.055 g/cm^3 matched values of 1.112 ± 0.006 g/cm^3 for human skeletal muscle [40] and 1.0597 g/cm^3 for rabbit and canine muscle accepted more generally for mammalian muscle [31].

There were, however, dissimilarities between baboon and human in certain features which required compensation. The body mass for baboons was 23.9 ± 1.2 kg in this study and can vary between 15 and 31 kg [13]. The body mass of a human lean adult male is 60.4 kg [41] while it was 90.3 kg for the VHM [35]. A degree of positive allometry was found for the upper limb of the baboon and the VHM. Considering the *Pectoralis major*, the ratio of muscle to body mass was 0.0062 ± 0.0016

for baboons and 0.0079 for the VHM with $V_m = 676.4$ cm^3 [17] and density of 1.0597 g/cm^3 [31]. Another expected difference related to the *Pectoralis major* attachment angles: Although not directly measured, these angles were assumed to be larger for the baboon than for the human due to different chest curvature at the implantation site.

The suitability evaluation considered morphometric/physiological parameters with significant and non-significant intra-species effect on F_T in baboons [10]. This was motivated by the fact that a non-significant effect of a parameter in an MLR may stem from; (a) non-linear effect on F_T, (b) intra-specific invariance or (c) negligible or no effect on F_T. The extended assessment addressed this limitation. It was found that experimental parameters with significant effect on F_T remained proportional to their corresponding model parameters when scaled between baboon and human. Of the non-significant parameters, only ψ_1 and ψ_2 did not exhibit a linear relationship with F_T. While ψ_1 and ψ_2 have an influence on F_T according to Eq. (8), they were considered sufficiently invariant in the baboon cohort and hence without significant intra-species effect in the MLR analysis [10]. Due to the substantial differences between baboons and humans, it was, however, required to account for the inter-species effect of the attachment angles on F_T. However, the correction term for the attachment angles in Eq. (10) approaches unity for inter-species similarity of attachment angles, which ensures validity of the proposed transfer function, should future studies indicate such a finding.

The intra-species correlation was considered linearly scale variant between baboons and humans with a body mass of $23 < M_b < 90$ kg on the condition that the effect of the *Pectoralis major* attachment angles was accommodated appropriately. This was achieved by extending the intra-species correlation, Eq. (4) with a correction term based on the mean angles of *Pectoralis major* attachment for the baboon cohort and subject-specific *Pectoralis major* attachment angles for the human. It was possible to provide a function for the prediction of F_T on a sub-muscular pectoral pacemaker implant in a patient. This function employs subject-specific morphometric and physiological parameters that can be determined non- or minimal invasively, e.g., by electromyography and medical imaging. In addition, the function facilitates findings that the maximum muscle stress in a particular muscle is the same in different human subjects [25] and does not differ significantly between males and females despite significant differences in height, weight and muscle strength [30].

As an example of the use of this correlation, consider an in-line force of $F_{IL} = 462$ N reported for the human *Pectoralis major* at maximum voluntary contraction [6]. With a PCSA of 18.3 cm^2 (Table 2), this force results in a stress of $\sigma_m = 0.256$ N/mm^2, based on the relationship $\sigma_m = F_{IL}/\text{PCSA}$ [10]. With the assumption of equal *Pectoralis major* attachment angles in baboon and human, i.e., $(\cos y_1 + \cos y_2)_B/(\cos y_1 + \cos y_2)_H = 1$, length of the *Pectoralis major* along the line of action $L_m = 210$ mm for an adult human (unpublished data), the width $w_m = 89.4$ mm (mean value for baboons from Table 2) assuming equal size of implanted pacemaker in baboon and human, the inter-species transfer function (Eq. 13) provides a transverse force $F_T = 160.5$ N for an adult human.

A constraint of the current study was the small experimental sample size, mainly demonstrating the feasibility of the developed approach for the assessment of in vivo mechanical loading conditions of implantable pacemakers. Further research with larger sample sizes will provide data to verify intra-species correlation and inter-species transfer function established in this study. There may also be potential to refine these relationships by quantifying and extending morphometric parameters and implant dimensions. Additional morphometric parameters can include the thickness of *Pectoralis major* and *Pectoralis minor* at the implant site, the change in thickness of these muscles during contraction, *Pectoralis major* attachment angles, optimal fibre length, pennation angle as well as parameters relating to the compliance of skeletal structures surrounding the implant. While the strength of the intra-species correlation was not affected by the estimation of the muscle parameters $L_f/L_{f,opt}$ and θ [10], the quantification of these parameters can contribute to the validation of the initial values of coefficients a_i of the transfer function. The consideration of repeated load cases at sub-maximum level and potential fatigue, both of which exceeded the scope of the current study, may constitute a further beneficial extension of the presented transfer function.

The inter-species transfer function serves as basis for the prediction of patient-specific mechanical loadings, in particular maximum levels, on a sub-muscular pectoral device implants, such as cardiac pacemakers. Such data will be beneficial for the development of smaller implantable devices while ensuring mechanical integrity and reliability of current designs. In verification studies, the transfer function may be refined to provide additional information required to aid in the design of such implantable devices.

Acknowledgments The authors thank Professor Stephen Beningfield, Petronella Samuels, Sharon Heyne and Nazlea Behardien-Peters of the Department of Radiology, University of Cape Town, for MRI and CT imaging.

References

1. Antretter, H., Colvin, J., Schweigmann, U., Hangler, H., Hofer, D., Dunst, K., Margreiter, J., Laufer, G.: Special problems of pacing in children. Indian Pacing Electrophysiol. J. **3**, 23–33 (2003)
2. Baxter, W.W., McCulloch, A.D.: In vivo finite element model-based image analysis of pacemaker lead mechanics. Med. Image Anal. **5**, 255–270 (2001)
3. Biewener, A.: Scaling of terrestrial support: differing solutions to mechanical constraints of size. In: Brown, J.H., West, G.B. (eds.) Scaling in Biology, pp. 51–65. Oxford University Press, New York (2000)
4. Binder-Macleod, S.A., Lee, S.C.K., Russ, D.W., Kucharski, L.J.: Effects of activation pattern on human skeletal muscle fatigue. Muscle Nerve **21**, 1145–1152 (1998)
5. Brinker, J., Midei, M.G.: Techniques of pacemaker implantation and removal. In: Ellenbogen, K.A., Wood, M.A., Kenneth, A. (eds.) Cardiac Pacing and ICDs, 4th edn, pp. 196–264. Blackwell Publications, Malden (2005)
6. Chang, Y.-W., Hughes, R.E., Su, F., Itoi, E., An, K.-N.: Prediction of muscle force involved in shoulder internal rotation. J. Shoulder Elbow Surg. **9**, 188–195 (2000)

7. Cleland, J.G.F., Daubert, J.-C., Erdmann, E., Freemantle, N., Gras, D., Kappenberger, L., Tavazzi, L.: The effect of cardiac resynchronization on morbidity and mortality in heart failure. N. Engl. J. Med. **352**, 1539–1549 (2005)
8. de Vaal, M.H., Neville, J., Litow, M., Scherman, J., Zilla, P., Franz, T.: Patient-specific prediction of intrinsic mechanical loadings on sub-muscular pectoral pacemaker implants based on an inter-species transfer function. J. Biomech. **44**, 2525–2531 (2011)
9. de Vaal, M.H., Neville, J., Scherman, J., Zilla, P., Litow, M., Franz, T.: The in vivo assessment of mechanical loadings on pectoral pacemaker implants. J. Biomech. **43**, 1717–1722 (2010)
10. de Vaal, M.H., Neville, J., Scherman, J., Zilla, P., Litow, M., Franz, T.: Mechanical loadings on pectoral pacemaker implants: correlation of in-line and transverse force of the *pectoralis major*. Ann. Biomed. Eng. **38**, 3338–3346 (2010)
11. Ding, J., Lee, S.C.K., Johnston, T.E., Wexler, A.S., Scott, W.B., Binder-Macleod, S.A.: Mathematical model that predicts isometric muscle forces for individuals with spinal cord injuries. Muscle Nerve **31**, 702–712 (2005)
12. Eng, C.M., Smallwood, L.H., Rainiero, M.P., Lahey, M., Ward, S.R., Lieber, R.L.: Scaling of muscle architecture and fiber types in the rat hindlimb. J. Exp. Biol. **211**, 2336–2345 (2008)
13. Fleagle, J.G.: Primate Adaption and Evolution, 2nd edn. Academic Press, San Diego (1999)
14. Fortescue, E.B., Berul, C.I., Cecchin, F., Walsh, E.P., Triedman, J.K., Alexander, M.E.: Patient, procedural, and hardware factors associated with pacemaker lead failures in pediatrics and congenital heart disease. Heart Rhythm **1**, 150–159 (2004)
15. Friedman, R.A.: Pacemakers in children: medical and surgical aspects. Tex. Heart Inst. J. **19**, 178–184 (1992)
16. Furman, S.: The future of the pacemaker. Pacing Clin. Electrophysiol. **25**, 1–2 (2002)
17. Garner, B.A., Pandy, M.G.: Musculoskeletal model of the upper limb based on the visible human male dataset. Comput. Methods Biomech. Biomed. Eng. **4**, 99–126 (2000)
18. Hauser, R.G., Hayes, D.L., Kallinen, L.M., Cannom, D.S., Epstein, A.E., Almquist, A.K., Song, S.L., Tyers, G.F.O., Vlay, S.C., Irwin, M.: Clinical experience with pacemaker pulse generators and transvenous leads: an 8-year prospective multicenter study. Heart Rhythm **4**, 154–160 (2007)
19. Hill, T., Lewicki, P.: Statistics Methods and Applications. StatSoft, Tulsa (2007)
20. Holzbaur, K.R.S., Murray, W.M., Gold, G.E., Delp, S.L.: Upper limb muscle volumes in adult subjects. J. Biomech. **40**, 742–749 (2007)
21. Kenny, T.: The Nuts and Bolts of Cardiac Pacing. Blackwell Futura, Malden (2005)
22. Kistler, P.M., Eizenberg, N., Fynn, S.P., Mond, H.G.: The subpectoral pacemaker implant: it isn't what it seems. Pacing Clin. Electrophysiol. **27**, 361–364 (2004)
23. Knaflitz, M., Merletti, R., De Luca, C.J.: Inference of motor unit recruitment order in voluntary and electrically elicited contractions. J. Appl. Physiol. **68**, 1657–1667 (1990)
24. Kron, J., Herre, J., Renfroe, E.G., Rizo-Patron, C., Raitt, M., Halperin, B., Gold, M., Goldner, B., Wathen, M., Wilkoff, B., Olarte, A., Yao, Q.: Lead- and device-related complications in the antiarrhythmics versus implantable defibrillators trial. Am. Heart J. **141**, 92–98 (2001)
25. Li, L., Tong, K., Song, R., Koo, T.K.K.: Is maximum isometric muscle stress the same among prime elbow flexors? Clin. Biomech. **22**, 874–883 (2007)
26. Lieber, R., Fridén, J.: Functional and clinical significance of skeletal muscle architecture. Muscle Nerve **23**, 1647–1666 (2000)
27. Maisel, W.H., Moynahan, M., Zuckerman, B.D., Gross, T.P., Tovar, O.H., Tillman, D.-B., Schultz, D.B.: Pacemaker and ICD generator malfunctions: analysis of food and drug administration annual reports. J. Am. Med. Assoc. **295**, 1901–1906 (2006)
28. Marden, J.H., Allen, L.R.: Molecules, muscles, and machines: universal performance characteristics of motors. Proc. Natl. Acad. Sci. U. S. A. **99**, 4161–4166 (2002)
29. Mattke, S., Muller, D., Markewitz, A., Kaulbach, H., Schmockel, M., Drwarth, U., Hoffmann, E., Steinbeck, G.: Failures of epicardial and transvenous leads for implantable cardioverter defibrillators. Am. Heart J. **130**, 1040–1044 (1995)

30. Maughan, R.J., Watson, J.S., Weir, J.: Strength and cross-sectional area of human skeletal muscle. J. Physiol. **338**, 37–49 (1983)
31. Mendez, J., Keys, A.: Density and composition of mammalian muscle. Metabolism **9**, 184–188 (1960)
32. Pasquet, B., Carpentier, A., Duchateau, J., Hainaut, K.: Muscle fatigue during concentric and eccentric contractions. Muscle Nerve **23**, 1727–1735 (2000)
33. Powell, P.L., Roy, R.R., Kanim, P., Bello, M.A., Edgerton, V.R.: Predictability of skeletal muscle tension from architectural determinations in guinea pig hindlimbs. J. Appl. Physiol. **57**, 1715–1721 (1984)
34. Shmulewitz, A., Langer, R., Patton, J.: Convergence in biomedical technology. Nat. Biotechnol. **24**, 277–280 (2006)
35. Spitzer, V., Ackerman, M.J., Scherzinger, A.L., Whitlock, D.: The visible human male: a technical report. J. Am. Med. Inform. Assoc. **3**, 118–130 (1996)
36. Van Loocke, M., Lyons, C.G., Simms, C.K.: Viscoelastic properties of passive skeletal muscle in compression: stress-relaxation behaviour and constitutive modelling. J. Biomech. **41**, 1555–1566 (2008)
37. Viano, D.C., King, A.I.: Biomechanics of chest and abdomen impact. In: Bronzino, J.D. (ed.) The Biomedical Engineering Handbook, vol. 1, 2nd edn, pp. 398–409. CRC Press LLC, Boca Raton (2000)
38. Vining, G.G.: Statistical Methods for Engineers. Brooks/Cole, London (1998)
39. Voisin, J.L.: Clavivle, a neglected bone: morphology and relation to arm movements and shoulder architecture in primates. Anat. Rec. **288A**, 944–953 (2006)
40. Ward, S.R., Lieber, R.L.: Density and hydration of fresh and fixed human skeletal muscle. J. Biomech. **38**, 2317–2320 (2005)
41. Westerterp-Plantenga, M.S., Goris, A.H.C., Meijer, E.P., Westerterp, K.R.: Habitual meal frequency in relation to resting and activity-induced energy expenditure in human subjects: the role of fat-free mass. Br. J. Nutr. **90**, 643–649 (2003)
42. Wilkie, D.R.: The relation between force and velocity in human muscle. J. Physiol. **110**, 249–280 (1949)
43. Zhang, J.Y., Chen, S.J., Cooke, D.J., Hansgen, A.R., Wu, H.A., Carroll, J.D., Giudici, M.: Analysis of intracardiac lead bending stresses and motion characteristics of RVA versus RVOS pacing leads using an innovative 3-D reconstruction technique. In: Summer Bioengineering Conference, Sonesta Beach Resort in Key Biscayne, Florida (2003)
44. Zhao, Y., Baxter, W., Johnson, B., Schendel, M., McCarty, J., McMahon, C., Lahm, R., Sun, H., Morissette, J., Laske, T., Miller, J.: The use of nonlinear fea modelling to determine the in vivo cardiac pacing lead coils for fatigue evaluation. In: Summer Bioengineering Conference, Sonesta Beach Resort in Key Biscayne, Florida (2003)

Errata to: In Vivo Mechanical Loading Conditions of Pectorally Implanted Cardiac Pacemakers

Thomas Franz, Michael Hamman de Vaal, James Neville, Jacques Scherman, Micah Litow and Peter Zilla

Errata to: In Vivo Mechanical Loading Conditions of Pectorally Implanted Cardiac Pacemakers, DOI 10.1007/8415_2013_160

Figures 1, 3 and 4 are reproduced from Ref. [9] with permission.
Figure 5 is adjusted from Ref. [9] with permission.
Figures 6, 7, 8 and 9 are reproduced from Ref. [10] with permission.
Figures 10, 11, 12, 13 and 14 are reproduced from Ref. [8] with permission.

The online version of the original chapter can be found at 10.1007/8415_2013_160.

T. Franz (✉) · M. H. de Vaal · J. Scherman · P. Zilla
Cardiovascular Research Unit, Chris Barnard Department of Cardiothoracic Surgery, University of Cape Town, Observatory, South Africa
e-mail: Thomas.Franz@uct.ac.za

T. Franz
Programme for the Enhancement of Research Capacity, Research Office, University of Cape Town, Mowbray, South Africa

T. Franz
Centre for Research in Computational and Applied Mechanics, University of Cape Town, Rondebosch, South Africa

J. Neville
Cardiac Rhythm Disease Management, Medtronic Inc, Minneapolis, MN, USA

M. Litow
Neuromodulation Division, Medtronic Inc, Minneapolis, MN, USA

Stud Mechanobiol Tissue Eng Biomater (2014) 15: 239–239
DOI: 10.1007/8415_2013_167

Published Online: 15 March 2014

Errata to: Development of a Fabric-Reinforced Porous Graft for Vascular Tissue Engineering Using Finite Element Methods and Genetic Algorithms

Mark S. Yeoman, B. Daya Reddy, Deon Bezuidenhout, Hellmut C. Bowles, Peter Zilla and Thomas Franz

Errata to: Development of a Fabric-Reinforced Porous Graft for Vascular Tissue Engineering Using Finite Element Methods and Genetic Algorithms, DOI 10.1007/8415_2013_162

Figures 1, 2, 3, 4, 5 and 6 are reproduced from Ref. [27] with permission.
Figures 8, 9, 10, 11 and 12 are reproduced from Ref. [28] with permission.

The online version of the original chapter can be found at 10.1007/8415_2013_162.

M. S. Yeoman (✉)
Continuum Blue Ltd., Tredomen Innovation and Technology Park, Hengoed, UK
e-mail: mark@continuum-blue.com

B. D. Reddy
Centre for Research in Computational and Applied Mechanics,
University of Cape Town, Cape Town, South Africa

D. Bezuidenhout · P. Zilla · T. Franz (✉)
Cardiovascular Research Unit, Chris Barnard Division of Cardiothoracic Surgery,
Faculty of Health Sciences, University of Cape Town, Private Bag X3, Observatory,
Cape Town 7935, South Africa
e-mail: thomas.franz@uct.ac.za

H. C. Bowles
Finite Element Analysis Services (Pty.) Ltd., Parklands, South Africa

T. Franz
Research Office, University of Cape Town, Cape Town, South Africa

T. Franz
Centre for Research in Computational and Applied Mechanics, University of Cape Town,
Cape Town, South Africa

Stud Mechanobiol Tissue Eng Biomater (2014) 15: 241–241
DOI: 10.1007/8415_2013_168

Published Online: 7 March 2014

Author Index

Stud Mechanobiol Tissue Eng Biomater
DOI: 10.1007/978-3-642-53836-0